Application of numerical simulation for a better characterization of red blood cells by impedance measurement

Pierre Taraconat

THÈSE POUR OBTENIR LE GRADE DE DOCTEUR
DE L'UNIVERSITE DE MONTPELLIER

En Mathématiques et Modélisation

École doctorale : Information, Structures, Systèmes

Unité de recherche : Institut Montpelliérain Alexander Grothendieck

Application of numerical simulation for a better characterization of red blood cells by impedance measurement

Présentée par Pierre Taraconat

Le 17/01/2020

Sous la direction de Franck Nicoud
et Simon Mendez

Devant le jury composé de

Franck Nicoud	Professeur, IMAG - Univ. Montpellier	Directeur
Simon Mendez	Chargé de recherche, IMAG - Univ. Montpellier	Co-directeur
Julien Favier	Maître de conférences, M2P2 - Univ. Aix-Marseille	Rapporteur
Thomas Podgorski	Directeur de recherche, LIPhy - Univ. Grenoble Alpes	Rapporteur
Annie Viallat	Directrice de recherche, CINaM - Univ. Aix-Marseille	Présidente du jury
Magalie Faivre	Chargée de recherche, INL - Univ. Claude Bernard Lyon	Examinatrice
Damien Isèbe	Ingénieur de recherche, HORIBA Medical SAS - Montpellier	Invité

UNIVERSITÉ
DE MONTPELLIER

Résumé

La Numération Formule Sanguine (NFS) est un des examens les plus prescrits dans le monde car il fournit aux praticiens une information sur l'état de santé global du patient. De manière générale, une NFS recense les différentes cellules sanguines, tels que les globules rouges (GRs), les globules blancs et les plaquettes. En outre, une mesure du volume de ces cellules est également fournie. Ces analyses sont aujourd'hui pratiquées en routine à l'aide d'automates d'hématologie assurant une analyse rapide des échantillons : environ 120 tests par heure.

La majorité des modules composant les automates d'hématologie actuels découlent du principe Coulter [21], qui consiste à aspirer les cellules une par une pour les faire passer dans une zone de détection. Le concept originel est illustré sur la Fig. 1: les cellules sont diluées dans une solution électrolytique et aspirées à travers un micro-orifice dans lequel un fort champ électrique est imposé par deux électrodes. Ainsi, la cellule, isolante, engendre une augmentation de résistance lorsqu'elle traverse l'orifice, ce qui se traduit par une perturbation de tension aux bornes des électrodes, que l'on désignera par le terme "pulse". En comptant les pulses, on dénombre les cellules, et l'amplitude du pulse est considérée proportionnelle au volume de la particule associée. Notamment, les travaux théoriques de Kachel [74, 75] donnent le volume de la particule V_p en fonction du maximum de la perturbation

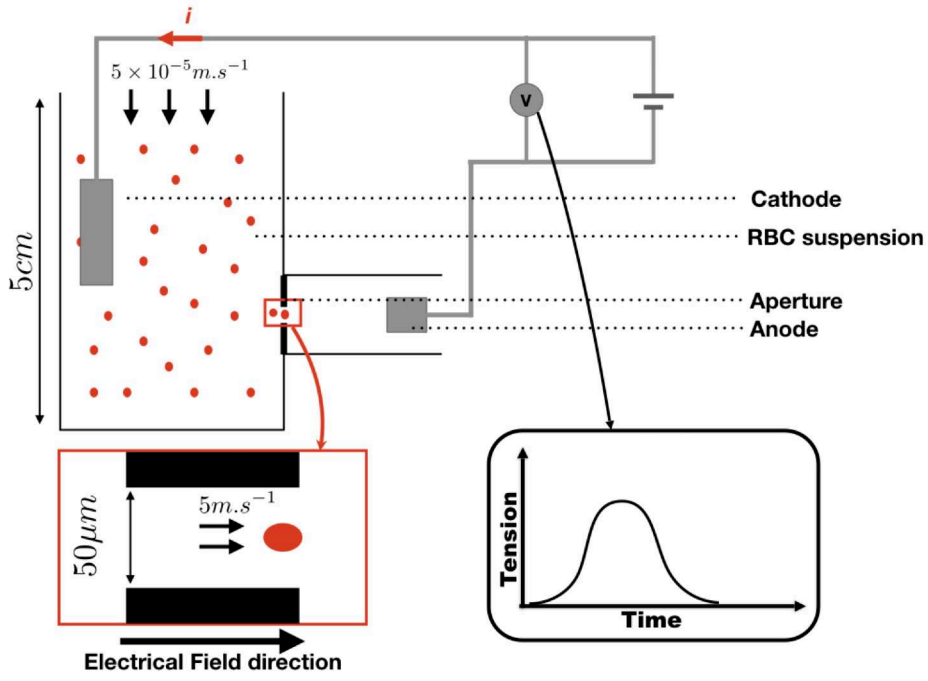

Figure 1 – Principe de détection pour le comptage et la volumétrie des cellules par principe Coulter.

électrique ΔU_m comme suit :

$$V_p \propto \frac{1}{E^2 f_s} \Delta U_m, \tag{1}$$

avec E, le champ électrique vu par la cellule, et f_s, le facteur de forme dépendant de la forme et de l'orientation de la particule. Ce système simple a été amélioré et complexifié plus récemment afin de fournir des analyses plus fines et complètes des éléments figurés du sang en utilisant notamment des circuits fluidiques plus sophistiqués. Cependant, la mise en application du système original est encore très répandue, notamment grâce à son faible coût de production. Cette thèse s'intéresse à l'analyse des GRs par les systèmes classiques tel qu'illustrés sur la Fig. 1.

Utilisés de manière intensive depuis le milieu du siècle dernier, on pourrait penser que les compteurs Coulter sont parfaitement connus et maitrisés. Au contraire, plusieurs artéfacts de mesure pouvant conduire à des erreurs sont toujours mal compris. Ces artéfacts s'expliquent par un champ électrique E inhomogène dans la zone de détection et par des variations de f_s découlant des déformations et rotations du GR. Etant donné que E et f_s ne sont pas fixes, il devient impossible d'évaluer V_p par une mesure de ΔU_m (voir Eq. 1). Ces effets se produisent lorsqu'une cellule évolue près des parois de l'orifice. En effet, dans cette région, sont observés un champ électrique fortement inhomogène et d'importants taux de cisaillements du champ de vitesse pouvant conduire à des dynamiques complexes de la cellule. Dans les systèmes commerciaux actuels, ces défauts sont contournés par des mises en oeuvre plus complexes du principe Coulter, ou par des approches de filtrage des signaux associés à des passages proches paroi. Parmi ces méthodes, on peut trouver la 'focalisation-hydrodynamique' [154] ou le tri par seuillage du temps de passage [173]. L'hydrofocalisation force les cellules à emprunter des trajectoires au centre de l'orifice pour s'affranchir totalement des effets de bord, mais implique une mise en oeuvre plus compliquée. En partant du postulat que les cellules passant près des murs sont transportées à des vitesses plus faibles, la méthode de tri proposée par Waterman [173] consiste à rejeter les pulses les plus longs. Cependant, la durée du pulse est fonction du volume de la particule, rendant ainsi la calibration du seuil de tri difficile. De plus, il s'avère en pratique que les méthodes de tri actuelles ne s'affranchissent pas totalement des effets de bord.

Pour résumer, dans les systèmes classiques, des artéfacts de nature électrostatique et dynamique faussent les mesures et sont toujours incompris. En outre, les déformations du GR induites par les forts gradients de vitesse proches des parois influent sur la forme du pulse au travers de f_s. Il est donc probable que la signature électrique contienne une information sur la forme et la deformabilité du GR. Il est à noter que bon nombre de pathologies affectant les GRs influent sur leur forme et leur déformabilité (malaria [48, 112, 115, 115, 143], sphérocytose [5, 123], elliptocytose [18, 163], sickle cell [118, 138]). Ainsi, les travaux effectués dans cette thèse sont dédiés à la compréhension des phénomènes en jeu lorsqu'un GR évolue proche des murs de l'orifice, et au traitement des informations morphologiques et rhéologiques contenues dans les pulses associés à de telles trajectoires.

S'attaquer à ces problématiques avec une approche expérimentale s'avèrerait compliqué en raison des problèmes d'accessibilité de la zone de mesure: taille de

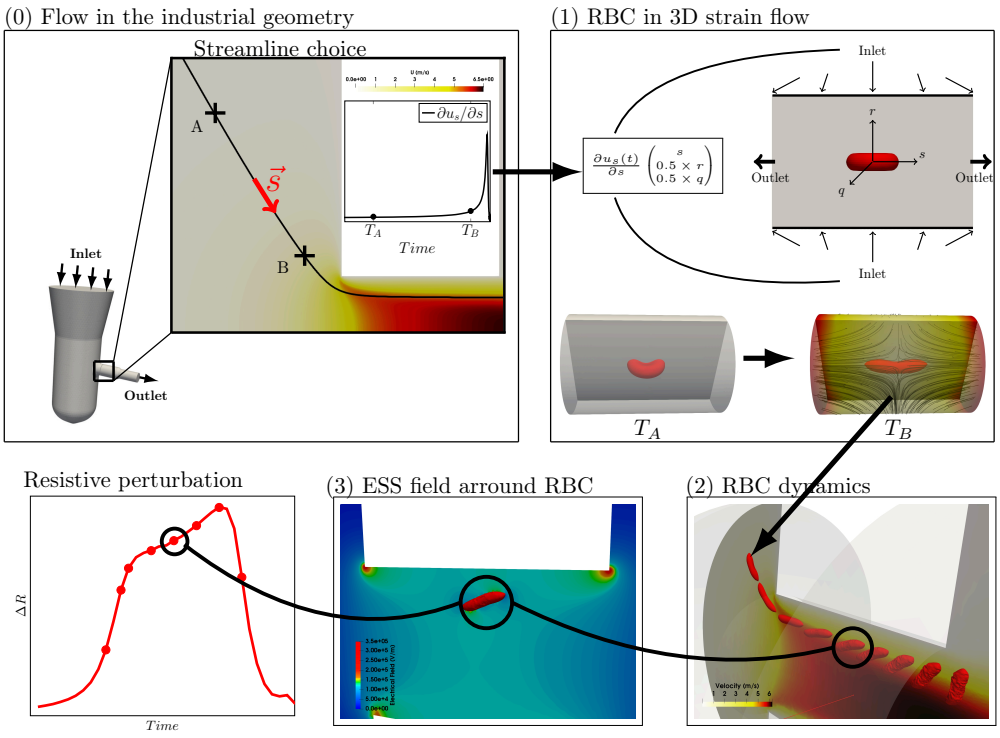

Figure 2 – Simulation numérique de la mesure d'impédance dans un compteur Coulter industriel.

l'orifice (quelques microns), vitesse de passage des cellules (plusieurs m.s^{-1}), pas de fenêtre optique sur la zone de mesure. C'est pourquoi une approche numérique est retenue pour ces travaux.

Simuler le comportement d'une particule déformable dans un compteur Coulter induit une problématique des rapports d'échelle : loin en amont de l'orifice la particule évolue sur une longue distance à des faibles vitesses, alors qu'elle est détectée dans un orifice de quelques microns ou elle avance à des vitesses de l'ordre de 5 m.s^{-1} (voir Fig. 1). Ainsi, simuler l'évolution entière d'un GR dans le compteur Coulter n'est pas possible à cause du temps de calcul requis pour la partie amont, alors que la zone d'interêt est limitée au voisinage de la perforation. Les premiers chapitres traitent de cette problématique. Plus particulièrement, une méthode permettant de s'affranchir de ces problèmes d'échelles est proposée [162] et illustrée sur la Fig. 2. Elle consiste à simuler la dynamique du GR en deux parties (1 et 2 sur la Fig. 2). La première (1) est une configuration d'écoulement extensionnel qui mime l'élongation de la cellule dans la partie en amont de la zone de détection. La pertinence de cette simulation est validée par comparaison avec un calcul fait dans la configuration réelle complète, sur la partie amont de l'orifice. Une fois étiré (résultat du calcul 1), le GR est placé juste avant l'entrée de l'orifice dans un domaine réduit de la configuration industrielle, afin de calculer la dynamique du GR dans la zone de détection (2). La perturbation du champ électrique associée à la dynamique de la cellule est calculée séparément par une série de simulations électrostatiques (3). Le pulse électrique est déduit en post-traitement des calculs électrostatiques (4). Il est important

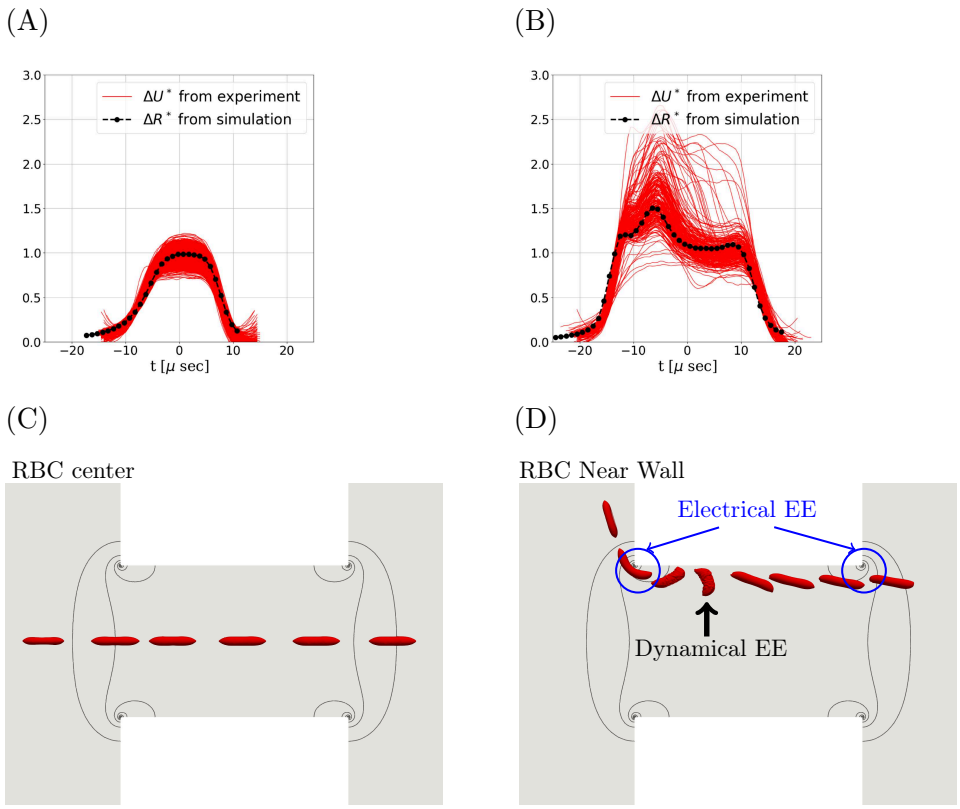

Figure 3 – Comparaison des résultats numériques avec des pulses provenant d'une acquisition expérimentale obtenue en analysant un échantillon de sang (A et B). Les dynamiques du GR correspondant aux illustrations A et B sont représentées en C et D, respectivement.

de noter que la simulation dans la configuration extensionnelle (1) requiert le taux d'écoulement perçu par la cellule lorsqu'elle se déplace dans la partie en amont de l'orifice. C'est pourquoi un calcul sans particules dans la configuration totale du compteur Coulter est nécessaire (0). Une ligne de courant (LDC) provenant de ce calcul préliminaire peut être extraite. L'évolution temporelle du taux d'écoulement le long de la LDC choisie est donnée en paramètre du calcul (1), comme illustré sur la Fig. 2.

Cette méthode a été validée au regard des lois empiriques et par comparaisons avec des résultats expérimentaux. Par exemple, la Fig. 3 superpose des résultats numériques avec des données expérimentales, pour des GRs. Les pulses ont été simulés en considérant un GR passant au milieu de la zone de détection et proche de la paroi (A et B, respectivement). Plus précisément, une LDC passant par le centre de l'orifice est retenue pour obtenir le pulse numérique montré sur la Fig. 3A, alors que la Fig. 3B provient d'une LDC passant à 5 μm de la paroi. Les dynamiques de GR associées aux pulses numériques illustrés en A et B sont montrées en C et D, respectivement.

Les résultats numériques mettent en lumière les effets de bord de type hydrodynamique et électrique (voir Fig. 3D). Pour un passage au centre, une signature

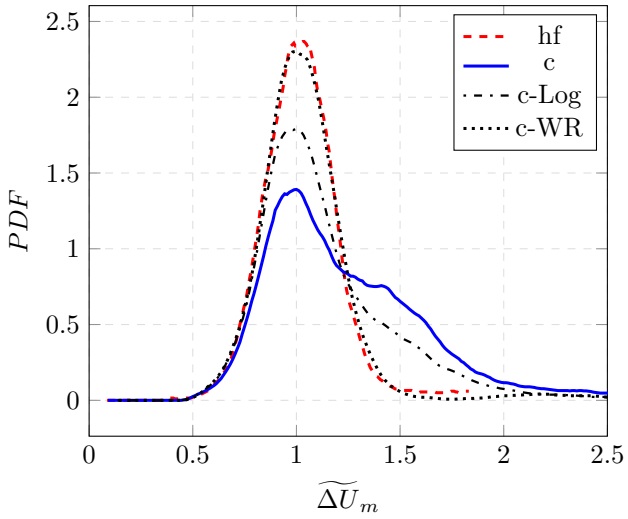

Figure 4 – Distributions des hauteurs de pulse obtenues sur un système hydrofocalisé (hf) et un système classique (c), avec différentes méthodes de tri ($c-Log$ et $c-WR$). Le cas $c-Log$ est obtenu à l'aide du tri actuellement employé dans les automates d'HORIBA Medical, alors que $c-WR$ est obtenu avec la méthode de tri proposée dans cette thèse.

électrique simple en forme de 'cloche' est obtenue (voir Fig. 3A), alors qu'un pulse affecté par les effets de bord est plus complexe (voir Fig. 3B). En évoluant près de la paroi, le GR tourne ce qui produit un pic sur le pulse, et tend à surestimer le volume mesuré (le maximum du pulse). En effet, en prenant le maximum du pulse comme mesure du volume, la taille de la cellule sera évaluée plus grande pour une trajectoire au bord que pour une trajectoire centrale (voir Fig. 3A et B). Dans le Chap. 5, il est proposé de détecter la rotation de la cellule à partir de la forme du pulse associé pour avoir un meilleur tri de signaux et une meilleure volumétrie des particules. Il est également montré que cette nouvelle méthode de tri fournit des résultats similaires à l'hydrofocalisation, qui est un système coûteux permettant de forcer les GRs à passer au centre des orifices, ce qui élimine les artéfacts de mesure. Sur la Fig. 4, on compare la distribution de $\widetilde{\Delta U}_m$ (ie. maximum des pulses) obtenue à l'aide d'un système hydrofocalisé ('hf') avec des distributions obtenues avec un système classique, pour différentes méthodes de tri ('c', '$c-Log$', '$c-WR$'). Le cas 'c' fait référence à l'acquisition classique, sans tri appliqué. La distribution référencée par '$c-Log$' est obtenue après application de la méthode de filtrage implémentée dans les automates d' HORIBA Medical. Enfin, la distribution '$c-WR$' est obtenue grâce au tri proposé dans cette thèse. On constate qu'avec l'hydrofocalisation, la distribution des volumes (ie. hauteurs de pulse) est symétrique et Gaussienne (cas 'hf'), alors que sur le système classique les volumes mesurés sont dissymétriques ('c'). Le tri '$c-Log$' améliore la symétrie de la distribution mais le résultat n'est toujours pas en accord avec l'hydrofocalisation. En revanche la méthode proposée ('$c-WR$') est symétrique et se superpose au résultat provenant du système hydrofocalisé.

Les signaux rejetés par le tri discuté ci-dessus sont impactés par les effets de

bord et contiennent potentiellement une information sur la déformabilité et la forme des cellules. Le Chap. 6 est dédié au traitement de ces informations. Par exemple, dans une approche expérimentale, la morphologie et la rhéologie des cellules dans un échantillon ont été modifiées, et les signaux générés lors de l'analyse ont été enregistrés. En soumettant l'échantillon à des molécules de glutaraldehyde, des GRs plus rigides sont obtenus. De plus, l'ajout de SB3-12 (fournit par Sigma-Aldrich) dans la solution électrolytique tend à rendre les GRs sphériques. Des acquisitions faites à plusieurs concentrations en SB3-12 et glutaraldehyde montrent des résultats en dehors d'une normalité préétablie. On a notamment pu définir des métriques (non détaillées ici) qui mettent en exergue les acquisitions faites sur des échantillons anormaux (dans lesquels du SB3-12 ou du glutaraldehyde a été ajouté).

Les méthodes discutées ci-dessus ne sont pas adaptées pour detecter des anomalies n'affectant qu'une petite proportion des cellules. Détecter des sous-populations implique un diagnostic de l'anormalité à l'échelle du pulse et non à l'échelle de l'acquisition. Autrement dit, il faut répondre à la question : est-ce que le pulse provient d'un GR normal ou anormal? Des investigations allant dans ce sens sont proposées dans le Chap. 6. Les méthodes retenues pour déterminer si la cellule est anormale au regard du pulse associé sont basées sur des modélisations par réseaux de neurones. Par exemple, la Fig. 5 concerne la modélisation par un réseau de neurones du problème qui consiste à classifier les pulses en trois familles suivant si ils ont été générés par un GR normal, traité au SB3-12 (anormalement sphérique) ou traité au glutaraldehyde (anormalement rigide). L'architecture du modèle est représentée sur la Fig. 5A et la précision du modèle après l'apprentissage est renseignée sous la forme d'une matrice de confusion en Fig. 5B. Il est à noter que la matrice de confusion est évaluée à partir d'un jeu de données qui n'a pas été impliqué dans la phase d'apprentissage. Montrant une précision supérieure à 92 % pour chaque classe, ce modèle est encourageant et ouvre la voie à la détection de sous populations de GRs pathologiques. En outre, il est possible de détecter le type d'anomalie (ie. rigide ou sphérique) à partir du pulse. Par conséquent, être spécifique sur le type de pathologie peut également être envisagé par ce type de méthode.

En résumé, les travaux effectués s'intéressent aux systèmes d'analyse cellulaires par la mise en oeuvre du principe Coulter originel. Une méthode numérique pour simuler le comportement des GRs dans ces systèmes est introduite. Cette dernière est validée par comparaisons avec une approche expérimentale, et semble donc reproduire les principaux mécanismes en jeu. De manière inédite, cette étude numérique propose des scenarii crédibles expliquant les pulses complexes générés par des passages proches-paroi. Cette compréhension nouvelle des signaux a permis l'élaboration de critères de tri fournissant une mesure plus précise du volume des cellules. Enfin, dans une approche expérimentale, il est montré que les pulses induits par des passages proche paroi sont sensibles à la forme et à la deformabilité du GR. De plus, des méthodes dédiées au traitement des informations de morphologie et de rhéologie cellulaire sont proposées.

(A)

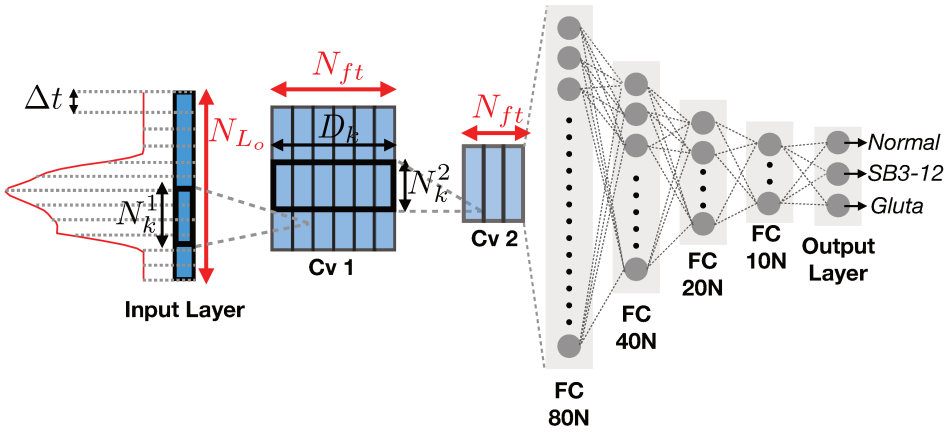

(B)

Confusion Matrix	Targeted Normal	Targeted SB3-12	Targeted Gluta
Normal	96.0 %	1.0 %	3.0 %
SB3-12	2.4 %	92.5 %	5.1 %
Gluta	4.4 %	3.9 %	91.8 %

Figure 5 – Modélisation par réseau de neurones pour la classification des GRs à partir des pules d'impédance. (A) Architecture du modèle, qui prend une pulse en entrée (voir 'input layer') et renvoie le résultat de la classification : GR normal, GR traité au SB3-12, GR traité au glutaraldehyde. (B) Matrice de confusion évaluée sur un jeu de données de test, après l'apprentissage du modèle.

Contents

Chapter 1

Introduction

Chapter contents

1.1 Context

The work presented in this thesis was performed in the framework of a collaboration between HORIBA Medical and IMAG ('Institut Montpelliérain Alexander Grothendieck'). HORIBA Medical is the segment among the five branches of the group HORIBA that is dedicated to the development and the manufacturing of haematological automata. At IMAG, numerical software devoted to the analysis of medical devices in contact with blood is developed (YALES2BIO https://imag.umontpellier.fr/~yales2bio/).

Coulter counters are empirical systems dating back to the middle of the last century and make part of the current haematological instruments. They allow the counting and the volumetry of blood cells by monitoring their electrical print when they flow in a sensing zone. The blood analysis provided by such systems is an essential part of clinical diagnosis, which makes blood analysis one of the most frequent medical analysis performed worldwide. Because haematological analysis provided by industrial automata is nowadays a common practice, it might be thought that Coulter counters are perfectly mastered. However, it appears that misunderstood artefacts falsify the volume measurements of cells and the information contained in results from Coulter counters is not fully exploited.

Motivated by recent increases in computers power, numerical simulation has encountered major breakthroughs and intended to provide relevant indications on the dynamics of blood cells in Coulter counters, and the associated electrical prints. The purpose of this work is to bring new insights on the empirical haematological system by the use of numerical simulation and to elaborate methods for a more complete and accurate diagnosis of the analysed cells. For this purpose, associating the strong industrial expertise of HORIBA Medical (that has been on the haematological market for decades) with the knowledge and tools developed at IMAG appears to be a suited approach.

Hence, in this first chapter, grounding concepts on haematology, Coulter counter, and numerical simulation are given.

1.2 Basic concepts in haematology

1.2.1 Composition and principal functions of blood

Human tissues need to be supplied continuously in oxygen and nutrients to ensure the vital functions of the human body. In addition, wastes produced by human tissues such as carbon dioxide must be evacuated. These two essential tasks are maintained during the entire life of living beings by the cardiovascular system. It is composed of the blood vessels and of the heart, a muscle ensuring an uninterrupted flow of blood that contains the aforementioned substances.

Blood is made up of a carrying fluid called plasma and blood cells, such as Red Blood Cells (RBCs), white blood cells and platelets (see Fig. 1.1). The plasma is a fluid mostly composed of water (around 90 %) in which are diluted a variety of substances like hormones, proteins or urea. RBCs are in charge of the transport of dioxygen from the lungs to the different organs and the removal of carbon dioxide, waste of the organs works. They represent about 45% of the total blood volume and 98% of the total number of cells in suspension in the plasma. Platelets are small cell fragments that play a role in the coagulation reaction that occurs in case of injuries of the blood vessel endothelium. White blood cells are the cells of the immune system and fight off foreign germs, bacteria or viruses, for instance.

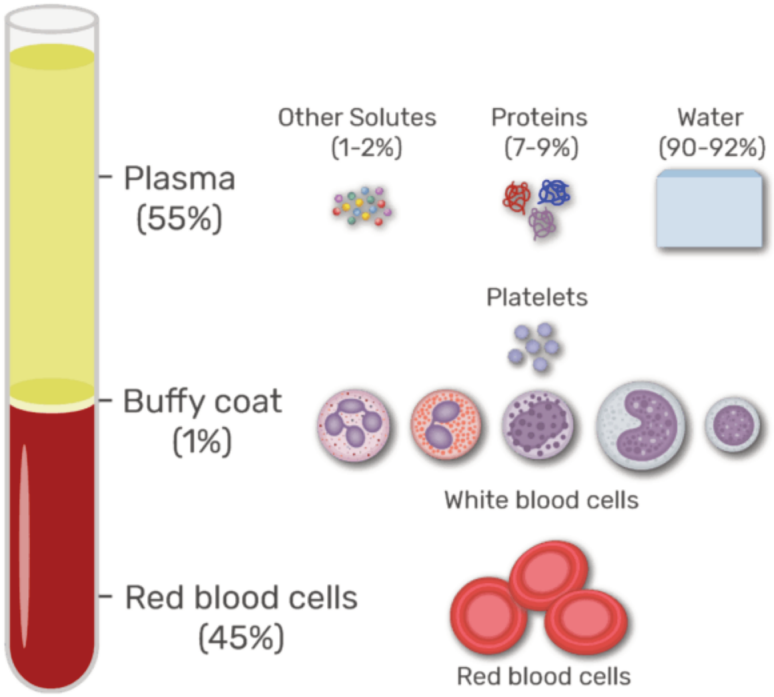

Figure 1.1 – Blood composition.

1.2.2 Haematopoiesis

Each type of blood cells has a specific role, but all of them originate from the bone marrow in which they are produced in a process called hematopoiesis (see Fig. 1.2). All blood cells arise from the evolution of a stem cell called hemocytoblast. In the bone marrow, hemocytoblasts may undergo various evolutions that are represented by the different branches in Fig. 1.2.

The branch denoted by thrombopoiesis in Fig. 1.2 refers to the platelet production. The initial stem cell evolves to a megakaryocyte in the bone marrow. Being too large to join the blood circulation, megakaryocytes split in several cell fragments (called platelets) when leaving the bone marrow to enter in the circulating blood.

RBCs stem from the erythropoiesis (see Fig. 1.2) in which the stem cell matures through erythroblast and reticulocyte stages. Between these two steps, the erythroblast loses its nucleus to become a reticulocyte (a better view is given in Fig. 1.3A and B, respectively). Reticulocytes are RBCs (or erythrocytes) that contains RNA that will disappear after a few days (about 72 hours). Some of the reticulocytes complete their maturation to RBCs in the blood circulation. A normal concentration of reticulocytes in the blood is around 80 000/mm^3, which represents about 1% of the RBCs population. However, if the RBCs production is abnormally high, the circulating blood contain more reticulocytes and even erythroblasts. This may occur in case of severe hemorrhage, bleeding, or regenerative anemia. Note that RBCs are the sole enucleated cells, allowing them to deform and cross microscopic blood vessels, called microcapillaries. This is where most of gases exchanges (dioxygen and carbon dioxide) take place.

Branches referred to as granulopoiesis, monocytopoiesis and lymphopoiesis illustrate the genesis of the three main types of white blood cells (viz. granulocytes, monocytes, and lymphocytes, respectively) that are shown in Fig. 1.3D, E and F. The three main populations of white blood cells may be subdivided into more subpopulations. For example, granulocytes originating from granulopoiesis (see Fig. 1.2) include basophils, neutrophils, and eosinophils. Each population of white blood cell is dedicated to the safeguard against specific foreign invaders. This means that an abnormal population of a specific white blood cell type may provide information on the kind of infection the immune system faces. Granulocytes (basophils, neutrophils, and eosinophils) have characteristic sizes between 11 μm and 15 μm, while monocytes are the biggest with sizes included in between 15 μm and 25 μm. Regarding lymphocytes, specifically 'small lymphocytes' (see Fig. 1.2), sizes around 9 μm are generally encountered whereas 'large lymphocytes' have sizes similar to granulocytes. However, these latter ('large lymphocytes') represent only 10% of lymphocytes.

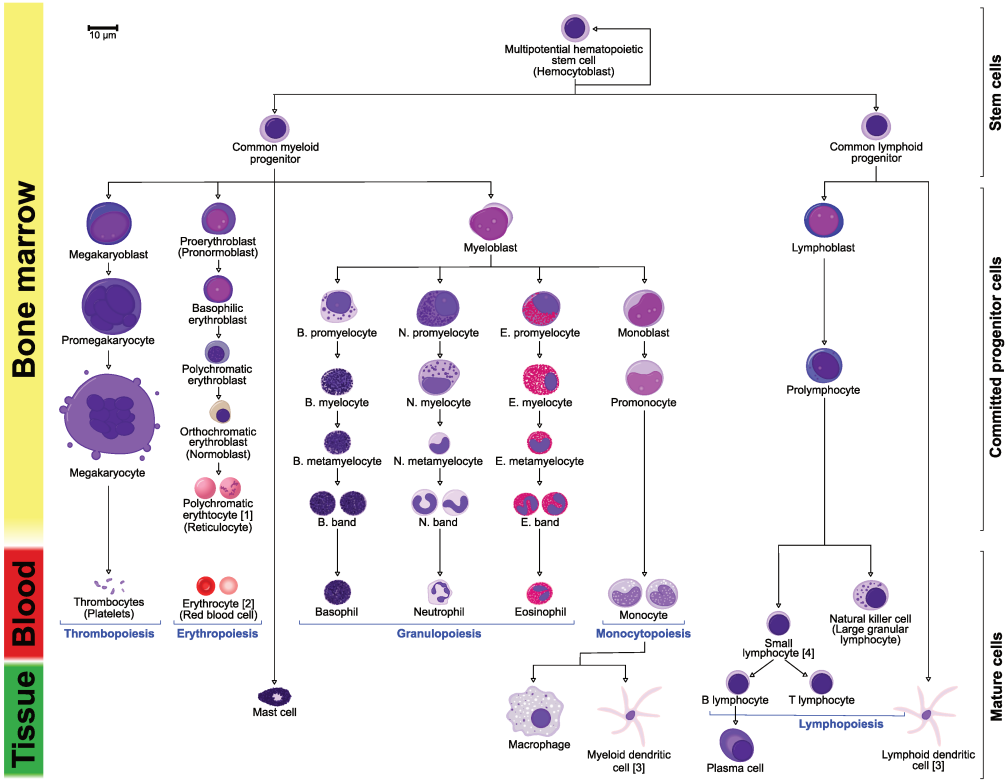

Figure 1.2 – Haematopoiesis: evolution of the initial multi-potential stem cell to blood cells (coming from https://en.wikipedia.org/wiki/Haematopoiesis)

1.2.3 Haematological parameters currently available in industrial automata

Haematology is the science dedicated to the study and the treatment of blood diseases. This includes the study of pathologies affecting directly plasma and blood

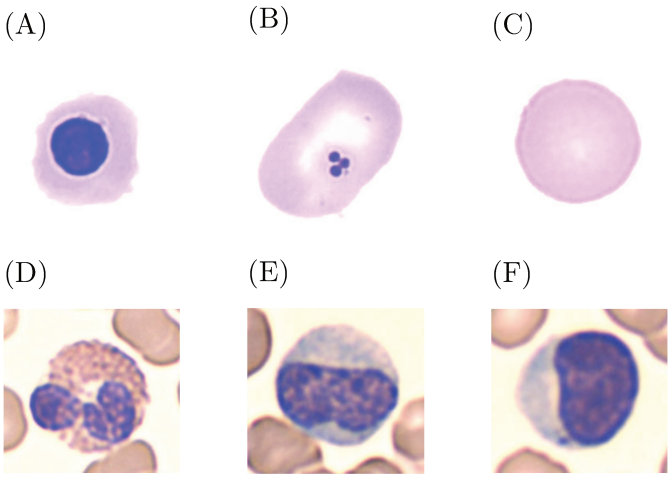

Figure 1.3 – Microscope views of blood cells. (A) erythroblast, (B) reticulocyte, (C) erythrocyte, (D) granulocyte, (E) monocyte, (F) lymphocyte.

cells, but also disorders in their production. Measuring the concentration and the size of white blood cells provides information on the presence of undesirable foreign agents such as bacteria and viruses, but also on inflammations. Defaults in organs oxygenation are deduced from abnormal RBCs populations. Consequently, numbering and sizing blood cells provide clinicians with a global idea on the patient health state. Since the middle of the 20th century, haematological automata rendering rapidly and automatically a Complete Blood Count and differentiation of cells (CBC+DIFF) have been commercialized. The efficiency, the moderate cost and the rich indications provided by haematological automata make the CBC+DIFF exam one of the most performed clinical analysis (about 80 CBC+DIFF each minute in the US in 2014). Table. 1.1 gives a non-exhaustive list of parameters evaluated by haematological automata. Parameters related to blood cells concentrations are provided (RBC, PLT, WBC, Monocytes, Lymphocytes, Granulocytes). Parameters giving indications on RBCs and platelets volumes (MCV, RDW, MPV) may also be found in CBC+DIFF outcomes. Note that haemoglobin contained in RBC is also measured (Hb). This may be done by absorbance measurement. An idea of the normal range is also provided in Tab. 1.1 although it should be noted that the normality depends on the sex, the ethnic group, and the age of the patient [83, 157]. This must be accounted for in the diagnosis based on CBC outcomes.

Haematological parameters are of first importance in the clinical decision making. In particular, a combination of MCV and RDW was historically used for a classification of anemias[34, 44], but more recently RDW arouse interest of many research groups as a marker of various human disorders such as: inflammatory Bowel disease [178], heart failure [99], coronary artery disease [92] and cancers[82, 93, 145], for instance. The reader is referred to the synthesis work of Salvagno *et al.*[144] for an overview of pathologies related to RDW.

Most of the parameters provided in CBC+DIFF are related to cells volumes and their concentration. In the following section, the empirical method introduced by Coulter [21] to assess such quantities is presented.

Parameter	Normal range Min	Max	Description
RBC [10^{12}/L]	4.01	6.04	RBCs concentration.
MCV [fL]	80	100	Mean Cell Volume (MCV) of RBCs.
RDW [%]	12.2	15.4	RBCs Distribution Width, giving an indication on the volume distribution around the MCV.
Hb [g/L]	130	180	Haemoglobin concentration.
Hct [%]	33	50	Hematocrit.
WBC [10^9/L]	4	11	White Blood Cells concentration.
Monocytes [10^9/L]	0.2	0.8	Monocytes concentration.
Lymphocytes [10^9/L]	1.5	4.5	Lymphocytes concentration.
Granulocytes [10^9/L]	2.0	8.0	Granulocytes concentration.
PLT [10^9/L]	150	450	Platelets concentration.
MPV [fL]	8	14	Mean platelets volume.

Table 1.1 – Typical haematological parameters rendered in a Complete Blood Count and differenciation of cells (CBC+DIFF) and the associated range of normal values.

1.3 Coulter counters

Some of the haematological parameters currently provided in CBC+DIFF require the counting and the sizing of blood cells. In 1953, Coulter [21] introduced a fast and automatic device dedicated to the numeration of a large number of microscopic cells and the measurement of their volume.

The Coulter principle is depicted in Fig. 1.4: particles suspended in an electrolytic solution are pumped into a micro-orifice commonly called aperture, sapphire or ruby. An electrical field is imposed with a constant intensity using two electrodes. According to Ohm's law, a particle flowing through the sapphire changes the total resistivity of the system and induces a tension pulse. If sufficiently separated from the others, one particle produces one pulse, and its maximum is assumed to be proportional to the particle volume. Thus, counting the pulses and measuring their amplitude give the concentration and the volume distribution of the cells.

A typical volume distribution obtained by analyzing directly a blood sample is shown in Fig. 1.5A. Two blood cells types appear in the distribution: RBCs, corresponding to the larger cells with volumes around 90 μm^3; platelets, observed at low volumes around 10 μm^3. As stated in Tab. 1.1, platelets are fewer than erythrocytes, thus explaining their low count compared to RBCs. The volume distribution of RBCs is right-skew, which is a typical result of Coulter counters[12]. This point is discussed in detail in the following sections. Because of their small concentration (see Tab. 1.1), white blood cells are not visible in Fig. 1.5A. They are expected to account for in the RBCs population but are negligible from a statistical point of view. Measuring the white blood cells populations requires to first lyse the RBCs before the sample analysis. Using the ABX Minilyse LMG reagent (HORIBA Medical), the three kinds of white blood cells are observable. This solution ensures the RBCs lysis and affects white blood cells populations in such a way they may be

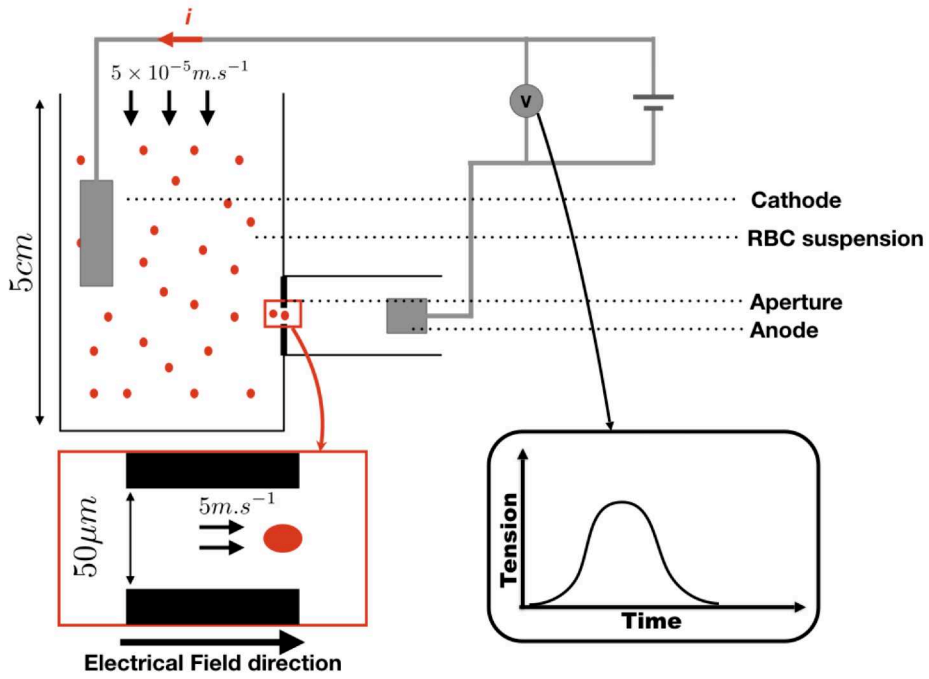

Figure 1.4 – Principle of a Coulter counter device for particle counting and sizing and typical orders of magnitude of size and flow velocity.

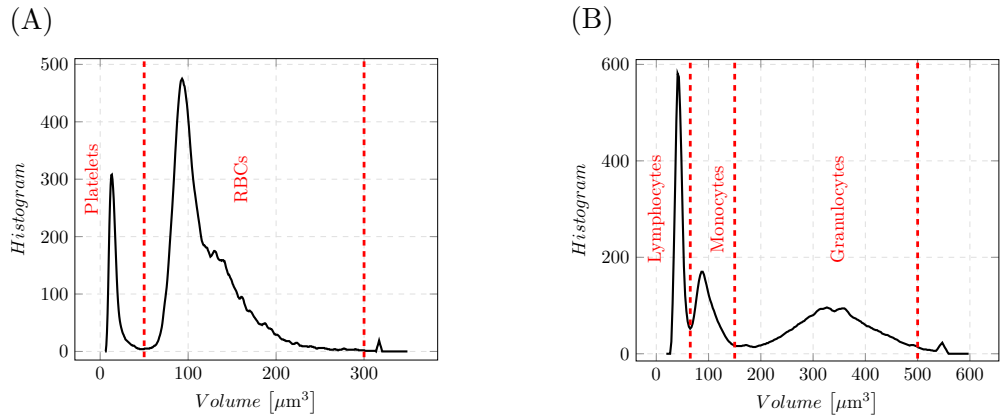

Figure 1.5 – Typical volume histograms obtained by analysing a blood sample with a Coulter counter. (A) is obtained when the blood sample is analysed directly. (B) is obtained by diluting the blood sample in a ABX Minilyse LMG solution (HORIBA Medical) : RBCs are lysed and the three main types of white blood cells are visible.

segregated with size criteria. The Coulter principle thus allows the differentiation of three types of white blood cells. However, more complex systems equipped with an optical sensor can separate the three subtypes of granulocytes. Such systems are often included in top-of-the-range automata.

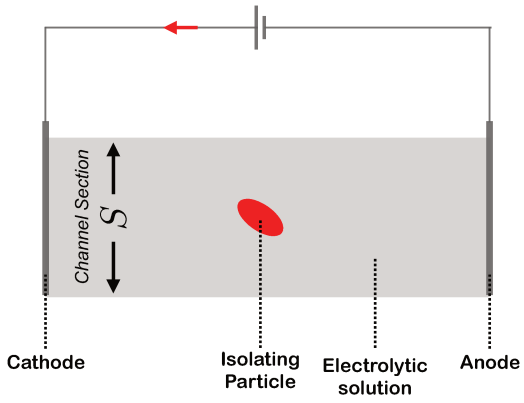

Figure 1.6 – Simplified configuration of a detection aperture used in theoretical studies.

1.3.1 Theoretical background for cells volumetry

Analytical studies of Grover *et al.* [53] and Hurley [68] show that the change of resistivity caused by the presence of an infinitely small and insulating particle in a homogeneous electrical field is proportional to its volume:

$$\Delta R = \frac{\rho_e f_s}{S^2} V_p, \tag{1.1}$$

with ΔR the resistance variation, V_p the particle volume, ρ_e the fluid resistivity, S the aperture cross-section and f_s the particle shape factor depending on the shape and the orientation of the cell. The configuration considered in analytical developments is illustrated in Fig. 1.6. The homogeneity of the electrical field is allowed whether the cathode and anode are located at the channel inlet and outlet (see Fig. 1.6). Furthermore, the particle must be small compared to the aperture so that the electrical field is disturbed only in the close neighbourhood. Regarding Eq. 1.1, the measurement of the change of resistivity yields the particle volume if and only if its shape and its orientation are constant. RBCs are able to deform and reorient when submitted to hydrodynamic forces, which may cause changes in their shape factor. Note also that the electrical field in the sensing zone is not homogeneous owing to the device geometry, as shown in numerical simulations of Isèbe & Nérin [69] and the experimental measurements of Kachel [74] (see Fig. 1.7, **left** picture), contrary to the assumption made in Eq. 1.1 [53, 68]. This is due to the electrodes location that are placed away from the aperture in practice (see Fig. 1.4), contrary to the idealized case of the analytical developments (see Fig. 1.6).

Concerning the electrical field heterogeneity, the experimental observations of Kachel [74] support a linear relationship between the squared electrical field and the electrical perturbation, thus leading to a second version of Eq. 1.1:

$$\Delta R = \frac{E^2 f_s}{\rho_e i^2} V_p, \tag{1.2}$$

The intensity is denoted by i (see Fig. 1.4) while E designates the electrical field magnitude . If the shape factor f_s is constant, the electrical pulse is proportional to

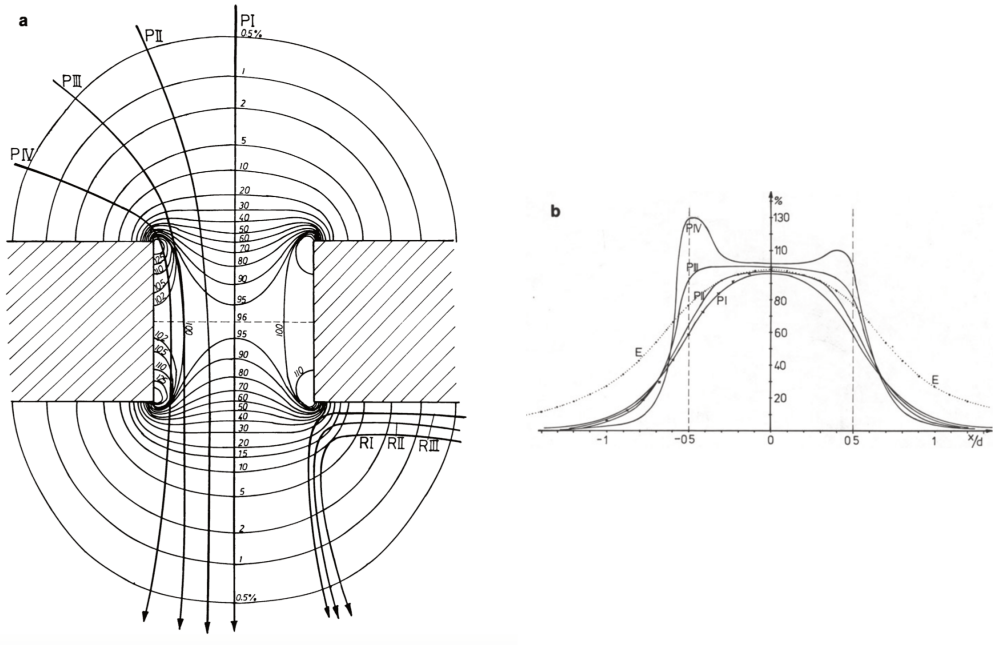

Figure 1.7 – Figure proposed by Kachel in [74] and [75]. The **left** picture shows the squared electrical field (E^2) isolines in percentage of E^2 assessed in the orifice middle section. The **right** picture depicts E^2 undergone by particles following the four trajectories of the **left** figure. E^2 is expressed according to the dimensionless axial position in the orifice (x/d). With d the orifice diameter and x the coordinate along the aperture principal axis. Vertical dashed lines represent the orifice limits.

the squared electrical field E^2 observed by the particle along its trajectory. Typical E^2 seen by particles depending the path followed are shown in Fig. 1.7. Note that the volume measurement is taken as the maximum of the electrical perturbation because all pulses are assumed to have a 'bell-shape' (see centered paths in Fig. 1.7).

Analytical expressions for the shape factor are available for the case of particles with simple shapes, such as spheres and ellipsoids [53, 170]. Examples of shape factors for different particle shapes are presented in Fig. 1.8A [173]. In particular, model by Velick *et al.* [170] may be applied for any ellipsoid with one of its principal axes aligned with the electrical field. Breitmeyer *et al.* [10] later modelled the impact of the ellipsoid orientation on the shape factor:

$$f_s = f_{//} - (f_{//} - f_{\perp})cos^2\theta \tag{1.3}$$

For a given ellipsoid principal axis, $f_{//}$ and $f_{\perp}$ denote the ellipsoid shape factors when the chosen principal axis is aligned and perpendicular to the electrical field, respectively. The angle θ denotes the orientation between the electrical field and the chosen principal axis. Qin *et al.* [133] retrieved numerically the impact of the particle orientation on the electrical resistance variation as shown in Fig. 1.8B. The resistance variation is shown to increase when the particle longest axis gets perpendicular to the electrical field. On the contrary, the minimal resistive perturbation is observed when it is aligned with the electrical field (see Fig. 1.8B). Golibersuch obtained pulses presenting several peaks analyzing RBCs by the use of a Coulter counter

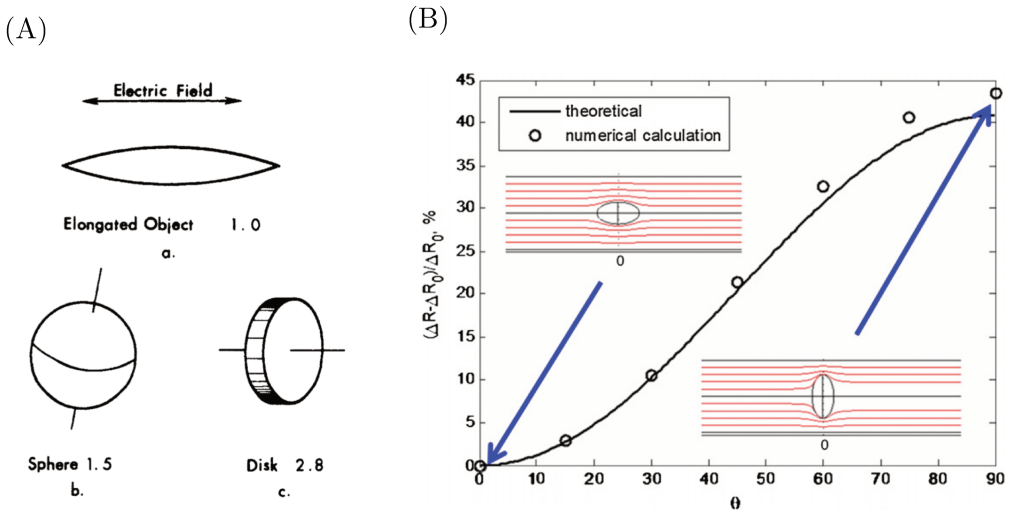

Figure 1.8 – (A) Shape factor for simple particles shapes as presented by Waterman *et al.* [173]. (B) Resistance variation caused by an ellispsoid particle in a homogeneous electrical field depending on its orientation (figure presented by Qin *et al.* [133]).

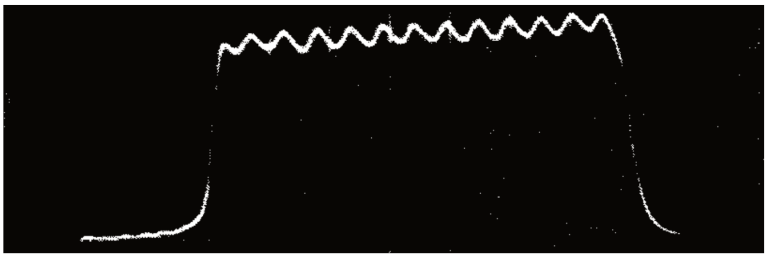

Figure 1.9 – Pulse showed by Golibersuch [50] displaying several peaks, that are supposed to be induced by rotations of the particle.

with a long aperture [50] (see Fig. 1.9). These peaks are explained by a rotation of the cell that induces a periodic variation of the shape factor.

In summary, the impact of the electrical field inhomogeneity is better understood since Kachel's publication [74] and the shape factor for simple and rigid particles is well characterized. However, the description and understanding of how deformable particles behave in this kind of configurations and the consequences on the apparent shape factor along their passage through a Coulter counter are still lacking.

1.3.2 Undesirable artefacts

As shown by Fig. 1.7, cells flowing in the vicinity of the aperture walls encounter regions with a dense electrical field. Hence, according to Eq. 1.2, the electrical pulse arising from a near-wall path is intended to reach higher values than a pulse generated by a cell evolving in the core region of the aperture, independently on the actual cell volume.

As previously discussed, RBCs rotations were pointed out in the literature. In particular, Kachel [76] observed reorientation of RBCs when they cross the detection

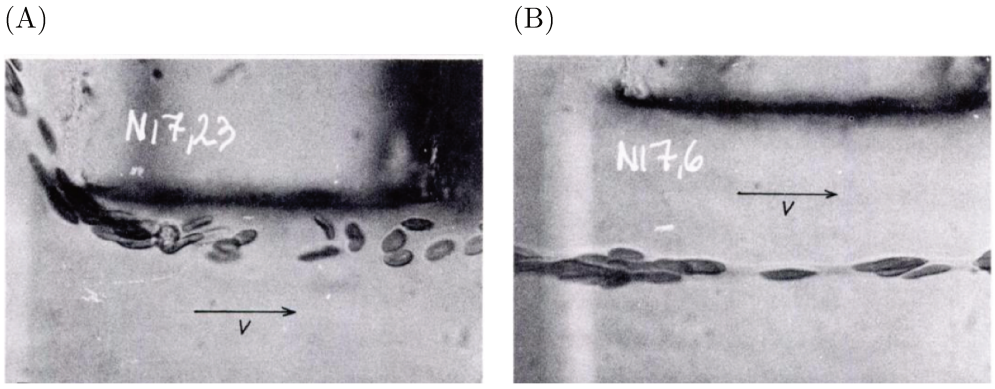

Figure 1.10 – Observation of RBCs crossing a constricted channel as shown by Kachel in [76]. In (A), cells are enforced to move by the wall while in (B), cells go through the orifice by following a central trajectory.

area in the proximity of the aperture walls, while cells are oriented with the axial direction when they flow in the center of the micro-orifice (see Fig. 1.10). Regarding Eq. 1.3 and Eq. 1.2, changes in the particle orientation would modify the electrical perturbation through variations of the shape factor f_s. Actually, such rotations are induced by a substantial velocity shear by the wall. Indeed, Reynolds number (Re) of about 200 is indicative of such configurations, that is based on the aperture diameter (about 50 μm) and a typical velocity inside of the aperture (around 5 m.s^{-1}). Based on the approximation 0.05×D×Re [31] (D being the orifice diameter), the hydrodynamic entry length is thus evaluated to 500μm, while a typical orifice length is 75μm. As a consequence, the velocity profile is flat in the core region of the micro-orifice and rotation may occur only for near-wall trajectories, where large velocity shear is present. Besides, biological cells are deformable and RBCs were shown to undergo complex deformations and dynamics [2, 3, 91, 110] under shear flows. Deformations are intended to play an important part in the changes of shape factor but no quantitative assessment of f_s for deforming cells is available in the literature.

Two types of edge-effects occur in Coulter counters. The first type is purely electrical and arises when a particle reaches the intense electrical field around the aperture corners (see Fig. 1.7). The second type, of hydrodynamical nature, is observed when the particle is subjected to shear rates large enough to induce rotations and deformations. These edge-effects tend to overestimate the volume of particles undergoing trajectories close to the orifice edges and explain the right-skew volume distribution observed for RBCs (see Fig. 1.5A), instead of a Gaussian-like distribution [129]. Methods consisting in rejecting from the analysis the pulses impacted by edge-effects were introduced, as in the work from Waterman *et al.* [173] that supports the removal of long pulses. Although this approach is found to sharpen the measurements, the volume distribution still displays a right-skew curve, as shown in Fig. 1.11. Because the pulse length depends directly on the cell size (viz. the targeted feature), thresholding the pulse duration may operate differently from a sample to another, depending on particle volumes in the sample. This is why filter-

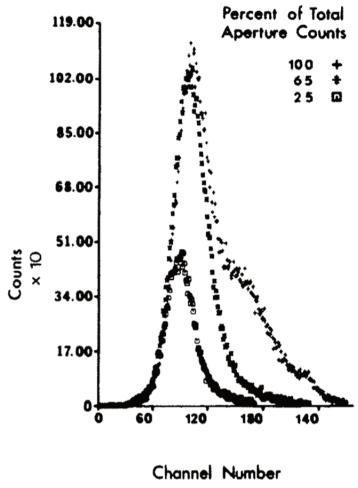

Figure 1.11 – Pulses height distributions obtained by Waterman *et al.* [173]. The represented distributions are related 25 %, 65 % and 100 % of the total acquisition. The percentage of retained pulses depends on the rejection criterion applied to the duration of the pulses.

ing strategies accounting for both the pulse duration and the pulse heigh (function of the cell size) were introduced. Such sorting strategies are still used today by the way. For instance, in HORIBA Medical automata, one may find the following condition that pulses must satisfy to be accounted for in the assessment of haematological parameters:

$$\mathcal{W} < A\sqrt{log(\mathcal{H}) - B}, \tag{1.4}$$

in which $\mathcal{W}$ and $\mathcal{H}$ denote the length and the maximum of the pulse, respectively. They are sometimes called the width and height of the electrical signature, respectively. Variable A and B are calibrated built-in parameter of the filter. The filter of Eq. 1.4 is developed by assuming that the pulse is defined by a function of time $f(t)$ whose expression is:

$$f(t) = \begin{cases} \mathcal{H} \times e^{-\frac{(t-t_0)^2}{2\sigma_1^2}} & , t < t_o \\ \mathcal{H} \times e^{-\frac{(t-t_0)^2}{2\sigma_2^2}} & , t > t_o \end{cases} \tag{1.5}$$

More information on such type of filter may be found in [70]. Brian [12] improved the volume distribution by spherizing the RBCs and taking longer apertures. In this respect, most of the dynamical edge-effects are hidden by the spherical aspect of the cell and the use of longer apertures provides a more homogenous electrical field [75]. However, extending the aperture length increases the probability of several cells passing through the sensing region at the same time, which makes the measurement unreliable. Moreover, spherizing cells implies the development of a specific reagent. In an alternative approach, Spielman [154] proposed to enforce central particles paths by using a sheathing flow, as sketched in Fig. 1.12. This method called 'hydrodynamical focusing' was proven to retrieve symmetrical and Gaussian-like volume distributions of RBCs.

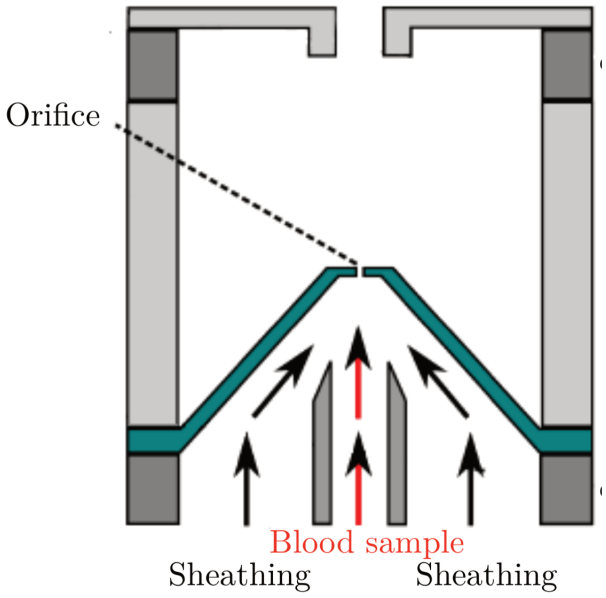

Figure 1.12 – Principle of the 'hydrodynamical focusing' systems (figure from [69]). The blood sample is pinched in the center of the orifice by the sheathing flow.

1.3.3 Motivations

A variety of pulse signatures are reported in the literature. Grover [53] observed 'bell-shaped' pulses and 'M-shaped' pulses when spheres pursue central and near-wall trajectories, respectively (see Fig. 1.13A and B, respectively). These pulses signatures are in agreement with the E^2 profiles proposed by Kachel [74] (see Fig. 1.7). Analyzing aspherical pollen particles, Grover [54] retrieved long pulses presenting a peak as shown in Fig. 1.13C and D. Stating that particles evolving near the orifice edges are transported at a lower velocity, he concludes that such signatures are generated by near-wall paths. RBCs following a central path generate 'bell-shaped' pulses as well but complex signatures are obtained if they undergo near-wall trajectories [75] (see Fig. 1.13E and F, respectively). The complex signatures arising from near-wall paths are related to measurement errors, so that intensive efforts have been made to eliminate them from the analysis. Generally, the efficiency of methods ensuring the processing of 'bell-shaped' pulses of centred paths goes hand in hand with their complexity of implementation. Furthermore, the improvement in the accuracy of the measurements with a simple method is still an interesting task, from an industrial point of view.

Although they are unsuited for the volume measurement, pulses impacted by dynamical edge-effects may provide information on the shapes and deformations of the particles. For instance, by the use of a long aperture in which all particles may rotate several times, Golibersuch [49] claimed the assessment of the particle sphericity from the electrical pulse. As previously discussed, velocity gradients present near the wall are expected to deform biological cells, thus inducing changes in the shape factor. Hence, the electrical pulse may contain indications on the ability of the cell to deform, on its "deformability". The deformability of blood cells may be altered in the case of pathologies. Methods such as micro-pipette [136, 146], optical tweezers

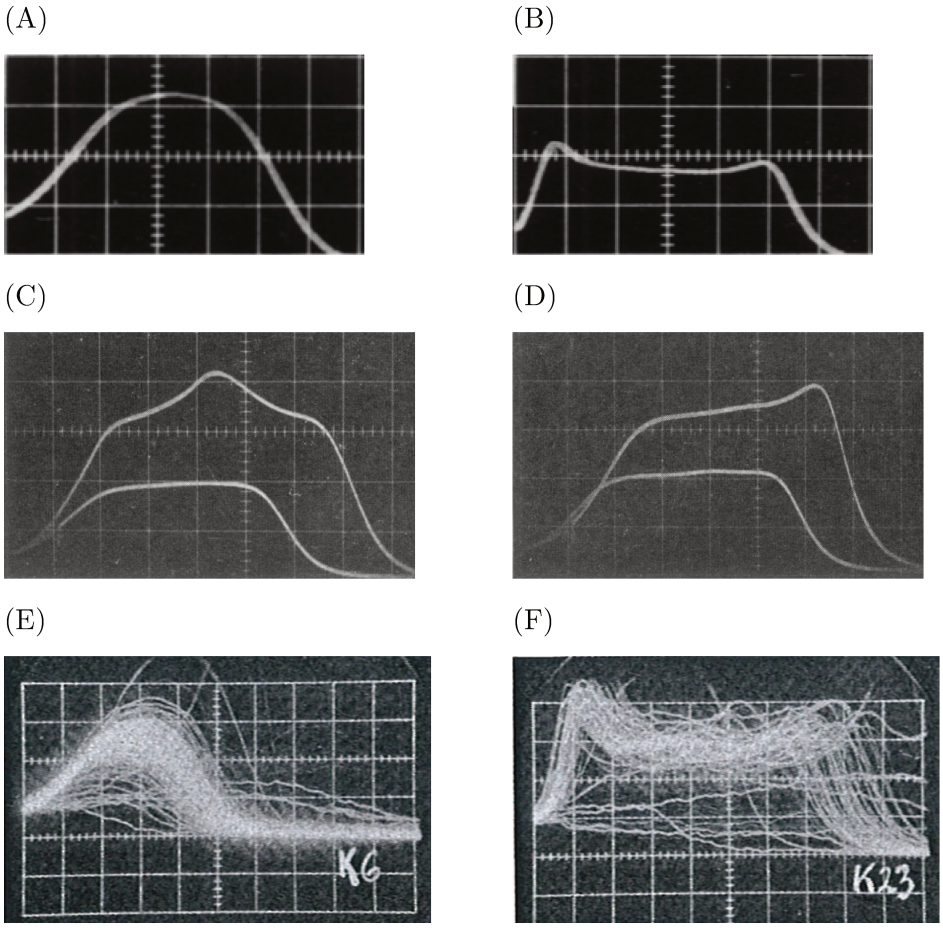

Figure 1.13 – Oscilloscope graphs obtained by Grover with spherical particles [53] (A and B) and aspherical pollen particles [54] (C and D). The horizontal axis refers to time and the vertical axis expresses the electrical perturbation (in Volt). In C and D, long pulses generated by near-wall path are superimposed with shorter pulses coming from central trajectories. Pictures (E) and (F) originating from Kachel[75] work are oscilloscope observations of pulses generated by RBCs evolving in the center and near the wall, respectively.

[23, 64, 94, 98], and atomic force microscopy [11, 60, 77] allows an assessment of the deformability of cells, but only for limited number of cells in a sample. In this respect, diseases affecting the mechanical behaviour of a small portion of cells cannot be treated with such approaches. Besides, the aforementioned techniques are not automatic and generally require the intervention of a specialist. This explains the emergence of various methods achieving a deformability diagnosis of a large number of blood cells, in a moderate time. Among this large panel of high throughput methods one should cite measurement systems based on: Transit Through Constrictions [1, 9, 141, 183], hydrodynamic streching [13, 14, 28, 51, 182] and optical cytometry [55, 56, 134, 155]. Because Coulter counters analyse thousands of cells in a few seconds, assessing the deformability from impedance pulses would represent a novel high throughput technique for the rheological characterization of blood cells.

Considering rigid spheres that maintain a constant shape factor, the pulses sig-

natures are well known and explained by the squared electrical field (see Eq. 1.2). On the contrary, in the case of deformable cells, pulses impacted by edge-effects are still misunderstood. Due to the difficulties in accessing the RBC dynamics within the measurement zone (small sensing region (tens of μm), large velocity (≈ 5 ms^{-1}), no optical access, very short time of exposure (10 μs)), numerical simulations would be an appealing way of tackling this question. Also, simulations allow controlling the input parameters, which is particularly difficult to do in experiments with biological cells. In other words, numerical simulation of the dynamics of the RBCs in Coulter counters and of the associated electrical perturbation is expected to bring new information useful to explain and characterize the links between the mechanical properties of the cells and their electrical signatures.

Once a relation is made between geometrical and mechanical properties of cells and their electrical responses, one may rely different statistical methods to process the experimental signals and infer the properties of the cells. For instance, neural networks enable the building of complex models from a database: they represent an interesting approach to process cells information embedded in electrical prints, in a complementary way to numerical simulation. Remind that industrial Coulter counters are nowadays widely exploited to assess patients CBC. Consequently, from a hardware point of view, no further developments are needed and implementing an additional signal processing to assess richer information about cells would be most probably doable at low industrial development cost.

The present work is dedicated to RBCs, the most deformable and numerous blood cells. The remaining of this opening chapter presents an overview of the existing methods to simulate flowing RBCs.

1.4 Numerical simulation of RBCs

An appealing approach for investigating electrical prints generated by RBCs in the microscopic aperture of Coulter counters is the numerical simulation. In this section, the properties of RBCs in terms of shape, composition and mechanical behaviour are first presented. Then, an overview of the existing numerical models and their applications in the prediction of RBCs dynamics is given. Finally, the challenges of simulating deformable RBCs in Coulter counters are succinctly introduced.

1.4.1 A close-up look on red blood cells

Erythrocytes are enucleated cells. Hence, a RBC may be viewed as a microscopic drop of fluid (cytoplasm) surrounded by a thin solid membrane. Measurements of Evans and Fung [33] shed light on the discocyte shape of the cell, for which they proposed the following parametrization:

$$z(r) = \pm\frac{R_O}{2}\sqrt{1-\left(\frac{r}{R_O}\right)^2}\times\left(C_0 + C_2\left(\frac{r}{R_O}\right)^2 + C_4\left(\frac{r}{R_O}\right)^4\right) \tag{1.6}$$

Figure 1.14 illustrates the RBC shape as stipulated by Eq. 1.6, by defining $R_O =$ 3.91 μm, $C_0 = 0.81$ μ, $C_2 = 7.83$ μm and $C_4 =$ -4.39 μm. A typical RBC volume is

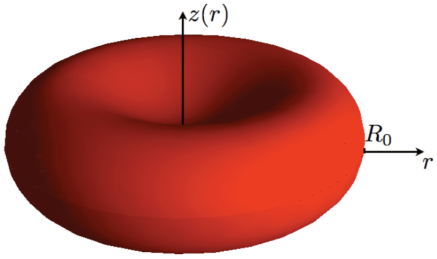

Figure 1.14 – Discocyte shape of RBCs as shown by Abkarian and Viallat [4].

Membrane elastic parameters	
G_s	$5.5\pm3.3 \times 10^{-6}$ N.m^{-1}
E_a	0.39 ± 0.11 N.m^{-1}
E_b	$1.14\pm0.9 \times 10^{-19}$ J

Table 1.2 – Typical mechanical parameters of the membrane of RBCs[4, 46].

93 μm^3 while the membrane area is about 133 μm^3 [33] . By defining the reduced volume ($\mathcal{Q}$) as the cell volume divided by the volume of the sphere having the same surface than the membrane, a typical $\mathcal{Q}$ for RBCs is 0.65. Note that for a spherical particle, the reduced volume ($\mathcal{Q}$) equals 1.0, thus 0.65 emphasises the deflated aspect of RBCs. This property plays an important role in the deformability of such cells.

Because the membrane is supposed infinitely thin, its mechanical response only depends on three types of deformation: changes of area, shear deformations, and bending [4, 113]. Area and shear deformations are observed in the membrane two-dimensional plane whereas bending expresses changes of the membrane profile. The RBCs membrane is a complex structure composed by a lipid bilayer underlined by a cytoskeleton. The lipid bilayer regulates the membrane permeability while the cytoskeleton preserves the cell integrity [4]. Both account in the membrane mechanical behaviour: the lipid bilayer was shown to resist bending and surface variations, while the cytoskeleton resists shear deformations and area dilatations (but less than the lipid bilayer). These elastic properties come in addition to a membrane viscosity that is often neglected in numerical simulations [19, 20, 107, 161]. Such behaviours of the membrane are measurable with various methods. The reader is referred to the review by Darling and Dino Di Carlo [24] for more information on the subject. In general, the membrane is viewed as a continuous medium and the mechanical modulus quantifying the aforementioned behaviours are defined. Classical values of the membrane global (lipid bilayer + cytoskeleton) parameters are given in Tab. 1.2, in which G_s stands for the shear modulus, E_b, the bending modulus and E_a, the area modulus. These parameters rate the rigidity of the membrane against the three aforementioned modes of deformation. The cytoplasm content also plays a part in RBCs mechanical behavior. Measurements reported in the literature [16, 79] support an internal viscosity six times higher than plasma, at the body temperature. The internal to external viscosity ratio was proven to drive the cell dynamics in shear flows [2, 4, 91, 107, 110, 152].

RBCs pathologies may impact the membrane mechanical parameters (see Tab. 1.2),

the reduced volume ($\mathcal{Q}$), the cell shape, and its content. For instance, malaria (plasmodium falciparum) increases the cell reduced volume [115, 143] and the membrane shear modulus [48, 112, 115] but also reduces the haemoglobin concentration [122], that is related to the internal viscosity [79]. Furthermore, the presence of the parasite within the membrane should change the global rigidity of the cell. Spherical and ellipsoidal RBCs arise from hereditary spherocytosis [5, 123] and elliptocytosis [18, 163], respectively. One may also cite sickle cell anemia that leads to rigid RBCs with a sickle-like shape [118, 138]. Hence, morphological and rheological information of RBCs represent a real interest to diagnose pathologies.

1.4.2 RBCs simulations, State of the art

Simulating flowing RBCs implies the modelling a Fluid-Structure Interaction (FSI) problem between incompressible fluids (internal and external fluids) and a thin membrane. Remind that RBCs are highly deformable, thus making the small deformation assumption invalid. The modelling of FSI for large solid deformations represents a challenging task that is still investigated.

Different methods to achieve such modelling are proposed in the literature. These methods may differ in the way the fluid and/or the membrane are treated. The fluid dynamics may be predicted by approaching the solution of Navier Stokes equations using a finite volume [111], a finite difference [6, 32, 179] or a finite element method [26, 71]. The Lattice-Boltzmann equation that was shown to converge to Navier-Stokes equations (by the Chapman-Enskog expansion) is also widely used [86, 87, 104, 137, 158–160]. Navier-Stokes equations write the conservation laws of the fluid macroscopic quantities whereas the Boltzmann equation expresses the advancement of a mesoscopic quantity that is the probability density function of the molecules composing the fluid to go in different directions. Particle based methods are also used, such as the dissipative particles dynamics (DPD) method [37, 39] and the multiparticle collision dynamics (MPC) method [108, 109]. Concerning the modelling of the solid membrane, two main approaches are generally combined with Particle based, LB and Navier-Stokes methods. The first one [7, 19, 20, 86, 111, 111, 175–177] consists in describing the membrane as a continuous medium by the use of strain energy functions. For example, the RBC membrane is generally modeled with the Skalak law [151] that accounts for the shear and area modulus (see Tab. 1.2) and the Helfrich bending energy [63] that models the bending withstanding of the membrane. The principle of the second approach is to consider the membrane as a set of particles linked to each others by a network of springs [38, 39, 121]. Finally, assuming a Stokes flow, the boundary integral method has been used by many authors [29, 30, 41, 43, 88–90, 171, 172].

The different models have been validated and, in the case of RBCs, were mostly applied in simple configurations such as optical-tweezers [36, 95, 149, 150], Shear Flows [25, 91, 107, 152] and micro channels [40, 165, 181], for instance. Numerical simulation of the dynamics and deformation of RBCs under flow has tremendously developed over the last years, but the application to industrial geometries is still limited. Its application to Industrial Coulter counters is expected to yield new insights

in the behaviour and the electrical signature of RBCs in the sensing region, but has never been performed before to fully characterize an industrial system. Numerical studies of particles dynamics in Coulter counters have mainly considered rigid particles, both spherical [57] and aspherical [69]. Gibaud *et al.* [46, 47] performed the first simulations of deformable RBCs in Coulter counters, but the study was restricted to hydrofocalized analysers, and the simulations suffer from limitations on the initial conditions, as detailed in the next paragraph.

1.4.3 Issues involved when tackling the numerical simulation of RBCs in Coulter counters

A computation of the entire analysis of RBCs by Coulter counters is not possible, due to the large number of cells and above all the huge ranges in both length and time scales when the entire device is considered. As shown in Fig. 1.4, the size of the measurement region (where the electrical field is strong enough so that the cell can be detected) is of a few tens of micrometers and cells pass through the sapphire in a few tens of microseconds. On the contrary, far from the sapphire, they are suspended in a tank of a few centimeters (5 cm) and they flow at a velocity of the order of 10^{-3} ms^{-1}. The separation of scales leads to prohibitive computational times, while the measurement region is very limited. An option is to focus on the measurement region only, but cells deform before being detected by the counter [74]. Gibaud *et al.* [46, 47] computed the signal associated with RBCs but neglected part of the upstream deformations for computational reasons. This explains why most existing numerical simulations have only considered rigid particles [57, 69], thus circumventing the challenge of the scale separation by reducing the computational domain to the region where the impedance signal is detected. This cannot be done when deformable particles are considered. A method to tackle such simulations was developed in this thesis and has been published in[162]. It will be detailed in Chap. 4.

1.5 Thesis objectives and outlines

Numerical simulations of RBCs would give a new insight on the electrical prints arising from industrial Coulter counters. In this respect, an original sequence of simulations is proposed to overcome the multi-scale issue that arises naturally. A numerical pipeline dedicated to rigid spheres is presented in Chap. 3 and extended to deformable particles in Chap. 4. The numerical results are validated by comparisons with theoretical statements and experimental measurements. The simulations of the pipeline are performed with different solvers of YALES2BIO software, that are presented in Chap. 2, at first.

In particular, the proposed numerical approach is employed to highlight the variety of complex pulses originating from RBCs evolving near the aperture walls (see the end of Chap.4). Besides these pulses are associated with particular dynamics in the aperture and the shape factor of a deforming RBC is modeled. These numerical

results thus explain the mechanisms involved in the complex pulses obtained from particles flowing along a near-wall trajectory.

Errors in the volume measurement generated by near-wall trajectories were discussed in Sec. 1.3.2. These deficiencies are currently balanced by filtering strategies or hardware improvements of the original Coulter principle. Filtering methods are simpler of implementation but the lack of knowledge on the edge-effects limited their development in the past. Thanks to the understanding brought by the numerical simulation, an original filter is proposed in Chap. 5 and shown to accurately reproduce results from hydrodynamical focusing.

In Chap. 6, cells morphology and rheology are shown to impact the measurement. Then, methods for processing the cells features from the electrical pulses are introduced. Among them, NNs are employed to characterize the RBCs. The training of such NNs requires a database composed of many couples a^{in}/a^{obs}, in which a^{in} is the pulse and a^{obs} the cell parameters. Note that knowing a^{obs} may be problematic with an experimental approach. This is the case if a^{obs} represents the mechanical parameters (G_s, E_a ...) of the cell, for instance. Numerical simulation allows constructing any couples a^{in}/a^{obs}, which makes the association of numerical simulations with NNs promising. In particular, this strategy is used in Chap. 6 for modeling the inverse problem of numerical simulations and is also employed in Chap. 5 to develop a filtering method. However, because of simulations times, the main drawback of such a coupling is the computational cost to pay for a sufficient number of couples a^{in}/a^{obs}. This is why the strategy of achieving NN models from experimental data will be preferred in some applications of Chap. 6.

Chapter 2

Numerical models for the simulations of impedance measurements

Chapter contents

In Coulter counters, RBCs suspended in an electrolytic solution flow through a micro-orifice in which a dense electrical field is imposed by two electrodes (see Fig. 1.4). Moreover, RBCs are enucleated cells viewed as a drop of fluid surrounded by a solid membrane. Hence, simulating the impedance measurement of RBCs in a Coulter counter implies a three-way coupling problem: Solid/Fluid flow; Solid/Electrical field; Fluid flow/Electrical field.

In practice, the suspending fluid and the cells move at velocities much lower than the velocity of light. The electrostatic assumption is then made which means

the electrical field develops instantly despite the fluid and particles motions. Coupling between the fluid-flow and the electrostatic field are neglected. In addition, dielectrophoretic forces acting on the membrane are not accounted for, despite the ability of RBCs to be polarized [116, 132]. These assumptions allow considering a Solid/Fluid problem completely separated from Solid/Electrostatic problems since RBCs motions depend only on Fluid-Structure Interactions.

In YALES2BIO software, Solid/Fluid and Solid/Electrostatic problems are treated with two distinct solvers (FSIS and ESS, respectively). The solvers employed in the context of this thesis are as follows:

1) A Navier Stokes Solver (NSS) that computes the flow of incompressible fluids.

2) A Fluid-Structure Interaction Solver (FSIS) that couples solver NSS with infinitely thin membranes.

3) An Electrostatic Solver (ESS) calculating the electrical field in the presence of cells.

In the present chapter, each solver is described and validation cases are presented. Solver NSS is introduced in the first section. Then, the coupling of NSS with solid membranes in FSIS is detailed. Finally, the solver ESS is presented.

2.1 Flow solver (NSS)

The electrolytic solution in which cells are in suspension is mainly water. Consequently, the fluid motions are modeled according to incompressible Navier Stokes equations:

$$\frac{\partial \vec{u}}{\partial t} + \nabla.(\vec{u} \otimes \vec{u}) = -\frac{1}{\rho}\nabla P + \nabla.[\nu \nabla \vec{u}] + \nabla.[\nu(\nabla \vec{u})^T] \tag{2.1}$$

$$\nabla.\vec{u} = 0 \tag{2.2}$$

where $\vec{u}$ denotes the fluid velocity, P the pressure, ρ the fluid density and ν the kinematic viscosity. Note that the viscosity ν may vary in the fluid domain. This section focuses on the numerical method in solver NSS to solve Eq. 2.1 and 2.2.

2.1.1 Time advacement

The fluid equations presented above are solved with a prediction correction method [17]. From the fluid quantities at the beginning of the time step (indicated by a superscript n), a predicted velocity ($\vec{u}^*$) is computed by advancing the momentum equation Eq. 2.1 without the pressure term. For the sake of simplicity, an explicit Euler time advancement scheme is retained in the following development:

$$\frac{\vec{u}^* - \vec{u}^n}{\Delta t} = -\nabla.(\vec{u}^n \otimes \vec{u}^n) + \nabla.[\nu^n \nabla \vec{u}^n] + \nabla.[\nu^n(\nabla \vec{u}^n)^T] \tag{2.3}$$

Generally, $\vec{u}^*$ is not divergence free as prescribed in Eq. 2.2, thus a correction must be performed on the predicted velocity. In this respect, the corrected velocity at the end of the time step ($\vec{u}^{n+1}$) must satisfies:

$$\frac{\vec{u}^{n+1} - \vec{u}^n}{\Delta t} = -\nabla.(\vec{u}^n \otimes \vec{u}^n) - \frac{1}{\rho}\nabla P^{n+1} + \nabla.[\nu^n \nabla \vec{u}^n] + \nabla.[\nu^n(\nabla \vec{u}^n)^T] \tag{2.4}$$

By subtracting Eq. 2.4 with Eq. 2.3, the following equation is obtained:

$$\frac{\vec{u}^{n+1} - \vec{u}^*}{\Delta t} = -\frac{1}{\rho}\nabla P^{n+1} \tag{2.5}$$

Then, applying the divergence operator on each side of the above equation leads to:

$$\nabla.\frac{\vec{u}^{n+1}}{\Delta t} - \nabla.\frac{\vec{u}^*}{\Delta t} = -\nabla.[\frac{1}{\rho}\nabla P^{n+1}]$$

Now imposing that the velocity $\vec{u}^{n+1}$ is divergence-free, a Poisson equation for the pressure is obtained:

$$\frac{1}{\rho}\nabla.[\nabla P^{n+1}] = \frac{1}{\Delta t}\nabla.\vec{u}^* \tag{2.6}$$

Once the Poisson equation (Eq. 2.6) solved, the velocity field is corrected using Eq. 2.5.

2.1.2 Space discretization

Finite Volume Method

According to the time advancement procedure, spatial discretizations for Eq. 2.3, 2.5 and 2.6 are needed. In YALES2BIO, this is done by the use of a Finite Volume Method (FVM) consisting in splitting the fluid domain into several control volumes that are represented by squares in Fig. 2.1. A control volume Ω_i is bounded by $\partial\Omega_i$ that is the union of several faces $S_{i,j}$. Each face $S_{i,j}$ is defined as the frontier between control volumes Ω_i and Ω_j. The macroscopic fluid quantities (P and $\vec{u}$) are assessed at the discretization nodes $\vec{x}_i$ assumed to be located at the center of mass of the control volumes Ω_i. The spatial discretization is then developed by integrating Eq. 2.3, 2.5 and 2.6 over each control volume Ω_i and balancing the fluxes over faces $S_{i,j}$.

Integrating Eq. 2.3 over a control volume Ω_i leads to:

$$\frac{1}{\Delta t}\int_{\Omega_i}(\vec{u}^* - \vec{u}^n)dV = \int_{\Omega_i} -\nabla.(\vec{u}^n \otimes \vec{u}^n) + \nabla.[\nu^n\nabla\vec{u}^n] + \nabla.[\nu^n(\nabla\vec{u}^n)^T]dV \tag{2.7}$$

Then, using the Ostrogradski theorem, integrals over Ω_i may be rewritten as integrals over $\partial\Omega_i$:

$$\begin{aligned}\frac{1}{\Delta t}\left(\int_{\Omega_i}\vec{u}^* dV - \int_{\Omega_i}\vec{u}^n dV\right) = &-\int_{\partial\Omega_i}[\vec{u}^n \otimes \vec{u}^n]\, d\vec{S} + \int_{\partial\Omega_i}\nu^n\nabla\vec{u}^n d\vec{S} \\ &+ \int_{\partial\Omega_i}\nu^n(\nabla\vec{u}^n)^T d\vec{S}\end{aligned} \tag{2.8}$$

By construction, integrals over $\partial\Omega_i$ equals the sum of integrals over faces $S_{i,j}$ (see Fig. 2.1):

$$\begin{aligned}\frac{1}{\Delta t}(\int_{\Omega_i}\vec{u}^* dV - \int_{\Omega_i}\vec{u}^n dV) = &-\sum_j\int_{S_{i,j}}[\vec{u}^n \otimes \vec{u}^n]\, d\vec{S} + \sum_j\int_{S_{i,j}}\nu^n\nabla\vec{u}^n d\vec{S} \\ &+ \sum_j\int_{S_{i,j}}\nu^n(\nabla\vec{u}^n)^T d\vec{S}\end{aligned} \tag{2.9}$$

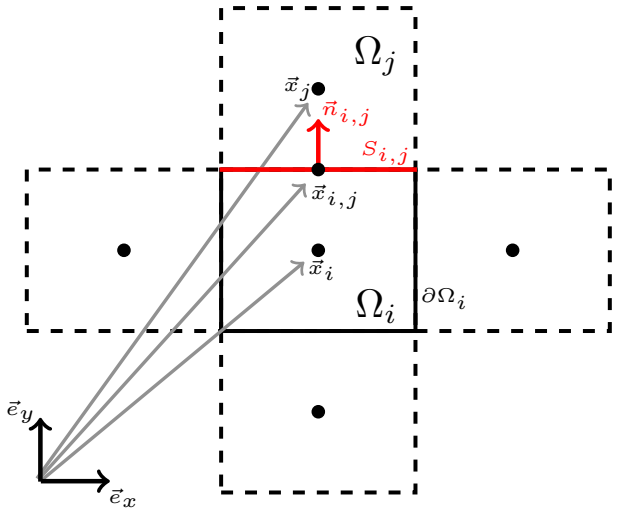

Figure 2.1 – Control volumes involved in the finite volume method for the spatial discretization. Although this representation is in two dimensions, the notations stand for three-dimensional control volumes.

When integrating $\vec{u}$ over Ω_i, the Taylor development implies:

$$\int_{\Omega_i} \vec{u} dV = \int_{\Omega_i} \vec{u}_i + \nabla \vec{u}|_i (\vec{x} - \vec{x_i}) + \mathcal{O}(||\vec{x} - \vec{x_i}||^2) dV \tag{2.10}$$

The discretization nodes $\vec{x}_i$ being placed at the center of mass of Ω_i, the integral of the second-order term vanishes. Hence, at the second-order of accuracy, the previous equation simplifies as:

$$\int_{\Omega_i} \vec{u} dV = \vec{u}_i V_i \tag{2.11}$$

With V_i referring to the volume of Ω_i. Then, using Eq. 2.11 to approximate the volume integrals in Eq. 2.9 leads to:

$$\begin{aligned} \frac{V_i}{\Delta t}(\vec{u}_i^{n+1} - \vec{u}_i^n) = &- \sum_j \int_{S_{i,j}} [\vec{u}^n \otimes \vec{u}^n] \, d\vec{S} + \sum_j \int_{S_{i,j}} \nu^n \nabla \vec{u}^n d\vec{S} \\ &+ \sum_j \int_{S_{i,j}} \nu^n (\nabla \vec{u}^n)^T d\vec{S} \end{aligned} \tag{2.12}$$

In an equivalent manner, Eq. 2.5 and Eq. 2.6 lead respectively to:

$$\frac{V_i}{\Delta t}(\vec{u}^{n+1} - \vec{u}^*) = -\frac{1}{\rho} \sum_j \int_{S_{i,j}} P^{n+1} d\vec{S}, \tag{2.13}$$

and

$$\frac{1}{\rho} \sum_j \int_{S_{i,j}} \nabla P^{n+1} . d\vec{S} = \frac{1}{\Delta t} \sum_j \int_{S_{i,j}} \vec{u}^* . d\vec{S} \tag{2.14}$$

By defining operators $\mathcal{C}(\vec{u}, \vec{u})$, $\mathcal{G}(P)$, $\mathcal{D}(\vec{u})$, $\mathcal{L}(P)$, $\mathcal{L}_{cv}(\nu, \vec{u})$ and $\mathcal{L}_{cv}^T(\nu, \vec{u})$ as:

$$\mathcal{C}(\vec{u}, \vec{u}) = \sum_j \int_{S_{i,j}} [\vec{u} \otimes \vec{u}] \, d\vec{S}, \tag{2.15}$$

$$\mathcal{G}(P) = \sum_j \int_{S_{i,j}} P d\vec{S}, \tag{2.16}$$

$$\mathcal{D}(\vec{u}) = \sum_j \int_{S_{i,j}} \vec{u}.d\vec{S}, \tag{2.17}$$

$$\mathcal{L}(P) = \sum_j \int_{S_{i,j}} \nabla P.d\vec{S}, \tag{2.18}$$

$$\mathcal{L}_{cv}(\nu, \vec{u}) = \sum_j \int_{S_{i,j}} \nu \nabla \vec{u}\ d\vec{S}, \tag{2.19}$$

and

$$\mathcal{L}^T_{cv}(\nu, \vec{u}) = \sum_j \int_{S_{i,j}} \nu [\nabla \vec{u}]^T d\vec{S}, \tag{2.20}$$

Eq. 2.12, 2.13 and 2.14 respectively write:

$$\frac{V_i}{\Delta t}(\vec{u}_i^* - \vec{u}_i^n) = -\mathcal{C}(\vec{u}^n, \vec{u}^n) + \mathcal{L}_{vc}(\nu^n, \vec{u}^n) + \mathcal{L}^T_{vc}(\nu^n, \vec{u}^n), \tag{2.21}$$

$$\frac{V_i}{\Delta t}(\vec{u}^{n+1} - \vec{u}^*) = -\frac{1}{\rho}\mathcal{G}(P^{n+1}), \tag{2.22}$$

and

$$\frac{1}{\rho}\mathcal{L}(P^{n+1}) = \frac{1}{\Delta t}\mathcal{D}(\vec{u}^*) \tag{2.23}$$

Operator $\mathcal{C}$ stems from the convective term of the momentum equation (Eq. 2.1). The pressure gradient of the correction equation (Eq. 2.5) is related to $\mathcal{G}$, while $\mathcal{D}$ is used to approximate the divergence of $\vec{u}^*$ in the Poisson equation (Eq. 2.6). $\mathcal{L}$ is employed for the Laplacian of P^{n+1} in Eq. 2.6, whereas $\mathcal{L}_{cv}$ and $\mathcal{L}^T_{cv}$ assess the viscous part of Eq. 2.1. In particular:

1) $\mathcal{L}$ assesses the Laplacian

2) $\mathcal{L}_{cv}$ is a Laplacian accounting for a variable coefficient

3) $\mathcal{L}^T_{cv}$ is close to $\mathcal{L}_{cv}$, the only difference being the transpose that is applied to the gradient (see Eq. 2.19 and 2.20).

Numerical schemes estimating the different operators ($\mathcal{C}$, $\mathcal{G}$, $\mathcal{D}$, $\mathcal{L}$, $\mathcal{L}_{cv}$ and $\mathcal{L}^T_{cv}$) are presented in the following.

Laplacian operators

Let $\vec{x}_{i,j}$ be the vertex placed at the intersection of face $S_{i,j}$ and vector $(\vec{x}_j - \vec{x}_i)$, as shown in Fig. 2.1. If the control volumes are regular, $\vec{x}_{i,j}$ is located at the center of mass of $S_{i,j}$, that allows the following second order developement of Eq. 2.18:

$$\mathcal{L}(P)|_i = \sum_j \int_{S_{i,j}} \nabla P.d\vec{S} = \sum_j \nabla P|_{i,j}.\vec{S}_{i,j} \tag{2.24}$$

Note that $\vec{S}_{i,j}$ equals $S_{i,j} \times \vec{n}_{i,j}$ (see Fig. 2.1). The value of ∇P at node $\vec{x}_{i,j}$ (denoted by $\nabla P|_{i,j}$) is required in the above expression. It is approximated by writing the Taylor developments of P at points $\vec{x}_i$ and $\vec{x}_j$, in the vicinity of $\vec{x}_{i,j}$:

$$P_i = P_{i,j} + \nabla P|_{i,j}.(\vec{x}_i - \vec{x}_{i,j}) + \mathcal{O}(||\vec{x}_i - \vec{x}_{i,j}||^2) \tag{2.25}$$

$$P_j = P_{i,j} + \nabla P|_{i,j}.(\vec{x}_j - \vec{x}_{i,j}) + \mathcal{O}(||\vec{x}_j - \vec{x}_{i,j}||^2) \tag{2.26}$$

Subtracting Eq. 2.26 to Eq. 2.25 and by keeping only terms of order 2 leads to:

$$P_j - P_i = \nabla P|_{i,j}.(\vec{x}_j - \vec{x}_i)$$

Then, it comes that:

$$\nabla P|_{i,j} = (P_j - P_i)\frac{(\vec{x}_j - \vec{x}_i)}{|\vec{x}_j - \vec{x}_i|^2} \tag{2.27}$$

The substitution of Eq. 2.27 in Eq. 2.24 gives the second-order accurate spatial discretization of the Laplacian operator:

$$\mathcal{L}(P)|_i = \sum_j (P_j - P_i)\frac{(\vec{x}_j - \vec{x}_i)}{|\vec{x}_j - \vec{x}_i|^2}.\vec{S}_{i,j} \tag{2.28}$$

Note that in the case where $(\vec{x}_j - \vec{x}_i)$ is parallel to $\vec{S_{i,j}}$, this simplifies to:

$$\mathcal{L}(P)|_i = \sum_j \frac{P_j - P_i}{|\vec{x}_j - \vec{x}_i|} S_{i,j} \tag{2.29}$$

At a second-order of accuracy, operator $\mathcal{L}_{cv}$ reduces as follows, provided $\vec{x}_{i,j}$ is the center of mass of $S_{i,j}$:

$$\mathcal{L}_{cv}(\nu, \vec{u})|_i = \sum_j \int_{S_{i,j}} \nu \nabla \vec{u} \; d\vec{S} = \sum_j \nu_{i,j} \nabla \vec{u}|_{i,j} \; \vec{S}_{i,j} \tag{2.30}$$

The velocity gradient at $\vec{x}_{i,j}$ ($\nabla \vec{u}|_{i,j}$) is treated as $\nabla P|_{i,j}$ in Eq. 2.27 but $\nu_{i,j}$ still needs to be expressed according to nodal values of viscosity ν_i and ν_j. This is done by writing the two following Taylor series expansions:

$$\nu = \nu_{i,j} + \nabla \nu|_{i,j}.(\vec{x}_i - \vec{x}_{i,j}) + \mathcal{O}(||\vec{x}_i - \vec{x}_{i,j}||^2) \tag{2.31}$$

$$\nu_j = \nu_{i,j} + \nabla \nu|_{i,j}.(\vec{x}_j - \vec{x}_{i,j}) + \mathcal{O}(||\vec{x}_j - \vec{x}_{i,j}||^2) \tag{2.32}$$

By summing Eq. 2.31 with 2.32, neglecting terms of order 3, and assuming $(\vec{x}_j - \vec{x}_{i,j})$ $= (\vec{x}_{i,j} - \vec{x}_i)$, $\nu_{i,j}$ expresses as follows:

$$\nu_{i,j} = \frac{\nu_i + \nu_j}{2} \tag{2.33}$$

In this way, $\mathcal{L}_{cv}(\nu, \vec{u})$ writes:

$$\mathcal{L}_{cv}(\nu, \vec{u})|_i = \sum_j \frac{\nu_i + \nu_j}{2}(\vec{u}_j - \vec{u}_i)\left[\frac{(\vec{x}_j - \vec{x}_i)}{|\vec{x}_j - \vec{x}_i|^2}.\vec{S}_{i,j}\right] \tag{2.34}$$

Furthermore, with a similar approach, $\mathcal{L}_{cv}^T$ yields:

$$\mathcal{L}_{cv}^T(\nu, \vec{u})|_i = \sum_j \frac{\nu_i + \nu_j}{2}\frac{(\vec{x}_j - \vec{x}_i)}{|\vec{x}_j - \vec{x}_i|^2}\left[(\vec{u}_j - \vec{u}_i).\vec{S}_{i,j}\right] \tag{2.35}$$

Divergence operators

This section is devoted to operators $\mathcal{D}$ and $\mathcal{C}$, that compute the divergence of $\vec{u}$ and $\vec{u} \otimes \vec{u}$, respectively. With $\vec{x}_{i,j}$ located at the center of mass of $S_{i,j}$, second-order approximations of $\mathcal{C}(\vec{u}, \vec{u})$ and $\mathcal{D}(\vec{u})$ read:

$$\mathcal{C}(\vec{u}, \vec{u})|_i = \sum_j \int_{S_{i,j}} [\vec{u} \otimes \vec{u}] \, d\vec{S} = \sum_j [\vec{u}_{i,j} \otimes \vec{u}_{i,j}] \, \vec{S}_{i,j}, \tag{2.36}$$

and

$$\mathcal{D}(\vec{u})|_i = \sum_j \int_{S_{i,j}} \vec{u}.d\vec{S} = \sum_j \vec{u}_{i,j}.\vec{S}_{i,j} \tag{2.37}$$

As developed for assessing ν at point $\vec{x}_{i,j}$ (see Eq. 2.33), $\vec{u}_{i,j}$ is approximated by:

$$\vec{u}_{i,j} = \frac{\vec{u}_j + \vec{u}_i}{2} \tag{2.38}$$

In this respect, injecting the above expressions in Eq. 2.36 and 2.37 yields:

$$\mathcal{C}(\vec{u}, \vec{u})|_i = \sum_j \left[\left(\frac{\vec{u}_j + \vec{u}_i}{2} \right) \otimes \left(\frac{\vec{u}_j + \vec{u}_i}{2} \right) \right] \vec{S}_{i,j} = \sum_j \frac{\vec{u}_j + \vec{u}_i}{2} U_{i,j}, \tag{2.39}$$

and

$$\mathcal{D}(\vec{u})|_i = \sum_j \frac{\vec{u}_j + \vec{u}_i}{2}.\vec{S}_{i,j} = \sum_j U_{i,j}. \tag{2.40}$$

$U_{i,j}$, that is defined as $\frac{\vec{u}_j + \vec{u}_i}{2}.\vec{S}_{i,j}$ represents the flow-rate across face $S_{i,j}$. Consequently, applying $\mathcal{D}$ to $\vec{u}$ (see Eq. 2.40) is equivalent to balancing the flow-rates $(U_{i,j})$ that come in and get out of the control volume Ω_i.

Gradient operator

With the same assumptions that enable Eq. 2.33 and Eq. 2.38, the pressure at $\vec{x}_{i,j}$ is assessable by:

$$P_{i,j} = \frac{P_j - P_i}{2} \tag{2.41}$$

This allows the following development of $\mathcal{G}(P)$:

$$\mathcal{G}(P)|_i = \sum_j \int_{S_{i,j}} P d\vec{S} = \sum_j P_{i,j} \vec{S}_{i,j} = \sum_j \frac{P_j + P_i}{2} \vec{S}_{i,j}, \tag{2.42}$$

once again, provided $\vec{x}_{i,j}$ is the center of mass of $S_{i,j}$.

High order schemes for the spatial discretization

The derivations of the different operators proposed in this section are second-order. Fourth-order assessments of surface integrals involved in the different operators are available in YALES2BIO and will be used in the following simulations. The reader is referred to works of Kraushaar [84], Vantieghem [169] and Puiseux [130] for more details on the implementation of the fourth-order schemes in YALES2BIO. One should also recommend the publication of De Stefano *et al* [156] for a more theoretical description of high order schemes in Finite-Volume Methods.

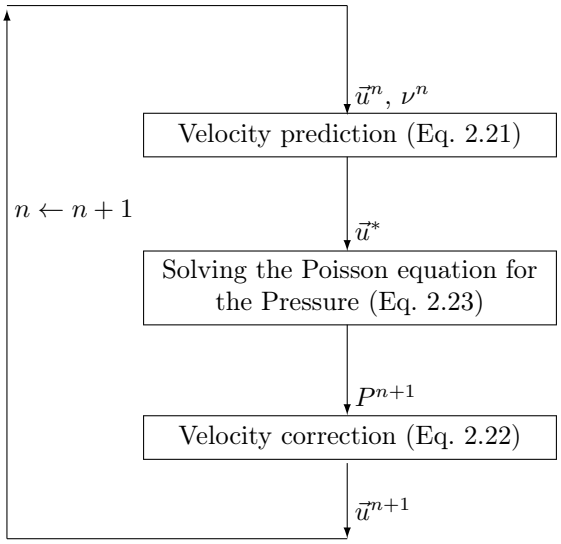

Figure 2.2 – Temporal loop involved in the Navier Stokes Solver (NSS).

2.1.3 Navier Stokes Solver (NSS) time stepping

Including the expressions of the different operators (see Eqs. 2.28, 2.34, 2.35, 2.39, 2.40 and 2.42) in Eqs. 2.21, 2.22, and 2.23 provides the discretization of Eqs. 2.3, 2.5 and 2.6 in both time and space. Instead of an explicit Euler scheme (used in the former sections as an illustration), a fourth-order Runge Kutta scheme (RK4) [148, 174] is preferred in practice. The velocity $\vec{u}^n$ is advanced to $\vec{u}^*$ in four sub-steps as:

$$\begin{cases} \vec{u}^1 = \vec{u}^n + \frac{1}{4}\Delta t \times RHS(\vec{u}^n, \nu^n) \\ \vec{u}^2 = \vec{u}^n + \frac{1}{3}\Delta t \times RHS(\vec{u}^1, \nu^n) \\ \vec{u}^3 = \vec{u}^n + \frac{1}{2}\Delta t \times RHS(\vec{u}^2, \nu^n) \\ \vec{u}^* = \vec{u}^n + \frac{1}{3}\Delta t \times RHS(\vec{u}^3, \nu^n) \end{cases} \tag{2.43}$$

with RHS referring to the right-hand side of Eq. 2.21. Note that the kinematic viscosity is not updated during the RK4 substeps.

A better view on the NSS solver time step is given in Fig. 2.2. The first step in the temporal loop consists in computing a velocity prediction $\vec{u}^*$ by using Eq. 2.21 (or Eq. 2.43 if a RK4 advancement is chosen). Note that $\vec{u}_i^*$ is evaluated for each node $\vec{x}_i$ representing the fluid domain. Given $\vec{u}_i^*$, Eq. 2.23 represents a linear system of equations for the pressure P_i^{n+1}. Hence, in a second step (see Fig. 2.2) the linear system 2.23 is solved with a Deflated Preconditioned Conjugate Gradient algorithm [105] (DPCG). Finally, once P_i^{n+1} is calculated, the divergence free velocity at the end of the time step ($\vec{u}_i^{n+1}$) is computed according to Eq. 2.22.

2.1.4 A few words on the boundary conditions

In the case where boundary velocities are prescribed, the following $\vec{u}^*$ condition is commonly imposed just after the prediction step (see Fig. 2.2):

$$\vec{u}^*|_{Bd} = \vec{u}^{n+1}|_{Bd} \tag{2.44}$$

Here, Bd refers to the boundaries of the computational domain. Besides, a vanishing pressure gradient along $\vec{n}_{Bd}$ (the boundaries normal) is imposed when the Poisson equation is solved in the second step (see Fig. 2.2):

$$\frac{\partial P^{n+1}}{\partial \vec{n}_{Bd}}|_{Bd} = 0 \tag{2.45}$$

As shown by Kim and Moin [80], applying such boundary conditions is only first-order accurate. They proposed an improved version of Eq. 2.44, that makes the method second-order accurate:

$$\vec{u}^*|_{Bd} = \vec{u}^{n+1}|_{B_d} + \Delta t \frac{1}{\rho} \nabla P^n|_{B_d} \tag{2.46}$$

For more information on the boundary conditions, readers are referred to [80, 169].

In practice, ∇P^n is included in the prediction step, so that only the increment of pressure between time step n and n+1 is calculated with the Poisson equation to correct the predicted velocity. Adding ∇P^n in Eq. 2.3 for the prediction $\vec{u}^*$ makes the method second-order accurate even with the boundary condition of Eq. 2.44, since the requirement of Eq. 2.46 is fulfilled on the domain bounds.

2.1.5 Fluid grids

The derivation of the spatial discretization of Sec. 2.1.2 is second-order accurate for regular and structured grids (as for square meshes shown in Fig. 2.1). Dealing with industrial configurations generally implies complex geometries that are difficult to discretize with regular meshes. In the present section, the meshing process is briefly explained.

Based on a tetrahedral grid provided by common meshing software such as GMSH or GAMBIT, the control volumes Ω_i are constructed around the vertices of the tetrahedra. Figure 2.3 illustrates the construction of a control volume from a 2D triangular mesh. However, this can easily be extended to 3D tetrahedral grids. The initial triangular mesh is shown in continuous lines while the control volume built around a vertex $\vec{x}_i$ is shown in dashed lines. The control volume is constructed by assessing the middle of the edges of the triangles (crosses in Fig. 2.3) and the centers of mass of the triangles (bold points in Fig. 2.3).

Regarding Fig. 2.3, it should be noted that the line $S_{i,j}$ (or surface $S_{i,j}$, for a 3D tetrahedral grid) is no more flat, contrary to the idealized case of Fig. 2.1. Hence, vector $\vec{S}_{i,j}$ required in the spatial discretization (see Sec. 2.1.2) takes a more intricate definition than $S_{i,j}\vec{n}_{i,j}$. Actually, it is defined as the sum of $S'_{i,j}\vec{n}'_{i,j}$ and $S''_{i,j}\vec{n}''_{i,j}$ (see Fig. 2.3).

Depending on the initial triangular mesh, $\vec{x}_i$ may not be the center of mass of the control volume. In the same way, nodes $\vec{x}_{i,j}$ are generally not corresponding to the centers of mass of faces $S_{i,j}$. As a consequence, the second-order spatial discretization developed in Sec. 2.1.2 becomes only first-order accurate. The more regular the mesh is, the less the order of accuracy decreases. That is why regular elements are highly recommended. Moreover, two neighbouring elements should be close in size.

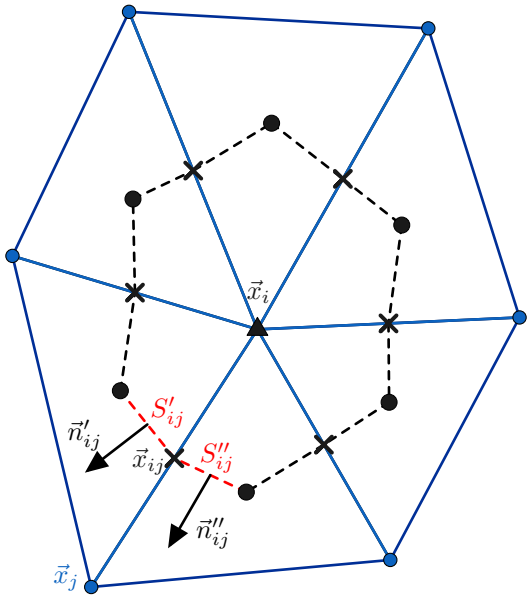

Figure 2.3 – Construction of the control volume Ω_i (drawn in dashed line) from a triangular grid. This illustration shown in 2D stands in 3D.

2.1.6 Applications

The present model has been applied in a large panel of simulations relevant to cardiovascular biomechanics. For example, Siguenza [148] showed that the Womersley profiles in 2D pulsatile flows are well predicted for several pulsation frequencies. Zmijanovic *et al.* [185] retrieved the transition from laminar to turbulent flow that was observed in a series of experiments performed in different FDA laboratories. Puiseux [131] confirms that NSS reproduces the pusatile and steady developement lengths in cylindrical channels, as reported by Durst *et al.* [31] and He *et al.* [61], respectively. He also validates the accuracy of NSS in a pipe bend in both pulsatile and stationary flows by comparisons with works of Timite [164] and Siggers [147], respectively. In a recent publication, the solver has shown really good velocity correlations with 4D flow MRI measurements performed in an in-vitro configuration [130].

2.2 Fluid Structure Interaction Solver (FSIS)

Simulating the dynamics of RBCs in flow implies the coupling of the membrane mechanics with the flow of an incompressible fluid. In solver FSIS, this is enabled by the Immersed Boundary Method (IBM) of Peskin [125]. This model is dedicated to the fluid-structure interactions between an infinitely thin and massless solid with an incompressible fluid (see Fig. 2.4). A curvilinear coordinates system ($\vec{e}_s$,$\vec{e}_r$,$\vec{e}_q$) is attached to the solid whereas the fluid is defined in the Eulerian coordinates system ($\vec{e}_x$,$\vec{e}_y$,$\vec{e}_z$). The system ($\vec{e}_s$,$\vec{e}_r$,$\vec{e}_q$) is orthonormal and defined in such a way plane ($\vec{e}_s$,$\vec{e}_r$) is tangential to the membrane and $\vec{e}_q$ is directed outward of the cell (see Fig. 2.4). The membrane is also observed with a Lagrangian point of view by $\vec{X}(r,s,t)$, which describes the membrane at time t. Because the solid dimension

along $\vec{e}_q$ is negligible, the coordinate q is not needed for tracking the membrane in such a formalism. The fluid motions are modelled according to incompressible Navier Stokes equations, as in NSS:

$$\frac{\partial \vec{u}}{\partial t} + \nabla.(\vec{u} \otimes \vec{u}) = -\frac{1}{\rho}\nabla P + \nabla.[\nu \nabla \vec{u}] + \nabla.[\nu(\nabla \vec{u})^T] + \frac{1}{\rho}\vec{f_v} \tag{2.47}$$

$$\nabla.\vec{u} = 0 \tag{2.48}$$

The term $\vec{f_v}$ is a source term accounting for the forces arising from the solid. Remind that the kinematic viscosity ν may vary in the domain, and as discussed in the following is higher inside of the RBC membrane. When deformed, the solid stores an elastic energy defined by $W(\vec{X}(r,s,t))$. To recover its reference shape, the membrane applies an elastic force on the surrounding fluid particles:

$$\vec{F}_E = \frac{\partial W}{\partial \vec{X}} \tag{2.49}$$

Peskin [125] proposed to account for the membrane forces in the momentum equation (Eq. 2.47) through the source term $\vec{f_v}$. The forces coming from the solid ($\vec{F}_E$) are regularized as follows:

$$\vec{f_v}(\vec{x}) = \int_{\Omega_s} \vec{F}_E(\vec{X}(r,s,t))\delta(\vec{x} - \vec{X}(r,s,t))drds \tag{2.50}$$

Note that $\vec{f_v}$ is expressed in an Eulerian formalism while $\vec{F}_E$ depends on the membrane Lagrangian coordinates $\vec{X}(r,s,t)$. The change of formalism is enabled by the integrated Dirac function δ. Assuming that the membrane mass is negligible, the solid is transported at the surrounding fluid velocity $\vec{u}$. This implies the interpolation of $\vec{u}$ at the membrane location:

$$\frac{d\vec{X}}{dt} = \int_{\Omega_f} \vec{u}(\vec{x})\delta(\vec{x} - \vec{X})d\vec{x} \tag{2.51}$$

Equations 2.47, 2.48, 2.49, 2.50 and 2.51 represent the system of equations solved in the solver FSIS. Note that without membrane in the domain, Eq. 2.49, 2.50 and 2.51 are not required, $\vec{f_v} = \vec{0}$ and FSIS reduces to NSS.

Note that if Fluid/Electrostatic interactions were taken into account, an additional forcing term in the right-hand side of Eq. 2.47 would be required [169]. Besides, when taking into account dielectrophoretic forces, membrane displacements and internal energy would depend on the electrostatic field, which is not the case here.

The treatment of Eq. 2.47 and Eq. 2.48 was detailed in Sec. 2.1. Hence, the present section details the computation of the membrane forces $\vec{F}_E$, at first. Then, the coupling procedure provided by Eq. 2.50 and 2.51 is presented for the discrete problem.

2.2.1 Membrane discretization

The membrane of each cell is described with triangular elements in 3D. For example, Fig. 2.5 shows the discrete membrane of one RBC. Only the cell membrane is meshed,

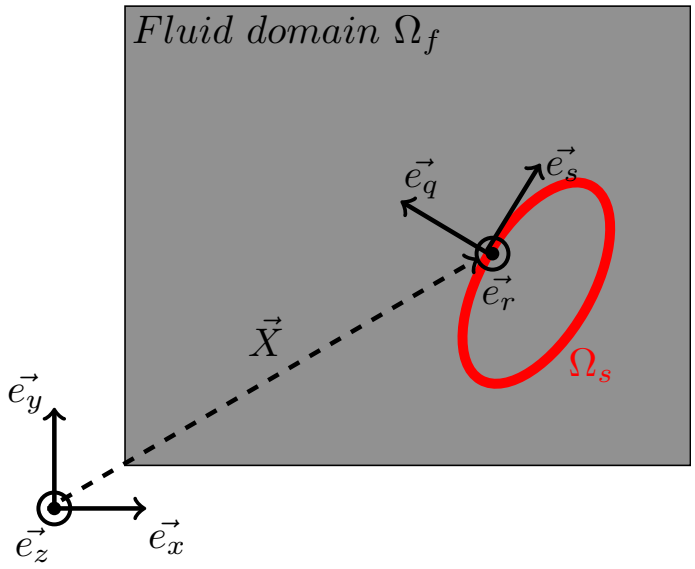

Figure 2.4 – Diagram of an infinitely thin membrane (Ω_s) immersed in a fluid domain Ω_f.

as highlighted in the cut view of Fig. 2.5. Besides, the surface grid is embedded in a tetrahedral grid on which Navier Stokes equations are solved with the procedure detailed in Sec. 2.1. Although internal and external fluids are different, they are both treated at the same time with the method of Sec. 2.1. The membrane acts by imposing forces on the fluid. The membrane elastic forces are split into two components: in-plane and out-of-plane parts. As discussed in Sec. 1.4, the in-plane contribution accounts for the area and shear resilience of the membrane while bending resistance is involved in the out-plane forces. The two following subsections detail the calculation of these two parts in the context of a triangulated membrane.

In plane elastic forces

The so-called Skalak law [151] provides one possible hyperelastic strain energy function W_{sk} of the membrane deformed in its plane:

$$W_{sk} = \frac{G_s}{4}[(\lambda_1^2 + \lambda_2^2 - 2)^2 + 2(\lambda_1^2 + \lambda_2^2 - \lambda_1^2\lambda_2^2 - 1)] + \frac{E_a}{4}(\lambda_1^2\lambda_2^2 - 1)^2 \qquad (2.52)$$

G_s and E_a are material parameters and denote respectively the shear and the area modulus. Terms λ_1 and λ_2 are the principal values of strain that are computed as the eigenvalues of the Cauchy-Green strain tensor $\bar{\bar{G}}$:

$$\bar{\bar{G}} = \bar{\bar{F}}^T\bar{\bar{F}} = (\mathbb{1} + \frac{\partial\vec{U}(\vec{s})}{\partial\vec{s}})^T(\mathbb{1} + \frac{\partial\vec{U}(\vec{s})}{\partial\vec{s}}) \qquad (2.53)$$

with $\bar{\bar{F}}$, the transformation tensor. The vector $\vec{s}$ refers to the material location in the membrane basis ($\vec{e}_s$,$\vec{e}_r$), while $\vec{U}$ is the displacement field of the membrane, expressed in ($\vec{e}_s$,$\vec{e}_r$) as well. $\bar{\bar{G}}$ is a matrix of size 2×2, defined in the membrane basis, and symmetrical by definition. Hence, $\bar{\bar{G}}$ is defined by three components: G_{11},

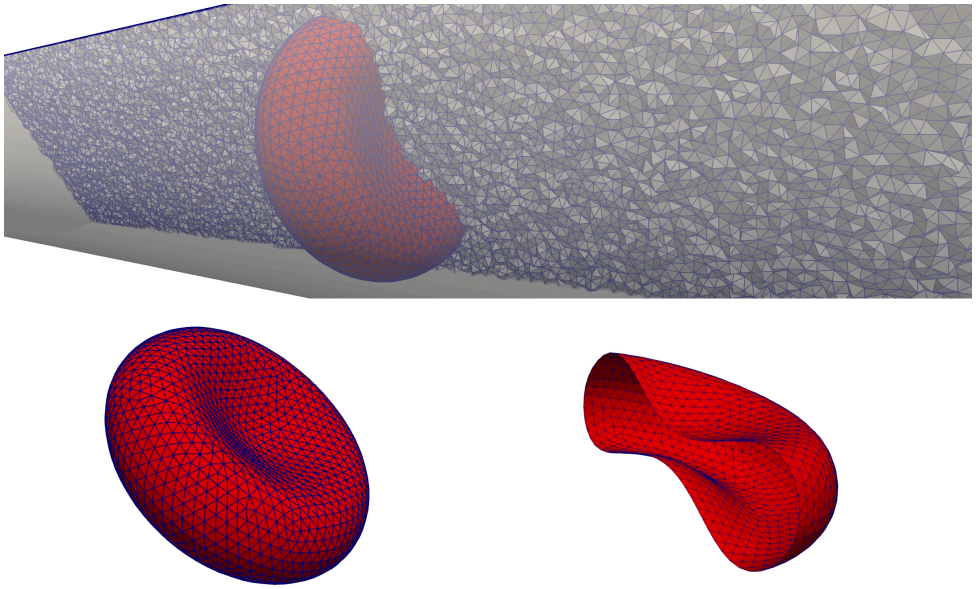

Figure 2.5 – **Top**: Example of a membrane triangular grid shown over a fluid tetrahedral mesh. **Bottom**: zoom on the membrane mesh (left) and cut-view of the membrane grid (right).

G_{22} and G_{12}: G_{11} and G_{22} are the two diagonal components of $\bar{\bar{G}}$ and G_{12} is the value taken by the non-diagonal terms of $\bar{\bar{G}}$ (since $G_{12} = G_{21}$). From G_{11}, G_{22} and G_{12}, the two principal values of $\bar{\bar{G}}$ (λ_1 and λ_2) involved in Eq. 2.52 may be written as follow:

$$\lambda_1^2 = \frac{1}{2}[G_{11} + G_{22} + \sqrt{(G_{11} - G_{22})^2} + 4G_{12}^2] \tag{2.54}$$

$$\lambda_2^2 = \frac{1}{2}[G_{11} + G_{22} - \sqrt{(G_{11} - G_{22})^2} + 4G_{12}^2] \tag{2.55}$$

The membrane is discretized with a first-order finite element method. From a reference state, the membrane grid is deformed as shown in Fig. 2.6. The method proposed by Charrier *et al.* [15] and detailed in the following computes for each triangular element the nodal forces (viz. the forces at the vertices of the triangles) induced by the strain energy W_{sk} stored in the membrane by an arbitrary deformation of the element. At the element scale, the displacement field $\vec{U}$ induces a deformation of the triangle in a local coordinates system tangential to the membrane ($\vec{e}_s$,$\vec{e}_r$), as shown in Fig. 2.6. In YALES2BIO, the local coordinates system is defined in such a way that $\vec{e}_s$ is lined up with an edge of the triangle, as illustrated in Fig. 2.6. However, for the sake of clarity, it is better to represent the deforming triangle as in Fig. 2.7. Both formalisms lead to the same result since the strain energy is invariant by rigid body movements. The triangle deformation is induced by the vertices displacements $\vec{U}^1$, $\vec{U}^2$, and $\vec{U}^3$, that move M_1, M_2 and M_3 to M_1', M_2' and M_3', respectively (see Fig. 2.7). Displacement $\vec{U}^i$ of a vertex M_i has U_s^i and U_r^i for components, according to $\vec{e}_s$ and $\vec{e}_r$, respectively. In the finite element formalism, the displacement $\vec{U}$ of an arbitrary material point $\vec{s}$ (see Fig. 2.7) belonging to the

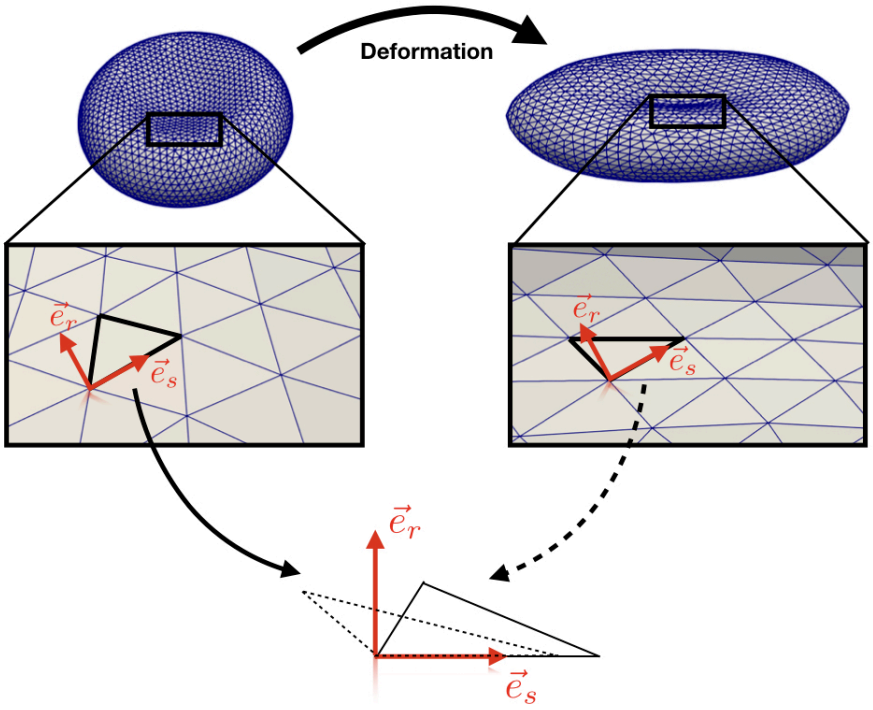

Figure 2.6 – Sketch of the deforming triangles in the membrane plane.

triangular element is approximated by $\vec{U}^h$:

$$\vec{U}^h(\vec{s}) = \begin{pmatrix} U_s^h(\vec{s}) \\ U_r^h(\vec{s}) \end{pmatrix} = \begin{pmatrix} \{N\}^T\{U_s^M\} \\ \{N\}^T\{U_r^M\} \end{pmatrix} \tag{2.56}$$

$\{\vec{U}_s^M\}$ and $\{\vec{U}_r^M\}$ contain the vertices displacements values such as:

$$\{\vec{U}_s^M\} = \begin{pmatrix} U_s^1 \\ U_s^2 \\ U_s^3 \end{pmatrix}, \{\vec{U}_r^M\} = \begin{pmatrix} U_r^1 \\ U_r^2 \\ U_r^3 \end{pmatrix} \tag{2.57}$$

The term $\{N\}^T$ in Eq. 2.56 is composed by the shape functions.

$$\{N\}^T = \begin{pmatrix} \phi_1(\vec{s}) & \phi_2(\vec{s}) & \phi_3(\vec{s}) \end{pmatrix} \tag{2.58}$$

In particular, ϕ are linear functions constructed in a way $\phi_i(\vec{s})$ equals 1 at node i and 0 at the remaining nodes. Thus, Eq. 2.56 consists in interpolating the displacements $\vec{U}^1$, $\vec{U}^2$, and $\vec{U}^3$ in $\vec{s}$.

Substituting Eq. 2.56 in Eq. 2.53 provides an approximation of the Green-Lagrange strain tensor in the triangular element:

$$\begin{aligned} \bar{\bar{G}} &= \begin{pmatrix} G_{11} & G_{12} \\ G_{12} & G_{22} \end{pmatrix} \\ &= \begin{pmatrix} 1 + \frac{\partial\{N\}^T\{U_s^M\}}{\partial s} & \frac{\partial\{N\}^T\{U_r^M\}}{\partial s} \\ \frac{\partial\{N\}^T\{U_s^M\}}{\partial r} & 1 + \frac{\partial\{N\}^T\{U_r^M\}}{\partial r} \end{pmatrix}^T \begin{pmatrix} 1 + \frac{\partial\{N\}^T\{U_s^M\}}{\partial s} & \frac{\partial\{N\}^T\{U_r^M\}}{\partial s} \\ \frac{\partial\{N\}^T\{U_s^M\}}{\partial r} & 1 + \frac{\partial\{N\}^T\{U_r^M\}}{\partial r} \end{pmatrix} \end{aligned}$$

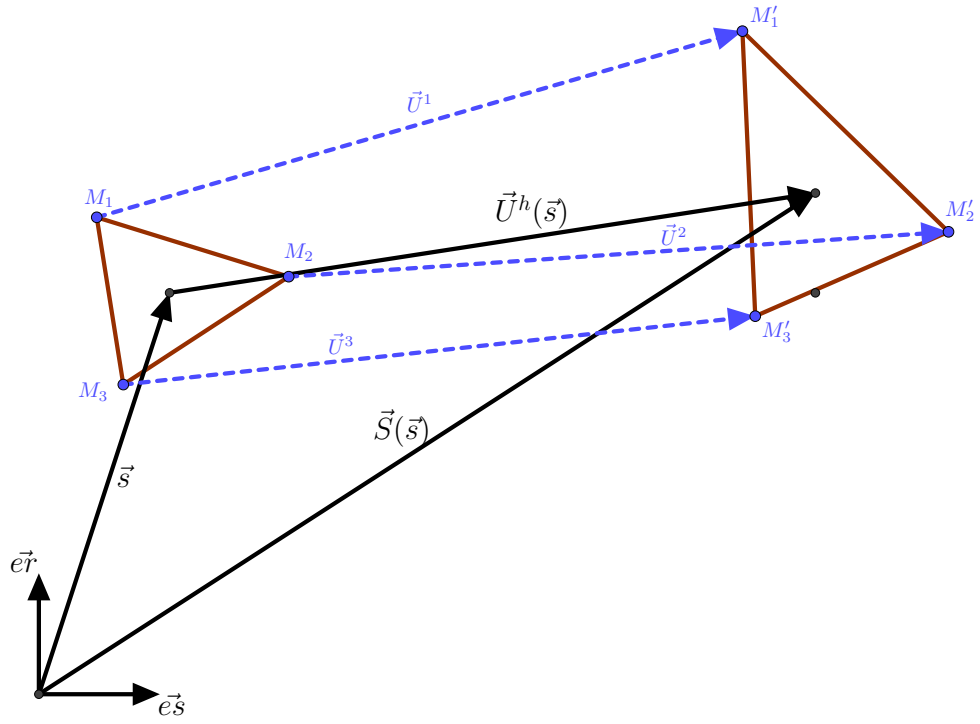

Figure 2.7 – Diagram of a deforming membrane triangular element in the local coordinates sytem.

It should be noted that $\{\vec{U}_s^M\}$ and $\{\vec{U}_r^M\}$ do not depend on s and r, consequently, after some algebra the components of $\bar{\bar{G}}$ write:

$$\begin{aligned} G_{11} = 1 + 2\frac{\partial\{N\}^T}{\partial s}\{U_s^M\} + \{U_s^M\}^T\frac{\partial\{N\}}{\partial s}\frac{\partial\{N\}^T}{\partial s}\{U_s^M\} \\ + \{U_r^M\}^T\frac{\partial\{N\}}{\partial s}\frac{\partial\{N\}^T}{\partial s}\{U_r^M\}, \end{aligned} \tag{2.59}$$

$$\begin{aligned} G_{22} = 1 + 2\frac{\partial\{N\}^T}{\partial r}\{U_r^M\} + \{U_r^M\}^T\frac{\partial\{N\}}{\partial r}\frac{\partial\{N\}^T}{\partial r}\{U_r^M\} \\ + \{U_s^M\}^T\frac{\partial\{N\}}{\partial r}\frac{\partial\{N\}^T}{\partial r}\{U_s^M\}, \end{aligned} \tag{2.60}$$

and

$$\begin{aligned} G_{12} = \frac{\partial\{N\}^T}{\partial r}\{U_s^M\} + \{U_s^M\}^T\frac{\partial\{N\}}{\partial r}\frac{\partial\{N\}^T}{\partial s}\{U_s^M\} \\ + \frac{\partial\{N\}^T}{\partial s}\{U_r^M\} + \{U_r^M\}^T\frac{\partial\{N\}}{\partial r}\frac{\partial\{N\}^T}{\partial s}\{U_r^M\} \end{aligned} \tag{2.61}$$

Note that, combining Eq. 2.52 with Eq. 2.54, 2.55, 2.59, 2.60 and 2.61, provides an estimation of the strain energy $W_{sk}(\{U_s^M\},\{U_r^M\})$, in the deformed element.

According to the principle of virtual works, an infinitesimal change in the vertices positions ($\{\delta U^M\}$) at which forces $\{F^M\}$ are applied results in a variation of the element strain energy δW_e:

$$\delta W_e = \{\delta U_s^M\}^T\{F_s^M\} + \{\delta U_r^M\}^T\{F_r^M\} \tag{2.62}$$

With the same convention used for nodal displacements, nodal forces $\{F_s^M\}$ and $\{F_r^M\}$ read:

$$\{\vec{F}_s^M\} = \begin{pmatrix} F_s^1 \\ F_s^2 \\ F_s^3 \end{pmatrix}, \{\vec{F}_r^M\} = \begin{pmatrix} F_r^1 \\ F_r^2 \\ F_r^3 \end{pmatrix}$$

Assuming a homogeneous deformation in the element implies:

$$\delta W_e = S_e \delta W_{sk}, \tag{2.63}$$

in which S_e is the element surface. Thus, Eq. 2.62 and 2.63 allow to write:

$$\{\delta U_s^M\}^T \{F_s^M\} + \{\delta U_r^M\}^T \{F_r^M\} = S_e \delta W_{sk} \tag{2.64}$$

Writing the second-order Taylor development of $W_{sk}(\{U_s^M\}, \{U_r^M\})$ provides the following expression for δW_{sk}:

$$\begin{aligned} \delta W_{sk} &= W_{sk}(\{\vec{U}_s^M\} + \{\delta\vec{U}_s^M\}, \{\vec{U}_r^M\} + \{\delta\vec{U}_r^M\}) - W_{sk}(\{\vec{U}_s^M\}, \{\vec{U}_r^M\}) \\ &= \vec{\nabla}(W_{sk}(\{\vec{U}_s^M\}, \{\vec{U}_r^M\}). \begin{pmatrix} \{\delta\vec{U}_s^M\} \\ \{\delta\vec{U}_r^M\} \end{pmatrix} \end{aligned}$$

That is equivalent to:

$$\begin{aligned} \delta W_{sk} &= (\frac{\partial W_{sk}}{\partial \{U_s^M\}}, \frac{\partial W_{sk}}{\partial \{U_r^M\}}). \begin{pmatrix} \{\delta\vec{U}_s^M\} \\ \{\delta\vec{U}_r^M\} \end{pmatrix} \\ &= (\frac{\partial W_{sk}}{\partial \lambda_1}\frac{\partial \lambda_1}{\partial \{U_s^M\}} + \frac{\partial W_{sk}}{\partial \lambda_2}\frac{\partial \lambda_2}{\partial \{U_s^M\}}, \frac{\partial W_{sk}}{\partial \lambda_1}\frac{\partial \lambda_1}{\partial \{U_r^M\}} + \frac{\partial W_{sk}}{\partial \lambda_2}\frac{\partial \lambda_2}{\partial \{U_r^M\}}). \begin{pmatrix} \{\delta\vec{U}_s^M\} \\ \{\delta\vec{U}_r^M\} \end{pmatrix} \\ &= (\frac{\partial W_{sk}}{\partial \lambda_1}\frac{\partial \lambda_1}{\partial \{U_s^M\}} + \frac{\partial W_{sk}}{\partial \lambda_2}\frac{\partial \lambda_2}{\partial \{U_s^M\}})\{\delta\vec{U}_s^M\} + (\frac{\partial W_{sk}}{\partial \lambda_1}\frac{\partial \lambda_1}{\partial \{U_r^M\}} + \frac{\partial W_{sk}}{\partial \lambda_2}\frac{\partial \lambda_2}{\partial \{U_r^M\}})\{\delta\vec{U}_r^M\} \end{aligned} \tag{2.65}$$

Finally, comparing Eq. 2.64 and Eq. 2.65, one may obtain the nodal forces ($\{F_s^M\}$ and $\{F_r^M\}$) induced by the element deformation:

$$\{F_s^M\} = S_e \frac{\partial W_{sk}}{\partial \lambda_1}\frac{\partial \lambda_1}{\partial \{U_s^M\}} + S_e \frac{\partial W_{sk}}{\partial \lambda_2}\frac{\partial \lambda_2}{\partial \{U_s^M\}} \tag{2.66}$$

$$\{F_r^M\} = S_e \frac{\partial W_{sk}}{\partial \lambda_1}\frac{\partial \lambda_1}{\partial \{U_r^M\}} + S_e \frac{\partial W_{sk}}{\partial \lambda_2}\frac{\partial \lambda_2}{\partial \{U_r^M\}} \tag{2.67}$$

Note that $\{F_s^M\}$ and $\{F_r^M\}$ represent the nodal forces induced by the deformation of a sole triangular element. Hence, the actual force at a membrane marker is calculated as the summation of contributions arising from all elements to which it belongs.

Out-plane curvature forces

Membrane bending forces derive from the Helfrich energy [63]:

$$W_b = \frac{E_b}{2}\int_S (2\kappa - c_o)^2 dS, \tag{2.68}$$

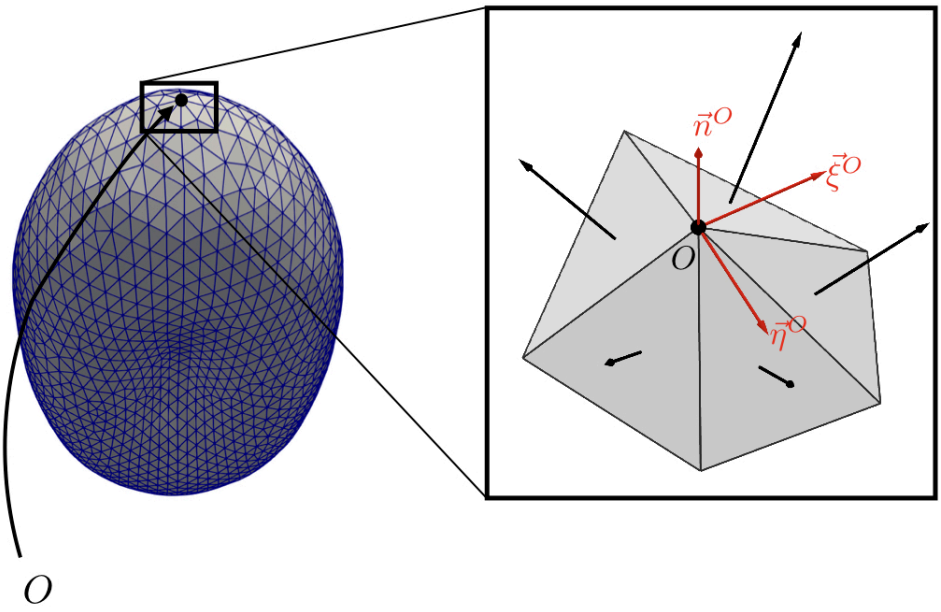

Figure 2.8 – Construction of the local coordinates system ($\vec{n}^O$,$\vec{\xi}^O$,$\vec{\eta}^O$) at a given membrane marker O.

in which κ denotes the mean curvature, E_b the bending modulus and c_o the spontaneous curvature. Developements by Zhong-can *et al.* [184] state that the membrane curvature force at a membrane marker O expresses:

$$\vec{F}_b^O = E_b[(2\kappa^O - c_o)(2[\kappa^O]^2 - 2\kappa_g^O + \kappa^O c_o) + 2\nabla^s \kappa^O]\vec{n}^O, \tag{2.69}$$

where κ_s is the Gaussian curvatures, ∇^s denotes the Laplace Beltrami operator (surface Laplacian) and $\vec{n}$ refers to the membrane normal. Superscript O refers to the marker O at which the quantities are evaluated. Note that $\vec{F}_b^O$ is a force per unit area.

Farutin *et al.* [35] proposed a method to compute the different curvatures of Eq. 2.69. For the sake of completeness, the principal steps are presented in the following. For more details in terms of theoretical developments, readers are referred to the original publication [35].

First, given a membrane marker O, the normal at vertex O denoted by $\vec{n}^O$ is computed as the averaged normal of the neighbouring triangular elements (represented as black arrows in Fig. 2.8). Moreover, a local coordinates system centered in O is defined by taking two vectors perpendicular to $\vec{n}^O$ that are referred to as $\vec{\xi}^O$ and $\vec{\eta}^O$ (see Fig. 2.8). Then, membrane nodes in the neighbourhood of O are chosen and their coordinates (ξ,η) in the local coordinates system ($\vec{\xi}^O$,$\vec{\eta}^O$) are computed. A marker near O whose location is $\vec{X}$ (expressed in ($\vec{e}_x$,$\vec{e}_y$,$\vec{e}_z$)), has the following ξ and η coordinates:

$$\begin{aligned} \xi &= (\vec{X} - \vec{X}^O).\vec{\xi}^O \\ \eta &= (\vec{X} - \vec{X}^O).\vec{\eta}^O \end{aligned} \tag{2.70}$$

With $\vec{X}^O$ the coordinates of O in the global system. The quadratic approximations of the global coordinates X_i (i=1,2,3) of the retained neighbours according to the local coordinates (ξ,η) are then performed:

$$X_i(\xi,\eta) = X_i^O + C_\xi^{X_i}|^O\xi + C_\eta^{X_i}|^O\eta + \frac{1}{2}[C_{\eta\eta}^{X_i}|^O\eta^2 + C_{\xi\xi}^{X_i}|^O\xi^2 + C_{\xi\eta}^{X_i}|^O\xi\eta] \quad (2.71)$$

Coefficients $C^{X_i}|^O$ are assessed by a classical least squares method. They represent the coefficients of the polynomial approximation of the global coordinate X_i in the local coordinate system of node O. Representing the surface coordinates as a function of a local curvilinear coordinate system (ξ , η) allows to use differential geometry expressions to calculate the locals curvatures. The curvatures at node O are given by:

$$\kappa^O = \frac{1}{2}tr(\bar{\bar{c}}^O[\bar{\bar{g}}^O]^{-1}) \quad (2.72)$$

$$\kappa_g^O = det(\bar{\bar{c}}^O[\bar{\bar{g}}^O]^{-1}) \quad (2.73)$$

With $\bar{\bar{c}}^O$ and $\bar{\bar{g}}^O$ depending of coefficient $C^{X_i}|^O$ such as:

$$\begin{aligned} \bar{\bar{g}}_{\alpha\beta}^O &= \sum_{i=1}^{3} C_\alpha^{X_i}|^O C_\beta^{X_i}|^O, \\ \bar{\bar{c}}_{\alpha\beta}^O &= \sum_{i=1}^{3} n_i^O C_{\alpha\beta}^{X_i}|^O, \\ &(\alpha,\beta \in \{\xi,\eta\}) \end{aligned} \quad (2.74)$$

n_i^O stems from the normal vector components ($\vec{n}^O$) in the global system. It should be noted that $\bar{\bar{g}}^O$ depends only on the first-order coefficients ($C_\xi^{X_i}|^O$ and $C_\eta^{X_i}|^O$) while $\bar{\bar{c}}^O$ relies on second-order coefficients ($C_{\xi\xi}^{X_i}|^O$, $C_{\eta\eta}^{X_i}|^O$ and $C_{\xi\eta}^{X_i}|^O$). Once κ^O is evaluated for all membrane markers O according to Eq. 2.72, a last quadratic approximation is achieved for the mean curvature κ:

$$\kappa(\xi,\eta) = \kappa^O + C_\xi^\kappa|^O\xi + C_\eta^\kappa|^O\eta + \frac{1}{2}[C_{\eta\eta}^\kappa|^O\eta^2 + C_{\xi\xi}^\kappa|^O\xi^2 + C_{\xi\eta}^\kappa|^O\xi\eta] \quad (2.75)$$

Finally, from coefficients $C^\kappa|^O$, the remaining operator $\nabla^s\kappa^O$ is computed as:

$$\nabla^s\kappa^O = C_{\alpha\beta}^\kappa|^O[g_{\alpha\beta}^O]^{-1} - ([g_{\alpha\beta}^O]^{-1}C_{\alpha\beta}^{X_i}|^O)([g_{\gamma\epsilon}^O]^{-1}C_\gamma^\kappa|^O C_\epsilon^{X_i}|^O) \quad (2.76)$$

Equations. 2.2.1, 2.72, 2.76 and Eq. 2.69 provide the curvature force ($\vec{F}_b^O$) at node O.

2.2.2 Coupling

The total elastic forces ($\vec{F}_E$) are obtained by summing the bending part with the in-plane deformation part (see Sec. 2.2.1). As stated in Sec. 2.2, the elastic forces are accounted in the fluid momentum equation (Eq. 2.47) as a source term $\vec{f}_v$. This is done by the regularisation equation of Peskin [125] (Eq. 2.50). These forces are a consequence of the membrane displacement induced by the fluid. The membrane nodes movements are computed by the interpolation equation (Eq. 2.51). Both

interpolation and regularisation equations involve the integration of a Dirac function allowing the change of formalism (from Eulerian to Lagrangian and inversely). Hence, in the continuous case, exchanged quantities (forces and velocities) are simply transmitted and the coupling between solver NSS and the solid membrane is achieved straightforwardly. However, considering the discrete problem implies a complication concerning the Dirac function. Indeed, regarding Fig. 2.5, it should be noted that the membrane markers (viz. the vertices of the triangular meshes) are not conforming with the fluid discretization nodes (i.e. tetrahedra vertices). Consequently, using directly Eq. 2.50 and Eq. 2.51 is not suited. The Dirac function is then replaced by window function that must satisfy specific properties [140] and is the equivalent in the discrete space of the Dirac function in the continuous space. Moreover, as reported by Pinelli *et al.* [127], the use of irregular fluid meshes requires a specific adaptation of the window function.

The present section deals with such issues. After introducing the discrete form of regularization and interpolation equations (Eq. 2.50 and Eq. 2.51), the approximated Dirac function used for the discrete problem is presented. Then, the method of Pinelli *et al.* [127] to adjust the discrete Dirac function to irregular grids is explained. Finally, the method employed to impose a different viscosity inside the cell is dealt with.

Discrete spreading and interpolation equations

Assuming that the fluid domain is discretized with N control volumes and the membrane by M markers, one may approximate Eq. 2.50 and Eq. 2.51 by:

$$\frac{\partial \vec{X_j}}{\partial t}(t) = \sum_{i=1}^{N} \vec{u_i} \delta_h(\vec{x_i} - \vec{X_j}(t)) V_i \tag{2.77}$$

and

$$\vec{f_v}(\vec{x_i}, t) = \sum_{j=1}^{M} \vec{F_E}|_j \delta_h(\vec{x_i} - \vec{X_j}(t)) S_j^m \tag{2.78}$$

$\vec{u_i}$ and $\vec{F_E}|_j$ stems from the fluid velocity at node $\vec{x_i}$ and the elastic force at marker $\vec{X_j}$. V_i is the control volume, while S_j^m denotes the area of the membrane part surrounding marker $\vec{X_j}$. In Eq. 2.77 and Eq. 2.78, the modified dirac function δ_h appears. As a matter of fact, if the membrane marker is not located on a fluid node, the classical Dirac function is not able to transfer the fluid velocity to the membrane and the solid forces to the fluid.

Approximation of the dirac by a window function

The main idea when designing δ_h is that Eq. 2.78 spreads force $\vec{F_E}$ to the neighboring fluid nodes and Eq. 2.77 interpolates the membrane velocity from the nearby fluid nodes. This may be done by a function with compact support that equals zero far from the solid membrane, so that the interaction only occurs near the solid markers. Figure. 2.9 illustrates the compact support of δ_h around a marker indexed by m. Fluid nodes, represented by a square are within the support and will have a nonzero

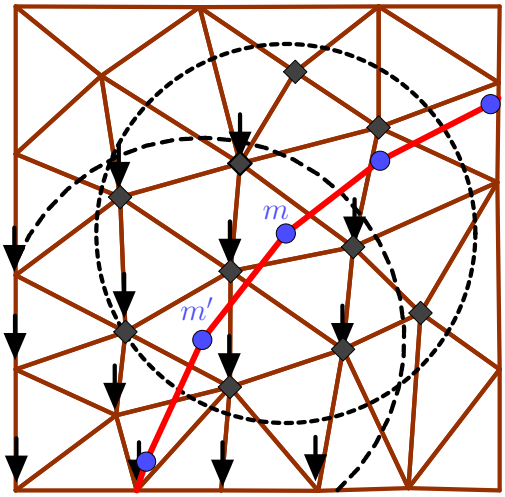

Figure 2.9 – Diagram of a membrane grid shown over a fluid triangular grid. Note that this diagram is shown in two dimensions, for the sake of clarity. Membrane markers are shown in bold blue points that are linked by red segments. Compact support of the window functions related to markers denoted by m and m' are illustrated by dashed circles. Fluid nodes located in the support of m are highlighted by diamond points, while those that are in m' support are pointed by black arrows.

contribution in the computation of marker m velocity (see Eq. 2.77). Moreover, elastic forces ($\vec{F}_E$) at marker m are spread over all diamond nodes of Fig. 2.9 by Eq. 2.78. The black arrows (see Fig. 2.9) mark the fluid nodes that are placed in the compact support of δ_h centred on a second marker denoted by m'. Hence, diamond points highlighted by a black arrow are coupled with both m and m'. This illustrates the fact that for a given fluid node $\vec{x}_i$, several solid markers may contribute to the applied volumic force ($\vec{f}_v|_i$).

The approximated Dirac function δ_h can not be chosen arbitrarily. It must satisfy specific conditions that are developed in the following. For an arbitrary function f, the window function δ_h is expected to lead to the approximation $f_h(\vec{x_o})$ the closest to $f(\vec{x_o})$ by assessing the following integral:

$$f_h(\vec{x_o}) = \int f(x)\delta_h(\vec{x} - \vec{x_o})dxdydz \tag{2.79}$$

Writing the Taylor expansion of $f(\vec{x})$ in the vicinity of $\vec{x_o}$ provides the following equation:

$$f(\vec{x}) = f(\vec{x_o}) + \sum_{i}^{\infty}\sum_{j}^{\infty}\sum_{k}^{\infty} f_{x^i,y^j,z^k}(\vec{x_o})(x - x_o)^i(y - y_o)^j(z - z_o)^k \tag{2.80}$$

Multiplying Eq. 2.80 by $\delta_h(\vec{x} - \vec{x_o})$ and integrating over the domain yields:

$$\begin{aligned} f_h(\vec{x_o}) = f(\vec{x_o}) &\int \delta_h(\vec{x} - \vec{x_o})dxdydz \\ &+ \sum_{i}^{\infty}\sum_{j}^{\infty}\sum_{k}^{\infty} f_{x^i,y^j,z^k}(\vec{x_o}) \int (x - x_o)^i(y - y_o)^j(z - z_o)^k \delta_h(\vec{x} - \vec{x_o})dxdydz \end{aligned} \tag{2.81}$$

Then, imposing $f_h(\vec{x_o}) = f(\vec{x_o})$, one may deduce from Eq. 2.81 the following conditions that δ_h must satisfy:

$$\begin{cases} M_{0,0,0} = \int \delta_h(\vec{x} - \vec{x_o}) dxdydz = 1 \\ M_{i,j,k} = \int (x - x_o)^i (y - y_o)^j (z - z_o)^k \delta_h(\vec{x} - \vec{x_o}) dxdydz = 0 \quad \forall i, j, k \end{cases} \tag{2.82}$$

Terms $M_{i,j,k}$ in Eq. 2.82 are the moments of the window function. Generally, only the conditions on the moments of order 0 and/or 1 are taken into account. One of the window functions implemented in YALES2BIO that fulfills the conditions on the first order is the following, proposed by Peskin [124] and restricted to Cartesian meshes of grid size h_s:

$$\delta_h(r) = \begin{cases} \frac{1}{4h_s}(1 + cos(\frac{\pi r}{2})) & \text{if} \quad |r| < 2 \\ 0 \quad \text{otherwise} \end{cases} \tag{2.83}$$

With $r = |\vec{x} - \vec{x}_o|$. This window function has a support of 4 grid spaces. Many other possibilities exist for regularization, notably over 3 [140] or 2 grid spaces [52], with more or less restrictions on the properties of the window function. The construction of the window function is notably discussed by Peskin [125].

IBM For irregular meshes

When irregular fluid grids are considered, classical window functions like Eq. 2.83 do not comply with the conditions of Eq. 2.82. Pinelli *et al.* [127], using the work of Liu and co-authors [100–102] on the so-called Reproducing Kernel Particle Method, introduced $\tilde{\delta}_h$, a calibrated version of δ_h:

$$\tilde{\delta_h}(\vec{x} - \vec{x_o}) = \sum_l \sum_m \sum_n b_{l,m,n} (x - x_o)^l (y - y_o)^m (z - z_o)^n \delta_h(x - x_o) \tag{2.84}$$

Equation. 2.84 is the product of a polynomial by an initial window function (δ_h). The polynomial coefficients $b_{l,m,n}$ are set in such a way that the requirements on the momentums of the calibrated window function are satisfied:

$$\begin{cases} \tilde{M}_{0,0,0} = \int \tilde{\delta_h}(\vec{x} - \vec{x_o}) dxdydz = 1 \\ \tilde{M}_{i,j,k} = \int (x - x_o)^i (y - y_o)^j (z - z_o)^k \tilde{\delta_h}(\vec{x} - \vec{x_o}) dxdydz = 0 \\ \forall i, j, k, \ with \ i + j + k \leq P \end{cases} \tag{2.85}$$

, with P the order of the method. The idea of the method is that the higher P, the closest the window function to a Dirac function. The correction of δ_h by a polynomial actually enables to define the moments of the corrected window function from those of the initial window function. Injecting Eq. 2.84 in Eq. 2.85 leads to:

$$\begin{cases} \sum_l \sum_m \sum_n b_{l,m,n} \int (x - x_o)^{0+l} (y - y_o)^{0+m} (z - z_o)^{0+n} \delta_h(\vec{x} - \vec{x_o}) dxdydz = 1 \\ \sum_l \sum_m \sum_n b_{l,m,n} \int (x - x_o)^{i+l} (y - y_o)^{j+m} (z - z_o)^{k+n} \delta_h(\vec{x} - \vec{x_o}) dxdydz = 0 \\ \forall i, j, k, \ with \ i + j + k \leq P \end{cases}$$

$$\iff \begin{cases} \sum_l \sum_m \sum_n b_{l,m,n} M_{l,m,n} = 1 \\ \sum_l \sum_m \sum_n b_{l,m,n} M_{i+l,j+m,k+n} = 0 \quad \forall i, j, k \ with, \ i + j + k \leq P \end{cases} \tag{2.86}$$

We impose the moments of the zeroth, first and second order to be 1, 0 and 0, respectively. Hence, Eq. 2.86 reduces to the following linear system:

$$\begin{bmatrix} M_{0,0,0} & M_{1,0,0} & M_{0,1,0} & M_{0,0,1} & M_{1,1,0} & M_{1,0,1} & M_{0,1,1} & M_{2,0,0} & M_{0,2,0} & M_{0,0,2} \\ M_{1,0,0} & M_{1,0,0} & M_{1,1,0} & M_{1,0,1} & M_{2,1,0} & M_{2,0,1} & M_{1,1,1} & M_{3,0,0} & M_{1,2,0} & M_{1,0,2} \\ M_{0,1,0} & M_{1,1,0} & M_{0,2,0} & M_{0,1,1} & M_{1,2,0} & M_{1,1,1} & M_{0,2,1} & M_{2,1,0} & M_{0,3,0} & M_{0,1,2} \\ M_{0,0,1} & M_{1,0,1} & M_{0,1,1} & M_{0,0,2} & M_{1,1,1} & M_{1,0,2} & M_{0,1,2} & M_{2,0,1} & M_{0,2,1} & M_{0,0,3} \\ M_{1,1,0} & M_{2,1,0} & M_{1,2,0} & M_{1,1,1} & M_{2,2,0} & M_{2,1,1} & M_{1,2,1} & M_{3,1,0} & M_{1,3,0} & M_{1,1,2} \\ M_{1,0,1} & M_{2,0,1} & M_{1,1,1} & M_{1,0,2} & M_{2,1,1} & M_{2,0,2} & M_{1,1,2} & M_{3,0,1} & M_{1,2,1} & M_{1,0,3} \\ M_{0,1,1} & M_{1,1,1} & M_{0,2,1} & M_{0,1,2} & M_{1,2,1} & M_{1,1,2} & M_{0,2,2} & M_{2,1,1} & M_{0,3,1} & M_{0,1,3} \\ M_{2,0,0} & M_{3,0,0} & M_{2,1,0} & M_{2,0,1} & M_{3,1,0} & M_{3,0,1} & M_{2,1,1} & M_{4,0,0} & M_{2,2,0} & M_{2,0,2} \\ M_{0,2,0} & M_{1,2,0} & M_{0,3,0} & M_{0,2,1} & M_{1,3,0} & M_{1,2,1} & M_{0,3,1} & M_{2,2,0} & M_{0,4,0} & M_{0,2,2} \\ M_{0,0,2} & M_{1,0,2} & M_{0,1,2} & M_{0,0,3} & M_{1,1,2} & M_{1,0,3} & M_{0,1,3} & M_{2,0,2} & M_{0,2,2} & M_{0,0,4} \end{bmatrix} \begin{pmatrix} b_{0,0,0} \\ b_{1,0,0} \\ b_{0,1,0} \\ b_{0,0,1} \\ b_{1,1,0} \\ b_{1,0,1} \\ b_{0,1,1} \\ b_{2,0,0} \\ b_{0,2,0} \\ b_{0,0,2} \end{pmatrix} = \begin{pmatrix} 1 \\ 0 \\ 0 \\ 0 \\ 0 \\ 0 \\ 0 \\ 0 \\ 0 \\ 0 \end{pmatrix} \tag{2.87}$$

Finally, once $b_{l,m,n}$ are assessed by solving Eq. 2.87, the calibrated window function reads:

$$\begin{aligned} \tilde{\delta_h}(\vec{x} - \vec{x_o}) = [b_{0,0,0} + b_{1,0,0}(x - x_o) + b_{0,1,0}(y - y_o) + b_{0,0,1}(z - z_o) + \\ b_{1,1,0}(x - x_o)(y - y_o) + b_{1,0,1}(x - x_o)(z - z_o) + b_{0,1,1}(y - y_o)(z - z_o) + \\ b_{2,0,0}(x - x_o)^2 + b_{0,2,0}(y - y_o)^2 + b_{0,0,2}(z - z_o)^2]\delta_h(\vec{x} - \vec{x_o}) \end{aligned} \tag{2.88}$$

It should be noted that coefficients $b_{l,m,n}$ depend on $\vec{x}_o$, the center of the approximated Dirac function. This means that the linear system of Eq. 2.87 is solved once for each membrane marker.

Variable viscosity coeficient

In some applications, the cytosol viscosity (ν_{in}) may differ from the suspending fluid viscosity (ν_{ext}). The internal viscosity (ν_{in}) is imposed by the use of the method presented in the front-tracking method of Unverdi and Tryggvason [168]. An indicator function I_i is computed for each fluid node $\vec{x}_i$, in such a way that I_i = 0 outside the membrane and I_i = -1 inside the cell. Hence, the viscosity field is assessed by:

$$\nu_i = \nu_{ext} + (\nu_{ext} - \nu_{in})I_i \tag{2.89}$$

The indicator function is obtained by solving the following Poisson equation:

$$\nabla.[\nabla I] = \nabla.\vec{G} \tag{2.90}$$

$\vec{G}$ is computed by spreading the membrane normals on the fluid grid as done for the elastic forces in Eq. 2.78:

$$\vec{G}(\vec{x_i}, t) = \sum_{j=1}^{M} \vec{n}^j \delta_h(\vec{x_i} - \vec{X}_j(t)) S_j^m \tag{2.91}$$

Equation. 2.90 is discretized with a finite volume method (as presented in Sec. 2.1.2) and takes the following discrete form:

$$\mathcal{L}(I)|_i = \mathcal{D}(\vec{G})|_i \tag{2.92}$$

This linear system for the indicator function (I_i) is solved with the DPCG method [105].

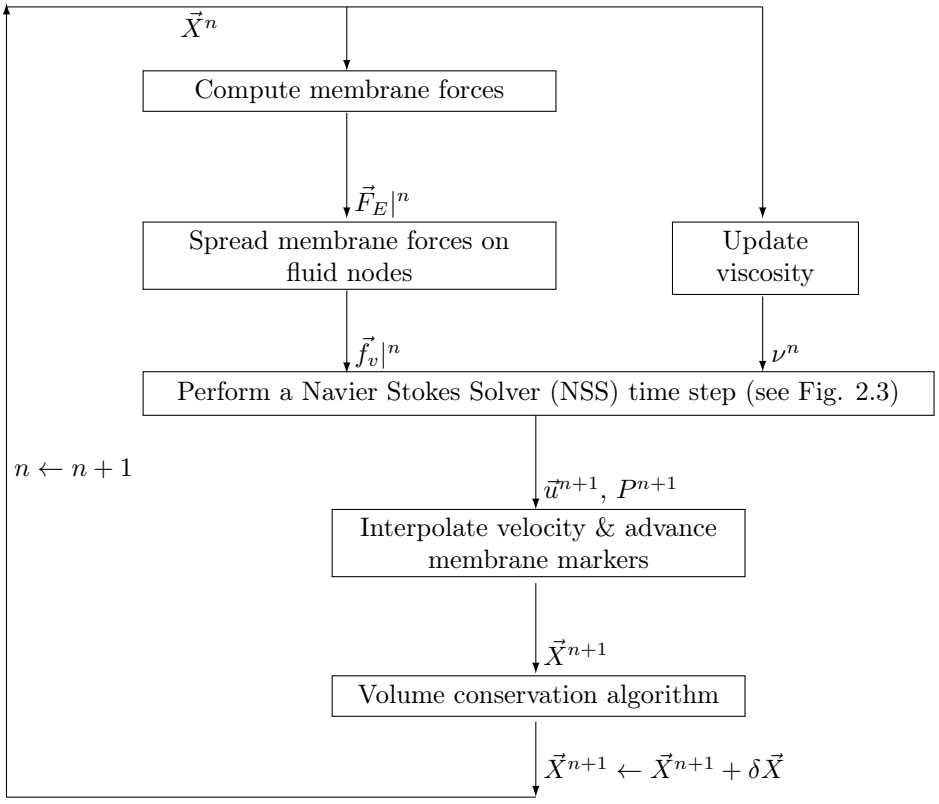

Figure 2.10 – Temporal loop of solver FSIS.

2.2.3 Algorithm of the Fluid-Structure Interaction solver (FSIS)

Figure. 2.10 summarizes the different steps required for solving the fluid-structure interaction between an elastic membrane and an incompressible fluid in the solver FSIS. At the beginning of the time step, the viscosity field is updated from the membrane markers positions ($\vec{X}^n$) according to Eq. 2.89. Then, membrane elastic forces are computed from $\vec{X}^n$ by applying Eq. 2.69 on each marker and assessing Eq. 2.66 and 2.67 on each triangular element. Thereafter, the membrane forces ($\vec{F}_E|^n$) are spreaded on the fluid nodes by applying the regularization equation (Eq. 2.78) with the calibrated window function. The source term ($f_v|^n$) and the viscosity (ν^n) being known, the fluid quantities ($\vec{u}$ and P) are advanced as done in solver NSS (see Fig. 2.2), the regularized membrane source term being treated explicitly. Finally, solid markers are updated by interpolating the velocity on the membrane with Eq. 2.77 and using an explicit Euler time advancement scheme. An additional step that has not been described is called 'volume conservation algorithm' (see Fig. 2.10), performed to correct the well-known problem of volume conservation of the immersed boundary method [97, 125]. It is performed at the end of the time step and is devoted to the volume conservation of the cell. It consists in solving an optimization problem to compute the smallest markers moves $\delta\vec{X}$ that ensure the conservation of the cell volume. More information on this optimization problem are available in [46, 150].

Solver FISIS of YALESBIO have been used in several publications, showing its

ability to recover typical dynamics behaviors of red blood cells in complex flows [72, 91, 103, 107, 110]. In the next section an example of application is given.

2.2.4 Test case: RBC flowing in a micro-capillary

Gases exchanges between tissues and the haemoglobin contained inside RBCs occur in micro-capillaries (vessels of a few micrometers of diameter). The shape taken by RBCs in such vessels is expected to play an important role in the exchanges of dioxygen and carbon dioxide. Previous experimental and numerical studies revealed several RBCs shapes in constricted channels, depending on the flow-rate and the constriction. The reported trends state that the discocyte is maintained at low flowrates while a parachute shape is observed for high flow regimes. In between, RBCs may tumble or present a slipper shape [40, 117, 166]. In this section, an illustration of the results obtained with the solver FSIS is presented. It consists in comparing the RBC shapes obtained from different couples constriction/flowrate with numerical results of Fedosov *et al.* [40].

The computations are monitored by the following dimensionless parameters:

1) The constriction χ:

$$\chi = \frac{D_{rbc}}{D_c}, \tag{2.93}$$

involving the channel diameter D_c and a RBC characteristic size D_{rbc}. It is defined as the diameter of the sphere having the same surface as the cell membrane.

2) The Foppl Von Karman number F_{VK}, that compares the membrane shear resistance with the bending resistance:

$$F_{VK} = \frac{G_s D_{rbc}^2}{E_b}. \tag{2.94}$$

3) The scaled shear rate $\dot{\gamma^*}$:

$$\dot{\gamma^*} = \frac{\rho \nu_{ext} D_{rbc}^3}{E_b} \dot{\gamma_m}, \tag{2.95}$$

in which $\dot{\gamma_m}$ is the shear rate assessed by $\dot{\gamma_m} = u_m/D_c$, with u_m the mean velocity in the channel.

4) The Reynolds number Re:

$$Re = \frac{u_m D_{rbc}}{\nu_{ext}}. \tag{2.96}$$

5) The viscosity ratio:

$$\mathcal{Y} = \frac{\nu_{in}}{\nu_{ext}} \tag{2.97}$$

Imposing χ to 0.71, F_{VK} to 2662, Re to 0.1 and $\mathcal{Y}$ to 1, three different $\dot{\gamma^*}$ are tested (5, 15 and 25). Note that if χ, F_{VK}, Re and $\dot{\gamma^*}$ are known, imposing D_{rbc}, ρ and E_b allows to derive u_m, D_c, G_s, ν_{in}, and ν_{ext}. The area modulus E_a and the spontaneous curvature c_o are not accounted for in the dimensionless parameters, that is why they are kept constant in the cases considered ($E_a = 31$ N.m^{-1} and $c_o = 0$ m^{-1}, respectively). In the following, $E_b = 3 \times 10^{-19}$ Nm and $\rho = 1000$

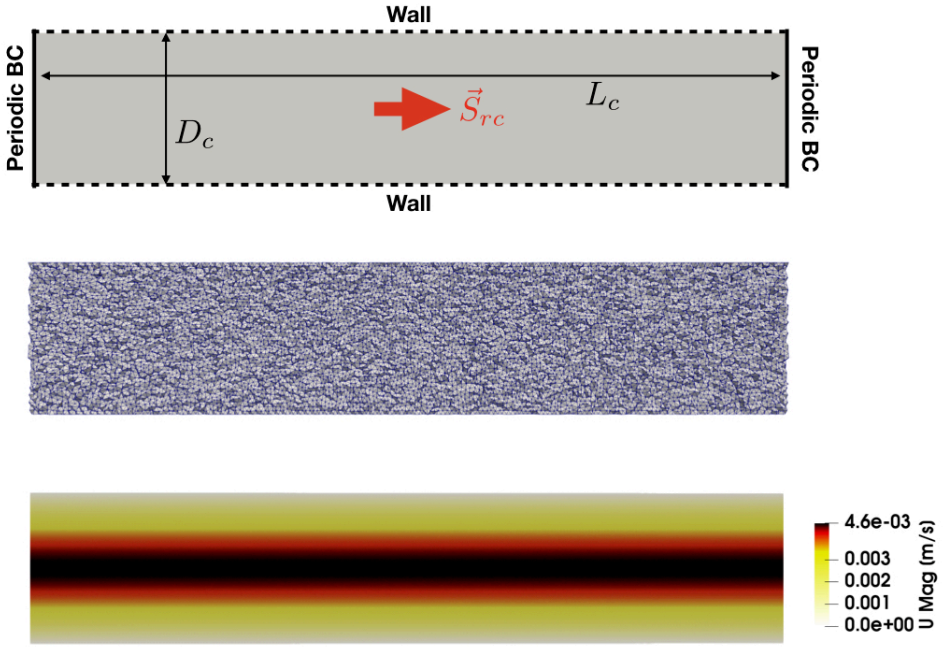

Figure 2.11 – Fluid domain used in the FSIS test case. The **top** picture illustrates the geometry and boundary conditions. The source term ($\vec{S}_{rc}$) is represented by a red arrow. Note that this source term is imposed on all nodes composing the fluid domain. The cylinder has a length L_c of 91.5 μm and a diameter D_c of 9.14 μm. The **middle** picture depicts the mesh used in the simulation. The **bottom** illustration displays the initial velocity field.

kg.m^{-3}. Moreover, the discocyte shape reported in [33], with a membrane area of 133 μm^2 and a volume of 93 μm^3 is retained and considered as the stress-free shape in the simulations. Hence, the RBC has a characteristic size D_{rbc} of 6.5 μm and the channel diameter (D_c) equals 9.15 μm, since $\chi = 0.71$. The RBC initially takes a discocyte shape and the membrane is meshed with triangular elements whose the typical size is 0.3 μm.

The fluid domain employed in the simulation that complies with $\chi = 0.71$ is shown in Fig. 2.11 (**top** figure). A null velocity is applied on the channel walls (edges indicated as 'wall' in Fig. 2.11) and a periodic condition is set on boundaries referred to as 'periodic'. The fluid flow is forced by means of a constant source term that is added in the volumic forces of the momentum equation:

$$\mathcal{S}_{rc} = \frac{8\nu_{ext}\rho u_m}{\left(\frac{1}{2}D_c\right)^2} \tag{2.98}$$

$\mathcal{S}_{rc}$ equals the pressure loss required for imposing a mean velocity of u_m in the channel, as supported by the analytical solution of the Poiseuille flow. The initial velocity is set according to the parabolic profile of Poiseuille:

$$u(r) = 2u_m\left(1 - \frac{r^2}{(D_c/2)^2}\right), \tag{2.99}$$

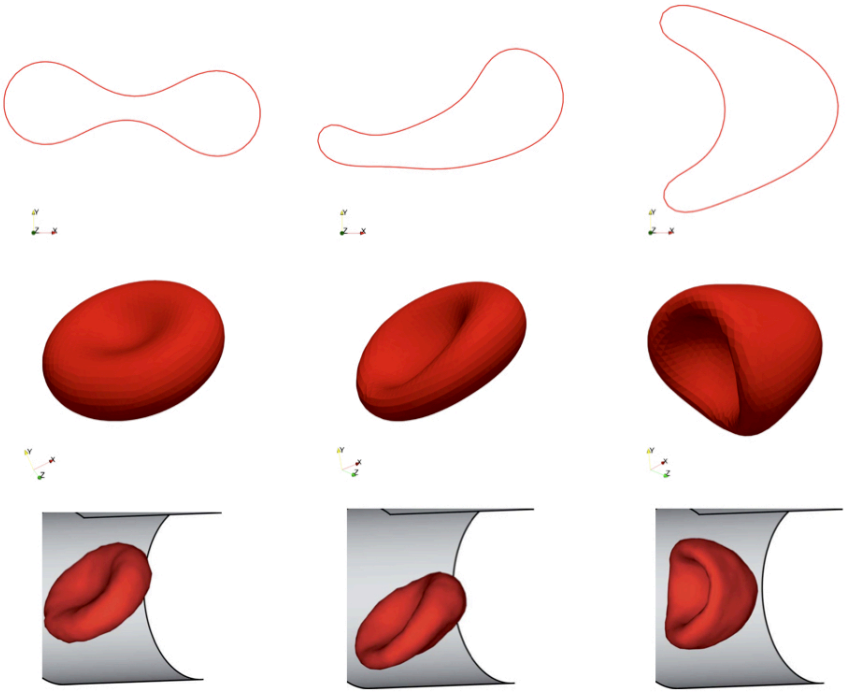

Figure 2.12 – Shapes depicted by RBCs flowing in a microcapillary defined by $\chi = 0.71$. **Top** row: cut view obtained with solver FSIS. **Middle** row: 3D view obtained with solver FSIS. **Bottom** row: typical RBCs shapes obtained by Fedosov *et al.*, coming from [40]. The **left**, **middle** and **right** columns refer to the discocyte, the slipper and the parachute shapes, respectively. The discocyte, the slipper and the parachute shapes obtained with solver FSIS of the YALES2BIO software are obtained by performing computations with $\dot{\gamma}^*$ equal to 5, 15 and 25, respectively (left, middle and right columns respectively). A Reynolds number (Re) of 0.1 and a Foppl Von Karman (F_{VK}) of 2662 are used in these simulations.

in which u is the velocity along the channel principal axis and r is the radial position in the channel section. The channel is meshed with tetrahedral elements having a characteristic size of 0.3 μm (see Fig. 2.11, **middle** image) and the initial velocity field is shown in Fig. 2.11 (**bottom** figure).

The first and the second rows of Fig. 2.12 depict the RBC shapes obtained from the three different values of $\dot{\gamma}^*$ (5, 15, 25) in a cut view and a 3D view, respectively. A discocyte shape is observed for the RBC that flows at a scaled shear rate of 5 (**left** column). Taking a $\dot{\gamma}^*$ of 15 leads to a slipper shape (**middle** column) while for 25, the parachute is retrieved (**right** column). These results are in agreement with those of Fedosov *et al.* [40] who reports the same shapes for the three presented cases. The **bottom** row of Fig. 2.12 shows typical shapes (discocyte, slipper, and parachute) they obtained and good comparisons with the solver FSIS are observed.

2.3 Electrostatic solver (ESS)

This section is devoted to the electrostatic solver (ESS) that enables the calculation of the electrical field perturbed by an isolating cell. In the following, the modelling assumptions and equations are introduced. Then, its implementation in the YALES2BIO software is presented. Finally, solver ESS is validated by comparison with analytical results.

2.3.1 Red blood cells in an electrostatic field

Maxwell-Ampere's law for a linear, isotropic and homogeneous medium writes :

$$\nabla \times \vec{B} = \iota_0 \iota_r (\vec{j} + \zeta_0 \zeta_r \frac{\partial \vec{E}}{\partial t}) \tag{2.100}$$

$\vec{B}$ and $\vec{E}$ are respectively the magnetic and the electrostatic fields, while $\vec{j}$ is the free electric current density. ζ and ι denote respectively the permittivity and the magnetic permeability. Indices 0 and r refer to the vacuum and the material relative quantities. The divergence of Eq. 2.100 leads to:

$$\nabla.(\vec{j} + \zeta_0 \zeta_r \frac{\partial \vec{E}}{\partial t}) = 0 \tag{2.101}$$

With the electrostatic assumption, Ohm's law ($\vec{j} = \sigma \vec{E}$) allows to rewrite the previous equation as follow:

$$\nabla.(\sigma \vec{E} + \zeta_0 \zeta_r \frac{\partial \vec{E}}{\partial t}) = 0 \tag{2.102}$$

With σ representing the material conductivity. If the electrical field $\vec{E}$ is constant, Eq. 2.102 leads to a Poisson equation for the electrical potential ψ, since $\vec{E}$=$\nabla\psi$. Actually, RBCs move and disturb the electrical field, which is why $\vec{E}$ varies in time. However, by performing a dimensional analysis of Eq. 2.102, one may conclude that the unsteady term of Eq. 2.102 is negligible in such configuration [46]. Hence, the electrical potential is obtained by solving :

$$\nabla.[\sigma \nabla \psi] = 0 \tag{2.103}$$

RBCs are assumed isolating as done in previous analytical developments [53, 68], which is not exactly true. Indeed, the RBC membrane is almost insulating depending on the strength of the electrical field, but cytosol has a conductivity of about 0.31 $S.m^{-1}$. In the present work, a zeroing conductivity is set in the volume covered by the RBC to represent the non-conducting nature of the membrane.

2.3.2 Numerical implementation

As discussed in Sec. 2.3.1, the electrical perturbation caused by the RBC in a Coulter counter is modeled with the Laplace equation for the electrical potential ψ (see Eq. 2.103) with a vanishing conductivity coefficient (σ) inside of the membrane.

Given the location of the membrane markers, the indicator function I is first computed according to Eq. 2.90. Then, as for the kinematic viscosity ν, the conductivity field is set as follow:

$$\sigma_i = \sigma_{ext} + (\sigma_{ext} - \sigma_{in})I_i \tag{2.104}$$

The assumed isolating nature of the cell is accounted by imposing $\sigma_{in} << \sigma_{ext}$. Note that the cell membrane location is only needed for imposing the variable conductivity field.

Once the variable conductivity field is imposed in the domain, the Laplace equation (Eq. 2.103) is solved on a tetrahedral mesh, as for the fluid flow. The Laplace equation is solved using a second-order operator inspired from the numerical approach of Specogna and Trevisan [153], that have better properties on irregular meshes than the classical finite volume operator (Sec. 2.1.3). Usual conditions imposed on the limits of the domain are:

1) The Dirichlet boundary conditions, that are used to impose the potential on the electrodes, for instance (see Fig. 1.4):

$$\psi_{Bd} = b_c \tag{2.105}$$

The indice Bd stems from the domain limits, while b_c is the imposed boundary condition, income of the problem.

2) The Neumann boundary conditions that are generally employed for modeling non-conducting walls of the domain:

$$\frac{\partial \psi}{\partial \vec{n}_{Bd}}|_{Bd} = 0 \tag{2.106}$$

The vector $\vec{n}_{Bd}$ represents the vector normal to the boundary.

2.3.3 Test case: Electrical perturbation of a sphere in a homogeneous electrical field

In this thesis, we need to calculate the electrical perturbation due to the presence of an isolating red blood cells in a Coulter counter, as a function of its position and deformation. Such a calculation has to be performed typically 20 times for the passage of 1 RBC, to discretize the electrical signal in time. Hence, we need a fast method to do so. In order to avoid re-meshing the geometry too many times, the presence of the particle is imposed in a immersed way. In the present section, the approach of modelling the electrical perturbation by assessing the solution of the Laplace equation with a variable conductivity coefficient is validated by comparison to analytical results and conformal meshes results. In particular, the resistance variation ΔR induced by a spherical particle immersed in a homogeneous electrical field is simulated and compared with the analytical development presented in Sec. 1.3.1 (see Eq. 1.1).

The configuration is a cylindrical domain as depicted in Fig. 2.13 (**top** figure) on which a voltage difference of 1.0 V is applied. The channel boundaries indicated as 'wall' are modelled as non-conducting walls as stated by Eq. 2.106. Three different computations are then performed (see Fig. 2.14). In the first simulation, the Laplace

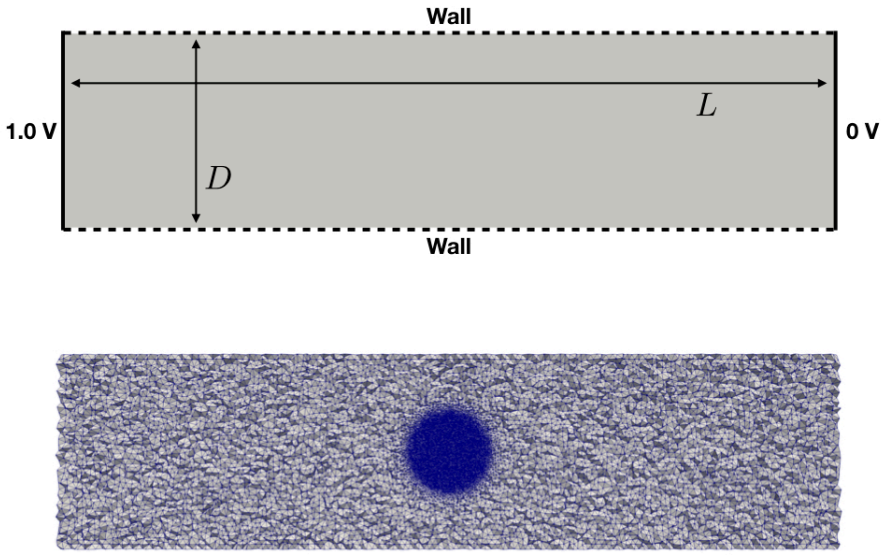

Figure 2.13 – Illustration of the geometry (**top**) and mesh (**bottom**) used in the ESS test case. Boundary condition are provided in the **top** picture, and the dimensions D and L are taken as 50 μm and 200 μm, respectivelly. Note that the mesh size is refined in the central region of domain with a size of 0.3 μm. The typical size of the tetrahedra then increases to 1.5μm with a growth rate of 1.2.

equation is solved with a constant conductivity equalling 2.27 S.m^{-1} in the entire domain (see the **top** row of Fig. 2.14). The second computation is also performed with $\sigma = 2.27$ S.m^{-1}, but with a spherical hole in the domain as shown in the **middle** row of Fig. 2.14. The spherical hole is located at the center of the domain and has a diameter of 5 μm. The spherical surface is assumed isolating and homogeneous Neumann boundary conditions are imposed, according to Eq. 2.106. Finally, in the third simulation, a variable conductivity coefficient is imposed while solving the Laplace equation. Using the method presented in Sec. 2.3, a value of $\sigma_{in} = 10^{-12}$ S.m^{-1} is imposed inside a spherical membrane of 5 μm diameter that is located at the center of the domain (see **bottom** row of Fig. 2.14). The conductivity outside of the spherical membrane is set to $\sigma_{ext} = 2.27$ S.m^{-1}, as in the former cases. It should be noted that cases of the **middle** and **bottom** rows model the presence of the same spherical particle, while case of the **top** row is used as reference for assessing the change of resistance (ΔR) induced by the particle. Cases of **top** and **bottom** rows (see Fig. 2.14) are performed with the mesh shown in Fig. 2.13. Regarding the case of the **middle** row (see Fig. 2.14) the grid is built similarly but with a hole of 5 μm of diameter in the center of the cylinder.

The potential ψ is solved for each case discussed above and the electrical field $\vec{E}$ is computed as: $\vec{E} = \vec{\nabla}\psi$. Figure. 2.15 shows the electrical field magnitude $|\vec{E}|$ for the three different cases. For the case without particle, the electrical field is

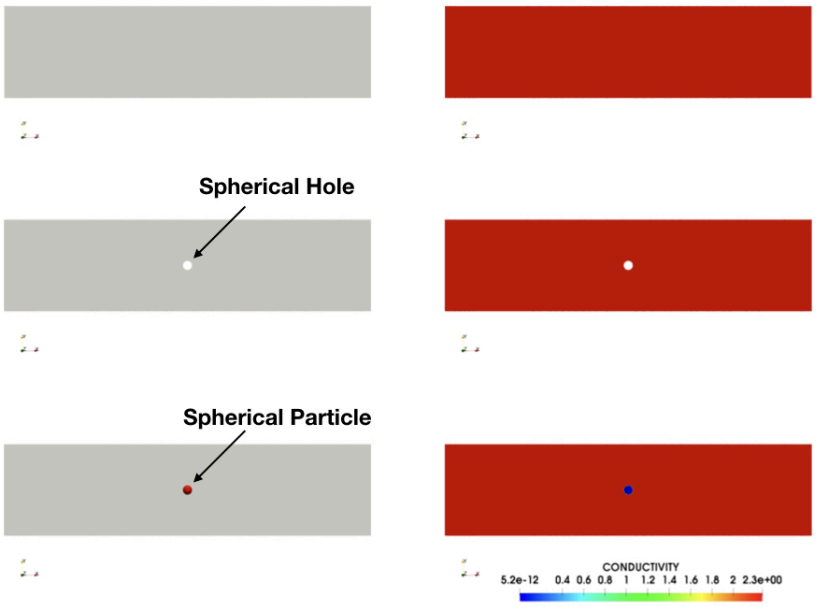

Figure 2.14 – Illustration of the three configurations investigated in the context of the validation case of solver ESS. The **top** row refers to the case without particle. In the case illustrated in the **middle** row, the presence of a spherical particle is modelled by a spherical hole in the computation domain. Note that the sphere surface is modelled as a non-conducting boundary. Finally, in the case of the **bottom** row, a vanishing conductivity coefficient is imposed inside a spherical membrane. Note that both the spherical membrane (**bottom**) and the spherical hole (**middle**) have diameters of 5 μm.

Case	$I[A]$	$R[\Omega]$	$\Delta R[\Omega]$
Empty	2.2275787E-05	44891.79	0.0
Hole	2.2270263E-05	44902.93	11.14
PTCL	2.2270370E-05	44902.71	10.92

Table 2.1 – Assessements of the current intensity (I), the resistance (R) and the resistance variation (ΔR) for the three different cases of Fig. 2.14. ΔR is computed as the difference with the 'empty' case.

perfectly homogeneous. In the contrary, the presence of a particle disturbs $\vec{E}$ in its neighbourhood (see Fig. 2.15). It is observed that the approach of vanishing the conductivity inside a spherical membrane provides an electrical field similar to the method that models the particle surface as a non-conducting wall.

For each computation, the current intensity I is calculated by integrating the free current density $\vec{j}$ over the inlet and outlet sections of the domain (ie. the surfaces were the tensions of 1.0 V and 0.0 V are imposed). Reminding that the current density equals $\sigma\vec{E}$ in the electrostatic assumption, I is computed as:

$$I = \int_S \vec{j}.d\vec{S} = \int_S \sigma\vec{E}.d\vec{S} \tag{2.107}$$

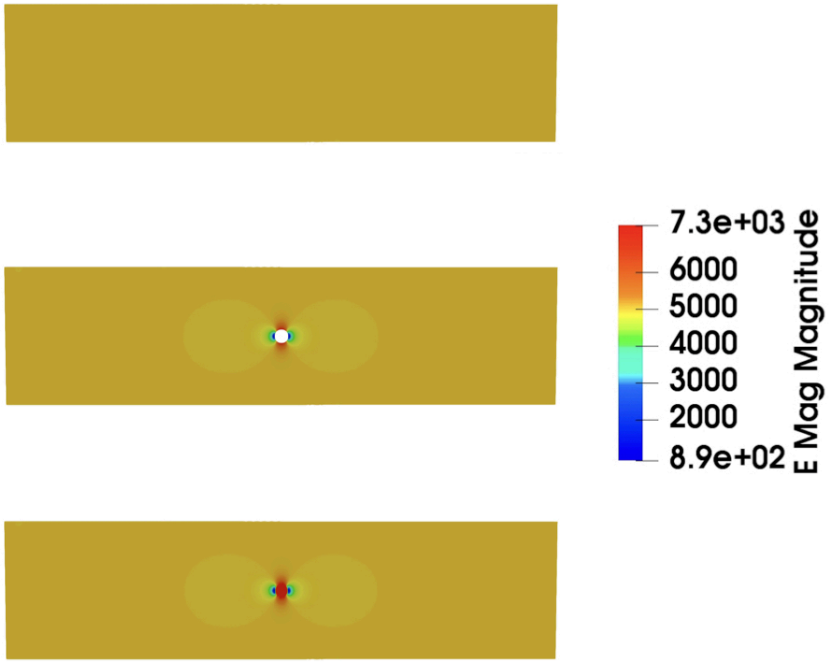

Figure 2.15 – Electrical field magnitudes obtained for the three different cases depicted in Fig. 2.14. The illustrations correspond to Fig. 2.14 in a row-wise fashion.

	PTCL	Hole	Theory
$\Delta R[\Omega]$	10.92	11.14	11.22
Error[%]	2.6	0.75	0.0

Table 2.2 – Comparison of the two approaches for modeling the resistive perturbation caused by a spherical particle, with the theoretical result.

It is verified that the current through the inlet is equal to the current throught the outlet. In Tab. 2.1, are reported the the current intensity I, and the resistance R that derives from Ohm's law with a tension equals to 1 V, for each simulation. Rows denoted by 'Empty', 'Hole' and 'PTCL' refer to cases of Fig. 2.14 (**top**, **middle** and **bottom** rows, respectively). ΔR, that is also provided in Tab. 2.1 is computed as the resistance variation according to the 'Empty' case. Results obtained with the two different approaches ('Hole' and 'PTCL') are close in terms of ΔR.

The analytical development of ΔR presented in Chap. 1 (see Eq. 1.1) predicts a value of 11.22 Ω, which is close to the numerical results. In Tab. 2.2 assessments of ΔR obtained numerically are compared with the theory. An error of 2.6 % is made using the variable conductivity approach while a difference less than 1 % is done with a spherical hole. Whereas the case 'hole' is shown to provide more consistent results, the variable conductivity approach is preferred in the following. Indeed, errors are reasonable, and above all, a sole mesh may be used for different particle shapes and locations in the domain.

Chapter 3

Simulation of the impedance measurement of rigid and spherical particles

Chapter contents

Dealing with rigid and spherical particles, this chapter represents a preliminary numerical study of an Industrial Coulter counter. As a part of this chapter, the configuration originating from ABX Micros 60 (HORIBA Medical) is introduced. The ABX Micros 60 operating system is the starting point of all developments made in the context of this thesis. Furthermore, this work paves the way to the following chapter that will extend the procedure proposed for rigid spheres to the case of deforming RBCs.

The first part (Sec. 3.1) is dedicated to the introduction of the numerical configuration arising from the ABX Micros 60 and the pipeline proposed to simulate the pulse associated to the passage of a rigid sphere in an industrial Coulter counter. Then, in a second part (Sec. 3.2), several spheres trajectories in the device are simulated on the basis of the method of Sec. 3.1. Dealing with spheres, the electrical edge-effects are retrieved, and comparisons with experimental measurements validate the modeling procedure.

3.1 Numerical Configuration

The aim is to compute the electrical signal produced by a spherical isolating particle passing through the industrial analyser. Depicted in Fig. 3.1, the ABX Micros 60 is a simple, compact and fully automatic instrument providing basic haematological analyses. More precisely, RBCs, platelets and the three main types of white blood cells are counted and sized by impedance measurements (see Sec. 1.3). For this purpose, this automaton is composed of two chambers (viz. two Coulter counters). In the chamber pointed as 'RBC chamber' in Fig. 3.1, platelets and RBCs are analysed by diluting the whole blood in an electrolytic solution (ABX Minidil, commercialized by HORIBA Medical). This set-up returns size distributions similar to Fig. 1.5A, in which both platelets and RBCs populations are observable. WBC are also sized, but their negligible concentration is assumed to not perturb the statistics. In the 'WBC chamber' (see Fig. 3.1), the blood sample is diluted in a solution containing a lysing reagent that is in charge of destroying the RBCs. As discussed in Sec. 1.3, this allows the differenciation of the three main types of white blood cells in a volume histogram (see Fig. 1.5B). This work focuses on the RBC chamber only. In this chapter, the particular case where the RBC chamber is filled with a suspension of rigid spheres is considered. It corresponds to a case notably performed in the industry for calibrating the diagnostic instrument.

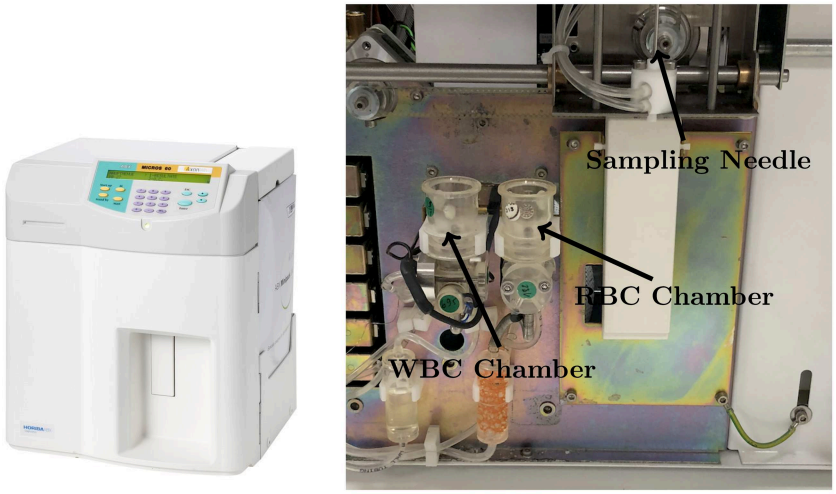

Figure 3.1 – Haematological automaton ABX Micros 60 developed by HORIBA Medical.

As discussed in Sec. 1.4.3, simulating the entire evolution of the particle in the device is not possible due to the separation of scales. However, the area of detection is restricted to the micro-orifice neighbourhood and dealing with rigid spheres allows starting the computations by depositing the rigid sphere just before the it enters the sensing region. Hence, the option adopted is to focus on a single particle evolving in the measurement region only. In that sense, the actual industrial geometry is reduced to the detection area. By applying suited boundary and initial conditions, it is shown that a reduced configuration reflects accurately what is happening in the orifice.

The modelling assumptions presented in Chap. 2 allow computing the particle dynamics in the orifice separately from the electrical perturbation. That is why two reduced configurations are introduced: the first one for computing the particle dynamics and a second one for solving the electrical field around the particle. Defining these reduced configurations implies preparatory computations without particles in the entire geometry. Indeed, the reliable boundary and initial conditions are deduced from the flow field and the electrostatic field stemming from simulations in the whole domain.

In the following section, simulations for assessing the flow field (NSS0) and the electrostatic field (ESS0) in the entire industrial geometry are presented. Then, based on computations NSS0 and ESS0, the two reduced configurations are introduced. Finally, the simulations of the particle dynamics (FSIS1) and the associated electrical pulses (ESS1) (in the reduced configurations) are detailed.

3.1.1 Preliminary simulations in the industrial geometry

Figures 3.2A and B show the entirety and a slice cut of the fluid domain that corresponds to the RBCs chamber of Fig. 3.1. The counting tank geometry presented in Fig. 3.2 includes the RBC chamber, where the RBC suspension is stored, the aperture where the detection of cells occurs, and an outlet duct. As already mentioned, the aperture is very small compared to the whole geometry: 50 μm in diameter and 75 μm long (see Fig. 3.2 C), while the height of the RBC chamber is of the order of 5 cm. The diluted blood sample enters by the boundary indicated as inlet and is vacuumed through the outlet surface (Fig. 3.2A), while the electrical field is imposed by the electrodes highlighted in Fig. 3.2B. The origin of the coordinates system ($\vec{e}_x$,$\vec{e}_y$,$\vec{e}_z$) is located at the center of the micro-orifice. The aperture is aligned with axis $\vec{e}_x$ while $\vec{e}_y$ is included in the middle slice plane shown in Fig. 3.2B, 3.2C ($\vec{e}_z$ is perpendicular to the ($\vec{e}_x$,$\vec{e}_y$) plane).

Carrying Flow (NSS0)

The electrolytes generally used in Coulter counters are mostly water and typical Reynolds numbers evaluated in industrial systems are higher than 100 (based on bulk velocity in the aperture and diameter). Hence, the flow can be predicted by the Navier Stokes equations for an incompressible fluid with constant kinematic viscosity $\nu = 10^{-6}$ m^2.s^{-1} and density $\rho = 1000$ kg.m^{-3}. The velocity ($\vec{u}$) and the pressure (P) in the domain (without particles) are then assessed by the use of solver NSS presented in Sec. 2.1.2. This simulation is referred to as NSS0 in the following. The flow is solved by imposing a 7.74×10^{-9} m^3.s^{-1} flow rate at the inlet (see Fig. 3.2A), which corresponds to a pressure drop of 200 mbar between the upstream and the downstream parts of the micro-orifice, in agreement with the operating regime of ABX Micros 60. This simulation is performed on the grid depicted in Fig. 3.3, for which a mesh refinement is performed around the aperture. Specifically, a characteristic mesh size of 1.6 μm is imposed inside of the micro-orifice, which allows a sufficient resolution of the flow field.

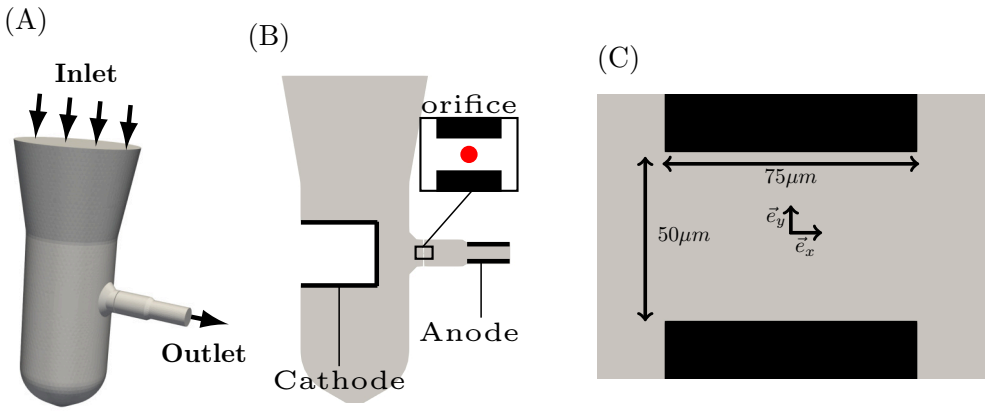

Figure 3.2 – (A) Fluid domain for red blood cells counting and sizing of ABX Micros 60 (HORIBA Medical). (B) Slice cut of the same geometry. The electrodes used for applying the electrical field in the micro-orifice are highlighted. (C) Zoom on the micro-orifice, where the cells are detected (indicative dimensions for length and diameter are given).

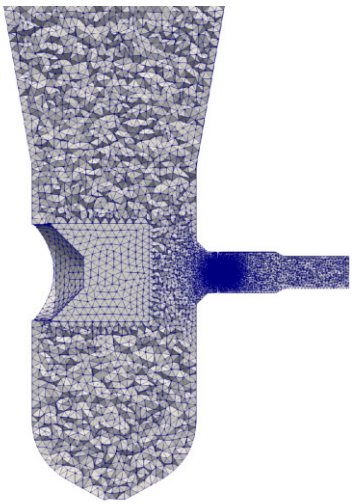

Figure 3.3 – Mesh of the entire industrial configuration. The meshes size inside the aperture is set to 1.6 μm and increases with a growth rate of 1.3 to 500 μm. The counting chamber is hence described by 5M nodes.

(A)

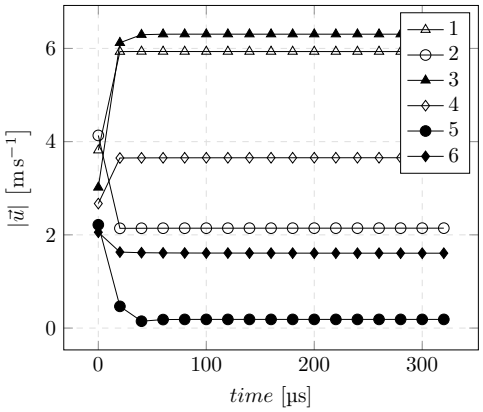

(B)

Probe number	x	y	z
1	0.0	0.0	0.0
2	0.0	22.0	0.0
3	-40.0	0.0	0.0
4	40.0	0.0	0.0
5	-40.0	30.0	0.0
6	40.0	30.0	0.0

Figure 3.4 – Time convergence of the velocity magnitude inside of the aperture in simulation NSS0 that computes the flow field without particles in the entire geometry. Picture (A) shows the evolution of the velocity magnitude $|\vec{u}|$ according to time, while (B) specifies the locations of the points at which the velocities are recorded.

Time evolutions of the velocity magnitude $|\vec{u}|$ at 6 probe points are recorded during the simulation and the flow appears to converge after a 50 μs, as shown in Fig. 3.4A. The different probes locations are given in the table of Fig. 3.4B. Figure .3.5A exhibits the velocity field once the simulation is converged. Close enough to the aperture, the flow is axisymmetric, of axis $\vec{e}_x$. In the following, the choice of restricting the study to the symmetrical plane ($\vec{e}_x$,$\vec{e}_y$) will be made.

Electrical Field without particles (ESS0)

The electrical field in the RBC chamber is obtained by solving the Laplace equation (see Eq. 2.103), as done in previous studies[46, 69]. Hence, solver ESS introduced in Sec. 2.3 is used to assess the electrostatic field in the industrial geometry of Fig. 3.2, in a simulation ESS0. Specified by HORIBA Medical, the conductivity of the electrolyte σ is set to 2.27 S.m^{-1}[46]. Note that the conductivity is imposed constant in the whole domain since no particles are considered in this computation. The electrical potential is imposed to 13.9 V on the cathode and 0.0 V on the anode (Fig. 3.2B), as in the industrial configuration. The remaining edges of the domain are modelled as non-conducting walls by applying a Neumann boundary condition according to Eq. 2.106. The potential ψ is solved on the mesh of Fig. 3.3 by solver ESS, and the electrical field $\vec{E}$ is computed from ψ as follows:

$$\vec{E} = \vec{\nabla}.\psi \tag{3.1}$$

Figure 3.5B shows the resulting electrical field magnitude ($|\vec{E}|$) around the aperture. In the corner of the orifice, regions of dense electrical field discussed in Sec. 1.3.2 are retrieved. In contrast, E is more homogeneous in the core region of the aperture. Besides, the obtained results are qualitatively in agreement with the electrical field shown in Fig. 1.7 that originates from Kachel works [74, 75]. Note also that according

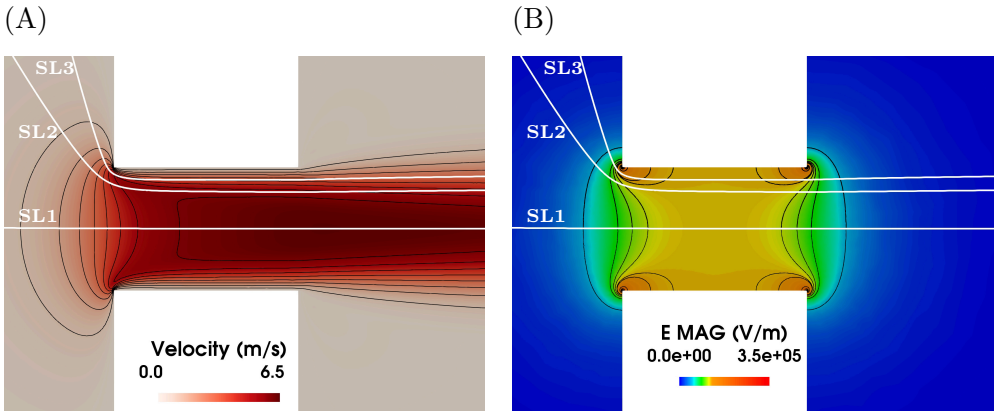

Figure 3.5 – Velocity field (A) and electrical field (B) obtained in simulations performed in the entire geometry (simulation NSS0 and ESS0). Isolines are depicted and show that most of the variations occur in a close zone around the micro-orifice. Three streamlines SL1, SL2, and SL3 illustrate different electrical field and velocity field that particles may undergo depending on their trajectory.

to the theory which predicts an electrical perturbation proportional to E^2, this perturbation is expected to be extremely small when the particle is a few tens of microns away from the aperture. This limits the interaction between the signals of the different particles of a sample.

3.1.2 Reduced configurations

As observed in Fig. 3.5B, the geometry of the industrial Coulter counter induces an electrical field that is concentrated in the micro-orifice. This property emphasizes the approach of reducing the computation to the sensing region since the particle is detected only in the micro-orifice. Limiting the computation domain to the orifice involves fewer discretization nodes and thus reduces computational costs. The shortened configurations for computing the particle dynamics and for assessing the electrical disruption are referred to as RC1 and RC2 in the following.

Reduced configuration for the fluid flow (RC1)

The reduced domain (RC1) for the fluid flow is shown in Fig. 3.6A. The initial velocity field and the boundary conditions on the 'inlet' surfaces (Fig. 3.6A) are interpolated from the time-converged velocity field obtained from the simulation in the entire industrial geometry (NSS0). On the wall faces, a zero velocity condition is imposed. On the outlet face, a convective outlet boundary condition is set to ensure mass conservation. In such a way, a stationary base flow inside the aperture equivalent to the flow simulated in the whole geometry (NSS0) is retrieved. Comparisons of velocity profiles arising from NSS0 and a simulation in RC1 are provided in Fig. 3.6B. Velocity profiles from the inlet, outlet and middle sections of the orifice are reported. The good agreement found between both approaches validates

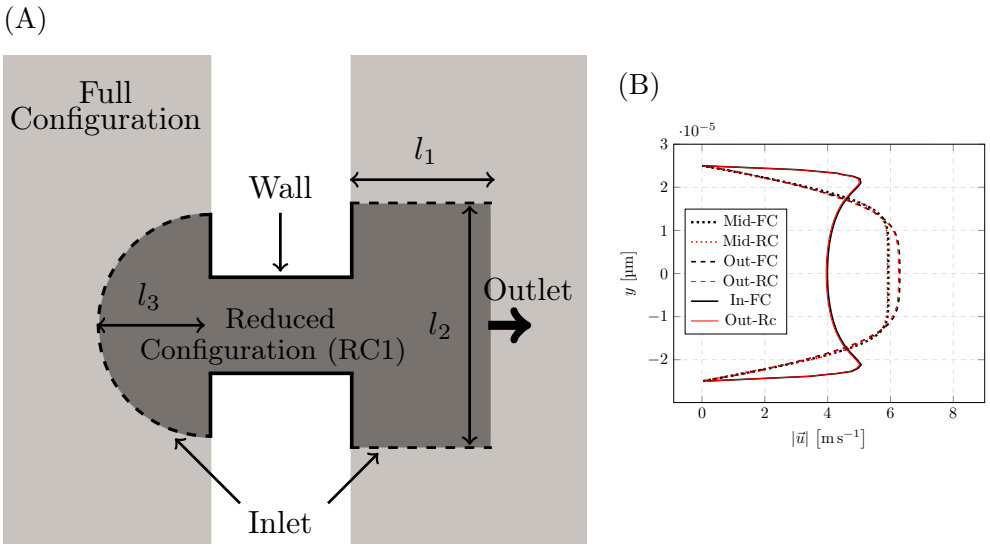

Figure 3.6 – (A) Schematic of the axisymmetric reduced configuration RC1 for computing the carrying flow. Slice cut of the reduced configuration shown over a small part of the full configuration. On boundaries indicated as Inlet, a velocity profile interpolated from computation NSS0 is imposed. The domain is characterized by l_1=75μm, l_2=130μm and l_3=60μm. (B) Comparison of the velocity profiles coming from computation NSS0 and a computation performed on the reduced configuration RC1 without particle. The velocity profiles are assessed at the inlet (x = -37.5 μm), middle (x = 0 μm) and outlet (x = 37.5 μm) sections of the aperture. 'Mid', 'In', and 'Out' refer to the inlet, middle and outlet sections, respectively. 'FC' and 'RC' stem from the full configuration and the reduced configuration, respectively.

the use of RC1 for computing the fluid flow inside the aperture instead of the full configuration.

Reduced configuration for electrostatic computations (RC2)

Figure. 3.7A shows the electrical potential ψ obtained from computation ESS0. From the potential field outcoming from ESS0, the reduced configuration RC2 is defined by relevant potential isolines. In Fig. 3.7A, isolines of ψ are shown and those which are highlighted by black arrows are retained for extracting RC2. They correspond to potentials of 13.05 V and 0.85 V. Figure. 3.7B depicts the reduced configuration corresponding to the selected isolines. Computing the electrical field in RC2 is done by imposing 13.05V and 0.85V on the cutting surfaces as depicted in Fig. 3.7B, and applying a Neumann boundary condition on boundaries indicated as 'Wall' (see Fig. 3.7B).

3.1.3 Simulation of the impedance measurements for rigid spheres

Dynamics of the particle inside of the aperture (FSIS1)

Because the flow is stationary, streamlines are considered as good approximations of achievable sphere trajectories. Given a streamline extracted from simulation NSS0,

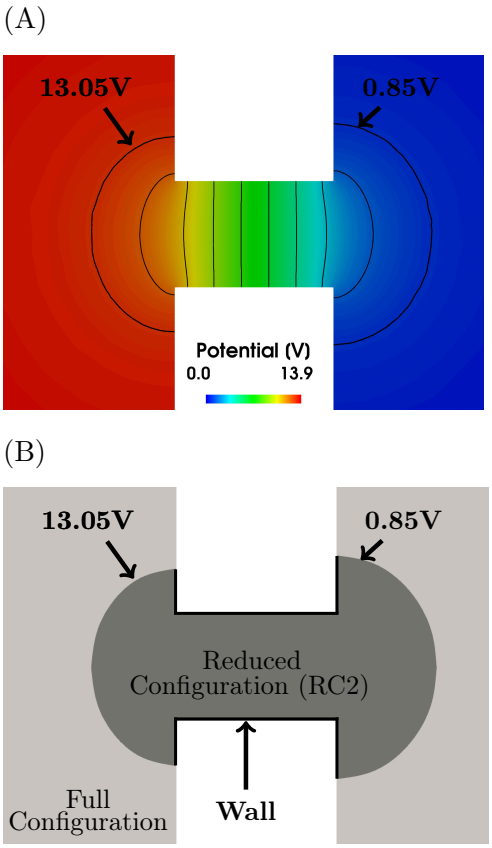

Figure 3.7 – (A) electrical potential obtained from the electrostatic simulation performed in the entire industrial geometry (ESS0). The potential isolines are shown in black continuous lines. The two isolines used for extracting the reduced domain RC2 are indicated by arrows. (B) Reduced configuration RC2, shown over the full configuration. The different boundary conditions are highlighted by arrows.

the lagrangian time (τ) of a fluid particle following this streamline is computed. Time $\tau = 0$ refers to the moment at which the streamline crosses the aperture inlet section (x = -37.5μm). This way, negative times refer to the upstream part of the aperture while positive times are related to the particle evolution inside of the orifice, and beyond. Then, computations of the particle dynamics start by placing the sphere in RC1, on the selected streamline at the location corresponding to τ = -5 μs (as illustrated in Fig. 3.8). It should be noted that the particles are not enforced to follow the streamlines (small deviations are observed in practice). Indeed, they are only needed to manage the particle path in the aperture. Rigid spheres are modelled with a spherical membrane of diameter 5 μm. The YALES2BIO solver is dedicated to deformable particle, so that rigid spheres are seen as viscous capsules with membranes having high elastic moduli: G_s, E_a, E_b, c_o and ν_{in} are set to 2.5×10^{-3} N.m^{-1}, 2.5×10^{-1} N.m^{-1}, 3.0×10^{-19} J, 0 and 50×10^{-6} m^2.s^{-1} respectively, which ensures that the particle remains spherical during the simulation (variations in diameter were less than 1 %). The particle dynamics is then solved using solver FSIS that is detailed in Sec. 2.2 in a simulation referred to as FSIS1. Note that the external viscosity ν_{ext} and the fluid density ρ are imposed as in

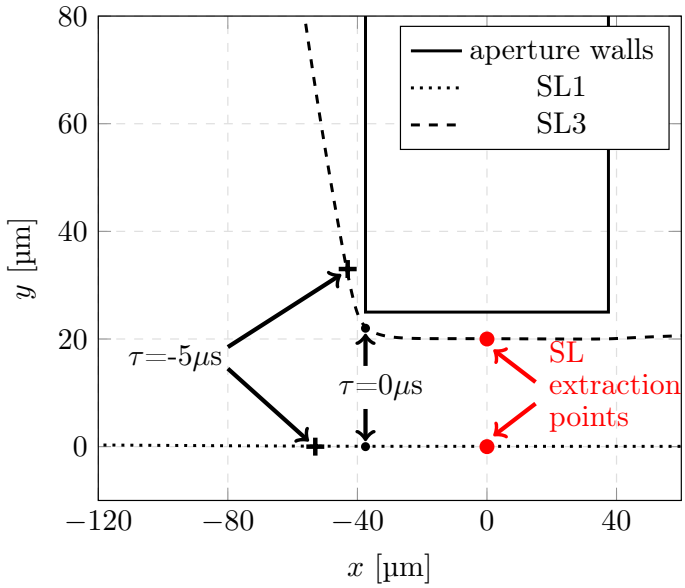

Figure 3.8 – Defining the particle initial position from a streamline. A streamline is extracted from NSS0 in such a way it passes through a chosen point (indicated as SL extraction point, in the graph). Then the particle initial location for computation FSIS1 is on the extracted streamline 5 μs before the orifice inlet section. This is illustrated for two streamlines SL1 and SL3 for which extraction points are taken as (0 , 0, 0) and (0, 20μm, 0), respectively.

computation NSS0.

Electrical Field around the particle (ESS1)

Computations of the electrical perturbations are performed once the simulation of particle dynamics inside the micro-orifice (FSIS1) is achieved. First, a series of membrane positions is stored (typically every microsecond) from simulation FSIS1. From the particle position predicted by the dynamics simulation FSIS1, a variable conductivity coefficient is imposed in the reduced domain RC2 by using of the method detailed in Sec. 2.3. The assumed isolating property of particles is accounted for by imposing a vanishing conductivity coefficient inside of the membrane. More precisely, an internal conductivity σ_{in} of 10^{-12} S.m^{-1} and an external conductivity σ_{ext} of 2.27 S.m^{-1} (value used in ESS0) are set. Finally, for each particle position of interest, the solver ESS is run on RC2 with boundary conditions indicated in Fig. 3.7 for assessing the electrical field disturbed by the particle. An example is shown in the **middle** illustration of Fig. 3.9 which shows a typical $|\vec{E}|$ around a spherical particle coming from the simulation of the dynamics (**left** illustration). This type of simulation is now referred to as ESS1.

Reconstruction of the electrical signal

From the electrical field $\vec{E}$ (see Fig. 3.9 **middle** picture), the resistance of the system is calculated, and compared with the resistance of the system without particle (computation ESS0). This yields ΔR, the resistance variation caused by the presence of

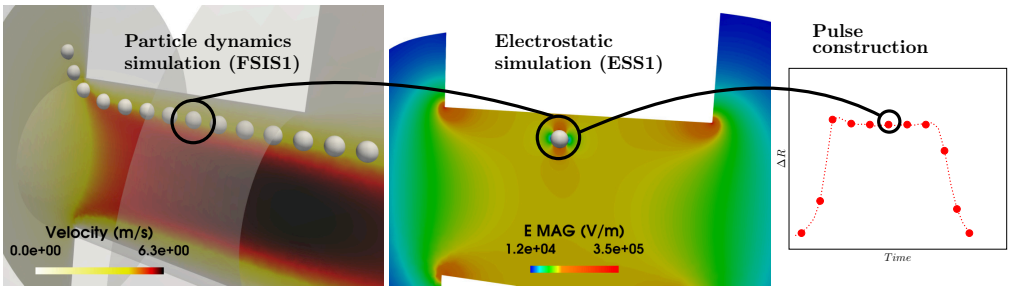

Figure 3.9 – Reconstruction of the electrical perturbation from the particle dynamics inside the aperture (FSIS1). The **left** figure shows typical sphere following positions in the micro-orifice over the velocity field. A membrane geometry coming from FSIS1 is used in an electrostatic simulation (ESS1) (see the **middle** figure). From the electrostatic simulation, the electrical perturbation ΔR is computed (**right** figure). Repeating this process for several consecutive membrane positions from FSIS1, the electrical pulse is built point by point.

the particle in the electrical field. An example of ΔR computation is provided in the test case of Sec. 2.3.3. Hence, repeating this process (ESS1 + ΔR calculation) for consecutive membrane positions inside the aperture allows the construction of the complete electrical perturbation over time, as shown in Fig. 3.9 (see **right** picture of Fig. 3.9).

3.1.4 Summary of the entire procedure

Tackling the simulation of the electrical print of a rigid sphere in an industrial Coulter counter is allowed by a shortening of the computation domain. This reduction implies a prior knowledge of electrical and flow fields in the entire geometry. Hence, the first steps of the proposed numerical pipeline (summarized in Fig. 3.10) are the computations NSS0 and ESS0, that are dedicated to simulations in the entire geometry of the flow field and the electrostatic field, respectively. Then, the simulation of the particle dynamics (FSIS1) is performed in a reduced configuration RC1 on which are applied boundary and initial conditions consistently with the flow field simulated in NSS0. The sphere is initially placed 5 μs away from the aperture entrance on a streamline extracted from NSS0. From FSIS1, N successive positions of the particle are used in N simulations ESS1. Computations are done in a reduced configuration RC2 that complies with potential isosurfaces of ESS0. Note that potential values related to the isosurfaces involved in the extraction are used as boundary conditions of RC2. In a simulation ESS1, a vanishing conductivity is set in the part of RC2 that is covered by the particle position arising from FSIS1, while the conductivity employed in ESS0 is used in the remainder of RC2. Finally, the resistive perturbation (ΔR) is obtained by comparing R_{WOP}, the resistance without particle stemming from ESS0, with R_{WP}, the resistance with particle obtained from each ESS1 calculation (see Fig. 3.10).

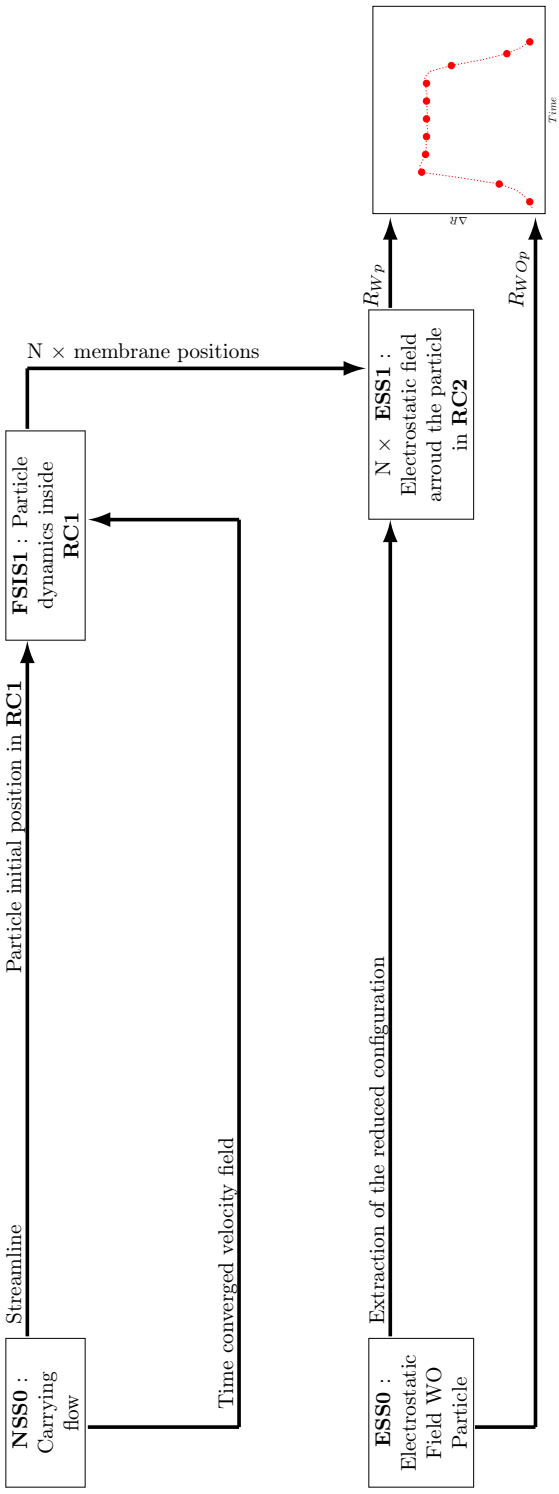

Figure 3.10 – Pipeline for computing the electrical pulse generated by rigid and spherical particles in an Industrial Coulter counter. The electrical pulse is discretized in time by N evenly spaced instants.

Case	x [μm]	y[μm]	z[μm]
1	0	0	0
2	0	5	0
3	0	10	0
4	0	12.5	0
5	0	15	0
6	0	16	0
7	0	17	0
8	0	18	0
9	0	19	0
10	0	20	0

Table 3.1 – Streamlines extraction points considered in the simulations.

3.2 Electrical pulses as a function of the spheres trajectory

Using the method detailed in Sec. 3.1 and summarized in Fig. 3.10, several spheres trajectories in the aperture were tested. In particular, 10 streamlines are extracted from the simulation NSS0, in such a way that they pass through points listed in Tab. 3.1. Examples of extracted streamlines are shown in Fig. 3.5, in which SL1, SL2, and SL3 refer to cases 1, 6, and 10 of Tab. 3.1, respectively. It should be noted that computations NSS0 and ESS0 (see Fig. 3.10) are preliminary simulations performed only once to characterize the flow and the electrical signal without particles. In other words, NSS0 and ESS0 are performed only once and remain valid for all cases of Tab. 3.1.

Using the IBM requires a fluid mesh size that equals the membrane mesh size [127]. In the simulations, the spherical membrane of 5 μm of diameter is meshed with triangles having a characteristic size of 0.3 μm. Considering computations FSIS1, the reduced configuration RC1 is meshed with a refinement of 0.3 μm around the expected trajectory (approximated by the streamline). That means ten different grids are needed for tackling the 10 different cases of Tab. 3.1. For instance, Fig 3.11A shows the grid used for case 1 in run FSIS1. Solver ESS is stationary and computations ESS1 represent only a small portion of the total computational cost. That is why the choice was made to perform all computations ESS1 on a unique well-refined grid adapted to all cases and shown in Fig. 3.11B. In this grid of RC2, the characteristic mesh dimension is downsized to 0.3 μm around all streamlines of Tab. 3.1.

Electrical pulses of Fig. 3.12A and the corresponding spheres trajectories of Fig. 3.12B arise from cases of Tab. 3.1. For a better visualisation, cases 2 and 3 are not represented in Fig. 3.12A, because variations in terms of electrical signatures are small between cases 1 and 4. The pulse duration is found to increase with the proximity to the aperture wall. As illustrated by SL1, SL2, and SL3 in Fig. 3.5A, a particle following a near-wall trajectory experiences lower velocities than on a central path. Hence, when evolving in the neighbourhood of the aperture

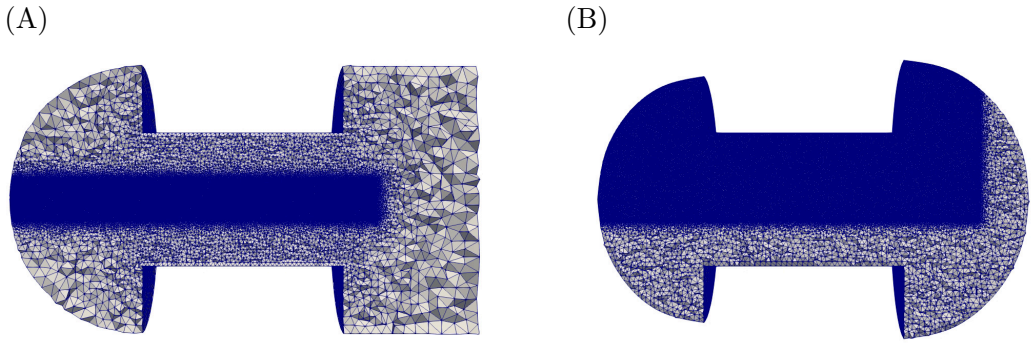

Figure 3.11 – Meshings of RC1 (A) and RC2 (B). The grid shown in (A) is devoted to the FSIS1 computation of a sphere following a central trajectory. The RC2 meshing of illustration (B) is used for all simulations ESS1 in this work.

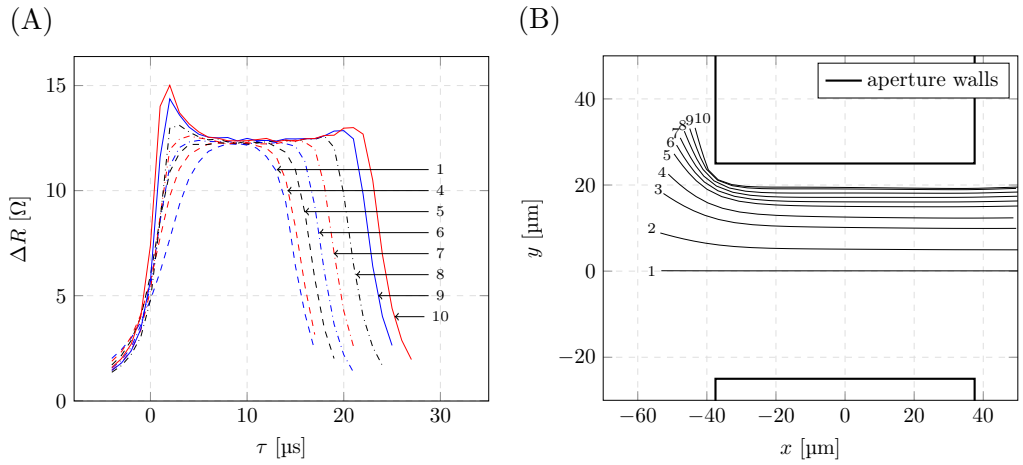

Figure 3.12 – Impedance pulses obtained numerically from spheres by considering the different streamlines of Tab. 3.1. Picture (A) shows the resistive perturbations obtained by the use of the proposed pipeline (see Fig. 3.10). Figure (B) depicts the sphere trajectories, outcomes of simulations FSIS1.

edges, the sphere spends more time in the sensing region, which induces a longer pulse. A flat velocity profile is present in the core region of the micro-orifice. This is illustrated by spaced velocity isolines in the central region of the aperture (see Fig. 3.5A), and by the velocity profiles in Fig. 3.6B. Such a flow explains the small variations in terms of pulse durations between cases 1 and 4. In the contrary, by the walls, the velocities decrease rapidely (see Fig. 3.5A and Fig. 3.6B), thus explaining the substancial differences of pulse lengths from case 5 to case 10.

3.2.1 When the electrical field shapes the pulse

In the case of rigid spheres, the shape factor f_s is constant so that a linear relation between the squared electrical field E^2 and the electrical perturbation ΔR is

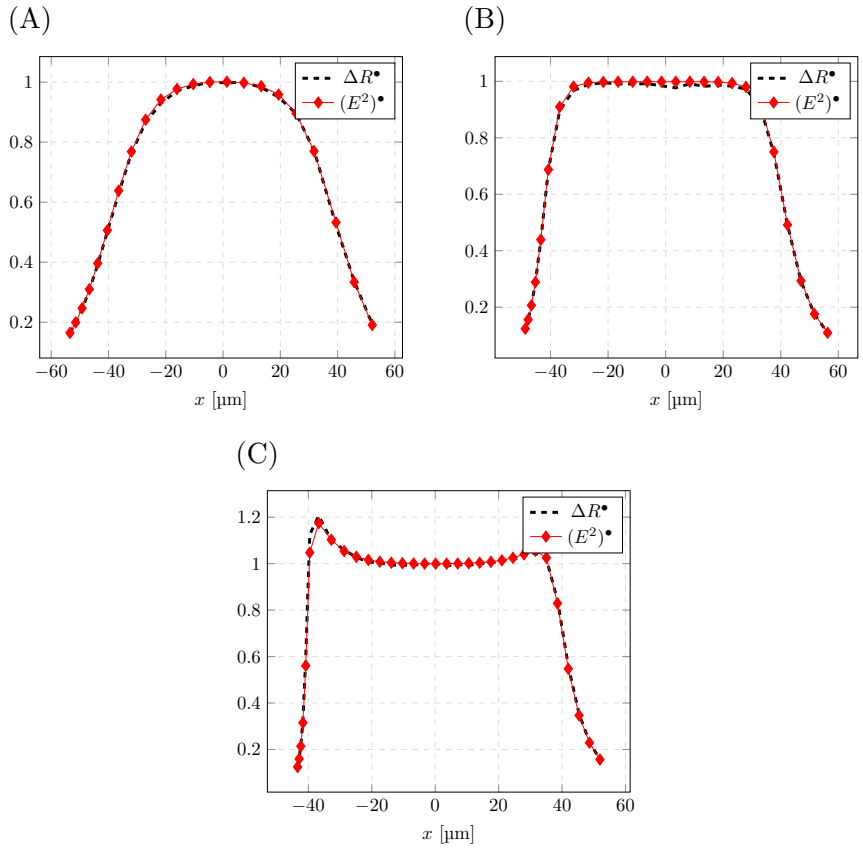

Figure 3.13 – Comparison between the squared electrical field magnitude E^2 along the particle trajectory with the resistive perturbation obtained from rigid spheres. Each quantity $\psi(x)$ is scaled as : $\phi^\bullet(x) = \phi(x)/\phi(x=0)$, with $\phi \in [\Delta R, E^2]$. $\Delta R^\bullet$ and $(E^2)^\bullet$ are graphed according to the particle axial position in the aperture (viz. x). (A), (B) and (C) stem from cases 1, 6 and 10 of Tab. 3.1, respectively.

expected:

$$\Delta R = \frac{E^2 f_s}{\rho_e i^2} V_p, \tag{3.2}$$

with V_p the particle volume, ρ_e the fluid resistivity and i the intensity. The aim is to validate the numerical simulations with the analytical trends. To do so, from simulation ESS0, the electrical field E is interpolated along the trajectories of Fig. 3.12B. In Fig. 3.13, the scaled squared electrical field, and the scaled resistance variation are shown for cases 1, 6 and 10. A good agreement between E^2 and ΔR is found, that confirms the linearity claimed by Eq. 3.2 [74]. Considering the other trajectories, the same agreement is observed (not shown). Note that this agreement is not obvious, as variations of E at the scale of the particle are not accounted for in the analytical formula.

3.2.2 Comparison with experimental data

Numerical results were shown to be consistent with the analytical statement of Kachel [74, 75]. In the following, the results obtained with the proposed pipeline are compared with experimental measurements obtained from the analysis of a polystyrene latex bead sample. Such spherical particles have the same size than in the simulations and are assumed undeformable and isolating.

Experimental acquisitions

With the aims of validating the numerical pulses of Fig. 3.12A, experimental signals were recorded during the analysis of a latex bead sample by an ABX Micros 60 (simulated devise, see Fig. 3.1). Latex beads have a well-controlled diameter of 5 μm, with a typical tolerance margin around 3 %. When the sample is presented to the ABX Micros 60, a needle withdraws a drop from the sample tube. Moved by an electrical motor, the needle distributes the collected volume in the two chambers (see Fig. 3.1) for analysis. In the 'RBC chamber', the sample is diluted by a factor 1/15000 in the ABX Minidil electrolytic reagent (HORIBA Medical). Finally, a vacuum pump aspirates the diluted suspension through the micro-orifices of both chambers while an electrostatic field is applied by electrodes. Remind that this study focuses on the RBC analysis, that is why the electrical signals are recorded for the 'RBC chamber' only. Note that in the 'RBC chamber', the pressure drop ensuring the flow and the electrical potential imposed on the electrodes agrees with the numerical set-up previously presented (see Sec. 3.1.1). This is a crucial point for a direct comparison of the signals over time. During the analysis, the terminal voltage is amplified by the ABX Micros 60 hardware system and given as an input of an in-house LabVIEW code. Increases of the electrical tension ΔU (ie. electrical pulses) are recorded with this set-up. Figure. 3.14 depicts the recorded signals according to time. In ABX Micros 60, the measurement sequence lasts about 16 s, which makes pulses of a few tens of μs undistinguishable in such representation. It is preferable to represent the acquisition by centring the pulses in time as done in Fig. 3.15. On this view of the experimental acquisition, 'M-shaped' and 'bell-shaped' pulses are recognisable. Incoherent signatures are observed among the recorded electrical prints. The latter can be explained by several particles crossing the sensing region at the same time (also called coincidences), but also by bubbles vacuumed through the aperture. For example, bubbles may arise from the electrodes and are generally much bigger than particles, thus generating pulses having an amplitude larger than the bounding box of the graph (see Fig. 3.14 and Fig. 3.15). However, the conception of industrial devices makes them infrequent.

Superimposing results from experiments with simulations

In this part, numerical pulses are compared with experimental data. Stating that the pulse duration contains an information on the particle trajectory, the choice was made to compare the predicted pulses of Fig. 3.12 with experimental pulses of Fig. 3.15 having almost the same duration. The pulse duration is measured by the

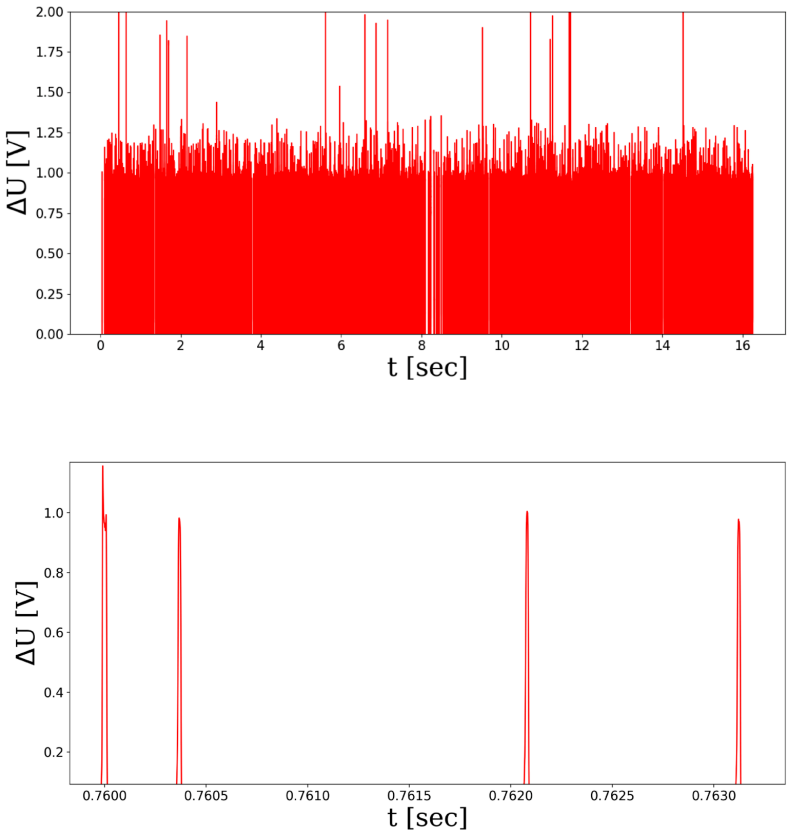

Figure 3.14 – Impedance pulses recorded during the analysis of a latex beads sample by an ABX Micros 60 (HORIBA Medical). The **top** illustration depicts the entire acquisition over 16 s, while the **bottom** picture shows a 3.5 ms sequence of the full acquisition and 4 pulses appear more clearly.

metric $\mathcal{W}$ (for width) that is defined as follow:

$$\mathcal{W}(thresh) = T_1 - T_0 \tag{3.3}$$

Regarding the definition of instants T_0 and T_1 provided by Fig. 3.16, $\mathcal{W}$ quatifies the time spent by the electrical perturbation above a given threshold [183] (see *thresh* in Fig. 3.16). The choice of a threshold intersecting the ascending and descending slopes of the pulse is crucial for $\mathcal{W}$ to measure relevantly the cell occupation time in the sensor.

Converting the experimental tension pulses to resistive pulses is not straightforward because of signal treatments performed by the ABX Micros 60 hardware system. Therefore, experimental and numerical data are scaled in amplitude before comparisons. Considering the experimental acquisition, the tension pulses are scaled with the mean of the 'bell-shaped' pulses maximum $\overline{\Delta U}_m|_{bs}$. 'Bell-shaped' signatures are generated by centred trajectories and were illustrated in Fig. 1.13A. They can be extracted from the entire acquisition by the use of a convenient pulse duration threshold. For instance, computing $\mathcal{W}(0.5V)$ for all pulses of Fig. 3.15, and keeping only those that have a duration (viz. $\mathcal{W}(0.5V)$) below 17.0 μs renders

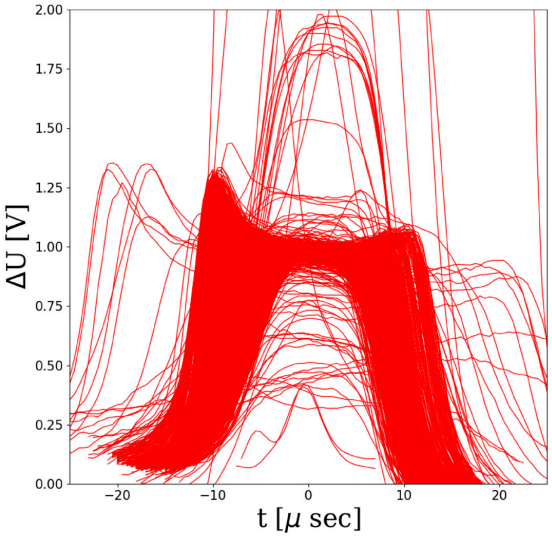

Figure 3.15 – Impedance pulses recorded during the analysis of a latex beads sample by a ABX Micros 60 (HORIBA Medical). For a better overview on the recorded electrical signatures, the pulses are centred in time in this representation.

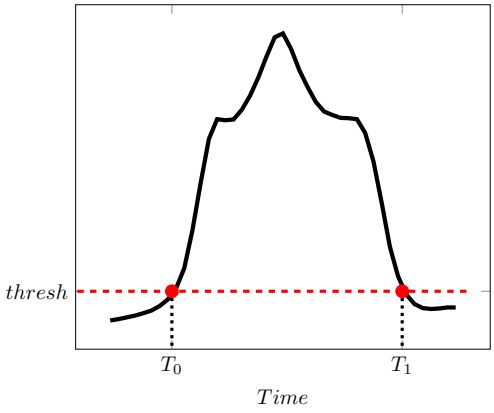

Figure 3.16 – Sketch of T_0, T_1 required for computing the $\mathcal{W}$ metric.

'bell-shaped' pulses (in this case). A simpler and more general method providing the extraction of 'bell-shaped' pulses is presented in Chap. 5. Regarding numerical resistive pulses of Fig. 3.12A, they are scaled with the maximum of case 1 (denoted by $\Delta R_m|_{bs}$), which depicts a 'bell-shape'. In summary, achieving the scaling procedure converts each experimental tension pulse $\Delta U(t)$ and each numerical resistive pulse $\Delta R(t)$ (functions of time) to dimensionless electrical disruptions $\Delta U^*(t)$ and $\Delta R^*(t)$, respectively. More precisely, $\Delta U^*(t)$ and $\Delta R^*(t)$ writes:

$$\Delta U^*(t) = \frac{\Delta U(t)}{\overline{\Delta U}_m|_{bs}}, \quad \Delta R^*(t) = \frac{\Delta R(t)}{\Delta R_m|_{bs}} \tag{3.4}$$

A width computed from a pulse scaled as stipulated by Eq. 3.4 (ΔU^* or ΔR^*) is relative to the 'bell-shaped' maximum, viz. $\overline{\Delta U}_m|_{bs}$ or $\Delta R_m|_{bs}$, depending on the source (experiment or simulation, respectively). For the sake of clarity, pulses durations computed from ΔU^* or ΔR^* are denoted by $\mathcal{W}^r$ in the following. Notice

that $\mathcal{W}^r$ may be computed directly from original pulses ΔU and ΔR with:

$$\mathcal{W}^r(thresh') = \mathcal{W}(thresh' \times \overline{\Delta U}_m|_{bs}), \tag{3.5}$$

or

$$\mathcal{W}^r(thresh') = \mathcal{W}(thresh' \times \Delta R_m|_{bs}), \tag{3.6}$$

respectively. The duration $\mathcal{W}^r$ is computed for each experimental and simulation pulses, with $thresh'$ equal to 0.5. Given a pulse duration ($\mathcal{W}^r$) derived from a numerical data, experimental signatures having the same length, with a tolerance margin of 1 μs are extracted for comparison. Figure 3.17 displays the numerical results superimposed with experimental pulses of corresponding $\mathcal{W}^r$, for the eight cases shown in Fig. 3.12. A good agreement is found between the numerical results and the experimental observations. Pulses that display a 'bell-shape' are the shortest (see Fig. 3.17A and B), while those having a 'M-shape' are the longest (see Fig. 3.17F, G and H). In between (see Fig. 3.17C, D and E), the electrical signatures depict a plateau.

3.3 Conclusion

This chapter was devoted to the simulations of rigid beads in Coulter counters. Dealing with undeformable spheres is a simple case since their initial state in the computations are known, thus allowing to focus the simulations on a restricted zone around the orifice. In particular, the electrical field is concentrated around the aperture so that it is sufficient to start the computation 5 μs before the orifice entrance in order to properly describe the electrical pulse.

The proposed method is a sequence of computations in which the sphere dynamics is solved in a Fluid-Structure Interaction (FSI) simulation and the electrical perturbation in several electrostatic calculi. Remind that the FSI solver (FSIS) implemented in YALES2BIO is devoted to highly deformable cells. Hence the sphere rigidity in the FSI computation is ensured by significant elastic modulus for the membrane and a substantial internal viscosity.

Several spheres trajectories are simulated and results are shown to retrieve the linearity between the pulse and the squared electrical field, as in the theory. Besides, the simulations are in good agreement with experiments made with rigid latex beads.

However, the presented pipeline is not suited to deformable particles. Indeed, in such cases, there is a need for computing the deformations occurring in the upstream part of the aperture so that depositing the particle 5 μs before the orifice inlet section is not relevant. Tackling the simulation of the deformable particle is the purpose of the following chapter.

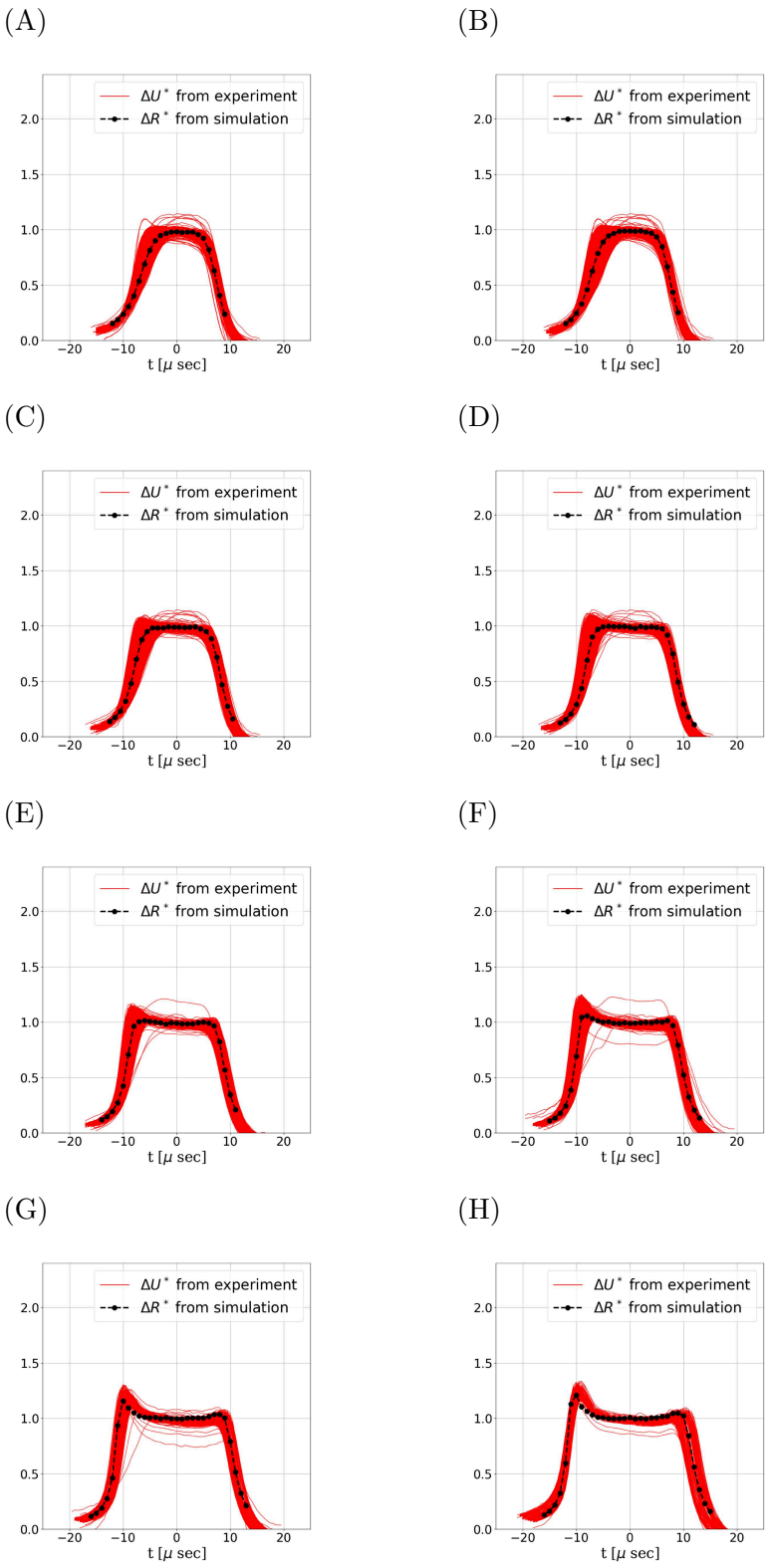

Figure 3.17 – Comparisons of simulated pulses for the case of spheres with experimental pulses coming from the analysis of a latex bead sample. Graphs A, B, C, D, E, F, G and H refers to cases 1, 4, 5, 6, 7, 8, 9 and 10, respectively (see Fig. 3.12).

Chapter 4

Numerical simulation of red blood cells in an industrial Coulter Counter

Chapter contents

The proposed method for handling the numerical simulation of deformable particles in an industrial Coulter counter gave rise to a research article[1].

Chap. 3 focuses on the introduction and the validation of a method enabling the simulation of rigid and spherical particles in Coulter counters. When considering rigid spheres, the hydrodynamic loads seen by the particle before it enters in the detection area does not impact its shape and the orientation of the sphere does not matter. Thus, what happens before the orifice is neglected, which allows to start the computations by placing the sphere near the aperture entrance. This is only valid when dealing with spherical and rigid particles. In contrast, RBCs (that are aspherical and deformable) can not be treated with this approach. As a matter of fact, deformed RBCs were observed before they enter in a constricted channel [75] (see Fig. 1.10). Hence, starting the simulations by placing a RBC at rest just before the orifice is irrelevant.

[1]Numerical simulation of deformable particles in a Coulter counter. International Journal for Numerical Methods in Biomedical Engineering, aug 2019

On the one hand, simulating the RBC evolution in the upstream part of the aperture is required to accurately reproduce the cell dynamics in Coulter counters. On the other hand, taking into account that part of the geometry induces far too long computations (see Sec. 1.4.3). In this context, the first section of the present chapter (Sec. 4.1) introduces a method to tackle such simulations with reasonable computational costs. This original strategy is based on the pipeline of Fig. 3.10 but adds a specific computation that accounts for the upstream dynamics of the cell. Section. 4.2 shows how this improved pipeline can be used to decrease the overall computational time (compared to a brute force strategy where the whole Coulter counter is computed) and specifies the conditions under which a relevant simulation can be performed. Finally, Sec. 4.3 presents numerical results for deformable RBCs in a ABX Micros 60 (see Fig. 3.1) and compares the results with both theoretical predictions and experimental data. The accuracy of the method is then illustrated, and the variety of pulses discussed in Chap. 1 is associated with various RBC dynamics in the aperture. Furthermore, this numerical method is shown to provide useful information about the shape factor in the presence of deformation and rotation of cells.

4.1 Numerical Pipeline

4.1.1 Overview of the numerical challenge

This section focuses on the principal issues associated with the simulation of an impedance pulse generated by a deformable particle in a Coulter counter and provides an overview of the method proposed to achieve this task.

As for the study dealing with the rigid sphere case (Chap. 3), the operating regime of ABX Micros 60 (HORIBA Medical) is used in the present chapter. Examples of electrical and velocity fields obtained by numerical simulations in this industrial configuration were shown in Chap. 3 (see Fig. 3.5A and 3.5B). Inside the micro-orifice, the electrical field is very large due to the flux conservation law; this is where particles are detected. The aperture allows concentrating the electrical field so that the resistance perturbation associated with the passage of a particle is large. Besides, the field decreases rapidly when getting out of the aperture, so that a microscopic particle is not detected outside of the orifice, which allows the sizing of cells one by one if the sample is sufficiently diluted. Due to the contraction of the geometry, the velocity inside the aperture is large, which yields high-throughput measurements but also generates high-velocity gradients and viscous stresses. In particular, high shear stresses are retrieved near the aperture walls. Due to these shear stresses, deformable particles such as RBCs may undergo rotational motions and complex deformations [91]. Before entering in the orifice, the velocity magnitude raises over a short distance, causing large longitudinal strain, so that RBCs align in the direction of the strain and elongate to a prolate ellipsoid shape, as reported by Kachel [74] and Gibaud [46]. Far from the aperture, velocity gradients are negligible, and no deformation is expected.

The industrial geometry may be conceptually divided into three parts, as de-

picted in Fig. 4.1. Indeed, the RBCs are first transported without deformation in the biggest part of the geometry (Part A). Then, they are stretched just before the aperture entrance by an extensional flow field (Part B). Finally, RBCs are deformed in the micro-orifice while disturbing the electrical field (Part C). Figure 4.1B reports the characteristic RBCs transit time in those three parts in the ABX Micros 60. In the method presented in the following, the choice was made to neglect Part A because no deformation nor electrical perturbation is expected. Thus, only Parts B and C are considered for the modelling. However, as shown in Fig. 4.1 B, the second part involves a time scale that is larger than the third one by several orders of magnitude. Therefore, instead of simulating the particle evolution in the whole domain where deformations occur (Parts B and C), we propose to split the calculation into two simulations. First, a simulation of the stretching of the cell by a relevant extensional flow is considered. This simulation is referred to as FSIS0. It predicts the elongation happening in Part B of the geometry. A variable strain rate that mimics that seen by the cell is imposed. It is extracted from the first simulation NSS0 (see Chap. 3), performed on the entire geometry without particles. The calculation in the extensional flow configuration FSIS0 yields a deformed particle, that is used in the computation of the particle dynamics inside the measurement region (FSIS1 introduced in Sec. 3.1.3) corresponding to Part C. The particle stretched after FSIS0 is placed near the orifice entrance in the reduced configuration of the whole geometry (RC1) that is a restricted region around the aperture, in order to reduce the computational cost of FSIS1. Finally, the electrical perturbation is computed by performing a series of electrostatic simulations (ESS1) using several particle positions extracted from FSIS1. The whole procedure is sketched in Fig. 4.2. It represents an improvement of the pipeline of Fig. 3.10 with an additional simulation (FSIS0) that computes the upstream dynamics. In the following, solely the case of RBCs is handled. However, the pipeline displayed in Fig. 4.2 may be applied to any deformable particle.

Simulation NSS0, ESS0, FSIS1, and ESS1 having already been presented (see Chap. 3), only FSIS0 is described in the following. When considering an aspherical and deforming particle, the initial orientation of the particle in FSIS1 must be specified. This point is also detailed in the following.

4.1.2 Extensional configuration setup

Assumption of an axisymmetric extensional flow in the upstream part

It is first shown that particles flowing in a Coulter counter are first subjected to a purely extensional flow before entering in the aperture. From the simulation performed in the whole domain (NSS0), three streamlines passing at different distances from the aperture edges are extracted. More precisely, the selected streamlines are chosen such as they pass through points located in the aperture at different distances from the wall: (0,0,0), (0,15,0) and (0,20,0), coordinates given in μm. Respectively denoted by SL1, SL2 and SL3, the streamlines were depicted in Fig. 3.5 in Chap. 3. The streamlines curvilinear coordinate system $(\vec{e}_s, \vec{e}_r, \vec{e}_z)$ is defined in the following way: $\vec{e}_s$ is aligned with the streamline; $\vec{e}_r$ is perpendicular to the streamline and belongs to the plane $(\vec{e}_x, \vec{e}_y)$ and $\vec{e}_z = \vec{e}_s \wedge \vec{e}_r$. Time τ is established from the La-

(A)

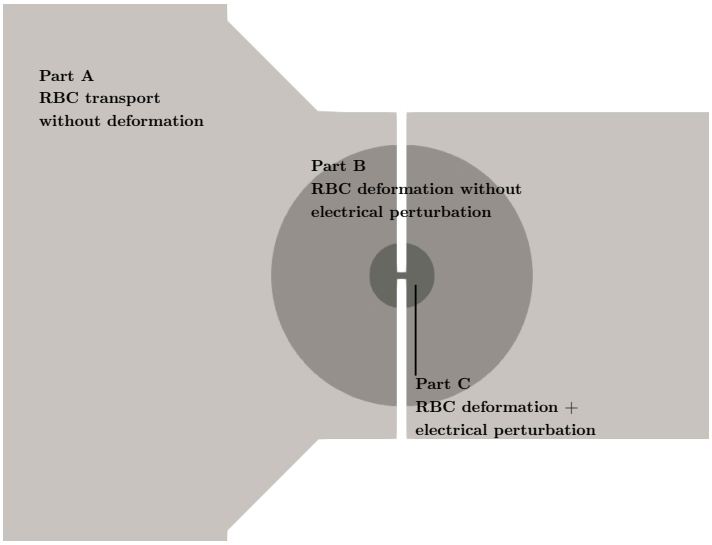

(B)

Part	Time Scale
A	$50s$
B	$12ms$
C	$20\mu s$

Figure 4.1 – (A) Schematic of the industrial geometry, divided in three parts depending on the existence of particles deformation and the impact on the electrical field. In Part A, the RBC is simply transported without deformations. In Part B, the particle may undergo deformations but is far from the detection area. In Part C, the RBC is deformed and disturbs the electrical field. (B) Table presenting characteristic time scales for these three parts, for the case of an ABX Micros 60 (HORIBA Medical).

grangian coordinates system of a fluid particle moving along the selected streamline, as done in Sec. 3.1.3. Remind that time τ is negative before the aperture entrance ($x < 37.5$ μm), and positive after the orifice inlet section. If the flow is an axisymmetric strain flow in the s direction, we should have $\frac{\partial U_s}{\partial z}$ = -2 $\frac{\partial U_z}{\partial z}$ = -2 $\frac{\partial U_r}{\partial r}$.

The velocity gradients in the curvilinear coordinates system are computed and are shown against τ in Fig. 4.3. Regarding the streamline SL1 which crosses the aperture center, Fig. 4.3A shows that $\frac{\partial U_z}{\partial z}$ perfectly equals $\frac{\partial U_r}{\partial r}$ for all the upstream part of the aperture. This equality remains valid for the other streamlines SL2 and SL3 except for very small negative values of τ (viz. except very close to the aperture inlet). From these observations, the assumption that a particle moving along a streamline behaves as in an axisymmetric and purely extensional flow up to -12 μs is made. This assumption is the basis of the FSIS0 simulation type described in the next section.

Extensional configuration setup (FSIS0)

For part B, where the RBC is deformed without impacting the electrical field, a fluid-structure interaction simulation is performed in a simplified domain used to impose an axisymmetric strain flow. The RBC is supposed to travel in part B along the streamline at the surrounding fluid velocity. The particle is initially placed at the center of a cylindrical fluid domain with possibly a non-zero initial orientation with

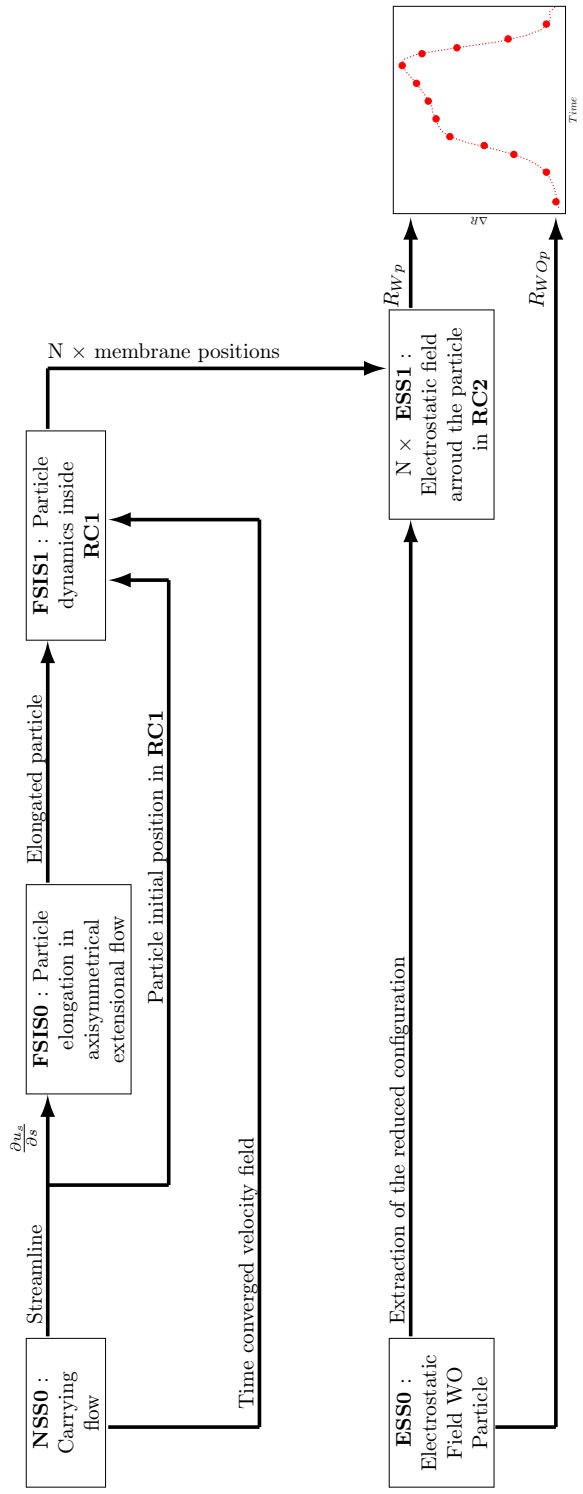

Figure 4.2 – Pipeline for the simulation of the electrical perturbation generated by a deformable particle in a Coulter counter. The electrical pulse is discretized in time by N evenly spaced instants.

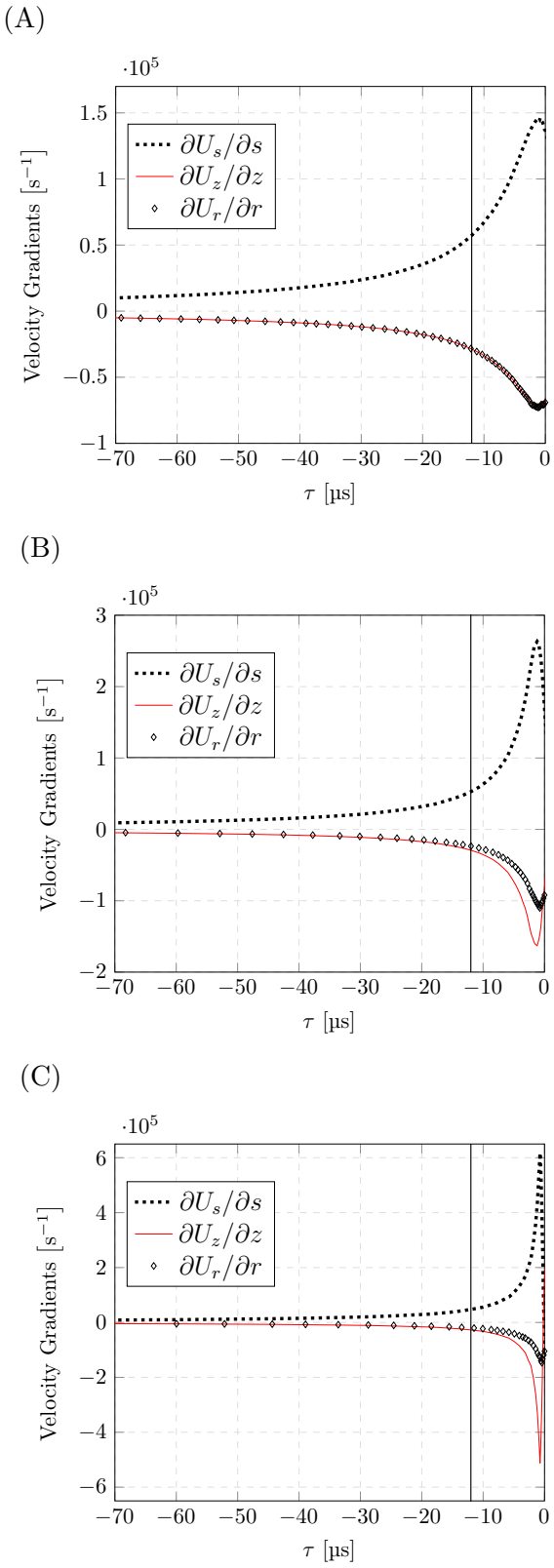

Figure 4.3 – Time evolution of the velocity gradients observed by a particle moving along the three different streamlines depicted in Fig. 3.5, as predicted from the simulation performed on the entire industrial configuration. The graphs A, B and C correspond to the streamlines passing by points (0, 0, 0), (0,1 5 μm, 0) and (0, 20 μm, 0), and are denoted by SL1, SL2 and SL3 in Fig. 3.5, respectively.

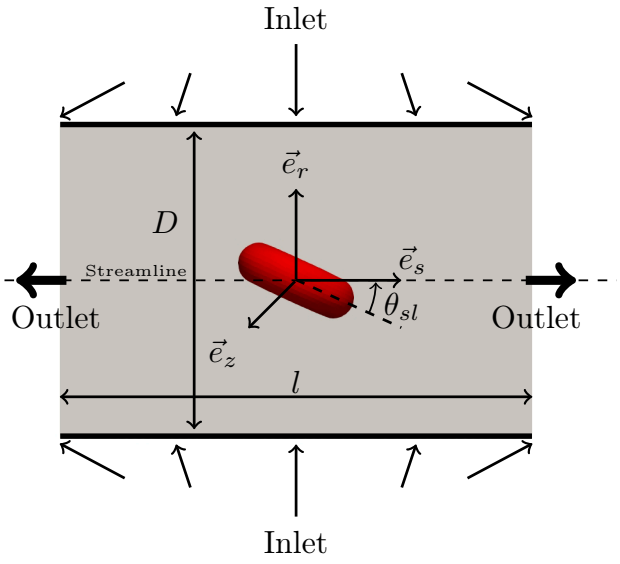

Figure 4.4 – Extensional configuration scheme (simulation FSIS0). The particle is initially placed at rest in the center of a cylindrical fluid domain. The cylinder diameter D and length l are respectively equal to 30μm and 50μm. Boundary conditions that insure an extensional velocity field are set according to Eq. 4.1.

respect to axis $\vec{e}_s$, as sketched in Fig. 4.4. From the time evolution of the stretch rate obtained for a particular streamline (Fig. 4.3), the following time varying boundary condition is imposed on the lateral boundary ($r^2 + z^2 = \frac{D^2}{4}$, s in $[-\frac{l}{2}, \frac{l}{2}]$) of the cylinder:

$$\vec{u} = \frac{\partial U_s(t)}{\partial s} \begin{pmatrix} s \\ -\frac{r}{2} \\ -\frac{z}{2} \end{pmatrix} \tag{4.1}$$

Convective outlet boundary conditions are imposed on the two circular faces s = $-l/2$ and s = $l/2$. According to the axisymmetric extensional assumption discussed previously, the particle stretching is performed until 12 μs before the aperture entrance. A discussion on the elongation starting point is provided in a following section. Note that the external viscosity ν_{ext} and the fluid density ρ are imposed as in computation NSS0 and FSIS. Of course, the RBC parameters (ν_{in}, G_s, E_a, E_b, c_o) employed in FSIS0 and FSIS1 must be consistent.

4.1.3 Initial state of a deformable particle in FSIS1

Once stretched during simulation FSIS0, the particle dynamics inside the micro-orifice is solved in simulation FSIS1. Contrary to the case of rigid spheres (see Chap. 3), the RBC orientation at the beginning of FSIS1 must be specified. The elongated cell is initially placed on the selected streamline at the point corresponding to time -12μs in a reduced configuration of the industrial geometry (RC1). The particle orientation θ_{sl} (see Fig. 4.4) at the end of the stretching step is recorded and applied as the initial angle of the particle with respect to the streamline for the dynamics simulation.

4.2 Validation

The pipeline detailed in the last section was first tested as explained in this section. From the computation NSS0, the streamline shown in Fig. 4.5A (SL2 in Fig. 3.5) is extracted and different simulations varying the initial conditions are performed. The computed cases are summarized in Fig. 4.5B. In a first study, which corresponds to cases 1 to 4, the impact of the RBC starting time (or the distance from the aperture at which the cell is deposited, see Fig. 4.5A) on its dynamics and the resulting impedance pulse is dealt with. For this study, the particle stretching in the extensional configuration (Simulation FSIS0) is bypassed and the RBC is dropped directly on the streamline at different positions, in a full simulation FSIS1. The initial positions are related to times corresponding to the lower bounds reported in the 'FSIS1' column of Fig. 4.5B. Then, the capability of the extensional simulation FSIS0 to reproduce the dynamics before the aperture is assessed. More precisely, as introduced in Sec. 4.1, the RBC is first stretched in an extensional flow simulation FSIS0, then its dynamics inside the orifice is solved in a simulation FSIS1, the final RBC state from FSIS0 being used as an initial condition for FSIS1. This runs sequence corresponds to case 5 in Fig. 4.5B and represents the same physical configuration as case 1. On the contrary, cases 2-4 denote different initial locations of the RBC. Note however that the final time (τ=18 μs) is the same for all cases.

All cases of Fig 4.5 B were computed using the same RBC. The membrane parameters (required in Eq. 2.52 and Eq. 2.69) are imposed as: G_s=2.5$\times$ 10^{-6} N.m^{-1}, E_a=2.5$\times$ 10^{-1} N.m^{-1}, E_b=6.0 $\times$ 10^{-19} J, c_0=0. All parameters are in agreement with the range of measurements provided in the literature [4, 20, 107]. Density variations between the internal fluid and the suspending medium are neglected since some test cases designed to assess the impact of higher density inside the RBCs have shown negligible effect (see App. A). In the studied configuration (ABX Micros 60, HORIBA Medical) the sample analysis is performed at ambient temperature (21°C). Hence, as measured in [79], higher values of internal kinematic viscosity are encountered instead of the physiological value of 6.0 $\times$ 10^{-6} m^2 s^{-1} at 37 °C. Deduced from Kelemen *et al.*'s measurements [79], an internal viscosity of 18.0 $\times$ 10^{-6} m^2 s^{-1} would be imposed. However, with the aim of challenging the pipeline in a configuration where the RBC is more deformable, the internal viscosity was set to 10.0 $\times$ 10^{-6} m^2 s^{-1} (for this validation part). The membrane was discretized with triangular elements with a characteristic size of 0.3 μm. The initial RBC orientation θ_{sl} with respect to the streamline (Fig. 4.7) is chosen as 0.43 rad for all cases excepted for run 5-FSIS1, where the outcome from run 5-FSIS0 was used. This problem is symmetric with respect to the $(\vec{e}_x, \vec{e}_y)$ plane, so that the orientation is only defined by an angle in this plane.

Using the IBM requires a fluid mesh size equal to the membrane mesh size [125, 127]. Hence, for computation FSIS0, the mesh size is simply imposed to 0.3μm in the whole cylinder (Fig. 4.6) while for FSIS1, a refinement of 0.3μm is achieved around the streamline as previously stated (Sec. 3.2).

For cases 1 to 4, the RBC starting position was willingly placed relatively far from the aperture entrance. A wider reduced configuration is used for these specific

(A)

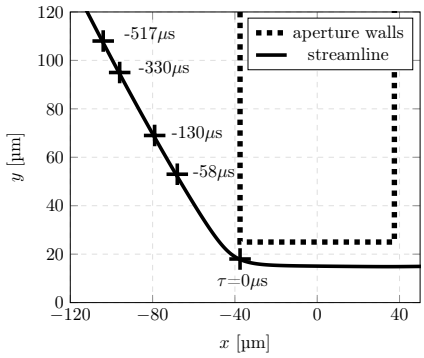

(B)

Case	FSIS0 (μs)	FSIS1 (μs)	Cost (CPU-hour)	$\dot{\epsilon}_0$ (s^{-1})
1	ø	[-517 , 18]	16400	1000
2	ø	[-330 , 18]	12000	2000
3	ø	[-130 , 18]	6500	5000
4	ø	[-58 , 18]	4600	12000
5	[-517 , -12]	[-12 , 18]	2000	1000

Figure 4.5 – Summary of the cases performed to assess the effect of the RBC initial position. (A) Initial RBC starting positions along the selected streamline.The streamline corresponds to SL2 (Fig. 3.5) and is extracted from the time converged velocity field of simulation NSS0. It is selected such as it passes by the point (0, 15, 0). (B) Characteristics of the simulations performed in terms of the physical time range in the extensional configuration (FSIS0) and in the reduced configuration (FSIS1). The overall computation cost and the typical strain rate ($\dot{\epsilon}_0$) experienced by the RBC at the beginning of the simulation are also reported.

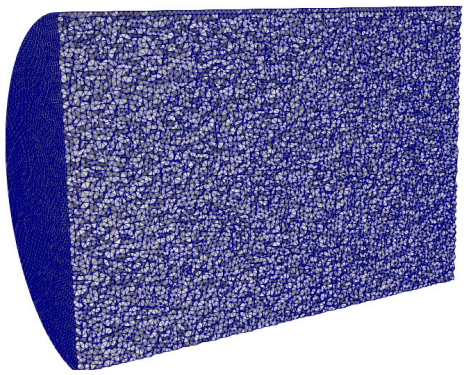

Figure 4.6 – Meshes used for the computation of the extensional configuration FSIS0. The mesh contains approximately 0.4M nodes.

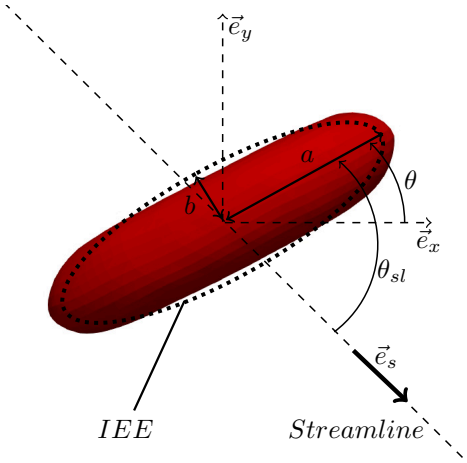

Figure 4.7 – Inertia Equivalent Ellipsoid (IEE) parameters and orientation. IEE parameters are shown over a RBC elongated shape. The sketch is represented in the symmetrical plane $(\vec{e}_x, \vec{e}_y)$ such as $\vec{e}_z$ is out of plane, as the IEE parameter c.

cases with l_3=150 μm (Fig. 3.6). In these cases (1 to 4), RBCs follow the streamline within a tolerance margin of 0.3 μm (one mesh size) when travelling in the part upstream of the aperture.

In the following, the Inertia Equivalent Ellipsoid (IEE) of the deforming RBC [135] is used to compare the different cases considered. From the membrane nodes position, the inertia matrix of the RBC at the center of mass is computed and diagonalized to obtain the eigenvalues and eigenvectors. The IEE parameters, a, b and c are then obtained by solving the following equation:

$$\begin{pmatrix} \lambda_1 & 0 & 0 \\ 0 & \lambda_2 & 0 \\ 0 & 0 & \lambda_3 \end{pmatrix} = \frac{V}{5} \begin{pmatrix} (b^2+c^2) & 0 & 0 \\ 0 & (a^2+c^2) & 0 \\ 0 & 0 & (a^2+b^2) \end{pmatrix} \tag{4.2}$$

The left and right terms of Eq 4.2 are respectively the diagonalized RBC inertia matrix and the empirical inertia matrix of an ellipsoid of axes a, b and c, with V denoting the IEE volume. Both are expressed in the eigenvectors basis. The RBC orientation is defined according to the angle between the IEE axis corresponding to the parameter a and the streamline (θ_{sl}) on the one hand and the $\vec{e}_x$ axis (θ) on the other hand (Fig. 4.7).

4.2.1 Impact of the starting position on the RBC dynamics

The purpose of this section is to illustrate the dependency of the RBC dynamics with respect to the starting position and to exhibit a starting distance from which the dynamics inside the aperture and the electrical perturbation are converged.

From the IEE orientation (Fig. 4.8A), one observes that for the upstream part of the micro-orifice ($\tau < 0$), the RBC initial angle progressively decreases to show an orientation perfectly aligned with the streamline just before the aperture entrance. However, inside the micro-orifice, the RBC displays a rotation that depends on the initial starting time. Regarding the ellipsoid parameters in the upstream part,

shown in Fig. 4.8 B-D, the RBC is deformed from an oblate shape to a quasi-prolate shape. Indeed, initially, $a = c$, and both are greater than b. Then, a increases and c decreases whereas b stays almost the same. In the aperture ($\tau > 0$), the RBC is compressed as shown by a decreasing a and an increasing b. This compression occurs as the RBC progressively turns inside the aperture. In fact, for the considered streamline, the RBC crosses a region with substantial velocity shears as it was shown by streamline SL2 in Fig. 3.5A of Chap. 3. The shear stress undergone by the RBC inside the aperture makes it rotate. Besides, the RBC gets compressed when its orientation approaches the compression axis in the shearing region.

The IEE parameters and orientation inside the aperture converge with respect to the RBC starting position. Indeed, taking case 1 as the reference, cases 2, 3 and 4 indicate that taking an earlier starting time (Fig 4.5 B) gives a result closer to the reference. Also, case 2 shows superimposed results with case 1, regarding the IEE parameters inside the micro-orifice (Fig. 4.8). This supports the fact that it is sufficient to use an initial RBC location in the region where the strain rate is of order 2000 s^{-1} (see Fig. 4.5) to accurately describe the RBC dynamics within the aperture.

As a direct consequence of the RBC dynamics, the electrical perturbation also exhibits a dependency with the starting time, as depicted in Fig. 4.9. As for the IEE parameters, the electrical pulses for cases 1 and 2 are practically identical while cases with a starting point closer to the orifice entry would give inaccurate results. The difference between case 1 and case 4 maxima is evaluated to 10%.

4.2.2 Extensional configuration validation

We now compare cases 1 and 5. In both cases, the RBC is deposited at the same location, but in case 5, the dynamics far from the aperture is computed in the dedicated extensional configuration (FSIS0) while it is included in a simulation FSIS1 in case 1 (remind that no calculation FSIS0 is performed for case 1).

First, Fig. 4.8 shows that the run 5-FSIS0 is in good agreement with the first part ($\tau <$ - 12 μs) of case 1. Thus the extensional axi-symmetrical configuration FSIS0 is proven to be suitable to reproduce the early stage of the RBC deformation. It should be noted that the orientation corresponding to run 5-FSIS0 in Fig. 4.8D is evaluated as the orientation of the IEE a-axis with respect to axis $\vec{e}_s$ of the extensional configuration (Fig. 4.4). Then, comparing run 5-FSIS1 to case 1, one may observe that a RBC dropped in the reduced configuration after being stretched in an extensional configuration behaves as if it had undergone the full elongation before entering the aperture. Moreover, cases 1 and 5 are perfectly consistent in terms of impedance pulse, as shown in Fig. 4.9. The approach of solving separately the particle elongation occurring before the sensing region allows a computation cost reduced by a factor 8 (cases 1 and 5 Fig. 4.5B). Regarding the results shown in Fig. 4.8 and Fig. 4.9, simulations should start at least 330 μs before the orifice entrance. Due to the low computation cost of the extensional simulation, the choice was made to simulate the cell elongation in the configuration FSIS0 from -517 μs to -12 μs. Computation FSIS1 then starts from -12 μs and ends after the RBC leaves

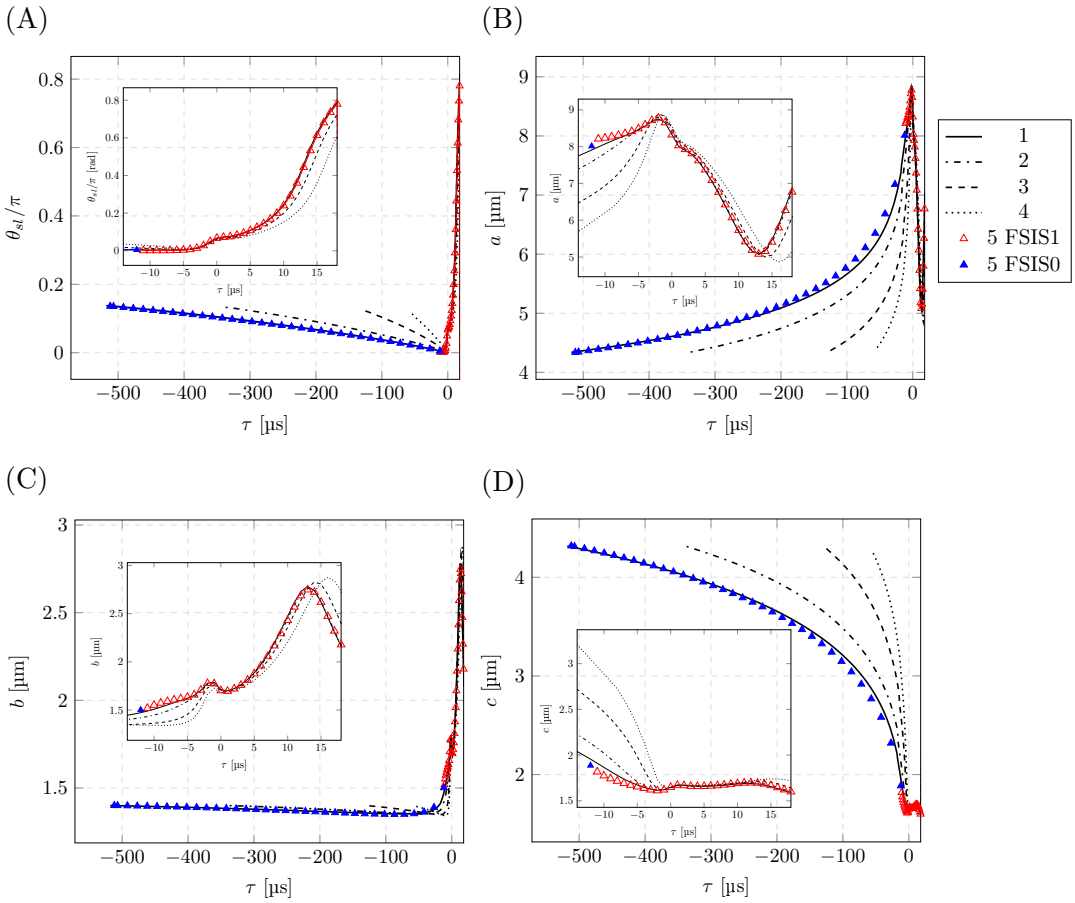

Figure 4.8 – Inertia equivalent ellipsoid principal axis and orientation for cases summarized in Fig. 4.5B. (A) Orientation of IEE axis a with the trajectory as defined in Fig. 4.7. (B) IEE parameter a, that tends to align with the extensional direction. (C) IEE parameter b, perpendicular to a in the symmetrical plane ($\vec{e}_x$,$\vec{e}_y$). (D) IEE parameter c that is out of the symmetrical plane lined up with $\vec{e}_z$.

the micro-orifice.

4.3 Results

Using the numerical pipeline of Sec. 4.1, the RBC dynamics and the induced electrical perturbation are simulated by considering the same streamlines employed for spheres in Chap. 3 (see Tab. 3.1). The RBC parameters are set as in Sec. 4.2 except for the internal viscosity which is 18×10^{-6} m^2.s^{-1}, to take into account the room temperature of the experimental acquisition [79]. The electrical responses obtained by applying the pipeline of Fig. 4.2 to streamlines of Tab. 3.1 are shown in Fig. 4.10A, while the trajectories followed by the RBC are depicted in Fig. 4.10B. For the most centred paths, 'bell-shaped' pulses with a short duration are obtained, while for trajectories near the aperture edges, more complex pulses with a longer duration are observed. Comparing qualitatively results from spheres (Fig. 3.12A) with result from RBCs (Fig. 4.10A) , it appears obvious that more complex phenomena

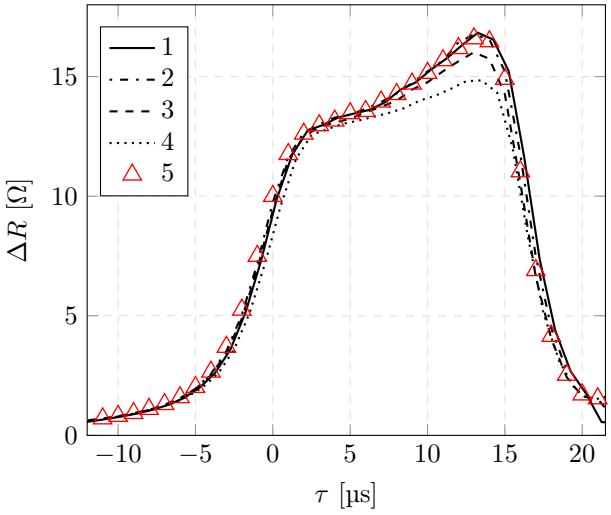

Figure 4.9 – Impedance pulses obtained from a RBC with the different initial conditions that are summarized in Fig. 4.5B.

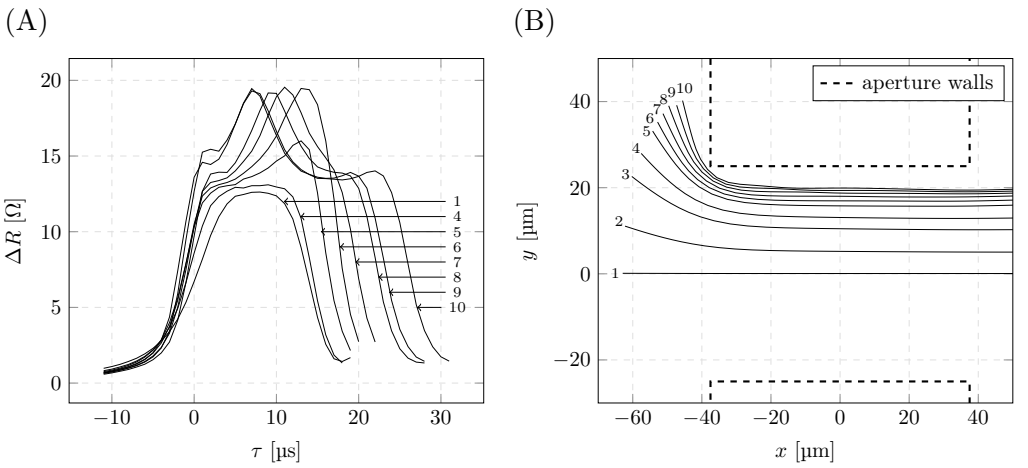

Figure 4.10 – Impedance pulses obtained numerically for different trajectories from RBCs. Picture (A) shows the impedance pulses and (B) illustrates the related RBC trajectories.

occur when the particle deforms and rotates.

4.3.1 Variety of deforming RBCs dynamics and impact on the pulse

RBC rotation inside the aperture

Figure. 4.11A depicts the evolution of the IEE orientation θ (see definition in Fig. 4.7) according to the cell position x, for each case of Fig. 4.10A (1, 4 and 5-10). For the most centred paths (1 and 4), the cell is oriented with the aperture principal axis ($\vec{e}_x$). In contrast, when considering near-wall trajectories such as 5 to 10, a substantial rotation is observed. For instance, Fig. 4.12 shows RBC consecutive positions in the aperture for cases 1 and 10. The cell rotation is observed for a near-

wall trajectory while an oblate elongated shape aligned with the aperture is obtained for the central path. An interesting result is that the closer the particle path to the aperture wall, the earlier the rotation in the aperture (see Fig. 4.11A). As stated in theoretical developements [10, 50], such variations in the particle orientation would induce changes in the electrical pulse. Hence, the infinity of rotation dynamics explains the huge variety of pulse signatures reported in the literature (remind the discussion of Sec. 1.3.2).

The electrical perturbations are shown according to the particle location in the micro-orifice (x) in Fig. 4.11B. Regarding Fig. 4.11A and Fig. 4.11B, the cell rotation induces a peak on the pulse, consisting of an increase in ΔR, that is shorter than the time spent by the cell in the sensing region (viz. shorter than the pulse duration). Considering cases 6-10, the pulses maxima are reached when the cell is perpendicular to the orifice principal axis ($\theta = \pi/2$). This is in agreement with results of Qin *et al.* [133] that showed an higher resistive perturbation when the particle longest axes is perpendicular to the electrical field (see Fig. 1.8 in Chap. 1). Despite the substantial rotation observed for case 5 (Fig. 4.11A), the pulse maximum does not match with the instant at which $\theta = \pi/2$ (see case 5 in Fig. 4.11B). This is because the RBC achieves a $\pi/2$ orientation outside of the orifice, where the electrical field rapidly decreases.

RBC deformations inside the aperture

By showing the evolution of the IEE parameters, Fig. 4.13 sheds light on the deformations experienced by RBCs in the micro-orifice. For the sake of clarity, only cases 1, 6 and 10 are depicted. Moreover, for the sake of completeness, the orientations θ are recalled in Fig. 4.13A. Regarding case 1, for which a constant orientation of 0 rad is observed, the cell shape is almost constant in the aperture ($\tau > 0$). In contrast, changes of orientation and deformations are visible when considering cases 6 and 10. It should be noted that in cases 6 and 10, the deformations are reflected in a compression of the RBC as it rotates. The compression is illustrated by a decreasing a and increasing b and c, as for the test case of Sec. 4.2. Moreover, the maximum of this compression occurs when the cell is perpendicular to the orifice principal axis.

When RBCs rotate in the aperture (see instant 8 μs for the near-wall case in Fig. 4.12), they may be severely compressed by the flow, which results in wrinkling of the surface. Wrinkling has been reported for deformable particles such as capsules and vesicles [78, 89] due to membrane compression. In particular, sudden compression of extended vesicles induces wrinkles whose characteristic length scale decreases with the compression rate. Assuming that RBCs would develop similar wrinkles, their size would be much smaller than our grid size [78] . As a consequence, the simulation develops surface small amplitude oscillations at the scale of the mesh size. This numerical artifact is classical in deformable particles simulations [67, 89, 135, 160] and has not been found to affect the large-scale results, although it may lead to instabilities when the membrane remains under compression for a long time. This is not the case here, where the RBCs rapidly flip and are stretched again by the shear flow.

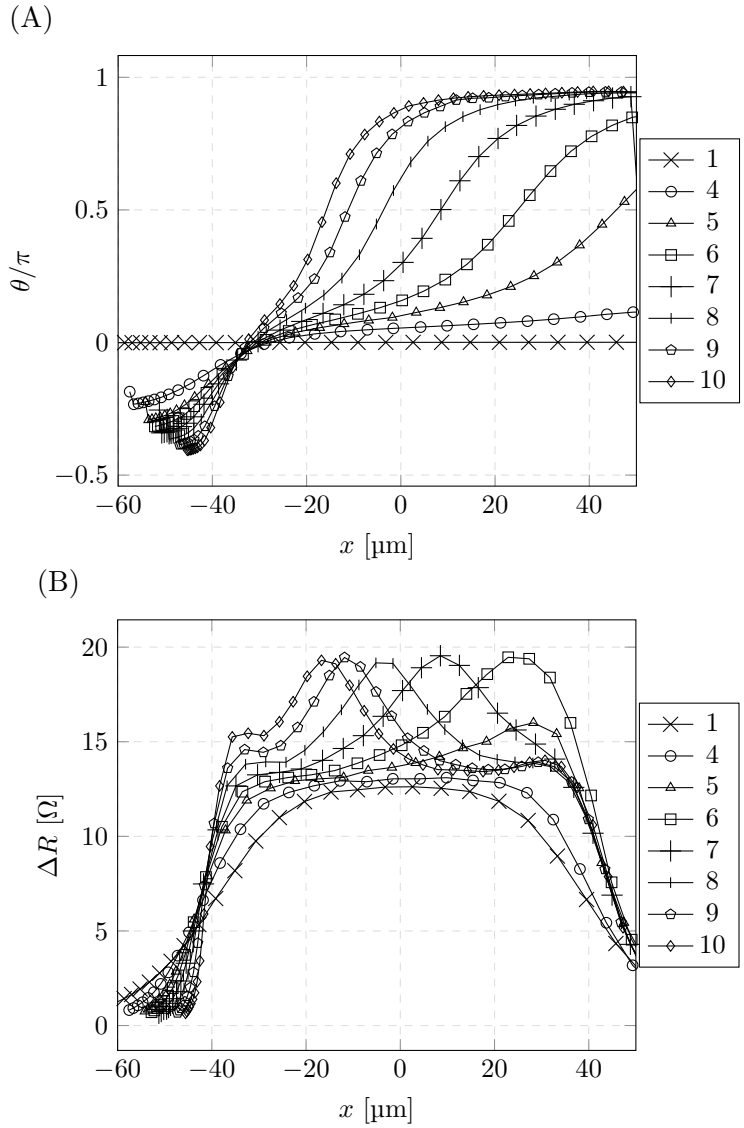

Figure 4.11 – Resistive pulses and RBC orientation according to the position inside the aperture. (A) RBC orientation (θ is zero when the particle is aligned with the aperture axis), (B) Resistive pulses obtained from the RBCs simulations.

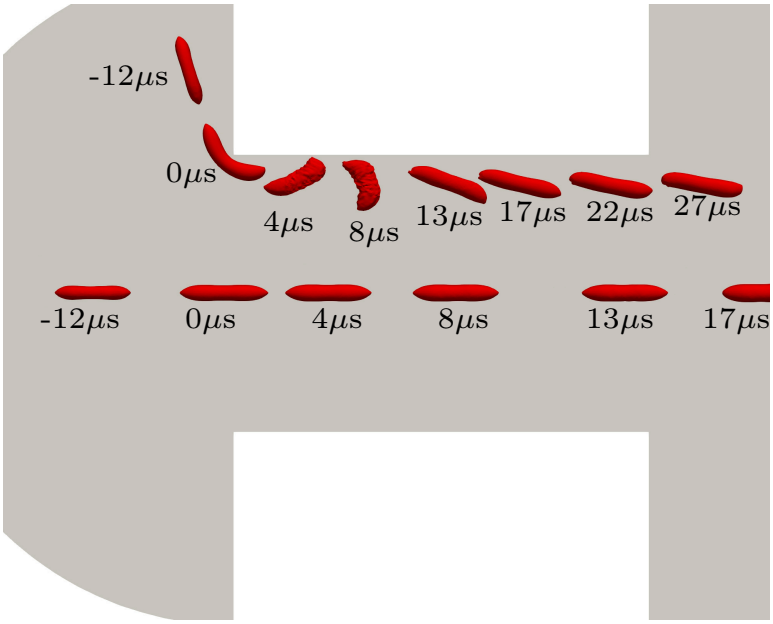

Figure 4.12 – RBC consecutive positions inside of the orifice for cases 1 (central trajectory) and 10 (near-wall trajectory).

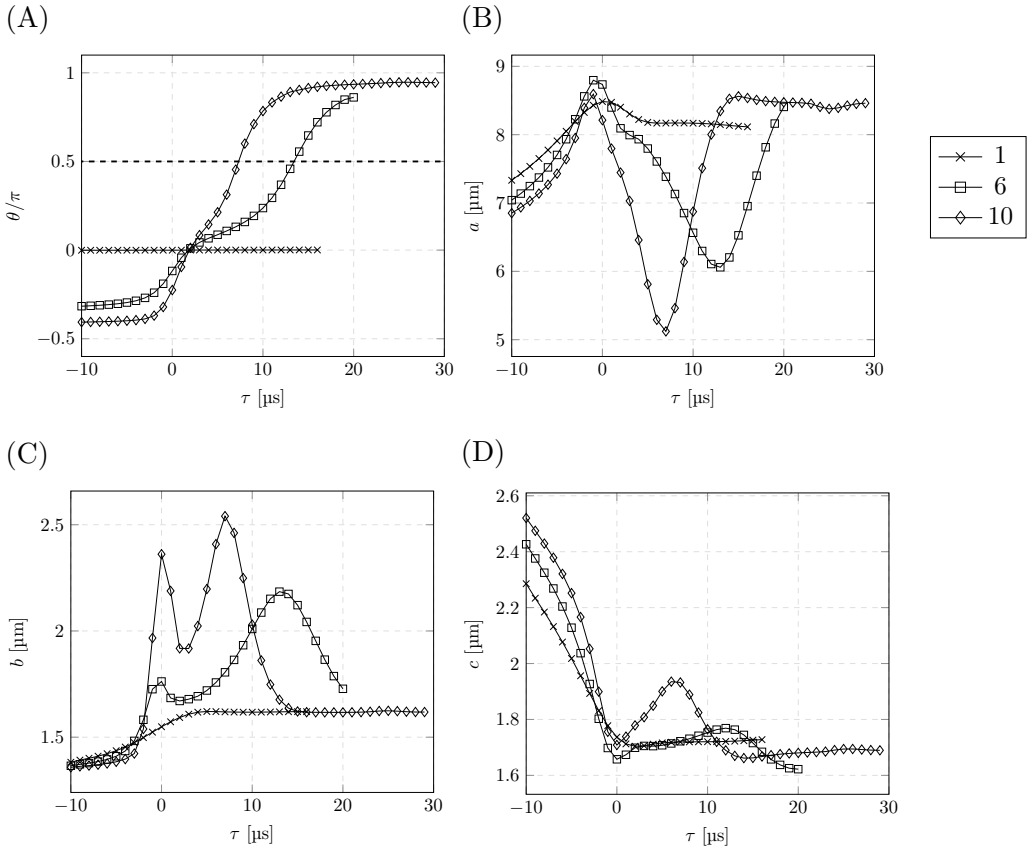

Figure 4.13 – RBC IEE orientation and parameters for cases 1, 6 and 10 of Fig 4.10.

Shape factor of deforming RBCs

In the case of rigid spheres, the shape factor f_s is constant so that a linear relationship between the squared electrical field and the electrical perturbation ΔR was observed (Sec. 3.2.1), supporting Kachel's statement [74] that, under the assumption of a constant shape factor, ΔR is directly proportional to E^2. Considering RBCs, deformations and rotations that may cause substantial shape factor variations are observed for near-wall paths. In this respect, no linearity can be expected between E^2 and ΔR (Eq. 1.2). Hereafter, the shape factor variations are modelled. This modelling effort aims at providing a finer analysis of the pulses signatures and uncorrelate the dynamical effects from the electrical ones.

In the following, the RBC shape factor is modeled using IEE orientation and parameters. Provided one of the ellipsoid principal axes is aligned with the electrical field $\vec{E}$, Velick and Gorin [170] state that, in the case of a non-conducting ellipsoid immersed in a homogeneous electrical field, the shape factor may be written as:

$$f_s = \frac{2}{2 - a\,b\,c\,L_\alpha} \tag{4.3}$$

where a, b and c denote the ellipsoid semi-axes and L_α is an elliptical integral that depends on the ellipsoid axis that is lined up with $\vec{E}$. As an example, if axis a is aligned with the electrical field, one has:

$$L_\alpha = L_a = \int_0^\infty \frac{d\lambda}{(a^2+\lambda)^{3/2}(b^2+\lambda)^{1/2}(c^2+\lambda)^{1/2}} \tag{4.4}$$

For the computation of L_b and L_c, the ellipsoid variables a, b and c are simply interchanged in Eq. 4.4. In order to take into account the RBC orientation inside the aperture, Eq. 4.3 is combined with the following relation [10]:

$$f_s = f_{//} - (f_{//} - f_\perp)cos^2\theta \tag{4.5}$$

where θ is the orientation of the IEE a-axis with respect to the electrical field, while the terms $f_{//}$ and $f_\perp$ denote the shape factor of the particle when the latter are computed with the use of Eq. 4.3 using L_a and L_b, respectively.

From the RBC IEE parameters reported in Fig. 4.13, the shape factor evolution inside the aperture is computed for cases 1, 6 and 10 by the use of Eq. 4.5. Figure 4.14 shows the scaled shape factor, the scaled electrical field squared, the scaled pulse and the scaled product of the shape factor with the electrical field squared. For the case of a centred path (Fig. 4.14A), the shape factor is constant within the micro-orifice as it was suggested by observing the constant IEE parameters and orientation in Fig. 4.13. In agreement with Eq. 1.2, the scaled electrical perturbation is then superimposed with the squared electrical field. For a near-wall trajectory, rotation and deformations of the RBC make the shape factor vary during the particle evolution inside the orifice. The squared electrical field is no more sufficient to explain the pulse signature, but as provided by equation 1.2, the product of f_s with E^2 shows a good comparison with the electrical perturbation. A loss of accuracy is nevertheless observed when approaching the aperture limits (x=$\pm$ 37.5μm). On the orifice limits, the electrical field $\vec{E}$ is not aligned with axis $\vec{x}$, thus the IEE

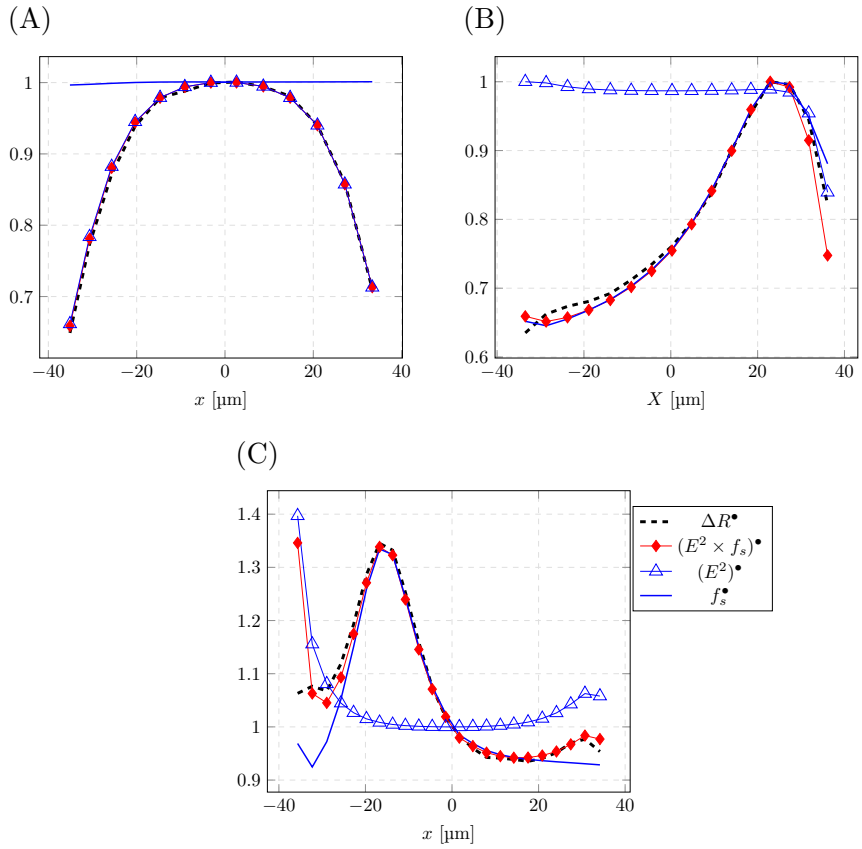

Figure 4.14 – Modelling of the pulse signatures for the case of a deformable particle such as RBC. On those graphs, the pulse, the squared electrical field, the shape factor and the product of the squared electrical field with the shape factor are shown. (A), (B) and (C) refer to cases 1, 6 and 10 of Fig. 4.10. In the shown graphs, each quantity $\phi(X)$ is scaled as: $\phi^\bullet(X) = \phi(X)/\phi(X=0)$, with $\phi \in \{\Delta R, E^2, E^2 \times f_s, f_s\}$.

orientation θ does not measure the expected angle for equation 4.5, which explains the differences. A correction would need to be implemented to make the model relevant outside the orifice.

Shape factors of an aligned and a perpendicular discocyte were evaluated according to Eq. 4.5 and compared with case 10 in Fig. 4.15. Assuming $\theta = 0$ and $\theta = \pi/2$, a discocyte has for shape factors 1.22 and 2.8 respectively, while a RBC evolving next to the aperture walls (see case 10) displays a shape factor that varies in between 1.06 and 1.6. The maximum f_s is obtained when the RBC is perpendicular to the electrical field, while the minimum value corresponds to a well-elongated shape that is almost aligned with the orifice principal axis (See Fig. 4.12). As shown in Fig. 4.15, the maximum shape factor for a deformable cell is smaller than the one calculated for a perpendicular discocyte (1.6 vs 2.8). This is because the RBC is compressed and even tends to fold during rotation as illustrated in Fig. 4.12. Moreover, the minimum value of the RBC shape factor is smaller than the one of a rigid discocyte aligned with the axis (1.06 vs 1.22). This is because the deformable cell is strongly elongated during the FSIS0 phase as illustrated in Fig. 4.8, thus

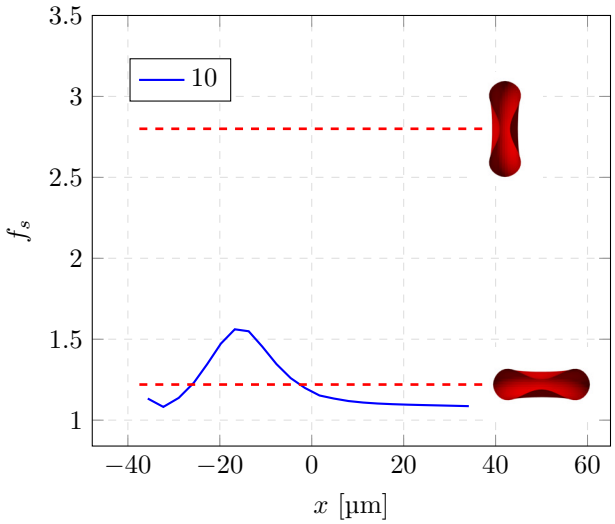

Figure 4.15 – Shape factor evolution according to the longitudinal particle position inside the micro-orifice. The shape factors of a discocyte aligned and perpendicular to the electrical field are also shown in red dashed lines.

reducing the projected area. Assuming that a rigid RBC (thus keeping its discocyte shape) rotates in the aperture, one would obtain pulses with a much more important peak. This illustrates the importance of taking into account deformations and cell dynamics when simulating the impedance measurement of RBCs.

Impact of RBCs parameters on the impedance pulse

Simulations over different trajectories are now performed by varying the shear modulus (G_s), the internal viscosity (ν_{in}) and the reduced volume ($\mathcal{Q}$) of the RBCs, one-at-time. In doing so, the original signatures are subject to modifications shown in Fig. 4.16. Only cases 1, 6, and 10 are displayed for the sake of concision. Pulses associated to the different RBC dynamics are scaled by the maximum of the pulse arising when the same cell (same shape and parameters) experiences a central trajectory. Regarding the central path (see Fig. 4.16A), the electrical print does not depend on variations of the RBC features. However, cases 6 and 10 change when the cell parameters are modified, as shown in Fig. 4.16B and C. Increases of ν_{in} and G_s yield pulses with a more important peak. The internal viscosity appears to have the same impact as the membrane rigidity (driven by G_s). Indeed, the cytosol viscosity reduces the instantaneous deformability of the cell. Hence, because of the short loading times experienced by RBCs in Coulter counters, an increase of viscosity yield a smaller RBC deformation inside the sensing region. As previously shown, a strong compression of the cell occurs while it rotates, which appears to mitigate the peak amplitude. Consequently, increases of ν_{in} and G_s make the RBC harder to compress and produce a larger peak. On the other hand, the amplitude of the peak decreases when the reduced volume ($\mathcal{Q}$) is increased in the simulations. A higher reduced volume implies a more spherical cell that tends to conceal the consequences of the cell rotation. Results of Chap. 3 for rigid spheres are also shown in Fig. 4.16 an confirm this hypothesis, since no peak of rotation are observed for pulses referred

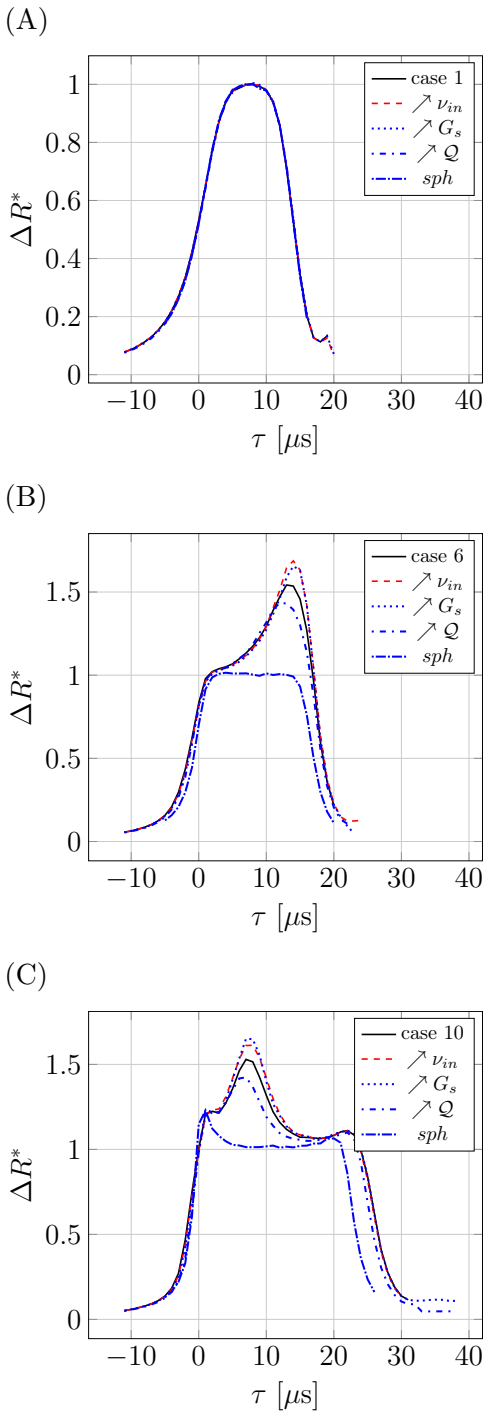

Figure 4.16 – One-at-a-time sensitivity analysis of the effect of the shear modulus G_s, the reduced volume $\mathcal{Q}$ and the internal viscosity ν_{in}. Picture (A), (B) and (C) refer to the original cases 1, 6 and 10, respectively. Reference cases shown in black are performed with $G_s = 2.5 \times 10^{-6}$ N.m^{-1}, $\nu_{in} = 18 \times 10^{-6}$m^2.s^{-1}, and $\mathcal{Q} = 0.65$. In cases referred as ↗ ν_{in}, ↗ G_s, and ↗ $\mathcal{Q}$, $\nu_{in} = 21 \times 10^{-6}$ m^2.s^{-1}, $G_s = 40.0 \times 10^{-6}$ N.m^{-1} and $\mathcal{Q} = 0.75$, respectively. Results for rigid spheres arising from Chap. 3 are also shown and referred as '*sph*'.

as '*sph*'.

Impacts of the bending modulus E_b and the spontaneous curvature c_o have shown insignificant effects on the results (not shown). Since changes of the membrane area are less than 1 % in the original computations, the impact of the area modulus E_a is not assessed. In a study presented in App. A, the effect of the cytosol density (ρ_{in}) is shown to have a negligible effect on the electrical print, when physiological values are considered.

4.3.2 Comparison with experimental data

Numerical results of Sec. 4.3.1 state that the RBC dynamics in the aperture depends on its trajectory. In particular, the distance from the aperture walls drives the time spent by the cell in the detection area and even the experienced rotation. More precisely, it is shown that particles traveling close to the aperture wall spend more time in the orifice and rotate earlier than the others. Besides, these dynamical effects are directly visible on the generated electrical print. On the one hand, the time spent in the orifice is linked to the electrical print duration. On the other hand, the cell rotation increases the shape factor that induces a peak on the pulse. In summary, approaching the orifice wall implies an increase of the duration and a shifting of the peak to the left-hand side of the pulse. This section aims at verifying these predictions on an experimental pulses acquisition. The pulse duration is measurable according to the metric $\mathcal{W}$ introduced in Chap. 3 (see Eq. 3.3) but a measurement of the moment at which the peak occurs still needs to be defined. This is done first by introducing the metric $\mathcal{P}$. Then, for each pulse obtained experimentally and numerically, $\mathcal{W}$ is plotted against $\mathcal{P}$ to emphasize the close links between trajectory, cell rotation and orifice occupation time. Finally, comparisons of the numerical pulses with experimental signatures are presented.

Measuring the Peak Position

The position of the peak is rated as follows:

$$\mathcal{P}(thresh) = \frac{T_2 - T_0}{T_1 - T_0} \times 100 \tag{4.6}$$

Figure. 4.17 illustrates the construction of instants T_0, T_1 and T_2 that are required in Eq. 4.6. Note that T_0 and T_1 depend on a threshold while T_2 corresponds to the moment at which the pulse maximum is attained. Hence, $\mathcal{P}$ consists in projecting the pulse maximum on a pulse width ($\mathcal{W}(thresh)$), and assessing its relative position. As a reminder, $\mathcal{W}(thresh)$ is defined as:

$$\mathcal{W}(thresh) = T_1 - T_0 \tag{4.7}$$

If the peak is observed at the beginning of the pulse, $\mathcal{P}$ tends to 0 %, whereas $\mathcal{P}$ increases as the peak is delayed on the pulse. The cutting threshold must be chosen in such a way it intersects the ascending and descending slopes of the electrical signature.

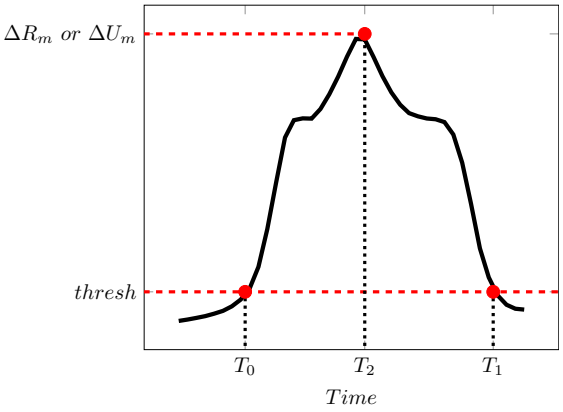

Figure 4.17 – Sketch of T_0, T_1 and T_2 calculus.

Graphing the pulse width against the peak position

An experimental acquisition is performed as described in Sec. 3.2.2, this time by analysing a blood sample coming from a healthy patient. As done in Sec. 3.2.2, the experimental pulses are scaled with the averaged maximum of the 'bell-shaped' signatures $\overline{\Delta U}_m|_{bs}$ while numerical results are scaled by the maximum of case 1 $\Delta R_m|_{bs}$ (see Fig. 4.10). This yields the scaled pulses ΔU^* and ΔR^*:

$$\Delta U^*(t) = \frac{\Delta U(t)}{\overline{\Delta U}_m|_{bs}}, \quad \Delta R^*(t) = \frac{\Delta R(t)}{\Delta R_m|_{bs}}$$

Note that a simple method allowing the extraction of 'bell-shaped' pulses from an experimental acquisition is provided in Chap. 5.

With the same convention that defines $\mathcal{W}^r$ as the width calculated on a scaled pulse (defined by Eq. 3.5 and Eq. 3.6), $\mathcal{P}^r$ denotes the peak position evaluated on ΔU^* or ΔR^*. Note that $\mathcal{P}^r$ may be calculated directly from ΔU and ΔR as:

$$\mathcal{P}^r(thresh') = \mathcal{P}(thresh' \times \overline{\Delta U}_m|_{bs}), \tag{4.8}$$

and

$$\mathcal{P}^r(thresh') = \mathcal{P}(thresh' \times \Delta R_m|_{bs}), \tag{4.9}$$

respectively. If the readers feel uncomfortable with these notations, they are referred to App. E, where they are summarized and illustrated.

Thereafter, the metrics $\mathcal{W}^r$ and $\mathcal{P}^r$ are assessed for each experimental signature and each numerical pulse, with $thresh' = 0.5$. In Fig. 4.18, the scatter plot of $\mathcal{W}^r$ as a function of $\mathcal{P}^r$ is shown: the experimental data are shown in red points and the numerical results are depicted in black points connected with a black dashed line. The numbers in Fig. 4.18 refer to the different simulated cases of Fig. 4.10.

In such a representation, electrical pulses are organized in two main branches that are connected at $\mathcal{P}^r \approx 80$ % and $\mathcal{W}^r \approx 17$ μs. The lower branch, for which $\mathcal{W}^r < 17$ μs, refers to cases 1-5 from simulations. More precisely, it corresponds to the region of the aperture that extends from the perfectly centred path, to the first trajectory for which the cell can reach a $\pi/2$ orientation inside the aperture (in-between cases 5 and 6). The upper branch ($\mathcal{W}^r > 17$ μs) corresponds to simulated

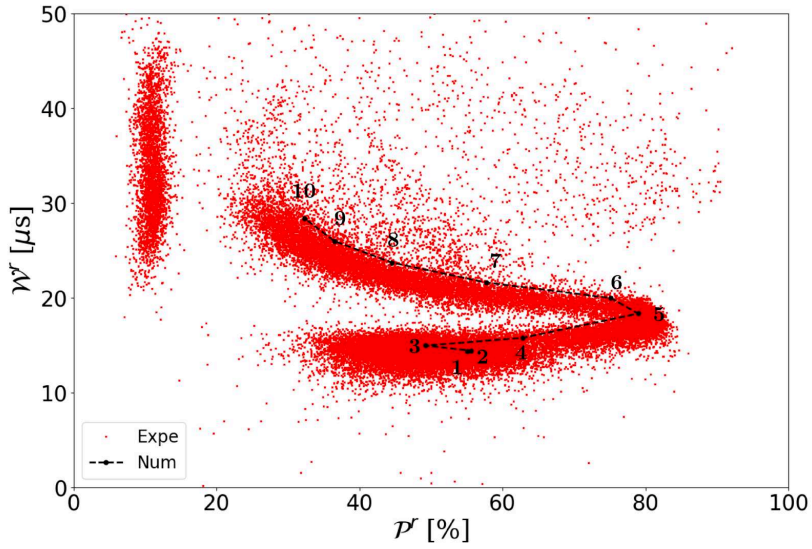

Figure 4.18 – Scatter plot of $\mathcal{W}^r$ according to $\mathcal{P}^r$ for the experimental acquisition (red points) and the numerical results (black points connected by a dashed line). Metrics are calculated with a relative threshold of 0.5.

trajectories 5-10 and display a decreasing pulse duration ($\mathcal{W}^r$) with respect to the peak position ($\mathcal{P}^r$). This is in agreement with the previous statement that when the trajectory progressively approaches the aperture wall, the peak occurs sooner and the pulse becomes longer.

A third cluster placed in the region of low $\mathcal{P}^r$ (between 5% and 15%) is observed experimentally, but not obtained by considering trajectories of Fig. 4.10 in the simulations. These pulses may be explained by trajectories even closer to the orifice edges. Considering such trajectories however leads to unstable computations. Further developments are needed to accurately reproduce this isolated cluster but preliminary indications are available in App. B.

Superimposing numerical and experimental pulses

Let define PP_n and W_n, respectively $\mathcal{P}^r$ and $\mathcal{W}^r$ computed for an arbitrary numerical pulse, as far as PP_e and W_e are the same metrics but for a given experimental pulse. In Fig. 4.19, each numerical pulse is superimposed with experimental pulses satisfying $PP_n - 2\% < PP_e < PP_n + 2\%$ and $W_n - 1\mu s < W_e < W_n + 1\mu s$. Note that the pulses are centred in time for better comparisons.

The pulse signatures predicted numerically are well retrieved experimentally despite the variable amplitudes that originates from the scattered RBC volumes within a blood sample. Nevertheless, some experimental pulses exhibit shapes that do not correspond to numerical results. However, these cases are rare and can be explained by particle coincidences in the aperture.

Note also that the amplitude of the numerical pulses associated with rotating

cells seem in the lower range of the experimental data. In other words, simulations possibly overpredict the compression of the rotating cells in the aperture. In our simulations, membrane viscosity has been neglected and this assumption is a possible cause for this relative discrepancy.

4.4 Conclusion

In this chapter, a method for tackling the numerical simulation of a deformable particle in a Coulter counter was presented. This approach takes into account the cell deformation occurring before it enters in the sensing region. A complex pipeline composed of several simulations is required to achieve results.

Note that in the range of the electrical field observed in the studied configuration (of the order of 1.0×10^6 V.m^{-1}), RBC electro-deformations were reported [132][116], so that greater deformation should be expected if dielectrophoretic (DEP) forces were taken into account. Besides, due to the short loading times experienced by RBCs in the presented simulations (a few tens of μs), the membrane viscosity would play an important role in the maintaining of the cell shape although it was not accounted for. Further investigations about the impact of DEP forces and membrane viscosity should be performed in the future. Still, good comparison with experimental data was obtained, demonstrated that the proposed pipeline and current assumptions are appropriate to represent the main mechanisms at play.

A variety of rotation dynamics was observed numerically and shown to depend on the RBC path in the aperture. On a perfectly centred path, the cell is aligned with the aperture principal axis during its entire evolution in the sensing region. Then, the more the trajectory is close to the aperture wall, the more the RBC experiences an important rotation, in such a way it achieves a half-turn in the near vicinity of the orifice edges. This infinity of rotation dynamics explains the huge variety of pulses reported in the literature for aspherical and/or deformable particles. The cell rotation produces an increase of the shape factor f_s, which yields a peak on the electrical pulse (viz. a short increase of the electrical perturbation). Hence, a particle flowing in the wall vicinity is seen bigger than if it has followed a centred path since the pulse maximum is taken as a measurement of the RBC volume. This explains and illustrates the dynamical edge-effects leading to measurement errors. A substantial deformation of the RBC is observed as it rotates on a near-wall path. This deformation consists of a cell compression that appears to limitate the rise in f_s and thus the peak amplitude. Consequently, the RBC deformability may impact the peak of rotation.

Regarding these results, two questions arise:

1) From the new understanding of the dynamical edge-effects, is it possible to develop an original filtering method to improve the volume measurements?

2) The electrical pulses originating from near-wall trajectories depend on the cell deformability. Hence, is it possible to process the RBC deformability from the associated electrical print?

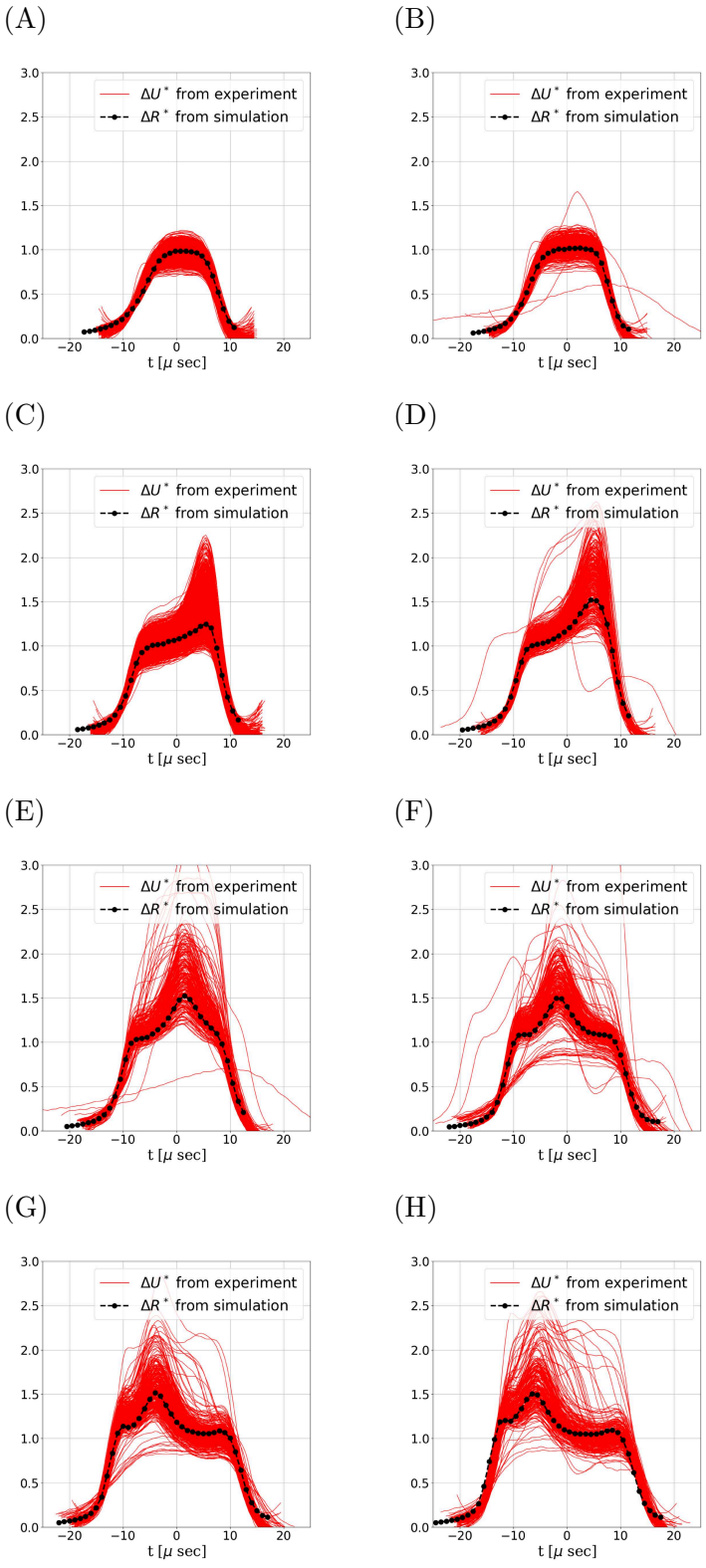

Figure 4.19 – Comparison of numerical and experimental pulses. The numerical pulses are superimposed with experimental (in red continuous line) data that have the same width and peak position metrics, with a tolerance margin of $\pm 1 \mu sec$ and $\pm 2\%$ respectively. Graphs A, B, C, D, E, F, G and H refers to cases 1, 4, 5, 6, 7, 8, 9 and 10, respectively.

Chapter 5

Improvement of red blood cells volume measurement with Coulter counters

Chapter contents

Results presented in this chapter gave rise to patent filing[1].

In Sec. 1.3.2, edge-effects producing skews in the measurement of the cell volume were discussed. These artefacts overestimate the volume of the RBC passing near the edge of the orifice, as demonstrated in the former chapter, and induce the typical 'right-skew' volume distribution (an example was shown in Fig. 1.5A). By enforcing particles to pursue central trajectories, hydrodynamical focusing [154] was found to produce a symmetrical distribution. However, this method implies a more complex, technologically demanding, implementation of Coulter counters. Methods consisting in rejecting inaccurate pulses were introduced [173]. Although improving the volume distributions of the analyzed particles, these methods are unable to retrieve a Gaussian-like distribution [129].

Generally, the pulse maximum is taken as the measurement of the particle volume V_p. However, in addition to V_p, the electrical perturbation depends on the squared electrical field E^2 and the shape factor f_s, which are directly impacted by the edge-

[1]Medical analysis device by impedance signal processing, 2019, Patent pending (FR)

effects. This explains the measurement errors, since the relationship between the measured volume and the actual volume V_p depends on whether the particle experienced edge effects or not. In particular, the numerical study of Chap. 4 shed light on electrical and hydrodynamical edge-effects. In particular, it was shown that both types may be stratified from their impact on the electrical print. On the one hand, electrical artefacts are related to increases in the electrical field E occurring near the aperture walls: particles passing close to the wall do not perturb the same electrical field as particles flowing on the aperture axis, hence the different signals. On the other hand, hydrodynamical edge-effects consist in particle rotation and deformation that lead to changes in the shape factor f_s. Variations in f_s are observed when cells undergo shear close to the walls. Such velocity gradients make the cell rotate, which increases f_s. Moreover, substantial deformation come with the rotation. These edge effects produce complex signatures such as 'M-shaped' when dealing with spheres (see Fig. 3.17F-H), or pulses with a peak if RBCs are considered (see Fig. 4.19D-H). In contrast with near-wall paths, cells flowing in the core region are edge-effects free and classical 'bell-shaped' pulses are observed: they are consistent with a constant f_s along the trajectory, and the pulse shape corresponds to the history of E experienced by the cell.

An overview on the impact of edge-effects is given in Fig. 5.1. Figure. 5.1A and B show respectively the dynamics of a RBC on a central and a near-wall trajectory, while the evolution of a rigid bead close to the wall is depicted in Fig. 5.1C. Electrical pulses associated to these particles dynamics are displayed in Fig. 5.1D. Note that results of Fig. 5.1 arise from simulations that were presented in former chapters. Electrical field isolines in the aperture are superimposed with the cell dynamics of Fig. 5.1A, B and C. Besides, regions of dense electrical field near the aperture corners and their impacts on the electrical pulse are highlighted by blue circles in Fig. 5.1B, C and D. Furthermore, the RBC rotation and the induced peak on the electrical print are indicated by black arrows (see Fig. 5.1B and D). In the considered regime, one may map the edge-effects as shown in Fig. 5.1. Considering the core region of the micro-orifice, the velocity profile is flat and the electrical field is homogeneous, thus no edge effects are observed in Part A. In part B, velocity gradients implying dynamical edge-effects are present. Finally, electrical edge-effects take place near the aperture corner (Part C).

This chapter aims at detecting and removing pulses impacted by edge effects to provide an accurate volume measurement of particles. Note that particles going through part C also get across part B. In other words, part C is covered by part B so that it is sufficient to detect dynamical edge-effects to filter irrelevant pulses out. Since particles rotate in the shearing region (Part B), it is proposed to filter hydrodynamical edge-effects by sensing the particle rotation from the associated electrical pulse. In the first part, the impact of rotation on the measured volume is shown. Then the original filter is described and applied to experimental data. Furthermore, it is shown that the proposed method provides results closer to hydrodynamical-focusing than the filter currently implemented in HORIBA Medical analysers. In the last section, a second method for the detection of particle rotations is introduced. Based on Neural-Network modelling, the latter is shown to provide results similar

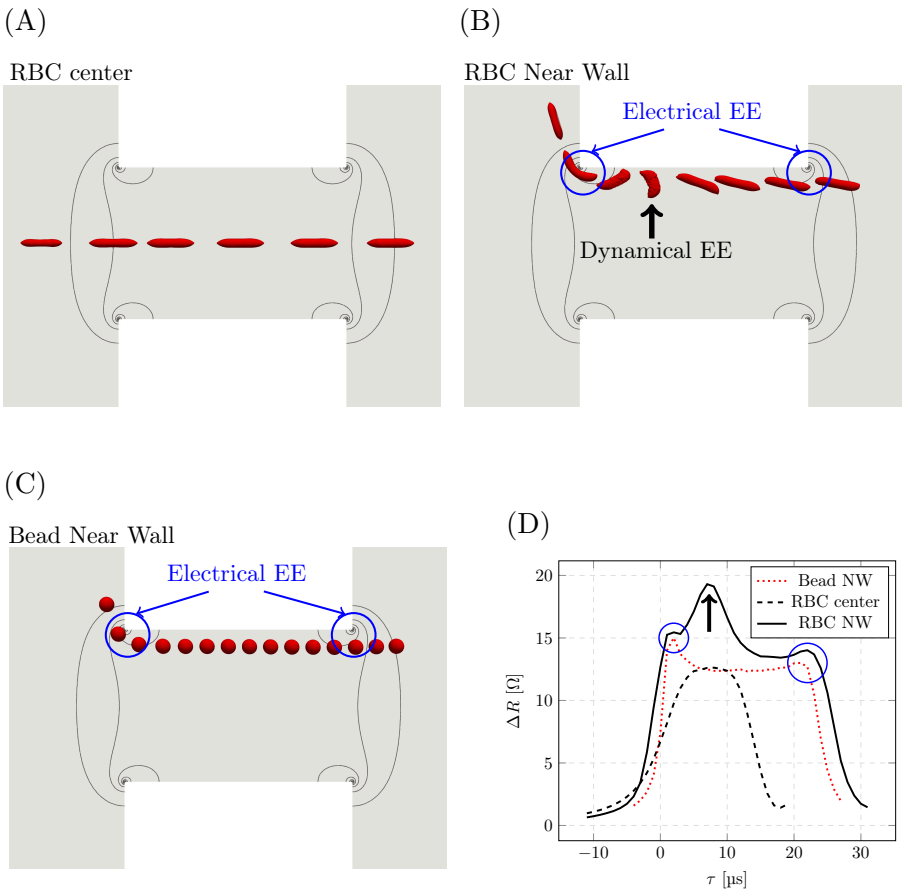

Figure 5.1 – Impact of the Edge Effects (EE) on the pulse shape. (A) and (B) show RBC consecutive positions inside the aperture over electrical field isolines for centred and near-wall trajectories, respectively (flow is from left to right). Picture (C), displays a rigid bead on a near-wall trajectory. The impedance pulses related to dynamics of (A), (B) and (C) are shown in picture (D). Notation 'NW' in (D) stems from Near Wall. The cell rotation observed in (B) generates a peak on the impedance pulses. This event is highlighted by a black arrow in (B) and (D). In addition, the electrical EE are outlined by blue circles, as shown in (B), (C) and (D).

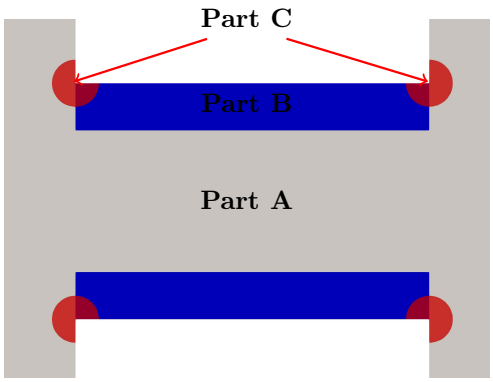

Figure 5.2 – Mapping of edge-effects in the micro-orifice. In part A, there is no edge effects. In part B, velocity gradient induces dynamical edge effects. In part C, regions of dense electrical field cause electrical edge-effects.

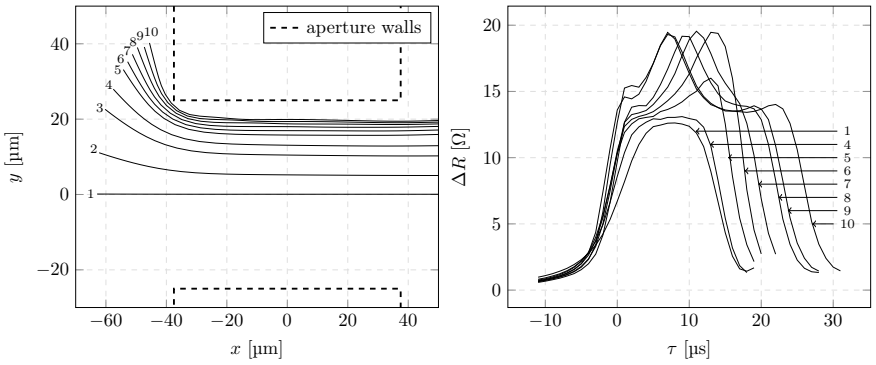

Figure 5.3 – Simulated impedance measurements (**right** plot) corresponding to a RBC following different trajectories (**left** plot). Impedance pulses are related to numerical simulations presented in Sec. 4.3 and shown in Fig. 4.10. For sake of clarity, the electrical pulses corresponding to trajectories 2 and 3 are not shown.

to the first method.

5.1 Discrepancy in the volume measurement with classical Coulter counters

This section aims at introducing the fundamental concept from which the proposed filters are derived. More precisely, the impact of the cell rotation on the measured volume and its link with the trajectory are explained. The argumentation is based on numerical results of Sec. 4.3. As a reminder, the electrical perturbation of a RBC was assessed for ten different trajectories. In all cases the same RBC is used, with identical geometrical characteristics and mechanical properties. Only its initial location (and thus its trajectory and dynamics in the aperture) changes. Some of the electrical pulses are reminded in Fig. 5.3.

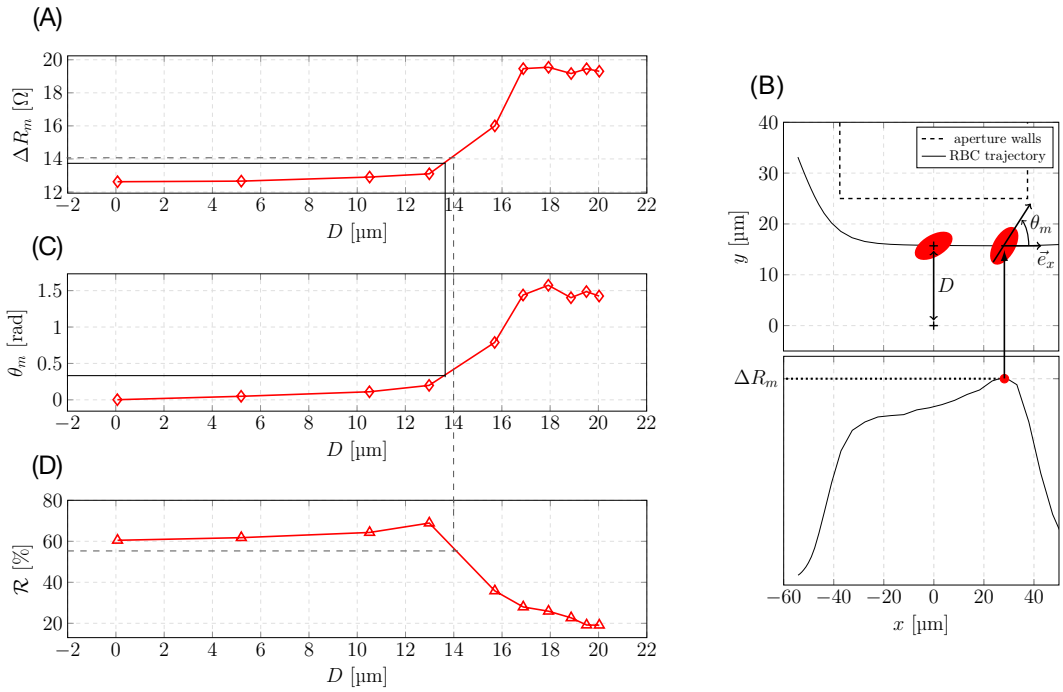

Figure 5.4 – Reliance of the measured volume (A), the particle orientation at the moment at which the pulse reaches its maximum value ΔR_m (C), and the $\mathcal{R}$ metric (D), according to the distance from orifice center of mass. Parameters p_u and p_d required for assessing $\mathcal{R}$ are set to 7/8 and 1/2, respectively. Picture (B) illustrates how the distance from the aperture center D and the orientation at ΔR_m (θ_m) are defined.

5.1.1 Errors in the measured volume

In a Coulter counter, the maximum ΔR_m is taken as a measurement of the particle volume V_p. One may thus conclude from Fig. 5.3 that errors of about 55 % may be made on the volume, depending on the trajectory. For instance, the maxima of cases 1 and 10 in Fig. 5.3 are respectively 12.6 Ω and 19.3 Ω, thus a RBC following a near-wall path is seen 1.53 times bigger than a cell evolving in the core region.

Figure. 5.4A displays the evolution of the measured volume ΔR_m according to the cell distance with respect to the aperture central axis D. As shown in Fig. 5.4B, D is evaluated as the distance between the RBC center of mass and point (0,0,0) at the moment when the trajectory crosses the orifice middle section (viz. plane $(\vec{e}_y, \vec{e}_z)$). From Fig. 5.4A, the measured volume in the core region of the aperture ($D \in [0\ ;\ 13\ \mu\text{m}]$) is stable around 12.6 Ω. Taking the perfectly centred path as the reference, the error at D=13 μm is 3 %. Overestimations of the cell volume become much larger for $D > 13\ \mu$m: ΔR_m is an increasing function of D between 13 μm and 17μm and then appears to stabilize around a value of 19.3 Ω. This discrepancy in measured volume explains the typical 'right-skew' volume distributions observed experimentally (discussed in Chap. 1, shown in Fig. 1.5A).

5.1.2 Impact of the cell rotation on the measured volume

As discussed previously, variations of the shape factor f_s are observed near the orifice edges. Such changes in f_s result in the cell rotation that increases the electrical perturbation. In that sense, the isolating particle resists more to the electrical current, which yields a peak on the electrical pulse and overestimates the cell volume (compared to a centred trajectory).

As represented in Fig. 5.4B, the orientation of the cell when the pulse maximum is reached (θ_m) is evaluated for the 10 cases of Fig. 5.3. In Fig. 5.4C, the evolution of θ_m according to D is depicted. If $D > 16$ μm, the time spent by the cell in the detection area is sufficiently long (because of low velocities near the wall) and the shear undergone by the particle is sufficiently strong for the RBC to reach a $\pi/2$ orientation inside of the aperture. On the contrary, in the core region of the micro-orifice, there is a flat velocity profile: the cell does not rotate and $\theta_m \approx 0$ when D < 13 μm. Between 13 μm and 16 μm, the cell undergoes shear but does not spend enough time in the aperture to reach $\theta_m = \pi/2$.

It should be noted that both ΔR_m and θ_m display a sigmoid-like profile (see Fig. 5.4A and C), thus supporting the approach of detecting the RBC rotation to select relevant pulses for the volume measurement. In particular, when $\theta_m \approx 0$ rad, ΔR_m takes a value close to 12.6 Ω (see $D < 13$ μm) whereas if $\theta_m = \pi/2$, ΔR_m shows its maximum value that is around 19.3 Ω ($D > 16$ μm). Moreover, if D is in the range [13 μm ; 16 μm], θ_m increases from 0 rad to $\pi/2$ rad, in a same way ΔR_m increases from its minimal value to its maximal value (12.6 and 19.3 Ω, respectively).

As highlighted by black arrows in Fig. 5.1B and D, the RBC rotation in the aperture produces a peak in the impedance pulse. A peak is defined as an increase in the electrical perturbation whose length is shorter than the pulse duration. A method designed to detect such peaks is described in the next section

5.2 Detection of the particle rotation from the electrical pulse

In Sec. 5.1, the link between the particle rotation and the error on the measured volume was established. Considering near-wall paths, RBCs rotate, which induces a peak on the electrical perturbation. A simple metric computed from the pulse is introduced in Sec. 5.2.1, which enables a separation between 'bell-shaped' pulses and pulses presenting a peak. In Sec. 5.2.2, this criterion is shown to provide an expected Gaussian-like volume distribution of RBCs. Furthermore, the proposed filter is compared with hydrodynamical-focusing [154] and the filter currently implemented in HORIBA Medical automata.

5.2.1 Metric definition

The metric denoted by $\mathcal{R}$ is computed as the ratio of the two pulse widths (see Eq. 3.3) defined in Fig. 5.5A. By defining W_u and W_d as $W_u = \mathcal{W}(\Delta R_m \times p_u)$ and

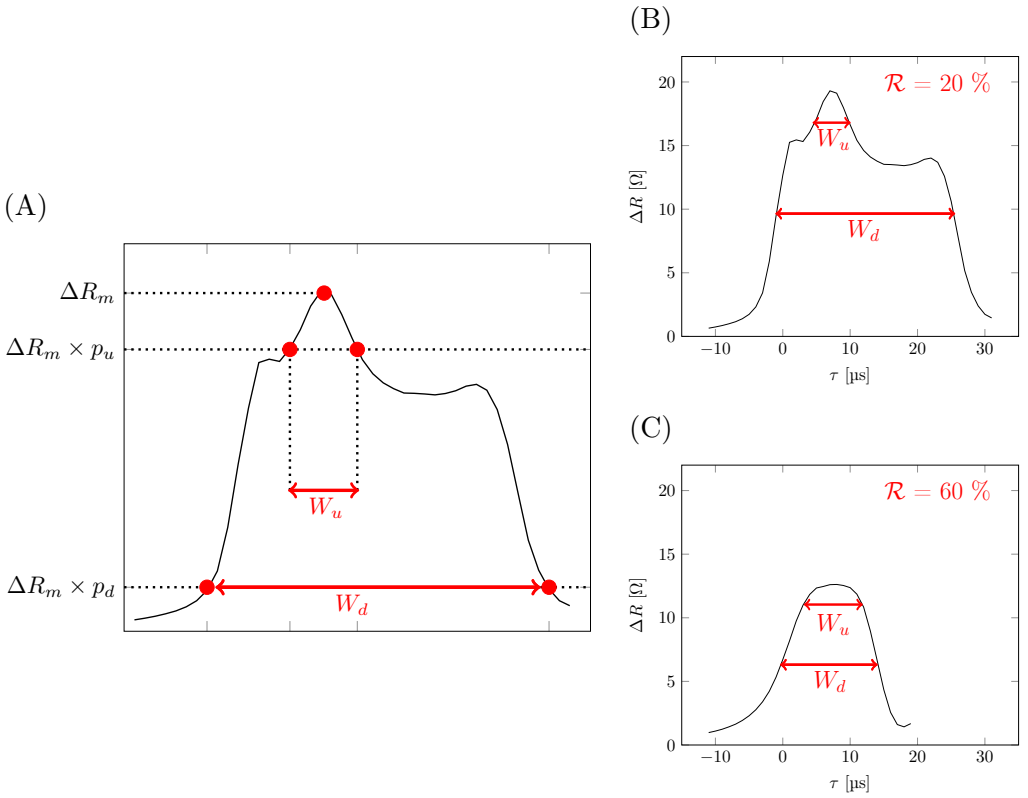

Figure 5.5 – Illustration of the calculation of W_u and W_d required for assessing the metric $\mathcal{R}$ (A). Calculation of $\mathcal{R}$ on case 1 and case 10 of Fig. 5.3 are given in (B) and (C), respectively. Computations of W_u and W_d are shown for resistive pulses ΔR, but the method stands for tension pulses ΔU.

$W_d = \mathcal{W}(\Delta R_m \times p_d)$, the metric $\mathcal{R}$ takes the following expression:

$$\mathcal{R} = \frac{W_u}{W_d} \times 100, \ in \ \% \tag{5.1}$$

Parameter p_d should be chosen in such a way $\Delta R_m \times p_d$ intersect the ascending and descending slopes of the pulse, and W_d informs on the time spent by the particle in the micro-orifice. If a peak is present on the pulse, W_u meant to measure the time spent in the peak. Hence, p_u must be defined so that $\Delta R_m \times p_u$ crosses the peak. Notice that in the absence of peak, W_u should be closer to W_d. Hence, $\mathcal{R}$ is intended to take a low value in case of peak of rotation (see Fig. 5.5B) and a high value for a 'bell-shaped' pulse without peak (see Fig. 5.5C). Note that W_d increases when the cell trajectory gets closer to the aperture edges. This is expected to reinforce the difference between W_u and W_d if the pulse presents a peak. $\mathcal{R}$ is evaluated for the 10 simulated cases depicted in Fig. 5.3 and its evolution according to D is shown in Fig. 5.4D. For assessing these $\mathcal{R}$ values, p_u and p_d are set to 7/8 and 1/2, respectively. When θ_m is small ($D < 13$ μm), high values of $\mathcal{R}$ are obtained (between 60 and 70 %), while for cases where the RBCs may reach $\theta_m = \pi/2$ ($D > 16$ μm), $\mathcal{R}$ is below 30 %.

By comparing Fig. 5.4A and D, it is seen that rejecting pulses for which $\mathcal{R}$ is below 55% would allow to reduce the maximum measured volume (ΔR_m) from 19.3

Ω to 14.0 Ω (ΔR_m for a central path being 12.6 Ω). Consequently, the maximum overestimation should be reduced from 53 % to 10 %. The $\mathcal{R}$ metric thus appears to be relevant to isolate the complex pulses presenting a peak of rotation from the 'bell-shaped' pulses for which RBCs do not rotate. Hence, a filter based on $\mathcal{R}$ may be introduced. This filter consists in rejecting pulses having a width ratio ($\mathcal{R}$) below 55%. Applying such a filter is expected to reduce errors in the measured volume and provide a more accurate assessment of haematological parameters related to the RBCs volumes. The accuracy of the $\mathcal{R}$ based filter is evaluated in the following section for the case of experimental data.

5.2.2 Application to experimental data

A blood sample coming from a healthy patient is analysed by the use of a Yumizen H2500 (HORIBA Medical). This haematology analyser is equipped with different measurement units dedicated to specific tasks. In a first device, RBCs counting and sizing are performed with a classical Coulter counter whose configuration was used for the numerical simulations (Sec. 3.1). In a second system, optical measurements are included in a hydro-focused Coulter counter. This module is used for detecting platelets among other blood cells (most of them being RBCs) by combining impedance and optical measurements. During the blood sample analysis, electrical pulses from both aforementioned systems are recorded. Pulses from the system equipped with hydrofocusing will be used as the reference for assessing the accuracy of the $\mathcal{R}$ based filter. Optical measurements performed in the second device are not needed and are not recorded.

For each pulse coming from the classical Coulter counter, the maximum (ΔU_m), the width ($\mathcal{W}$, see Eq. 3.3) and the width ratio ($\mathcal{R}$) are computed. Parameters p_u and p_d required for the calculation of $\mathcal{R}$ are taken as 7/8 and 1/2, respectively. The pulses durations ($\mathcal{W}$) are computed with a threshold of 0.28 V according to Eq. 3.3, a typical pulse amplitude being around 1.5 V. Figures. 5.6A and 5.6B show the scatter plots of $\mathcal{W}$ as a function of ΔU_m and $\mathcal{R}$ as a function of ΔU_m, respectively. Stating that longer pulses are related to near wall trajectories, Waterman *et al.* [173] proposed to reject pulses that have a width above a certain threshold. Such a filter may be represented as a horizontal line in Fig. 5.6A. In Yumizen H2500, instead of a constant width threshold, pulses that are placed above a logarithmic curve are rejected (see Fig. 5.6A). As discussed in Chap. 1, this curve is defined by the following expression:

$$\mathcal{W} = A\sqrt{log(\Delta U_m) - B}, \tag{5.2}$$

with A and B set to 2.01e-05 and -2.4, respectively. These two types of filters appear to split the pulse population arbitrarily. In contrast, two distinct clusters separated by a threshold of 52 % with respect to the $\mathcal{R}$ axis are observed (see Fig. 5.6B) This threshold agrees with the value of 55 % that was predicted numerically. It should be noted that the cluster located below $\mathcal{R} = 52$ % spreads between 1.25 V and 2.8 V along the ΔU_m axis, while the cluster above $\mathcal{R} = 52$ % takes ΔU_m values included in [0.7 V ; 2.2 V]. This supports the numerical results stating that pulses with low

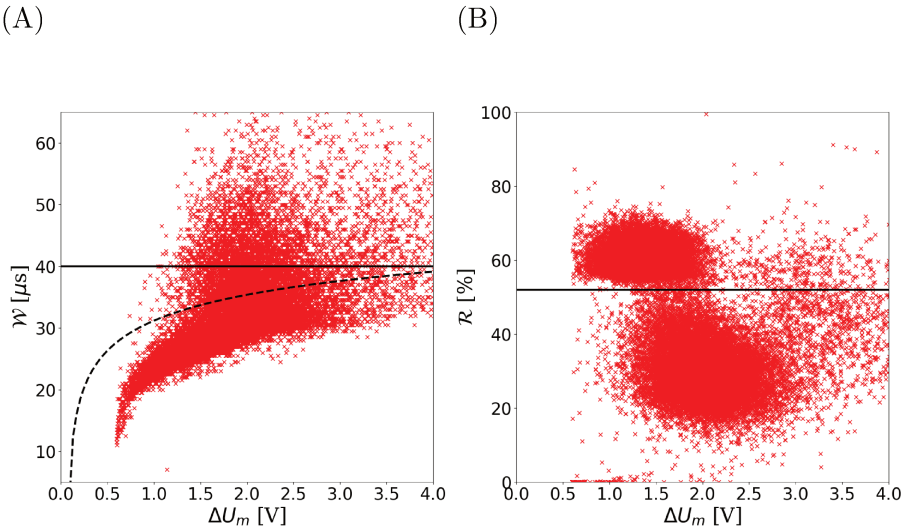

Figure 5.6 – Scatter plots of the experimental results for a blood sample analysed with Yumizen H2500 device. (A), Scatter plot of $\mathcal{W}$ against ΔU_m. (B), Scatter plot of $\mathcal{R}$ according to ΔU_m. Pulses width are calculated with a threshold of 0.28 V, while p_u and p_d required for assessing $\mathcal{R}$ are set to 7/8 and 1/2, respectively. In (A) the filter by Waterman [173] is illustrated with the horizontal continuous line, and the logarithmic filter from HORIBA Medical is shown in dashed line. In (B), the introduced $\mathcal{R}$-based filter is represented as a horizontal continuous line.

$\mathcal{R}$ are linked to cells rotations and volumes overestimations (see Fig. 5.4A ,C and D).

Histograms of ΔU_m obtained with the classical counter and the hydrofocused counter are shown in Fig. 5.7A. They are denoted by 'c' and 'hf', respectively. Using hydrodynamical-focusing gives a symmetrical and Gaussian-like ΔU_m distribution while a right-skewed volume distribution is retrieved with the Classical system. Two filters are applied on the data coming from the classical counter. Applying the built-in Yumizen H2500 filter that consists in rejecting the pulses placed above the logarithmic function of Fig. 5.6A provides the distribution indicated as 'c-Log' in Fig. 5.7A. Case 'c-Log' is more symmetrical than 'c', but is still right-skewed. However, rejecting pulses having a width ratio ($\mathcal{R}$) below 52 % renders a perfectly symmetrical distribution, as depicted by case 'c-WR' in Fig. 5.7A.

The signal is treated an amplified differently between hydrofocused and classical systems. This explains the offset between the distribution obtained from the hydrofocused system (case 'hf') and distributions arising from the classical system (cases 'c', 'c-Log' and 'c-WR'). Hence, in order to provide a quantitative comparison between both systems, pulses amplitudes are calibrated before computing the probability density functions shown in Fig. 5.7B. More precisely, pulses maxima coming from the classical counter system are calibrated with $\overline{\Delta U_m}|_{bs}^{c}$ (ie. the averaged ΔU_m of case 'c-WR') and ΔU_m from the hydrofocused device are scaled with $\overline{\Delta U_m}|_{bs}^{hf}$ (the averaged ΔU_m of case 'hf'). As illustrated in Fig. 5.7A, $\overline{\Delta U_m}|_{bs}^{hf} \approx$ 2.25 V and $\overline{\Delta U_m}|_{bs}^{c} \approx$ 1.3V. The calibrated volume measurements are denoted by

$\widetilde{\Delta U}_m$. A good comparison is observed between hydrofocused and classical systems, provided that the $\mathcal{R}$ based filter is used.

Electrical pulses arising from the classical and the hydrofocused Coulter counters were recorded for 4 blood samples more. The electrical signals from these two systems were respectively calibrated with $\overline{\Delta U}_m|_{bs}^{c}$ and $\overline{\Delta U}_m|_{bs}^{hf}$, measured on the first blood sample and illustrated in Fig. 5.7A. In other words, the blood sample from wich distributions of Fig. 5.7A arise is used as a calibrator. Then, averages and standard deviations of $\widetilde{\Delta U}_m$ are calculated and referred as $mean(\widetilde{\Delta U}_m)$ and $std(\widetilde{\Delta U}_m)$. Note that the averaged $\widetilde{\Delta U}_m$ assesses the Mean Corpuscular Volume (MCV), while the standard deviation leads to the RBCs Distribution Width (RDW) when divided by $mean(\widetilde{\Delta U}_m)$. As discussed in Chap. 1, such haematological parameters (in particular the RDW) are essential for the diagnosis of various diseases [144].

Figure 5.8 shows the correlations of $mean(\widetilde{\Delta U}_m)$and $std(\widetilde{\Delta U}_m)$ between the hydrofocused system and the classical system for different applied filters. Regarding the averages (Fig. 5.8A), good Pearson correlation coefficients (R^2) are obtained for all cases ('c', 'c-Log' and 'c-WR'). Showing a R^2 of 0.99, the $\mathcal{R}$-based filter is nevertheless in better agreement with the reference than cases 'c-Log' and 'c', whose $R^2 = 0.96$ and $R^2 = 0.93$, respectively. Regarding the standard deviation, results show that unfiltered data from the classical counter is poorly correlated to the reference data from the hydrofocused system (see Fig. 5.8B, $R^2 = 0.6$). The correlation is improved with the logarithmic filter (see case 'c-Log' in Fig. 5.8B), but the original filter appears to better correlate with the hydrodynamical-focusing ($R^2 = 0.78$ for 'c-Log' and $R^2 = 0.92$ for 'c-WR').

In summary, the introduced $\mathcal{R}$ metric enables a filtering of pulses impacted by the edge-effects. After filtering, symmetrical volume distributions in agreement with the results from an hydrofocused Coulter counter are obtained. Besides, very good correlations are obtained with the hydrofocused system in terms of statistics, thus paving the way to an accurate assessment of haematological parameters with a simpler and cheaper implementation. A further study is intended to defined the optimal couple p_u/p_d, and the sensibility of the $\mathcal{R}$-based filter to such parameters.

5.3 Neural Network modeling for detecting particles rotation

Detecting the particle rotation from the pulse and excluding the pulse from the measurement statistics is shown to fix the right-skewed volume distribution obtained with classical Coulter counters. The detection is enabled by a simple metric computed from the pulse (see $\mathcal{R}$ in Sec. 5.2.1). With the aim of proposing an alternative to sort the pulses, a second method based on this principle is proposed in the following. The detection of rotations is allowed by a Neural Network (NN) that is trained with numerical data, as explained in Sec. 5.3.1. Then, in Sec. 5.3.2, NN results are compared with the $\mathcal{R}$ based filter previously introduced.

NNs are models built by combining simple mathematical objects called neurons

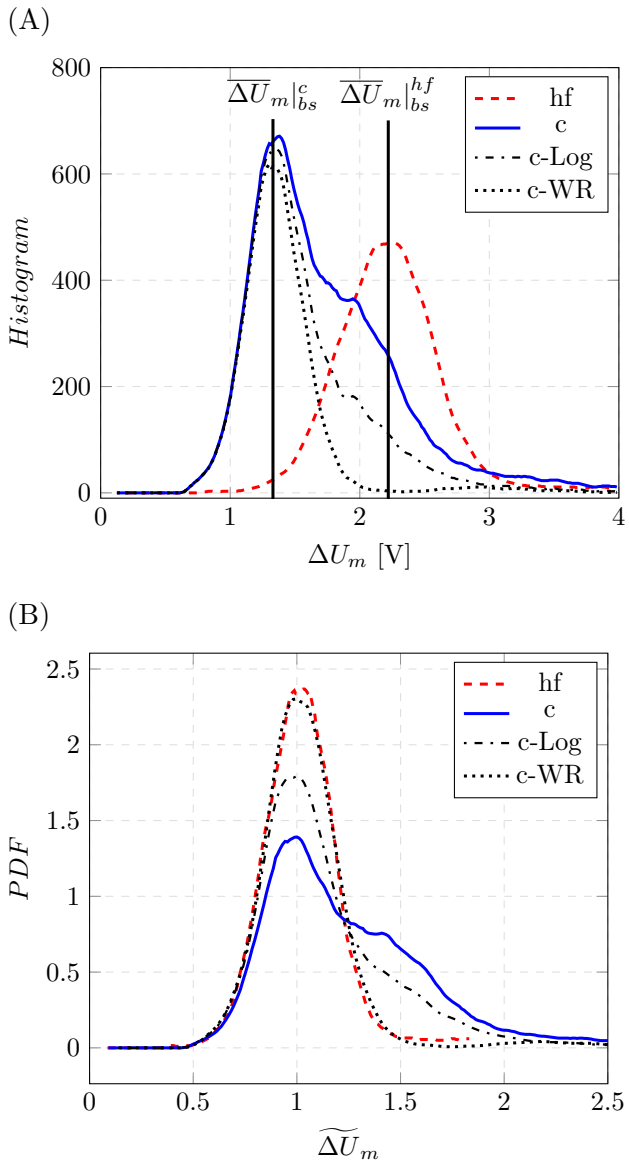

Figure 5.7 – Pulses maxima (ΔU_m) distributions depending on the system and the applied filter. (A) Histogram obtained from classical and hydrofocused Coulter counters are referred to 'c' and 'hf', while histograms obtained after applying the $\mathcal{R}$-based filter and the logarithmic filter on the classical system are denoted 'c-WR' and 'c-Log', respectively. The ΔU_m averages of cases 'c-WR' and 'hf' are referred to $\overline{\Delta U}_m|_{bs}^{c}$ and $\overline{\Delta U}_m|_{bs}^{hf}$ and highlighted by vertical black lines. (B) Probability density functions of the calibrated pulse maxima ($\widetilde{\Delta U}_m$). Pulses from the classical system are scaled with $\overline{\Delta U}_m|_{bs}^{c}$ while pulses from the hydrofocused counter are scaled with $\overline{\Delta U}_m|_{bs}^{hf}$.

(A)

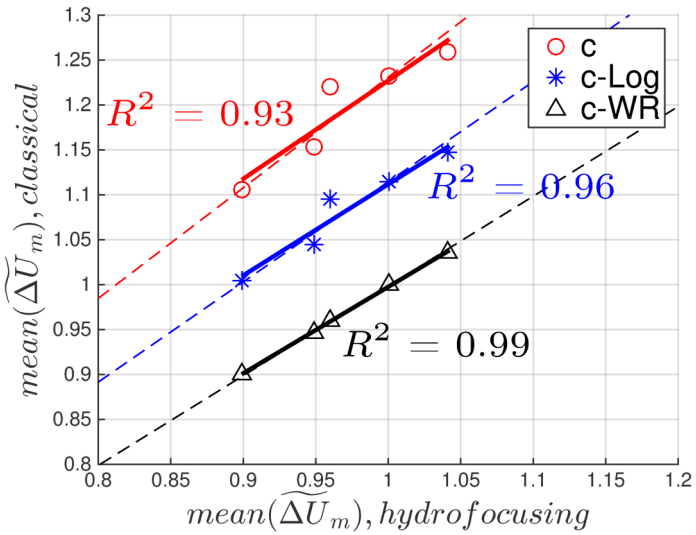

(B)

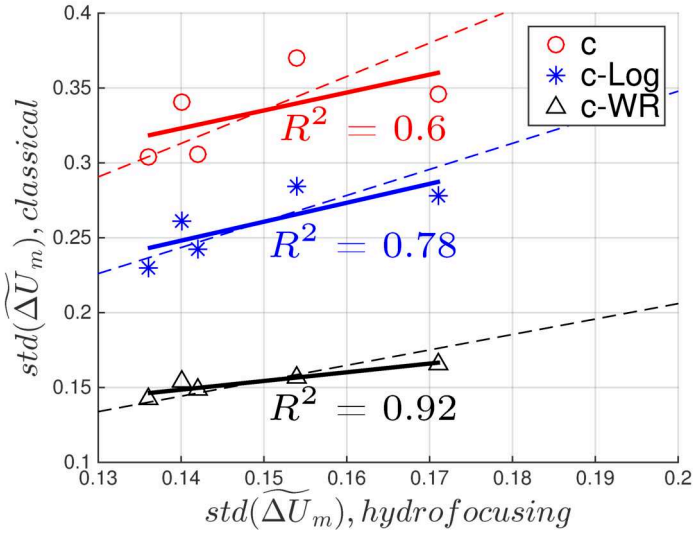

Figure 5.8 – Correlations of hematological parameters between the classical Coulter counter and the hydrofocused Coulter counter, depending on the applied filter. Correlations of averages and standard deviations are shown in (A) and (B), respectively.

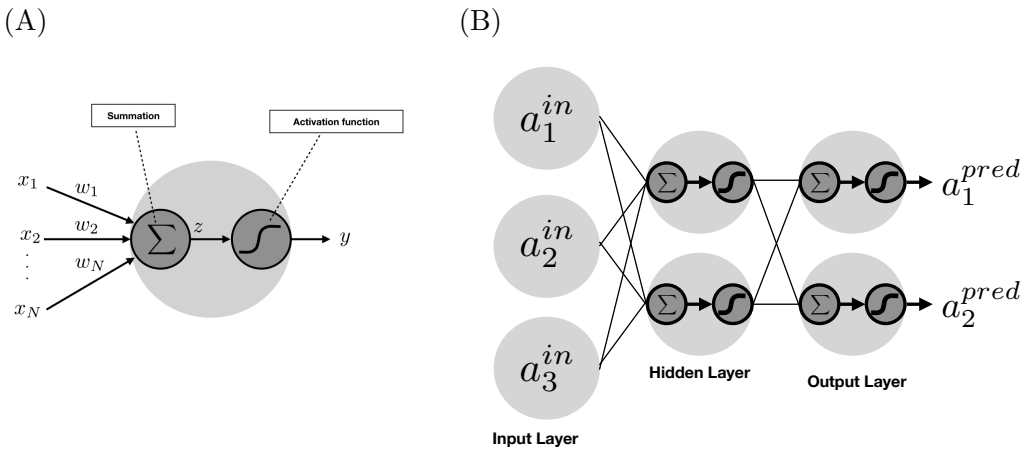

Figure 5.9 – (A) Principle of an elementary neuron that computes y from a given number of inputs x_i. (B) Illustration of a simple Neural Network (NN).

(see Fig. 5.9A). Given a number N of inputs x_i, it computes z, the sum of x_i weighted by parameters w_i:

$$z = \sum_{i=1}^{N} x_i w_i \tag{5.3}$$

Then, an activation function f_a is applied to the weighted sum z, that leads to the neural output y:

$$\begin{aligned} y &= f_a(z) \\ &= f_a\left(\sum_{i=1}^{N} x_i w_i\right) \end{aligned} \tag{5.4}$$

The combination of these elementary neurons enables the construction of complex and non-linear models. As illustrated in Fig. 5.9B, neurons are generally organised in layers: neurons are connected to each elements of the preceding and following layers. Such a NN structure is commonly called Multi-Layer Perceptron (MLP). Given a problem that consists in predicting $a^{pred} \in \mathbb{R}^{N_o}$ from $a^{in} \in \mathbb{R}^{N_i}$, the latter ($a^{in}$) is given as an income to the input layer. Then, a^{in} is propagated in the NN until the output layer, that yields the model prediction a^{pred}. In this respect, the input and output layers must contain N_i and N_o neurons, respectively. Hence, NNs may handle problems of arbitrary dimensions. Furthermore, provided the number of neurons is sufficient, NNs were proven to approach any continuous functions in a compact subset of space [22, 66]. From a database composed of couples a^{in}/a^{obs}, the model weights w are learned in such a way the NN predicts a^{pred} the closest to a^{obs}, given the corresponding a^{in}. This is done with a gradient descent method. (1) A a^{in} associated to a^{obs} is drawn randomly from the training database, and given to the MLP for assessing a^{pred}. Given a^{obs} and a^{pred}, the loss function F_L rates the prediction error. (2) The gradients of F_L with respect to the model weights are computed and used for enhancing the model. (3) A new couple a^{in}/a^{obs} is chosen and the procedure is repeated from step 1. Note that this procedure update the

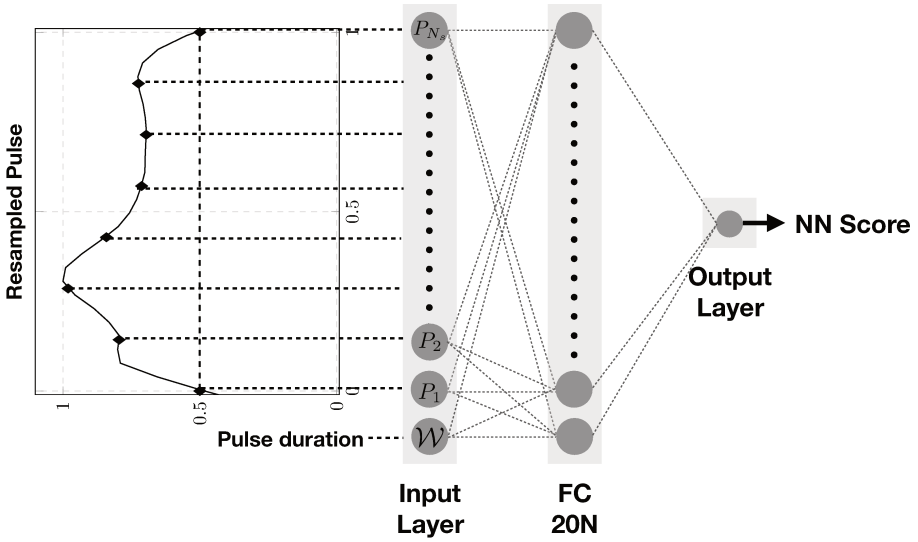

Figure 5.10 – Neural Network architecture used for detecting the particle rotation from the electrical pulse. The hidden layer is Fully-Connected (FC) to input and output layers and contains 20 Neurons (20N).

model parameters once for each couple a^{in}/a^{obs}. In practice, the training database is split in several batches (groups of pairs a^{in}/a^{obs}) that are treated at the same time for upgrading the model. All batches are employed for the weights updating in a training iteration commonly called 'epoch'. Generally, several epochs are required for the model to converge to an optimum. For a more detailed introduction to NNs, readers are referred to App. C.1.

5.3.1 Model description

The modelling is performed with a MLP whose architecture is shown in Fig. 5.10. It is composed of a single hidden layer and all activation functions of the model are sigmoid functions. The MLP takes an electrical pulse as input to predict whether the cell has undergone a rotation. In the following, we detail how input and output layers are designed to tackle this clustering problem. Then, the training step of the model from numerical data is presented.

NN Input Layer

Electrical pulses are temporal sequences whose sampling is monitored by a given time step (typically 1 μs). However, signals durations depend on the trajectory, so that pulses may be described with temporal series of variable sizes. For example, a long pulse like case 10 is described with more points than a shorter one like case 1 (see Fig. 5.3). This makes pulses unprocessable by the MLP because the input layer must have a specific size. This section describes the pulse treatment applied to address this issue.

Overcoming this problem is done by scaling the pulse with a pulse width ($\mathcal{W}$) (see Eq. 3.3) before resampling the signal with a series of N_s points. Figure. 5.11

illustrates the full strategy when applied to cases 1 and 10, from simulations. Information about the particle rotation is expected to be in the pulse shape but not in the pulse amplitude. This is why the choice was made to scale the electrical print by its maximum, as shown in Fig. 5.11A. Then, using a threshold of $0.5 \times \Delta R_m$, pulses widths $\mathcal{W}^1$ and $\mathcal{W}^{10}$ are computed for cases 1 and 10, respectively (see Fig. 5.11A). Once scaled in both amplitude and time, cases 1 and 10 may be represented as in Fig. 5.11B. Note that the part of $\Delta R/\Delta R_m$ above 0.5 is placed between $t/\mathcal{W}(\frac{\Delta R_m}{2}) = 0$ and $t/\mathcal{W}(\frac{\Delta R_m}{2}) = 1$, for the sake of convenience. Then, pulses are sampled with N_s points between $t/\mathcal{W}(\frac{\Delta R_m}{2}) = 0$ and $t/\mathcal{W}(\frac{\Delta R_m}{2}) = 1$. In this manner, cases 1 and 10 lead to '1 sampled' and '10 sampled', as shown in Fig. 5.11B.

Once treated, the pulse is described with a series of N_s values of $\Delta R/\Delta R_m$, denoted as P_i in Fig. 5.11C ($i \in [1\ ,\ N_s]$). This set of P_i is taken as the input of the NN. Furthermore the time during which the pulse is higher than a threshold is intended to provide relevant indications on the trajectory, which itself has been shown to drive the rotation undergone by particles (see Fig. 4.11A). Therefore, $\mathcal{W}(\frac{\Delta R_m}{2})$ is given as an input parameter, in addition to the set of P_i. In the table shown in Fig. 5.11D, the input values related cases 1 and 10 are shown in the 'input' column (for $N_s = 8$). This way, cases 1 and 10 are represented with the same number of variables ($N_s + 1$) while they are of different lengths initially. A drawback of this method is that short pulses are better described than longer ones. This implies the choice of a sufficiently large N_s to properly characterize the longest pulses. In practice, $N_s = 20$ will be used in the following sections.

This treatment is illustrated for numerical resistive pulses ΔR in Fig. 5.11 but the process remains valid for experimental tension pulses ΔU. Furthermore, the choice of scaling the pulse by its maximum was also motivated by the aim of designing a NN suited for experimental data, while it is trained from a numerical database.

NN output layer

The output layer is composed of a single neuron that renders the model prediction: did the cell undergo a rotation in the aperture or not? From a mathematical point of view, these two options constitute a binary choice that is translated by either 0 or 1, respectively. As shown in Fig. 5.1A, in case 1, the RBC does not rotate in the aperture, so that an output value of 1 is associated with case 1, as shown in Fig. 5.11D (see column 'Output'). In contrast, case 10 is associated with an output value of 0 because the RBC rotates in the orifice, as depicted in Fig. 5.1B.

As it was shown in Fig. 5.4C, a smooth transition in θ_m exists between cells that do not rotate at all and cells that can reach an orientation θ_m of $\pi/2$. Consequently, it is choosen to set an output of 1 if $\theta_m < 0.3$ rad and a value of 0 if $\theta_m > 0.3$ rad. This is represented as an horizontal line in Fig. 5.12A, which shows θ_m as a function of D for the database considered in the following (discussed in the next section).

Remind that the activation function used for all neurons is the sigmoid function. This is why the model is unable to give back a strict value of 0 nor 1 but renders a score included in [0 , 1] (due to the definition of the sigmoid function). Hence the clustering must be done by thresholding the NN score. A threshold of 0.5 on the

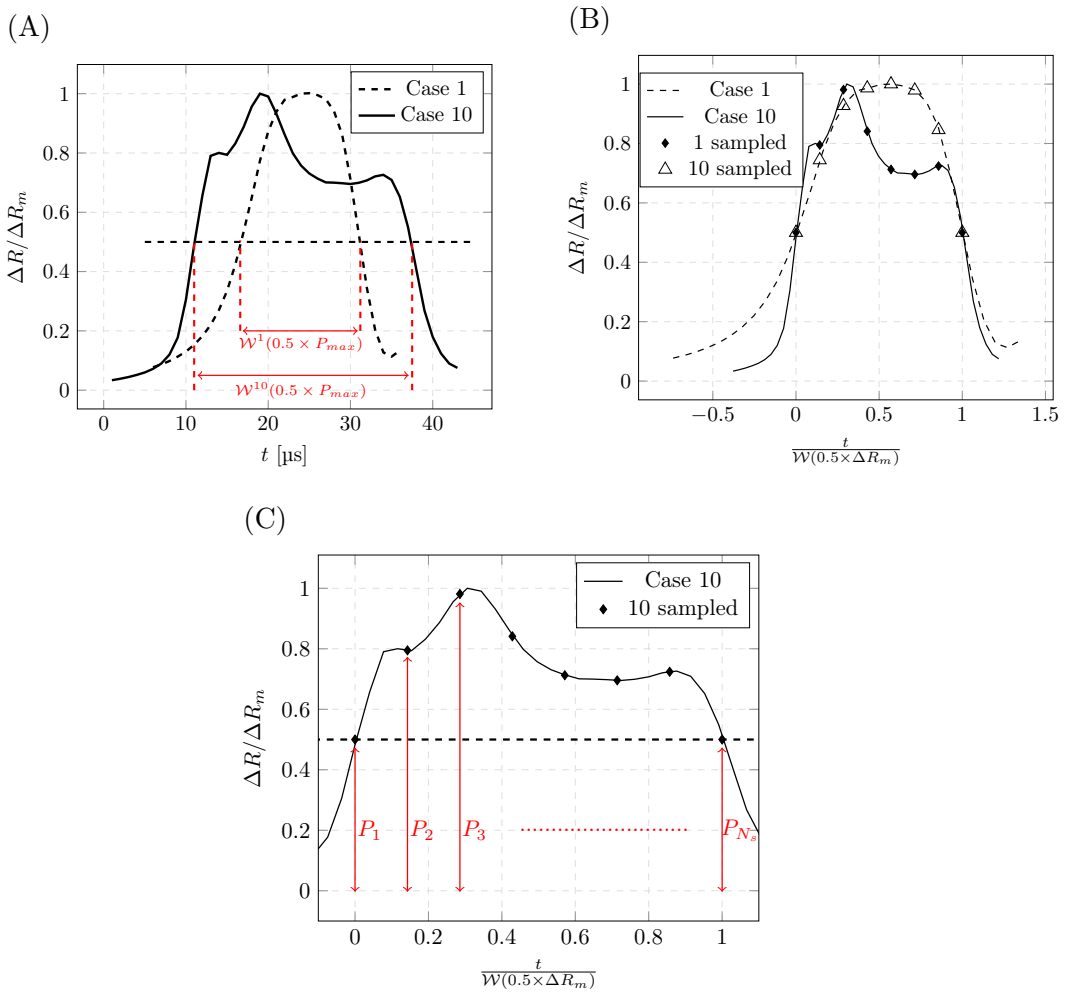

(D)

	Input									Output
Case	Sampling: P_1, ... , P_{N_s}								$\mathcal{W}(\frac{\Delta R_m}{2})$ [μs]	θ_m>0.3
1	0.5	0.74	0.93	0.99	1.0	0.97	0.84	0.5	14.4	1
2	0.5	0.8	0.98	0.84	0.71	0.69	0.72	0.5	26.3	0

Figure 5.11 – Treatment applied to pulses in order to make them readable by the MLP of Fig. 5.10. The process is illustrated for two different pulses predicted by numerical simulations (cases 1 and 10). (A) Pulses are first scaled by their maximum (ΔR_m). (B) The timescale is divided by the metric $\mathcal{W}$, computed with a threshold of 0.5 (see picture A). This is equivalent to calculate $\mathcal{W}$ with a of $0.5 \times \Delta R_m$ on the original pulse (ie. before it is scaled by ΔR_m). Note that for the sake of clarity, the part of the pulse that is above 0.5 is represented between 0 and 1. (C) The pulse is then resampled as a series of N_s P_i between 0 and 1. (D) The MLP of Fig. 5.10 takes as input the series of P_i amplitudes (i $\in \{1 ; 2 ; ... ; N_s\}$) in addition to the associated $\mathcal{W}$ (see input column, $N_s = 8$ in this example). The output associated with the pulse depends on whether θ_m is greater or lower than 0.3 rad (see output column). Note that the treatment is illustrated for a resistive pulse from simulation, but the procedure is applicable for tension experimental pulses.

NN score is an intuitive way to doing that for instance. Note that considering a score between 0 and 1 assesses the sharpness of the model decision-making (viz. if the NN is sure about its classification or not).

Numerical database

The numerical database involved in this modelling is composed of 85 simulations and their associated pulses. More precisely, it is composed by cases 1-85 of Tab. D.1 (see App. D). The streamline monitoring the particle trajectory varies in a range covering the major part of the aperture. It is defined by the scalar r_a (see Tab. D.1) that is related to the point (0, r_a, 0) from which the streamline is extracted. Moreover, the shear modulus G_s, the internal viscosity ν_{in}, the reduced volume $\mathcal{Q}$ and the cell volume were varied during the database building. This is done to make the model robust with respect to changes in the RBC properties.

Cases 1-85 of Tab. D.1 are represented in a scatter graph of θ_m according to D in Fig. 5.12A. The database is split into a 'training dataset' and a 'test dataset'. The 'training dataset' is used for updating the NN weights during the training step, while the 'test dataset' is only employed for assessing the model accuracy. More precisely, the 'test dataset' is made up of cases 2-21, of Tab. D.1 (see Appendix. D). The target value is set according to the condition on θ_m, as discussed in the previous section. Figures. 5.12B and C show cases that have a target value of 1 and 0, respectively (viz. $\theta_m < 0.3$ rad and $\theta_m > 0.3$ rad). Note that pulses are treated as detailed in Fig. 5.11 by using $N_s = 20$.

Training of the Neural Network

The NN illustrated in Fig. 5.10 is built by means of TensorFlow (https://www.tensorflow.org/). The model weights are updated with the ADAM method [81] which is a variant of the classical descent gradient method. In particular, error gradients are calculated with the back-propagation method presented in App. C. Furthermore, the loss function to minimize is the Root Mean Square (RMS) error. The training procedure is performed over 10 000 epochs (number of iterations, see App. C) with a batch size that equals the 'training dataset' size.

In the **right** column of Fig. 5.13 are shown NN scores against θ_m for different epochs of the training. The epoch is indicated by the vertical line shown in the graph of the **left** column (see Fig. 5.13), which depicts the evolution of the RMS error according to the training epoch. In the first epoch, the NN score is almost constant but rapidly takes a sigmoid-like profile according to θ_m (see first and second rows of Fig. 5.13). At epoch 4000, $\theta_m < 0.3$ and $\theta_m > 0.3$ are already separated by a threshold of 0.5 on NN score. As the model learning progresses, the transition in NN scores occurring around 0.3 rad becomes steeper. For instance, at the end of the NN training (epoch 10 000), NN scores between 0.95 and 1.0 are observed for $\theta_m <$ 0.3 rad, while NN scores between 0.0 and 0.05 are obtained when $\theta_m > 0.3$ rad.

Note that the 'test dataset' depicts the same trend than the 'training dataset', for all epochs of the training. This supports the fact that no overfitting takes place during the model training. As well, the error made on the 'test dataset' decreases

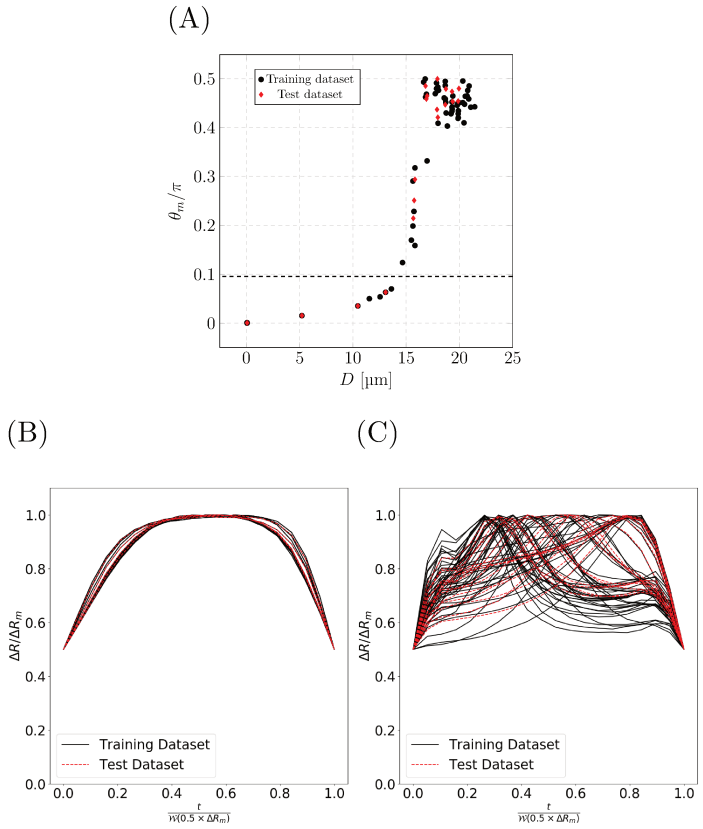

Figure 5.12 – Representation of the database used for training the MLP. Picture (A) display θ_m according to D for the training and test datasets. In (B) and (C), are shown pulses for which θ_m is greater and lower than 0.3 rad, respectively.

Confusion Matrix	$\theta_m < 0.3$ rad	$\theta_m > 0.3$ rad
NN Score > 0.5	5	0
NN Score < 0.5	0	15

Table 5.1 – Confusion matrix on the test dataset obtained by applying the MLP of epoch 10000.

during the whole training in a way similar to the error on the 'training dataset'. Reminding that the 'test dataset' is not used for updating the NN, one may conclude that the model successfully learned the problem. The confusion matrix assessed for the 'test dataset' in Tab. 5.1 emphasise this point by showing a perfect clustering of $\theta_m < 0.3$ and $\theta_m > 0.3$ with a threshold of 0.5 on NN score. The model of epoch 10 000 was used for assessing Tab. 5.1.

A robustness test was also performed by changing the test dataset. By defining cases 22-24, 26-31, and 33-38 (see Tab. D.1) as the 'test dataset' and the remaining cases included in 1-85 as the 'training dataset', the model was shown to converge and similar results were obtained (not shown).

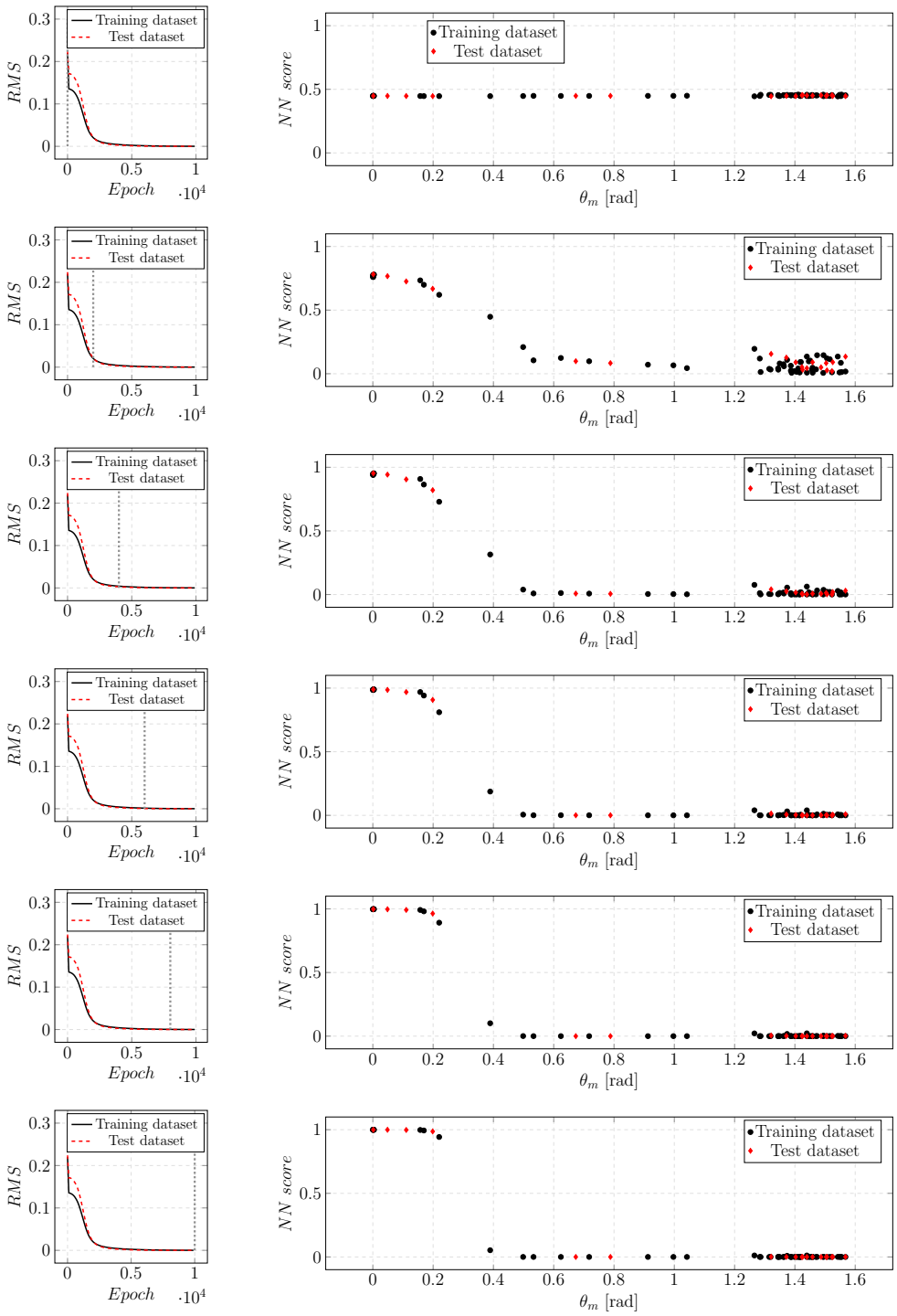

Figure 5.13 – Evolution of the MLP predictions (ie. NN score) according to θ_m, during the training step (**Right** graphs). **Left** pictures illustrate the considered epoch as a vertical line over the graph showing the RMS error against the training epoch. The six rows correspond to epochs 0, 2000, 4000, 6000, 8000 and 10000, from the top-down.

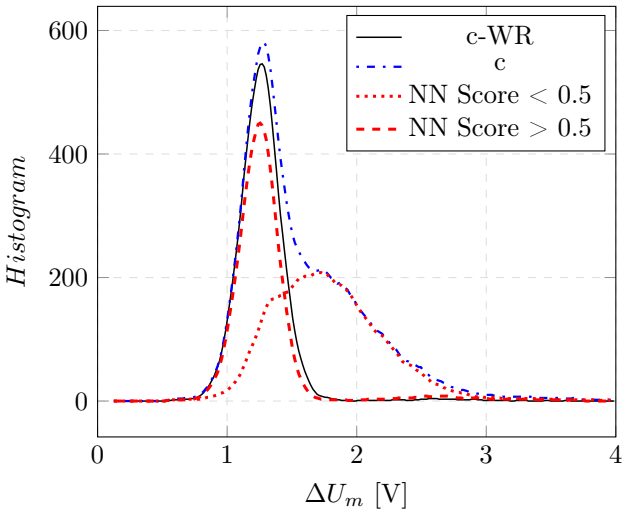

Figure 5.14 – Distributions obtained on an experimental pulses acquisition. Distributions shown refer to the entire acquisition 'c', the part of the acquisition for which $\mathcal{R} > 52$ ('c-WR'), and parts of the acquisition that shows a NN score above and below 0.5.

5.3.2 Comparison with the Width Ratio based filter

Concerning pulses predicted by numerical simulations, the NN has been shown to detect accurately the cell rotation (see Tab. 5.1). However, numerical data are not plagued with experimental errors and noise. Hence, there is a need for assessing the model accuracy in the case of experimental data. In this section, the $\mathcal{R}$-based filter of Sec. 5.2 is compared with the NN model of Sec. 5.3.1.

The experimental pulses coming from the analysis of the blood sample of Chap. 4 (see Sec. 4.3.2) are treated as done in Fig. 5.11 and given to the NN of epoch 10 000 for assessing the NN scores. Applying a threshold of 0.5 to the NN scores leads to two pulse populations. The ΔU_m histograms for these two populations and for the whole set of pulses are depicted in Fig. 5.14. Note that 'c' denotes the distribution arising from the entire acquisition, without filtering. Besides, the ΔU_m histogram obtained after applying the $\mathcal{R}$-based filter of Sec. 5.2 is shown for comparison (see 'c-WR' in Fig. 5.14). For the entire population (case 'c'), the typical right-skew distribution is again shown, while thresholding NN scores enables a symmetrical ΔU_m distribution. Pulses with a peak of rotation that yields an overestimation of the cell volume are well sorted and are gathered in the distribution of NN scores below 0.5. This is supported by higher values of ΔU_m recovered for case 'NN score < 0.5' compared to 'NN score > 0.5'. Although both 'NN score > 0.5' and 'c-WR' depict symmetrical distributions, the MLP seems more restrictive. Indeed, fewer pulses meet the 'NN score > 0.5' requirement than 'c-WR'. More precisely, the $\mathcal{R}$-based filter conserves around 55 % of the pulses while only 45 % of the whole acquisition is retained with the NN.

We now analyse the sorting with respect to different metrics of the pulses (their width, peak position, width ratio). Figure 5.16A and B show scatter plots of $\mathcal{W}^r$ as a function of $\mathcal{P}^r$ by coloring in blue the points that are related to pulses for which $\mathcal{R}$

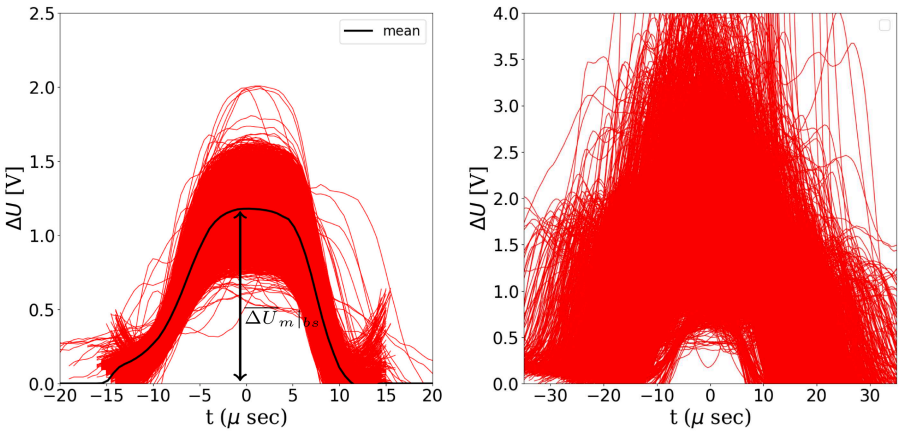

Figure 5.15 – Bell-shape signatures extracted from an experimental pulse acquisition by means of the NN filter: NN score > 0.5 (see **left** picture). The averaged signature is represented with a bold continuous black line, and $\overline{\Delta U}_m|_{bs}$ is illustrated with the double arrow. The **right** plot displays the remaining of the acquisition (viz. pulse for wich NN score < 0.5).

> 52 % and NN score > 0.5, respectively. The numerical results of Fig. 5.3 are also displayed in order to indicate the associated trajectories. Remind that $\mathcal{W}^r$ and $\mathcal{P}^r$ correspond to metrics $\mathcal{W}$ and $\mathcal{P}$ but computed from a threshold relative to $\Delta R_m|_{bs}$ or $\overline{\Delta U}_m|_{bs}$, whether a numerical or experimental pulse is considered, respectively. $\Delta R_m|_{bs}$ equals the maximum of case 1 in Fig. 5.3 while $\overline{\Delta U}_m|_{bs}$ is calculated as the averaged maximum of the 'bell-shaped' signatures, from the considered experimental acquisition. The extraction of 'bell-shaped' pulses for calculating $\overline{\Delta U}_m|_{bs}$ is allowed by the $\mathcal{R}$-based filter or the NN model (see Fig. 5.15). This convention was indispensable for comparing simulation and experimental results in former chapters (Chap. 3 and Chap. 4). An overview on all these quantities related to electrical pulses is given in App. E.

The $\mathcal{R}$-based filter seems to retain pulses generated by RBCs following trajectories between case 1 and case 5 (see blue points in Fig. 5.16A). More restrictively, the NN is shown to be limited to trajectories in between cases 1 and 4 (see Fig. 5.3 and Fig. 5.16B). This explains the fewer number of pulses accounted in case 'NN score > 0.5' compared to case 'c-WR in distributions of Fig. 5.14.

A better view of the differences between the two methods (viz. the $\mathcal{R}$ based filter and the NN) is provided by plotting $\mathcal{R}$ against $\mathcal{P}^r$, as done in Fig. 5.16C and D. Again, pulses whose $\mathcal{R}$ is above 52 % and NN whose score is higher than 0.5 are colored in blue in Fig. 5.16C and D, respectively. By representing the acquisition on a $\mathcal{R}/\mathcal{P}^r$ graph, the population for which $\mathcal{P}^r$ is around 80% is scattered in terms of $\mathcal{R}$ while it is concentrated along the $\mathcal{W}^r$ axes in a $\mathcal{W}^r/\mathcal{P}^r$ scatter plot. This highlights the transition between cases 4 and 6. As a reminder, the RBC slightly rotates in case 4, whereas it achieves a $\pi/2$ orientation in the orifice when considering case 6 (see Fig. 4.11A). Hence, by comparing Fig. 5.16C and D the conclusion that the NN is more sensitive to cells rotations is drawn. This is likely due to the fact that a condition of $\theta_m < 0.3$ rad is more restrictive than thresholding $\mathcal{R}$ to 52 %, in terms

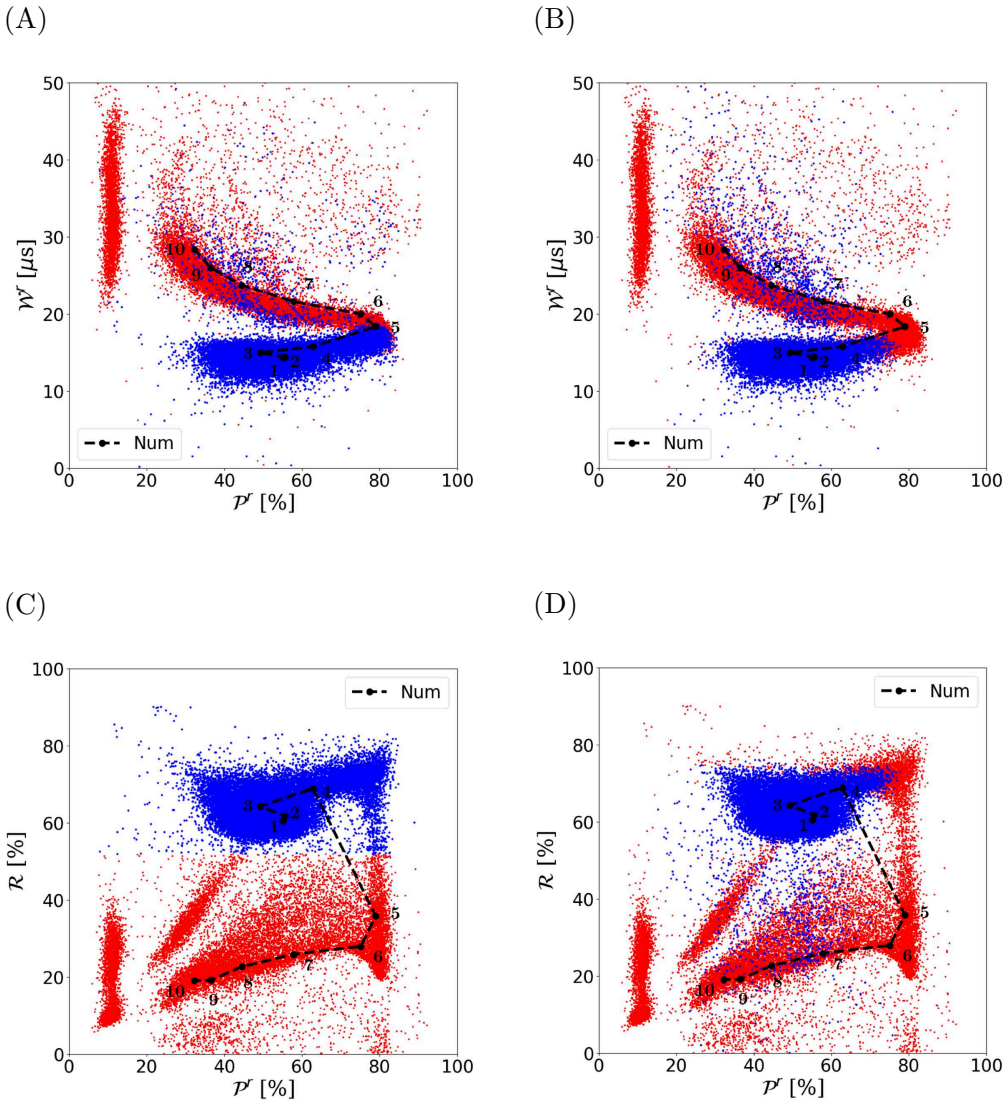

Figure 5.16 – Comparison of the $\mathcal{R}$ based filter and the NN filter on bi-dimensional representations of an experimental acquisition. Numerical results of Chap. 4 are also shown, which gives an idea on the pursued trajectories. The numbers shown in these graphs are related to the different cases of Fig. 5.3. Note that the same experimental acquisition used in Chap. 4 is considered in these graphs. **Top** row (A and B) graphs $\mathcal{W}^r$ against $\mathcal{P}^r$, while the **bottom** row (C and D) illustrates $\mathcal{R}$ according to $\mathcal{P}^r$. In graphs of the **left** column, pulse for which $\mathcal{R} > 52$ are highlighted in blue. In pictures of the **right** column, pulses for which NN score > 0.5 are colored in blue. The dimensionless threshold involved in the calculations of $\mathcal{W}^r$ and $\mathcal{P}^r$ is set to 0.5, as in Chap. 4.

of measurements errors (see Fig. 5.4).

5.4 Conclusion

In classical Coulter counters, errors in the assessment of the particle volumes may occur because of the edge-effects. This edge-effects overestimate the cell volume, thus leading to a right-skewed volume distribution. Hydrodynamical-focusing enforces centered trajectories of cells, removes the edge-effects and allows a Gaussian distribution. However hydrofocused systems are more expensive and complex in terms of implementation. This is why classical Coulter counters with methods aiming at filtering the edge-effects are still employed in haematological automata. Actually, the development of filtering strategies was limited by the lack of knowledge on the edge-effect and the expected Gaussian distributions are not obtained. Based on new insights provided by numerical simulations of RBCs in a classical Coulter counter, filtering methods were proposed in the present chapter. This original family of methods consists in detecting and rejecting from the analysis the pulses subjected to a cell rotation in the sensing region. Two examples for detecting the cell rotation were given, and both were shown to provide a Gaussian volume distribution. In a first method, a metric is used to isolate the 'bell-shaped' pulses (suited for measuring the volume) from pulses presenting a peak of rotation. This metric is defined as the ratio of two widths computed from the pulse and denoted by $\mathcal{R}$. In the second method, a NN is trained from a numerical database. More precisely, it is trained to reject pulses generated by RBCs that reach at least 0.3 rad in the micro-orifice.

The choice of parameters p_u and p_d required for $\mathcal{R}$ may likely be optimized for providing a better sorting. A further study on the impact of these parameters on the $\mathcal{R}$-based filter is intended in the near future. Note that the two proposed methods would be simple of implementation in current automata, in particular the $\mathcal{R}$-based filter.

Chapter 6

Towards a more complete characterization of RBCs by impedance measurement

Chapter contents

Classically, a Coulter counter is used to count the cells, and measure their size, yielding for the RBC population the mean corpuscular volume (MCV) and the RBCs distribution width (RDW). However, we have shown that non-hydrofocused counters measure an apparent volume, which is reliable only if cells pass close to the aperture axis. The pulses associated with cells passing close to the aperture wall are more difficult to interpret. Their amplitude is not only proportional to the volume but also depends on the cell dynamics. A hydrofocused counter would eliminate such pulses and provide a robust volumetry measurement. However, cells properties determine their dynamics underflow: instead of seeing the near-wall behaviour as a bias on the volume measurement, one may use non-hydrofocused counters to infer more RBCs properties than just their size.

Indeed, it is well-known that RBCs properties are affected by numerous pathologies (malaria, spherocytosis, elliptocytosis, sickle cell, thalassemia). Measuring sev-

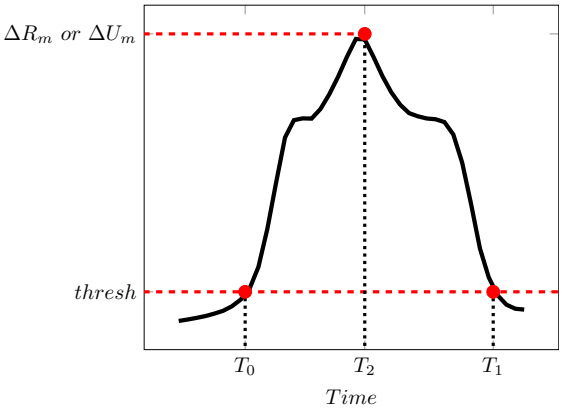

Figure 6.1 – Sketch of T_0, T_1 and T_2 calculus.

eral thousands of RBCs in routine exams may thus provide the physician with valuable information about the health of the patient. This exploratory chapter deals with the assessment of RBCs morphological and mechanical information from impedance pulses. Detecting abnormal pulses that could be generated by pathological cells implies the definition of standard impedance pulses (viz. the results which can be expected from healthy people). A normal (healthy) exam from a non-hydrofocused Coulter counter is thus defined in a first step. Then, by affecting the RBCs in an experimental approach, it is shown that results out of the normality ranges are obtained. This chapter ends with a preliminary study of the inverse problem of numerical simulations of Chap. 4. In particular, a NN assessing some of the RBCs parameters (shear modulus, internal viscosity ...) from the corresponding pulse is presented.

6.1 Defining the normality on a given system

Hereafter, several blood samples collected from healthy patients are analysed to define the normality of impedance signals. The normality is observable in a qualitative way on proper representations or may be assessed quantitatively by observing directly the pulses signatures and assessing their relative proportions. In the following, the pulses normality for an ABX Micros 60 is presented. Note that the normality would depend on the device and must be defined for each automaton.

6.1.1 Summary of the introduced pulses representations

In industrial counters, the pulse characterization is reduced to the assessment of their maxima (ΔU_m) and their duration ($\mathcal{W}$). The logarithmic filter currently implemented in Yumizen H2500 and ABX Micros 60 (see Sec. 5.2.2) is a perfect example of existing treatments applied to impedance pulses: it is only based on ΔU_m and $\mathcal{W}$. New insights, supplied by numerical simulations, led to the introduction of original metrics: $\mathcal{R}$ that measures the peak of rotation and $\mathcal{P}$, that indicates the moment at which the peak occurs in the pulse. As a reminder, $\mathcal{W}$ and $\mathcal{P}$ are expressed as

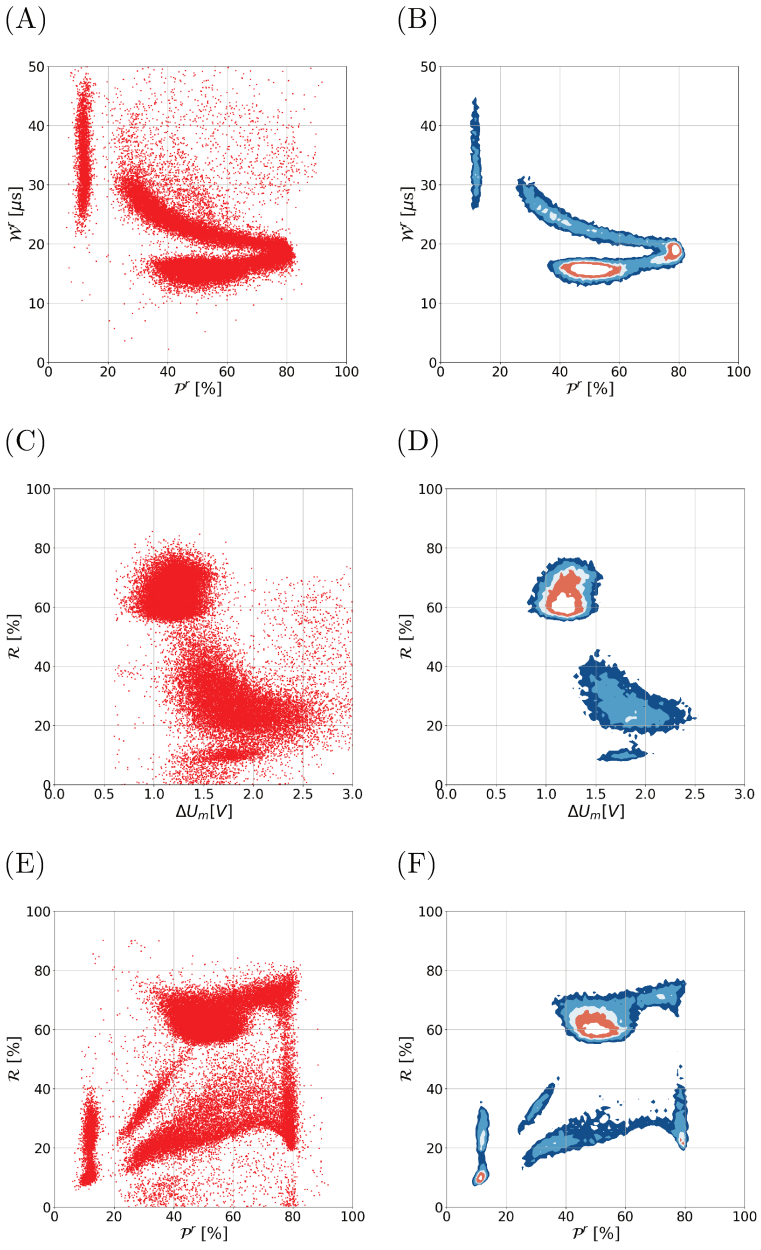

Figure 6.2 – Pulses representations introduced in the framework of this thesis. The **left** column shows the classical scatter plots while the **right** column shows the density contours. The retained density iso values are: 0.00025, 0.0005, 0.001, 0.0015, 0.0025. Metric $\mathcal{R}$ is calculated with $p_u = 7/8$ and $p_d = 1/2$, while $\mathcal{W}^r$ and $\mathcal{P}^r$ are computed by using a threshold of 0.5.

follow:

$$\mathcal{W}(thresh) = T_1 - T_0, \tag{6.1}$$

$$\mathcal{P}(thresh) = \frac{T_2 - T_0}{T_1 - T_0} \times 100, \tag{6.2}$$

in which instants T_0, T_1 and T_2 are defined as in Fig. 6.1. Besides, $\mathcal{R}$, that is defined as a width ratio reads:

$$\mathcal{R} = \frac{\mathcal{W}(p_u \times \Delta U_m)}{\mathcal{W}(p_d \times \Delta U_m)}, \tag{6.3}$$

with p_u and p_d being user-defined parameters defined so that: $0 < p_d < p_u < 1$.

Thresholding a pulse with absolute value as done in the computation of $\mathcal{W}$ and $\mathcal{P}$ makes the results dependent on the cell volume. Hence, in order to provide comparisons between different samples, it is preferable to scale the pulses with the mean amplitude of 'bell-shaped' signatures $\overline{\Delta U}_m|_{bs}$ (known as a robust measurement of the mean cell volume MCV), before calculating $\mathcal{W}$ and $\mathcal{P}$. Computing $\mathcal{W}$ and $\mathcal{P}$ in such a way makes them relative to the MCV, thus they are denoted by $\mathcal{W}^r$ and $\mathcal{P}^r$, for the sake of clarity. In other words, $\mathcal{W}^r$ and $\mathcal{P}^r$ writes:

$$\mathcal{W}^r(thresh') = \mathcal{W}(thresh' \times \overline{\Delta U}_m|_{bs}), \tag{6.4}$$

and

$$\mathcal{P}^r(thresh') = \mathcal{P}(thresh' \times \overline{\Delta U}_m|_{bs}), \tag{6.5}$$

Illustrated in App. E, this convention was used in former chapters for comparing numerical results with experimental data. Notice that this is not required for $\mathcal{R}$ that involves thresholds defined as percentages of the pulse maximum ΔU_m.

Based on these metrics, informative representations of the acquisitions are allowed, as illustrated in Fig. 6.2. Plotting $\mathcal{W}^r$ against $\mathcal{P}^r$ (Fig. 6.2A and B) was shown to organize pulses according to their trajectory in Chap. 4. Combining $\mathcal{R}$ and ΔU_m in a scatter plot highlights volume overestimations, and allows a filtering aiming at avoiding sizing errors (Fig. 6.2C and D). Finally, scatter plots of $\mathcal{R}$ against $\mathcal{P}^r$ (Fig. 6.2E and F) reveal the intermediate rotation dynamics in the aperture (viz. from trajectories related to small rotations in the orifice to the first trajectory on which particles may reach $\pi/2$ rad in the aperture). The representations of Fig. 6.2 are typical of healthy blood samples, but for the sake of concision, comparisons with other healthy blood samples are not shown.

6.1.2 Normality of pulses signatures

The purpose of this section is to evaluate the reproducibility of electrical signatures when healthy blood samples are considered. From graphs $\mathcal{W}^r/\mathcal{P}^r$ (see Fig. 6.2A and B), specific pulses signatures can easily be extracted, as stated in Chap. 4.

By analyzing 22 blood samples coming from healthy patients by the use of ABX Micros 60, graphs similar than Fig. 6.2 are obtained. For each acquisition, the procedure detailed in Chap. 5 ($\mathcal{R}$-based filter) is used to extract the 'bell-shaped' population and compute $\overline{\Delta U}_m|_{bs}$, the mean of their maxima. Then, metrics $\mathcal{W}^r$ and $\mathcal{P}^r$ are assessed for each pulse. Specific boxes on the $\mathcal{W}^r/\mathcal{P}^r$ representation are then used to extract typical pulse signatures from the acquisition. Figure 6.3 shows

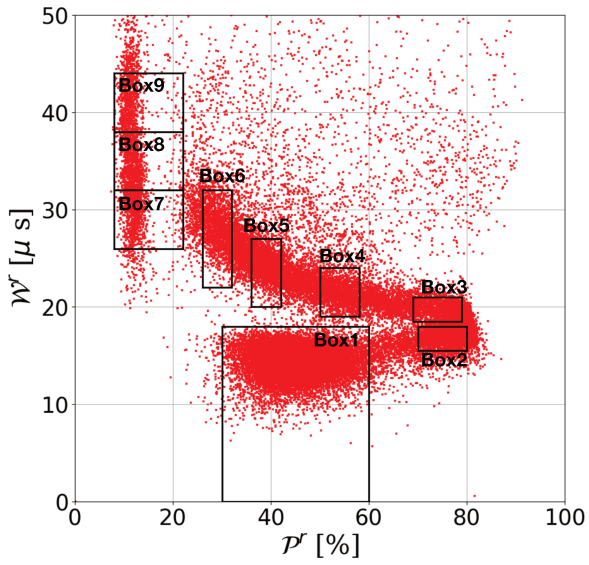

Figure 6.3 – Illustration of boxes employed for the extraction of pulse signatures, shown over the scatter graph $\mathcal{W}^r/\mathcal{P}^r$ for a healthy blood sample. A threshold of 0.5 is used for computing $\mathcal{W}^r$ and $\mathcal{P}^r$, according to Eq. 6.4 and 6.5.

the position of the chosen boxes, which were chosen after comparison of the results associated to numerous samples. Of course, this is only one example of a relevant set of boxes to sample the full measurement. Given a box of Fig. 6.3, pulses are extracted and the average pulse is calculated as illustrated in Fig. 6.4.

A comparison box by box of the mean pulses coming from the 22 acquisitions is presented in Fig. 6.5 (shown in black continuous lines). Note that each pulse is scaled in amplitude by $\overline{\Delta U}_m|_{bs}$ arising from the acquisition to which it belongs: the pulse that is expressed by a function of time $\Delta U(t)$ leads to $\Delta U^*(t) = \Delta U(t)/\overline{\Delta U}_m|_{bs}$. These comparisons support the reproducibility of pulses signatures from a healthy sample to another. Whatever the box, the average pulse from healthy samples are very similar, thus defining a 'normal' pulse expected for a healthy patient. A pulses normality can be defined, thus opening the way to the detection of abnormalities.

6.1.3 Pulses statistics

Indications provided by pulses signatures can be supplemented by their respective statistics. In particular, the pulses proportion in each box is evaluated for the 22 samples and the results are summarized in Fig. 6.6. Assessments on the 22 healthy samples are represented as bars in Fig. 6.6 while error margins are defined as twice the standard deviation. Almost one-half of the acquisition is located in box1 (around 45 %),which corresponds to central trajectories, while the remaining boxes contain only a few percent each. Error bars of Fig. 6.6 support that the pulses distribution between boxes is repeatable from a blood sample to another. Besides, they give indications on boxes sensitivity. For example, boxes 4, 5, 8 and 9 are intended to be more responsive to abnormalities than others, because of their small acceptable ranges.

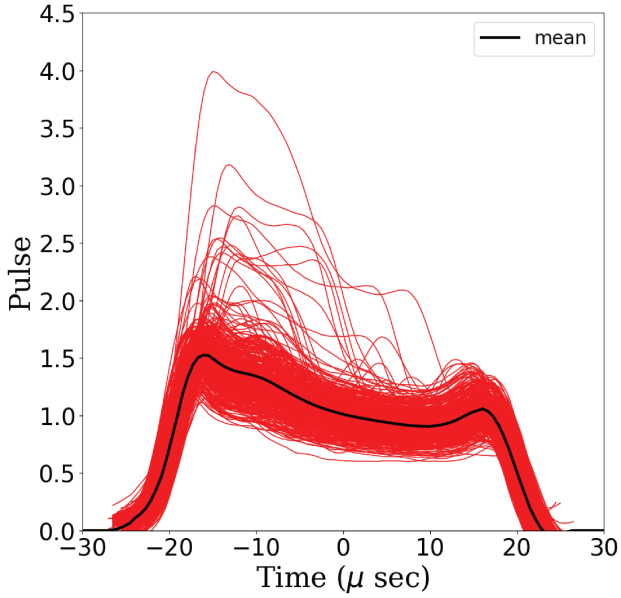

Figure 6.4 – Example calculation of an averaged pulse. In this example, pulses were extracted employing Box9.

One should recognize that the boxes definition could be optimized. Still, the presented approach is applicable to any set of boxes.

6.2 Detecting abnormal Cells

This section is dedicated to the detection of unusual pulses, that are assumed to be caused by abnormal cells. Abnormal RBCs are obtained by diluting a healthy blood sample in reagents affecting their shape and rheology. Two chemical agents are used separately: glutaraldehyde, which is known to fix the RBCs membrane [91], and a surfactant n-Dodecyl-N, N-dimethyl-3-ammonio-1-propanesulfonate also called sulfobetaine 3-12, noted SB3-12 in this report (provided by Sigma-Aldrich), that is shown to make RBCs spherical. Glutaraldehyde is a molecule that cross-links membrane proteins, thus stiffening the cell. Indeed, several studies reporting a reduction of the RBCs deformability when they are submitted to glutaraldehyde are available in the literature [42, 62]. Furthermore, this molecule was shown to fix RBCs, even if they are deformed in flow [91]. The discocyte shape of RBCs is maintained at low glutaraldehyde concentration [114]. Contrary to glutaraldehyde, SB3-12 has not been intensively studied. However, an expertise on the impact of this molecule on RBCs may be found at HORIBA Medical. Experiments revealed that RBCs are spherical at SB3-12 concentrations of about 100 mg.L^{-1} (see Fig. 6.7). In addition, such changes appear to produce rapidly, since all cells are round 20 s after they have been submitted to SB3-12.

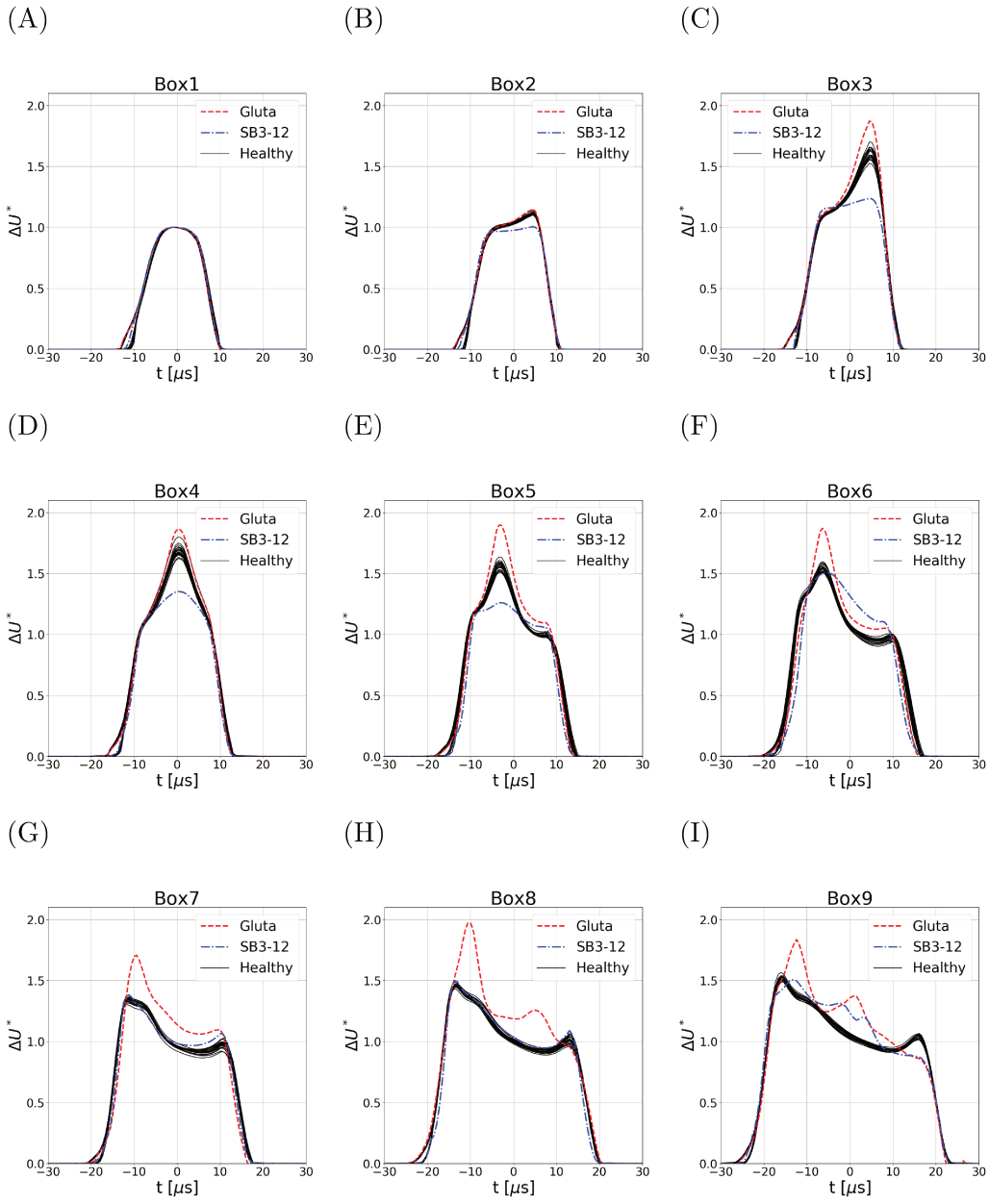

Figure 6.5 – Box-wise comparison of mean pulses. The extraction is done according to boxes of Fig. 6.3. 22 blood samples coming from healthy patients are shown in black lines in these graphs. Besides, results from samples treated with glutaraldehyde at 0.5 % and SB3-12 at 90 mg/L are displayed.

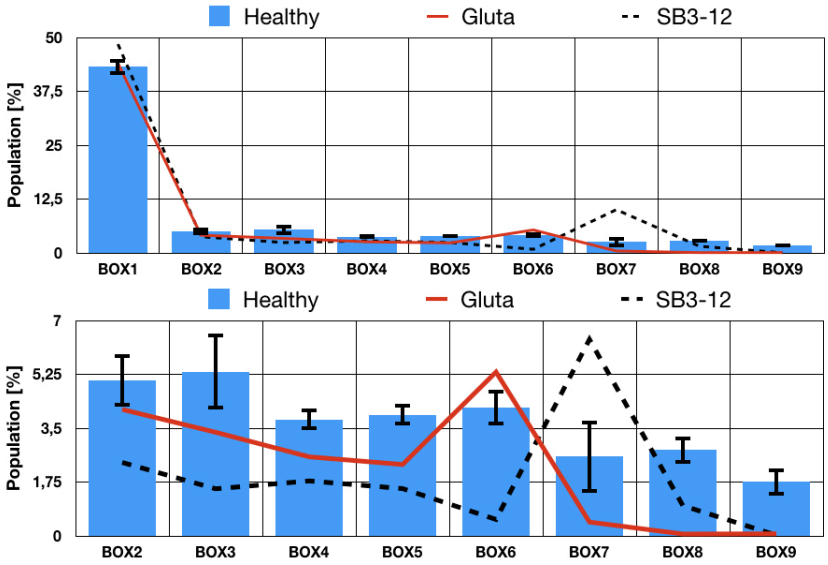

Figure 6.6 – Pulses populations in boxes of Fig. 6.3. Bars plot refers to the normality computed as the average of 22 healthy blood samples. The error margins are calculated as twice the standard deviations, which arise from the 22 healthy blood samples. The populations assessed for a blood sample treated with glutaraldehyde and SB3-12 at concentrations of 0.5 % and 90 mg.L^{-1} (respectively) are also shown.

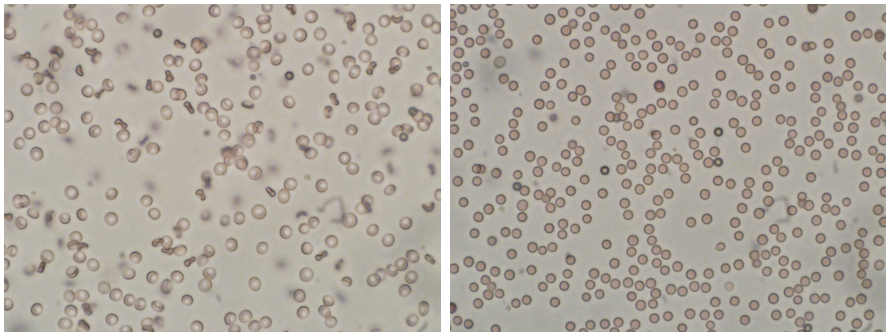

Figure 6.7 – Microscopic images of RBCs suspended in a PBS solution (**left** picture) and in a SB3-12 solution at 100 mg.L^{-1} (**right** picture).

6.2.1 Evidence of the geometrical and rheological information embedded in impedance pulses

Experimental protocol

Changing the RBCs geometrical and rheological characteristics is done by adding specific reagents in a ABX Minidil solution (ie. the electrolytic solution in which RBCs are suspended during the analysis). More precisely, dilutions of SB3-12 and glutaraldehyde in ABX Minidil at different concentrations are prepared. In particular, SB3-12 dilutions cover a range varying between 0 and 90 mg.L^{-1}, while glutaraldehyde is diluted at various concentrations in the range [0 % , 0.5 %]. Then, pulses acquisitions are performed with an ABX Micros 60, as usual, but replacing the classical reagent (ABX Minidil) with the modified solutions. On ABX Micros 60, the replacement of the electrolytic solution is done by interchanging the reac-

tant bottles with a simple 'plug and play' procedure. Besides, the 'CLEAN ALL REAGENT' command is run for removing the former solution from the needle and the system pipes. Two blood samples are analysed with these modified solutions. The first sample is used in acquisitions with the different SB3-12 solutions, while the second one is involved in experiments with the various glutaraldehyde preparations. Acquisitions are performed twice to make sure that results are repeatable. In addition, reference pulses acquisitions are also performed for all samples with the original ABX Minidil solution. Notice that such acquisitions were accounted for in the normality definition of Sec. 6.1.

Comparisons with the predefined normality

Figure. 6.8 displays typical $\mathcal{W}^r/\mathcal{P}^r$ representations arising from pulses acquisitions with SB3-12 and glutaraldehyde. Especially, graphs of the **left** column derive from the acquisitions at glutaraldehyde concentrations of 0 %, 0.15 % and 0.5 % (A, C and E, respectively), while figures of the **right** column arise from experiments involving the following SB3-12 concentrations: 0 mg.L^{-1}, 30 mg.L^{-1} and 90 mg.L^{-1} (B, D and F, respectively). Note that **left** and **right** columns are obtained with two different samples.

At zero concentrations of glutaraldehyde and SB3-12, graphs are in good agreement with the normal scatter plots expected (see the comparison between Fig. 6.8A and Fig. 6.8B with Fig. 6.2B). However, adding the aforementioned molecules in the electrolytic solution impacts the distribution and location of pulses in a $\mathcal{W}^r/\mathcal{P}^r$ representation, as shown in Fig. 6.8C, D, E and F. Moreover, the locations of pulses in such a plot are shown to be related to SB3-12 and glutaraldehyde concentrations.

Box-wise pulses proportions are assessed for the acquisitions with glutaraldehyde at 0.5 % and SB3-12 at 90 mg.L^{-1}. The obtained percentages are superimposed with the bar graph defining the normality in Fig. 6.6. Regarding the statistics, the added reagents induce deviations with respect to the normality. In particular, assessments for the acquisition involving SB3-12 are systematically out of the tolerance margins. In box6, SB3-12 produces a reduction of the population, in contrast with glutaraldehyde that increases the proportion of pulses. The two reagents have also opposite effects on box7. This suggests that a sample of rigid RBCs and a sample of spherical erythrocytes are distinguishable by statistical evaluations. It should be noted that glutaraldehyde leaves Box8 and 9 unpopulated, so does SB3-12 with Box9.

As done for healthy blood samples in Sec. 6.1.2, the averaged pulse is computed for each box of Fig. 6.3 from acquisitions corresponding to Fig. 6.8E and F (viz. with glutaraldehyde at 0.5 % and SB3-12 at 90 mg.L^{-1}, respectively). The resulting mean signatures are compared in a box by box manner with the normality in Fig. 6.5. Regarding boxes related to the most centred paths, small deviations, and even no deviations are observed in terms of averaged pulses (see Box1 and Box2 in Fig. 6.5). Stiffening RBCs with glutaraldehyde tends to increase the magnitude of the peak that emerges when the cell rotates (see case 'gluta' in Fig. 6.5C, D, E, and F). This is consistent with the numerical results of Chap. 4. As a reminder, when evolving in the vicinity of walls, the RBC rotation induces a peak on the associated pulse.

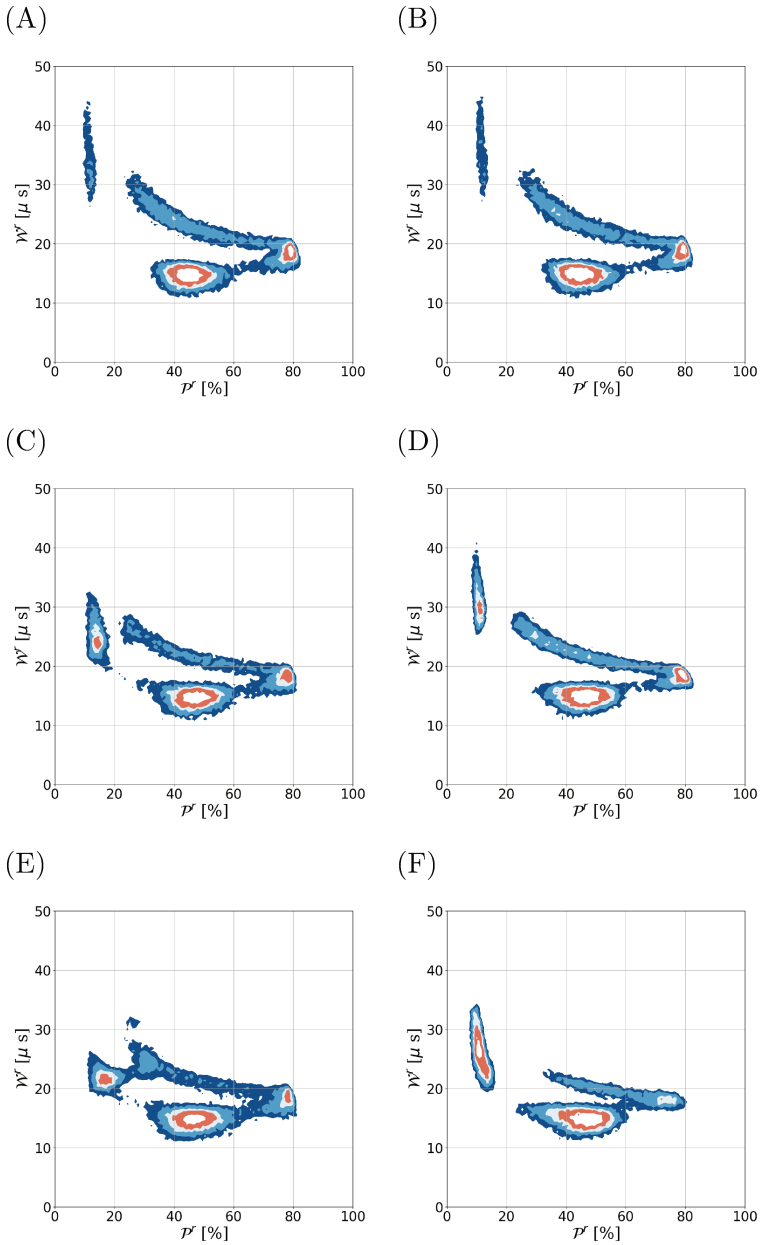

Figure 6.8 – Typical $\mathcal{W}^r/\mathcal{P}^r$ graphs obtained with different concentrations of SB3-12 and glutaraldehyde. Graphs are shown in terms of density iso values, that are taken as: 0.00025, 0.0005, 0.001, 0.0015, 0.0025. **Left** pictures are obtained from a blood sample that was treated with glutaraldehyde at concentrations of 0 % (A), 0.15 % (C) and 0.5 % (E). **Right** pictures are obtained from another blood sample but treated at SB3-12 concentrations of 0 mg.L^{-1} (B), 30 mg.L^{-1} (D) and 90 mg.L^{-1} (F). Metrics $\mathcal{W}^r$ and $\mathcal{P}^r$ are computed by using a threshold of 0.5.

Besides, a strong compression of the cell occurs while it rotates, which appears to mitigate the peak amplitude. Consequently, a rigid cell that cannot compress is expected to produce a larger peak. Regarding boxes 7, 8, and 9, a substantial effect of glutaraldehyde is observed. However, boxes 8 and 9 are sparsely populated with glutaraldehyde, which makes the averaged signatures irrelevant for these two cases (see Fig. 6.6 in which pulses proportions for the case of glutaraldehyde are available). Contrary to glutaraldehyde, SB3-12 is shown to reduce the importance of the peak (see Fig. 6.5C, D and E). Indeed, the consequence of cells rotations is limited by the spherical aspect taken by RBCs suspended in a SB3-12 solution. Simulations performed by increasing the reduced volume $\mathcal{Q}$ (thus the cell sphericity) have shown the same trend in Chap. 4. Note that box6 and box9 are emptied when RBCs are submitted to SB3-12 (see Fig. 6.6), which makes pulses referred to as 'SB3-12' in Fig. 6.5F and I irrelevant. Lastly, spherical RBCs generate pulses that conform with the normality, regarding box7 and box8 (Fig. 6.5G and H).

In summary, spherizing or stiffening RBCs directly impacts the electrical signatures. Omitting boxes 1 and 2, glutaraldehyde and SB3-12 have distinct effects on the electrical prints. In particular, spherizing the cell reduces the magnitude of the peak of rotation in contrast with a more rigid RBC that generates a more important peak.

Designing global markers

In the last section, morphological and rheological alterations of RBCs were shown to deviate the measurements from a predefined normality. The demonstrations were based on the $\mathcal{P}^r/\mathcal{W}^r$ plane. In the present section, indicators for abnormal samples are introduced but this time based on $\mathcal{P}^r/\mathcal{R}$ representations, since such plots appear more sensitive to RBCs disorders. As supported by Fig. 6.9 which is based on the same data as Fig. 6.8, $\mathcal{R}/\mathcal{P}^r$ graphs emphasize the differences between spherized and stiffened RBCs, even when intermediate concentrations of glutaraldehyde and SB3-12 are considered (see Fig. 6.9C and D, respectively). When monitoring the acquisitions with $\mathcal{P}^r/\mathcal{W}^r$ plots, discrepancies are less obvious, in particular for intermediate cases (see Fig. 6.8C and D). Indeed, in such a representation, acquisitions broadly conserve the same arrangement: two branches intersecting at $\mathcal{P}^r \approx 80$ %, and an isolated cluster located at $\mathcal{P}^r \approx 15$ %. Note that apart from the main cluster related to central paths, data organisation in a $\mathcal{R}/\mathcal{P}^r$ graph may completely differ from the normality when RBCs are altered (comparing Fig. 6.9A and B with Fig. 6.9C, D, E and F).

Stating that the representation of Fig. 6.9 is more sensitive to shape and mechanics alterations, a second set of boxes is defined, this time on a $\mathcal{R}/\mathcal{P}^r$ graph (see Fig. 6.10). This second set of boxes is indexed by a prim superscript. In each box, the pulses proportion but also averages of $\mathcal{R}$ and $\mathcal{P}^r$ are calculated. Boxes were chosen manually to maximize as much as possible the differences between the results with spherized RBCs and rigidified RBCs, regarding the computed quantities (viz. boxes statistics and averages of $\mathcal{R}$ and $\mathcal{P}^r$). In particular, box3$'$ is chosen because a considerable increase of the population is expected for spherical RBCs (see

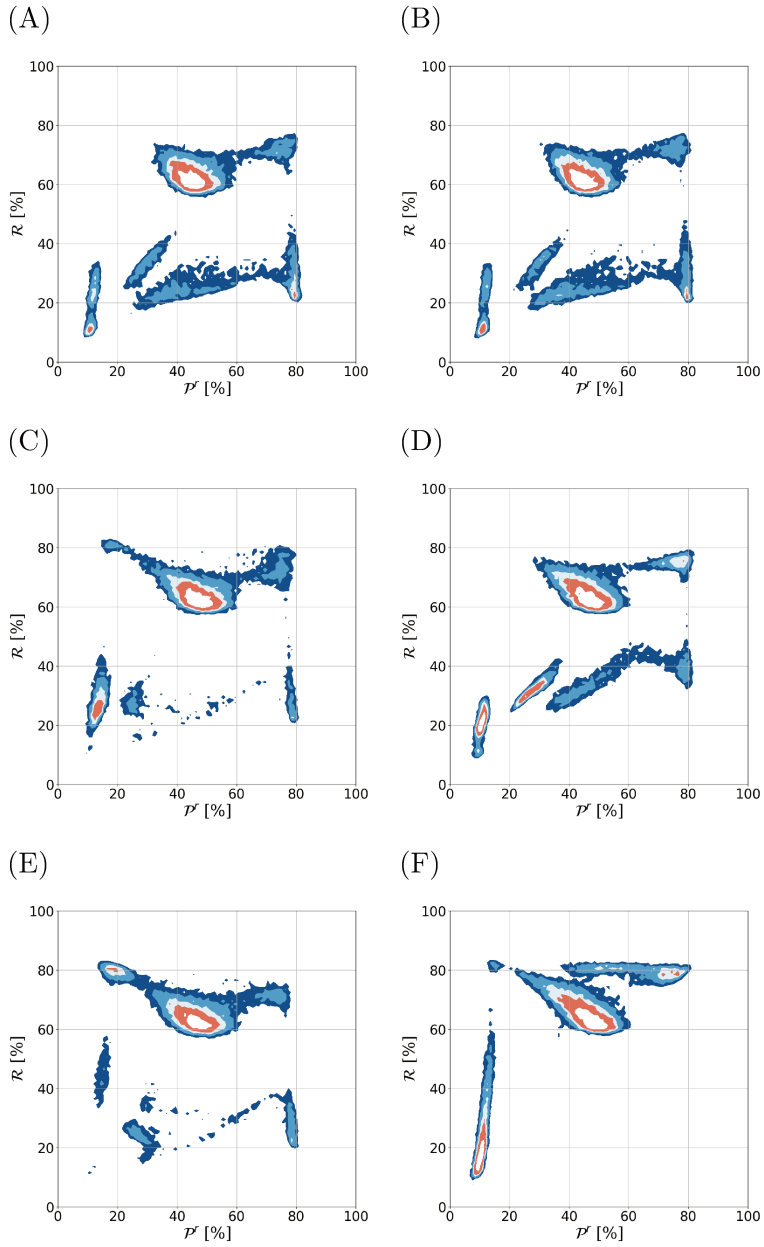

Figure 6.9 – Typical $\mathcal{R}/\mathcal{P}^r$ graphs obtained by analysing blood with solutions of SB3-12 and glutaraldehyde. Graphs are shown in terms of density iso values, that are taken as: 0.00025, 0.0005, 0.001, 0.0015, 0.0025. **Left** pictures are obtained from the same blood that was treated with glutaraldehyde concentrations of 0 % (A), 0.15 % (C) and 0.5 % (E). **Right** pictures are obtained from another blood sample, but treated with SB3-12 concentrations of 0 mg.L^{-1} (B), 30 mg.L^{-1} (D) and 90 mg.L^{-1} (F). Metric $\mathcal{R}$ is calculated with $p_u = 7/8$ and $p_d = 1/2$, while $\mathcal{P}^r$ is assessed by using a threshold of 0.5.

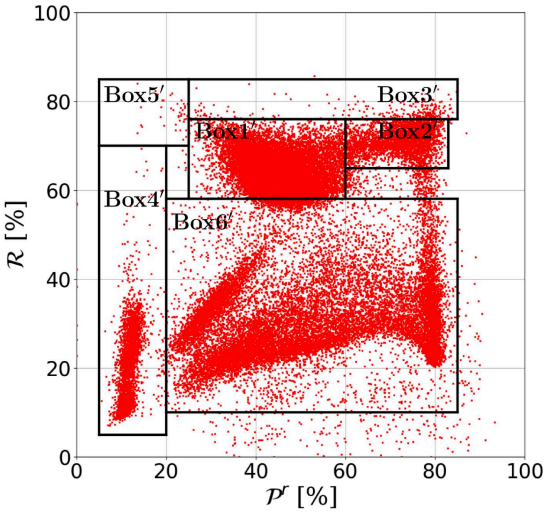

Figure 6.10 – Second set of boxes, defined over a $\mathcal{R}/\mathcal{P}^r$ graph. Metric $\mathcal{R}$ is calculated with $p_u = 7/8$ and $p_d = 1/2$, while $\mathcal{P}^r$ is assessed by using a threshold of 0.5.

Fig. 6.9F). Furthermore, box4′ is retained because rigid cells tend to leave this part of the plot unpopulated (see Fig. 6.9E), while spheres remain and spread along the $\mathcal{R}$ axis (see Fig. 6.9F). One should also cite box5', in which substantial differences between both types of alteration are observed (see Fig. 6.9E and 6.9F).

More sophisticated methods may provide automatically the set of boxes. The presented results must be viewed as an example of processing the data for assessing morphological and rheological information.

Overall, 18 values per sample are calculated from the 6 boxes of Fig. 6.10: for each of the 6 boxes, the proportion of pulses with respect to the total number of pulses, the mean value of $\mathcal{R}$ and the mean value of $\mathcal{P}^r$ are calculated. In the following, only the most relevant quantities are presented, for the sake of concision. Figure. 6.11 shows the evolutions of pulses proportions in box3′ and box5′ according to the concentrations of glutaraldehyde (A and B, respectively) and SB3-12(C and D, respectively). Remind that for each concentration the blood samples were analysed twice, which provides an indication of the repeatability of the observations. The normality is assessed by considering the 22 healthy blood samples of Sec. 6.1 and represented as horizontal lines in Fig. 6.11. The average over these 22 samples is depicted with a red continuous line, while the tolerance margin (defined as twice the standard deviation) is shown in black dashed lines.

As the concentrations of glutaraldehyde and SB3-12 increase, the populations in box3′ and box5′ get out of the normality. Assuming that SB3-12 and glutaraldehyde concentrations are respectively correlated to RBCs sphericity and rigidity, it appears that proportions in box3′ and box5′ measure such cells features. Both glutaraldehyde and SB3-12 tend to increase the pulses percentages in box3′ and box5′. Hence, considering a single quantity enables the detection of abnormalities and does not supply the type of disorder. Still, remind that the two types of alteration can be segregated by assessing the pulses proportions in box6 and box7 (see Fig. 6.6), for instance.

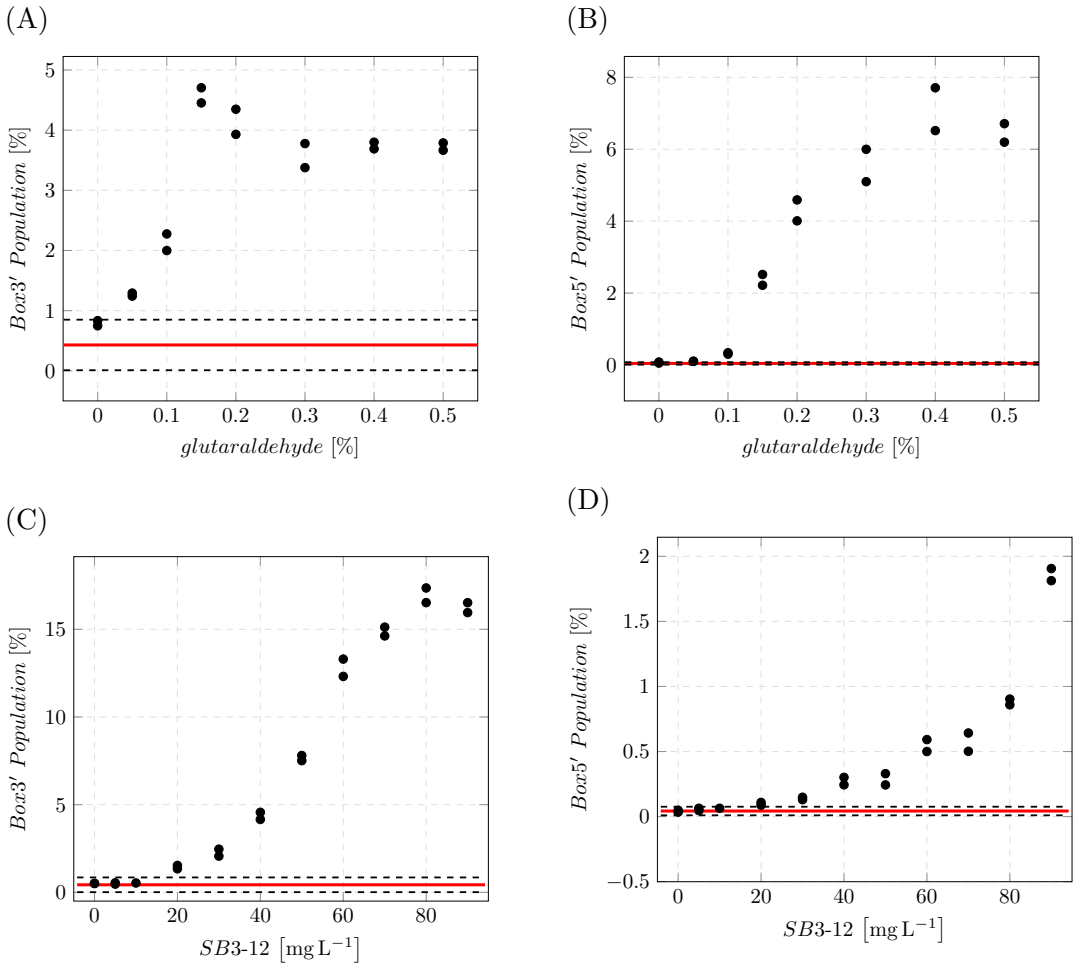

Figure 6.11 – Typical evolutions of boxes statistics according to glutaraldehyde and SB3-12 concentrations. The red and continuous line refers to the average on the 22 healthy blood introduced in Sec. 6.1, while the tolerance margin is represented in dashed lines. This range is defined as twice the standard deviation.

6.2.2 Screening RBCs subpopulations

In Sec. 6.2.1, it is shown that impedance pulses contain information about cell morphological and/or rheological disorders. Examples of signal processing enabling the diagnosis of the type of disorder have also been presented. The introduced methods require a normality definition that is available in Sec. 6.1. Although treatments achieved in Sec. 6.2.1 provide a straightforward detection of abnormalities, they are limited to pathologies affecting a substantial proportion of the RBC population. Remind that such procedures are based on statistical assessments and averaged quantities. Hence, more advanced methods allowing the cell diagnosis from the electrical pulse are required to capture small populations of abnormal RBCs. This section is devoted to neural network modellings that are built in that sense. Firstly, a NN is trained to detect abnormal pulses. Then, a second NN is trained with the

aim to detect the type of abnormality: rigidity or sphericity (viz. glutaraldehyde or SB3-12, respectively).

As described in Sec. 5.3, NNs are models made of interconnected neurons that are generally organised in successive layers. When neurons are linked to all neurons of the preceding and following layers, the NN is called multi-layer perceptron (MLP). Such an architecture may lead to models having a substantial number of parameters (called weights) when the problem suffer from high dimensionality issue. In following modellings, Convolutional Neural Networks (CNNs) are employed. Convolutional Neural Networks (CNNs) can prevent hyper-parametrized models by restricting relevantly inter-layer connections. They are dedicated to structured input variables from a single source, whose organisation is informative (as for pixels composing an image, and electrical pulses). CNNs involve convolution layers that consist in scanning the input data with several filters (also called kernels) to detect the presence of pertinent features to address the desired modelling. A convolution layer is thus parametrised by the number, the size (N_k) and the increment $\mathcal{S}$ of the kernels (step by which filters are moved on the input data). Scanning the input data with a kernel leads to a 'feature map', so that a convolution layers is composed of as many features maps as kernels involved. Features maps are taken as an input by the following layer, that can be either a convolution or a fully-connected layer. The reader is referred to App. C for more details on these concepts related to CNNs.

Abnormality sensor

CNN structure: The detection of abnormal pulses is performed by using a CNN. Depending on the trajectory followed by the cell, the generated pulse is more or less long. Hence, assuming a constant recording time step (Δt), electrical prints are described by temporal sequences of variable sizes. This is problematic since feedforward neural networks take as input an imposed number of variables. Using a CNN, the procedure introduced in Sec. 5.3.1 to tackle this issue is not suited. Indeed, CNNs involve convolution layers enabling the recognition of specific patterns when dealing with structured input data. The later defines data stemming from the same source whose arrangement is informative. Yet, this is not the case in the approach of Sec. 5.3.1, where both the pulse duration and the resampled signal are defined as input of the model (see Fig. 5.11). Hence, the treatment illustrated in Fig. 6.12 is performed directly on the pulses to make them all intelligible for the CNN. First, the pulse is scaled in amplitude by its maximum ΔU_m. The procedure consists in building the treated pulse from $\Delta U/\Delta U_m$, with chosen increment (Δt), duration (T_w) and threshold (see Fig. 6.12). The treated pulse is defined as the sequence of duration T_w, sampled with a time step Δt, which equals the maximum between the threshold and $\Delta U/\Delta U_m$. In doing so, all pulses are represented by N_{L_o}=$T_w/\Delta t$ points. **Left** and **right** pictures of Fig. 6.12 illustrate this process when performed on two pulses with different durations. Once treated, both are represented with temporal series of the same lengths. Note that the original signal must be located between instants 0 and T_w, as shown in Fig. 6.12.

The retained CNN is composed of 8 layers. In the following, T_w is set to 49 μs,

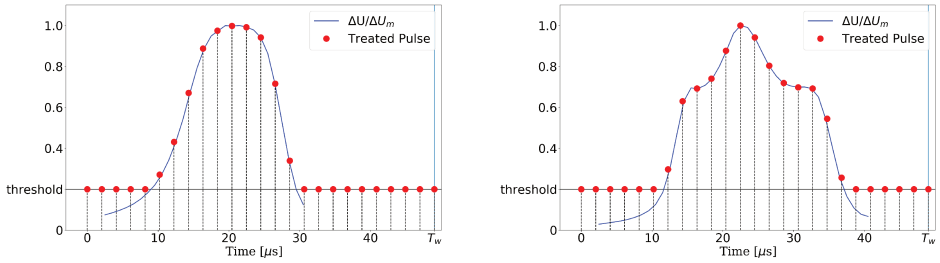

Figure 6.12 – The treatment performed on impedance pulses to define them all with a given number of points. **Left** and **right** pictures illustrate the method on two different initial pulses. The electrical signal is first scaled by its maximum ΔU_m. Given a threshold, the signal is completed with a constant Δt, until the pulse is defined between $[0\ ;\ T_w]$. In this example, T_w is set to 49 μs while Δt is chosen as 2 μs.

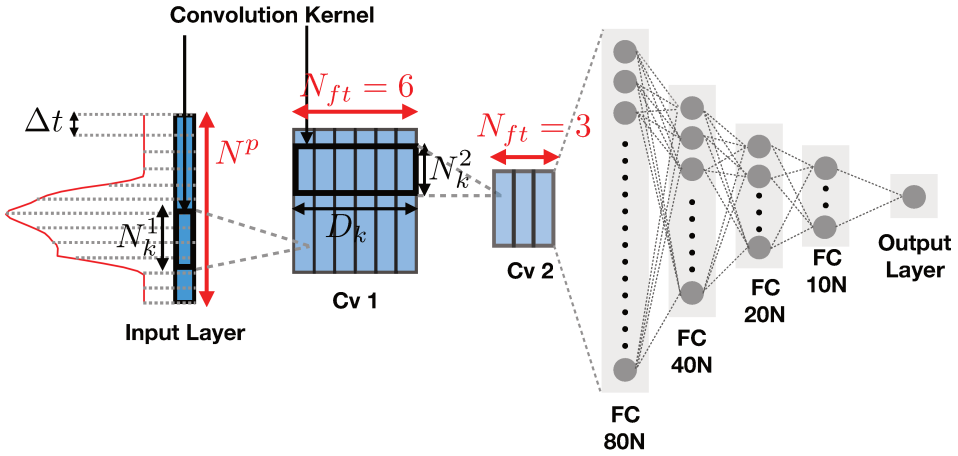

Figure 6.13 – CNN employed for the detection of abnormal pulses. In this illustration, 'Cv' refers to convolutional layers while 'FC' denotes fully-connected layers. Along with 'FC' notations, the number of neurons is specified as 'XN', with X the number of neurons belonging to the layer. The convolution kernels of 'Cv 1' and 'Cv 2' have sizes N_k^1 and N_k^2, equalling 8 and 3, respectively.

the threshold is taken as 0.2 and Δt equals 1.0 μs. Consequently, the size of the input layer is $N_{L_0} = 50$. The input layer is followed by two convolutional layers and four fully-connected layers leading to the output layer containing a single neuron. This architecture is sketched in Fig. 6.13. The first convolution layer (Cv 1) involves 6 kernels of size 8 (N_k^1) that scan the pulse with an increment S of 1. Remind that 6 kernels involve as many features maps ($N_{ft} = 6$). Considering the second convolutional layer (Cv 2), 3 kernels of size $N_k^2 = 3$ with a step $S = 1$ are defined. Note that the sizes of the fully-connected layers (see FC in Fig. 6.13), are filled out in the illustration. All neurons of the model are associated with a sigmoid activation function. Especially, by choosing a sigmoid function for the neuron of the output layer, the model renders a score included in $[0\ ;\ 1]$. A value of 1 refers to a normal pulse while 0 is associated with abnormal pulses.

Data Base

Normal	Abnormal	
ABX Minidil	Gluta [%] $\in$ [0.3 ; 0.5]	SB3-12 [mg.L^{-1}] $\in$ [60 ; 90]

Table 6.1 – Summary of the acquisitions selected for training the CNN aiming at detecting abnormal cells. The normality is defined by acquisitions made with ABX Minidil, while abnormal observations stem from acquisitions with SB3-12 and glutaraldehyde. The considered SB3-12 and glutaraldehyde concentrations are indicated.

Data base: Data stem from the experimental acquisitions previously discussed. In particular, pulses involved in the normality definition (Sec. 6.1) are retained in addition to pulses recorded when SB3-12 and glutaraldehyde are added in the suspending solution; only glutaraldehyde and SB3-12 concentrations included in [0.3 % ; 0.5 %] and [60 mg.L^{-1} ; 90 mg.L^{-1}] are accounted for. This means the model is designed to detect RBCs that are significantly impacted. Reagents used for the acquisitions belonging to the database are summarized in Tab. 6.1. As stated in Sec. 6.1, pulses obtained by using the ABX Minidil solution are considered as normal observations (see Tab. 6.1). An outlet value of 1 is then associated with such pulses, during the training procedure. Acquisitions made with SB3-12 and glutaraldehyde are considered as abnormal observations and are then coupled with an outlet value of 0.

Pulses observed while cells undergo central trajectories were shown to be less sensitive to changes in the RBCs characteristics (see Fig. 6.4A and B). Hence, these latter are removed from the database beforehand. The $\mathcal{R}$-based filter introduced in Chap. 5 enables this extraction as illustrated in Fig. 6.14. From a pulse, $\mathcal{R}$ is calculated and if it is above 52 % the pulse is rejected from the database. For example, in Fig. 6.14A pulses leading to $\mathcal{R}$ above 52 % are colored in blue. Figure 6.14B illustrates the acquisition in a $\mathcal{W}^r/\mathcal{P}^r$ graph, with the same color code than as in Fig. 6.14A. Then, Fig. 6.14C gives an insight on the retained signatures on a $\mathcal{W}^r/\mathcal{P}^r$ representation. In this manner, pulses from box1 and box2 (see Fig. 6.3 and Fig. 6.14B) are removed from the dataset. The process shown in Fig. 6.14 is applied to all acquisitions involved in Tab. 6.1.

CNN training: The database of Tab. 6.1 is split into two datasets: a training dataset and a test dataset. Only the training dataset is used in the CNN training, the test dataset is used for assessing the model accuracy. The CNN weights are updated with the ADAM algorithm [81] in a mini-batch gradient descent approach. The batch size is set to 200, and the learning is run over 1000 epochs on the training dataset. The loss function is the root mean squared (RMS) error and its gradients are calculated with a back-propagation method. During the training step, the error made on the test dataset is calculated. In Fig. 6.15A, the RMS errors on the training and test datasets are shown according to the training epoch. During the entire training, the error on the training data decreases. However, from epoch 500, the

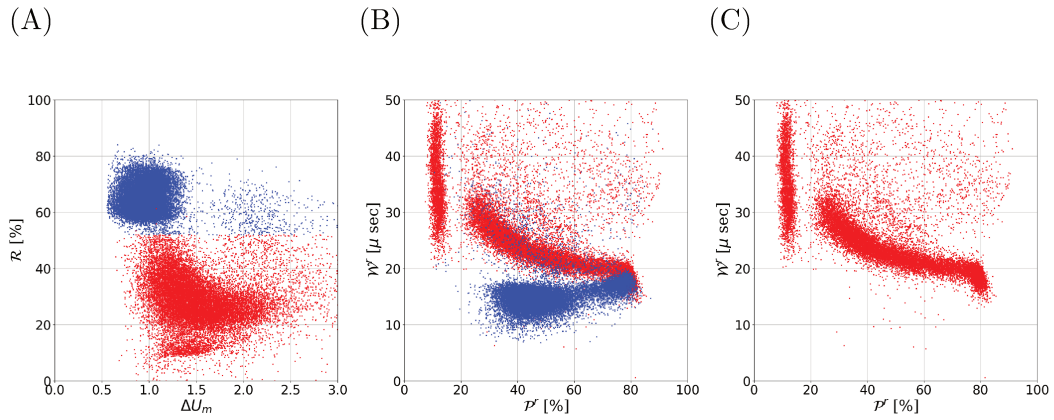

Figure 6.14 – Rejection of pulses induced by centred trajectories. This is done by keeping pulses from which $\mathcal{R}$ is below 52 % (A). In graph (B), the retained and conserved pulses are respectively represented in red and blue on a $\mathcal{W}^r/\mathcal{P}^r$ graph. In (C), solely the retained signatures are illustrated, on the same representation than in B. Metric $\mathcal{R}$ is calculated with $p_u = 7/8$ and $p_d = 1/2$, while $\mathcal{W}^r$ and $\mathcal{P}^r$ are computed by using a threshold of 0.5.

(A)

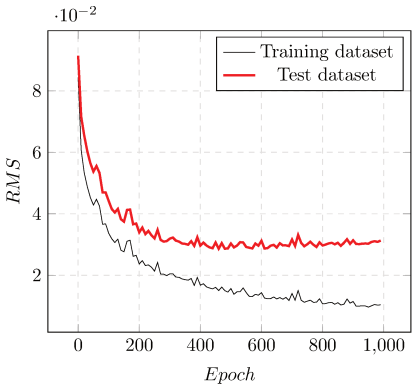

(B)

Confusion Matrix	CNN Score > 0.5	CNN Score < 0.5
Normal	95.7 %	4.3 %
Abnormal	3.1 %	96.9 %

Figure 6.15 – Overview of the CNN training (architecture shown in Fig. 6.13). (A) The evolution of the root mean squared (RMS) errors on both training and test datasets are graphed according to the epoch. (B) Confusion matrix obtained by applying the CNN of epoch 500 to the test dataset.

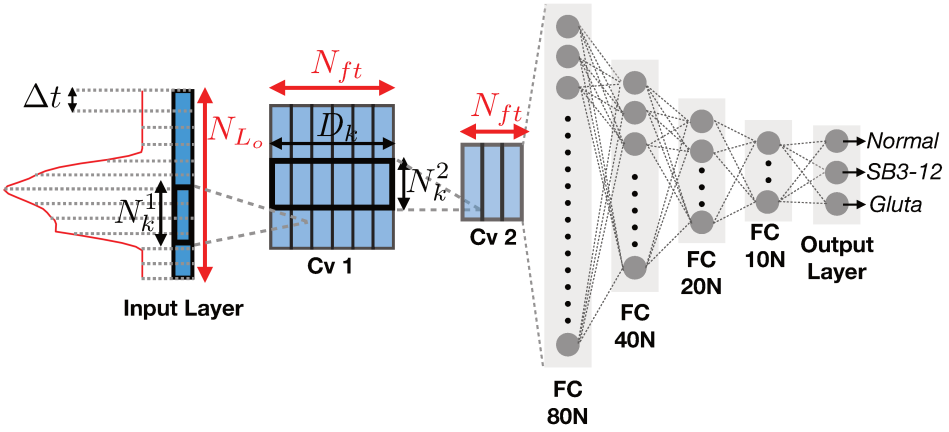

Figure 6.16 – CNN used for recognizing the type of disorder that affects the RBC. The architecture shown in Fig. 6.13 is the basis of the proposed CNN, but with two additional neurons in the output layer. Each neuron of the output layer is related to a specific class (Normal, SB3-12 or glutaraldehyde).

RMS error on the test data stalls and even takes a slightly increasing trend. This suggests that the model is over-fitting the training data. Hence, the accuracy of the CNN is assessed on the test dataset with the CNN configuration of epoch 500. The efficiency of the CNN is evaluated by comparing the model predictions with the expected values (viz. 1 for normal pulses and 0 for abnormalities). The CNN renders a score between 0 and 1. Hence, the CNN classification is done by applying a threshold on the CNN score: a CNN score above 0.5 predicts a normal pulse, while a score below 0.5 indicates an abnormal signature. In this way, the confusion matrix shown in Fig. 6.15B is obtained, which demonstrates the good accuracy of the model. Indeed , among normal pulses of the test dataset, about 96 % are predicted as normal, while 97 % of abnormal pulses are seen as abnormal.

Clustering types of abnormalities

An important issue arising from the results of the previous section is the possibility of diagnosing the type of abnormality affecting a sub-population. In the following, a first answer is given.

Again, a CNN modelling is employed to tackle this question. Based on the architecture of Fig. 6.13, the CNN of Fig. 6.16 is proposed. The only difference being in the output layer that contains 3 neurons instead of a single one. Each neuron is associated with a specific class, that allows the clustering of three groups: normal RBCs, spherized RBCs (submitted to SB3-12), and rigid RBCs (treated with glutaraldehyde). This is illustrated in Fig. 6.16 (see output layer). Depending on the class, the corresponding output neuron is expected to activate (viz. it takes a value of 1), while the remaining render a values of 0. Hence, during the learning step, pulses stemming from acquisitions with ABX Minidil are associated to an output of [1 ; 0 ; 0], pulses obtained with SB3-12 are coupled with [0 ; 1 ; 0], while signatures outcome of acquisitions with glutaraldehyde take a [0 ; 0 ; 1] output. The training is performed as done in the previous section: a batch size of 200 is chosen,

(A)

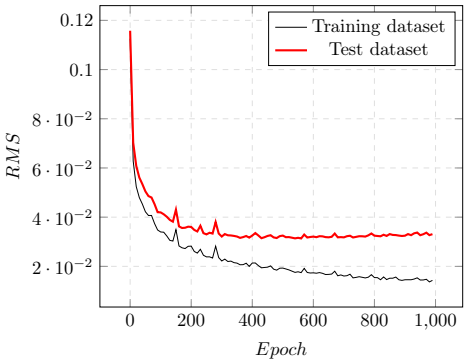

(B)

Confusion Matrix	Targeted Normal	Targeted SB312	Targeted Gluta
Normal	96.0 %	1.0 %	3.0 %
SB3-12	2.4 %	92.5 %	5.1 %
Gluta	4.4 %	3.9 %	91.8 %

Figure 6.17 – Overview of the CNN training (architecture shown in Fig. 6.16). (A) Root mean squared (RMS) error for the training and test datasets according to the epoch. (B) Confusion matrix obtained by applying the CNN of epoch 500 to the test dataset.

the learning is done with ADAM algorithm [81] in 1000 epochs on the database of Tab. 6.1, and the loss function is expressed as the RMS error. Note that the treatment illustrated in Fig. 6.14 is performed to reject pulses that are irrelevant for the assessment of RBCs morphological and rheological disorders. Figure. 6.17A depicts the evolution of the RMS errors on the training and test datasets during the CNN learning. Regarding the training dataset, the error falls during the whole learning, while the test dataset stalls from about epoch 500. Hence, the CNN state of epoch 500 is retained for the following applications.

Once the training step achieved, applying the model to the test data leads to the confusion matrix presented in Fig. 6.17B. Given a pulse, the CNN renders a vector of three components that are included in [0 ; 1]. The classification is then done by retaining the class corresponding to the output neuron of maximum value. Regarding normal pulses, both CNNs (see Fig. 6.13 and Fig. 6.16) have an accuracy of almost 96 %, as stated in Fig. 6.15B and Fig. 6.17B. The correctness on abnormalities is around 92 % for the two different types (SB3-12 and glutaraldehyde), as shown in Fig. 6.17B. Hence, recognizing the type of disorder from the pulse appears to be possible. Note that 5.1 % of the pulses obtained using SB3-12 are predicted as pulses stemming from acquisitions with glutaraldehyde, while 3.9 % of pulses generated by cells treated with glutaraldehyde are seen as signals resulting from an analysis with SB3-12. That means 97.6 % of RBCs in SB3-12 and 95.7 % of RBCs analysed in glutaraldehyde are diagnosed as abnormal. Hence, one may conclude that the two approaches (CNNs of Fig. 6.13 and Fig. 6.16) are almost equivalent in terms of

abnormality detection.

Future improvement

Results provided by CNNs of Fig. 6.13 and Fig. 6.16 are encouraging but further studies are needed to provide more accurate results. As shown by off-diagonal values in confusion matrices of Fig. 6.15B and Fig. 6.17B (i.e. the prediction errors), sub-populations representing only a few percent of the sample would be hardly traceable. It should be noted that coincidences (several particles crossing the orifice at the moment) are not removed from the dataset, which may alter the model training and skew assessments of Fig. 6.15B and Fig. 6.17B. Filtering signatures induced by such events is indispensable for detecting small abnormal populations (below 1 %, for instance). Furthermore, the reliance of the results on the CNNs architectures (Fig. 6.13 and Fig. 6.16) is intended in the future. This point represents an interesting direction for improving the prediction of both models.

6.3 Towards a complete RBCs characterization

The purpose of this section is to model the inverse problem of numerical simulations presented in Chap. 4. More precisely, one aims at evaluating the RBC parameters from the associated electrical print. In that respect, the retained approach is to train a NN from numerical pulses obtained with varying RBC parameters.

Numerical simulations allow the building of couples a^{in}/a^{obs}, in which a^{in} represents the electrical pulse and a^{obs} refers to the RBC parameters. In a first attempt of modelling, a^{obs} was composed by: the internal viscosity (ν_{in}), the shear modulus (G_s), the reduced volume ($\mathcal{Q}$) and the streamline. Remind that the streamline is used to manage the cell trajectory in the aperture. It is defined by a point (0 , r_a , 0), by which the streamline gets through. The coordinate r_a is included in [0 μm ; 25 μm], and refers to the distance from the aperture centerline. As previously stated, the flow is axisymmetric around the aperture, that is why all the considered streamlines are in the plane ($\vec{e}_x$,$\vec{e}_y$). The curvature modulus (E_b) and the spontaneous curvature (c_o) have been verified to have negligible effects in a reasonable physiological range. Hence, they are kept constant in all simulations of the numerical database. Moreover, the RBC area modulus E_a is also kept constant, since changes of area were less than 1 % in the reference simulations of Fig. 4.10 (see Sec. 4.3). Note also that the effect of the internal density on the electrical pulse is insignificant, as stated in App. A. It turns out that the learning step of such an inverse problem is not possible (not shown). In particular, the NN is unable to accurately predict internal viscosities and shear moduli (ν_{in} and G_s, respectively). As shown in Chap. 4 (see Fig. 4.16B and C), the shear modulus G_s and the internal viscosity ν_{in} have the same impact on the electrical signature. This highlights a non-uniqueness issue and explains why this attempt in modeling the inverse problem fails.

In the first section, the direct problem is modelled with a NN, and shown to support the assumption of non-uniqueness above-mentioned. Then, in a second section, it is proposed to combine ν_{in} and G_s in a single parameter for modelling

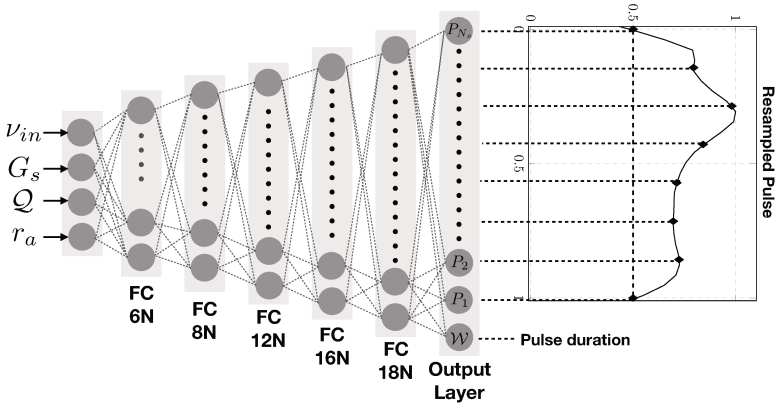

Figure 6.18 – The architecture of the MLP used to model the direct problem. The model takes as an input the RBC parameters and renders the electrical signature formatted as presented in Sec. 5.3.1. More precisely, the model output is composed of a resampled pulse of size N_s equalling 20, and the pulse duration ($\mathcal{W}(\frac{\Delta R_m}{2})$).

the inverse problem (see Sec. 6.3.2). This approach allows to manage a simplified inverse problem with a NN.

6.3.1 Direct problem

Handling the direct problem consists in building a Neural Network that takes the cell parameters as input and gives back the electrical pulse. Hence, in this section, couples a^{in}/a^{obs} in the numerical database are made of the RBC parameters (ν_{in}, G_s, $\mathcal{Q}$ and r_a) and the electrical pulse, respectively.

Model definition

A multi-layer perceptron (MLP) is retained for the modelling. The MLP architecture is illustrated in Fig. 6.18. Given the RBC parameters, the MLP is intended to provide a resampled pulse and its duration, assessed by $\mathcal{W}$ with a threshold of 0.5 $\times$ ΔR_m (ΔR_m is the pulse maximum). This formalism was detailed in Sec. 5.3.1: the pulse amplitude is scaled and the timescale is divided by the pulse duration ($\mathcal{W}(\frac{\Delta R_m}{2})$), prior to performing the pulse resampling with $N_s = 20$ points. In this way, the association of the series of N_s scaled amplitudes with $\mathcal{W}(\frac{\Delta R_m}{2})$ defines the electrical print by $N_s + 1$ variables (that equals 21 in the dealt case). Hence, the output layer of the MLP (see Fig. 6.18) contains 21 neurons. The MLP contains 6 hidden layers whose sizes are given in Fig. 6.18. The activation functions are sigmoid function except for the output layer for which the identity is used.

Training and accuracy of the model

The database is built by the use of the pipeline presented in Chap. 4 and all the performed cases are listed in App. D.1. Couples a^{in}/a^{obs} involved in the present study refer to cases 86-382 in App. D. The model is trained with cases 86-318 of Tab. D.1, while cases 319-382 define the test dataset. Pulses from the database are

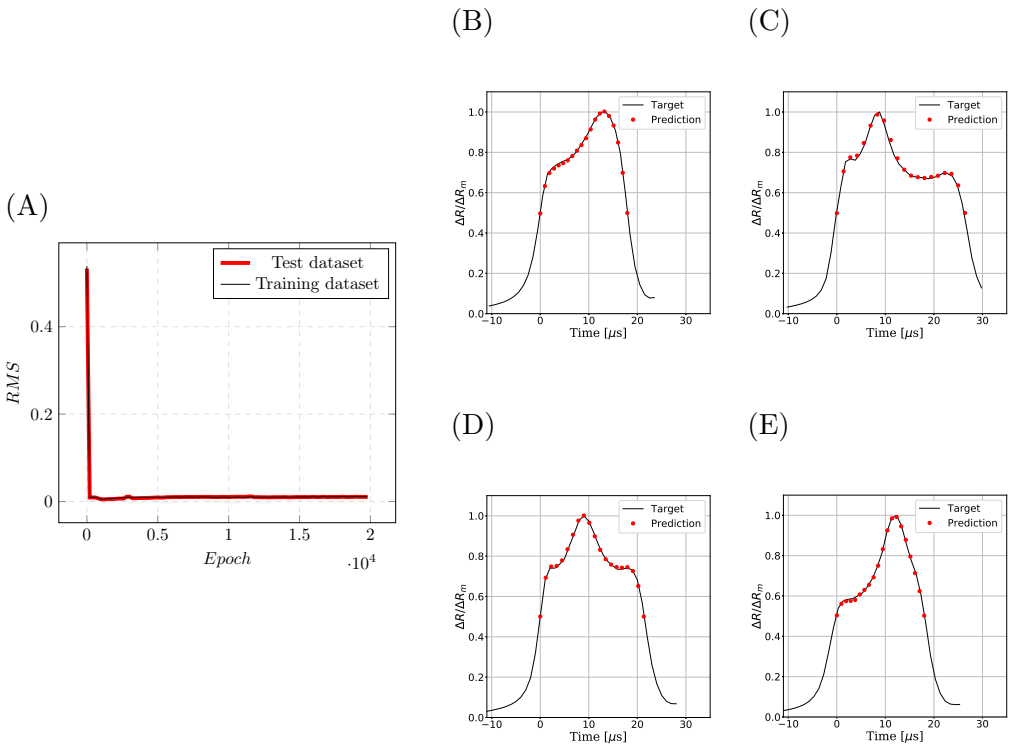

Figure 6.19 – Training and test of the direct model provided by the MLP of Fig. 6.18. Picture (A) shows the evolution of the RMS errors for the training and test data according to the epoch. Figures (B), (C), (D), and (E) are examples of pulses predicted by the MLP superimposed with the actual signatures from simulations. Note that pulses considered in (B), (C), (D), and (E) are part of the test dataset and stem from cases 326, 336, 351 and 364 of Tab. D.1 (in App. D), respectively.

converted as stated in Sec. 5.3.1. The batch size is the same as the training dataset and the gradient descent algorithm is performed over 20000 epochs. The learning step converges rapidly to an optimum as shown by Fig. 6.19A. In addition, the RMS for training and test data are similar, indicating that no over-fitting occurred during the learning. Indeed from epoch 1000 results do not change significantly.

Applying the trained MLP to the test data, it is observed that electrical pulses are accurately retrieved. For example, Fig. 6.19B, C, D, and E compare pulses predicted by the MLP with the original pulses stemming from numerical simulations, for 4 cases from the test dataset. Note that the predicted pulses in these graphs are reconstructed from the outcome of the MLP (see Fig. 6.18). This explains why the predictions take values included in 0.5 and 1, in terms of amplitude (see Fig. 6.19B, C, D, and E).

Remind that substantial efforts are required to simulate the numerical database from which the MLP arises. However, once trained, this MLP can provide the impedance pulse almost instantly by providing it with the RBC parameters. Hence, it may represent an efficient tool for simulating an entire acquisition.

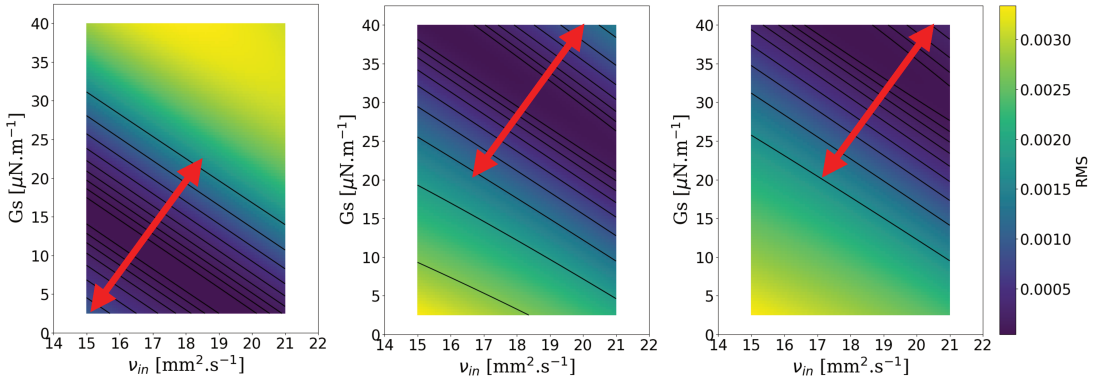

Figure 6.20 – Errors between the MLP prediction and target pulses according to ν_{in} and G_s. **Left**, **middle** and **right** stem from cases 320, 362 and 374 of Tab. D.1. Double arrows in these plots conform with Eq. 6.6.

Introduction of an original viscosity parameter

In this section, the trained MLP is used to emphasize the non-uniqueness of the inverse problem. A pulse from the test dataset is taken as the reference and compared with predictions of the MLP. By varying inputs ν_{in} and G_s in the MLP and by comparing predicted pulses with the reference pulse, an error map is obtained. The RMS error is employed for comparing MLP predictions with the reference. The two remaining parameters required for the MLP (viz. $\mathcal{Q}$ and r_a) are kept constant and equal the values associated with the reference pulse.

Figure. 6.20 illustrates the RMS error according to ν_{in} and G_s, for three different reference pulses. Note that the error is shown over the simulated ranges of G_s and ν_{in}. Error isolines are also represented in Fig. 6.20. No optimal couple G_s / ν_{in} minimizing the RMS error appears clearly in these graphs. Isolines are almost straight and parallel lines. Notice that in the case of perfectly straight and parallel isolines, an infinity of couples G_s / ν_{in} minimizes the RMS error. This statement supports the non-uniqueness issue encountered in the inverse problem previously discussed.

Circumventing this issue is done by replacing G_s and ν_{in} by a new parameter ν_{app}, the apparent viscosity. Remarking that all error isolines have almost the same slope (see Fig. 6.20), ν_{app} is defined as the projection of G_s and ν_{in} on a line perpendicular to error isolines. The projection direction is highlighted in Fig. 6.20 by red double arrows. In particular, ν_{app} is defined by:

$$\nu_{app} = \nu_{in} + \frac{G_s}{\mathcal{S}} \tag{6.6}$$

Regarding error isolines for several reference pulses from the test dataset, parameter $\mathcal{S}$ is set as 14 N.s.m^{-3}. For the calculation of ν_{app}, ν_{in} and G_s are expressed in the international units system, although it is not the convention used in Fig. 6.20. Hence, with ν_{in} covering a range [15×10^{-6} m^2.s^{-1}; 21×10^{-6} m^2.s^{-1}] and G_s included in [2.5×10^{-6} N.m^{-1}; 40×10^{-6} N.m^{-1}], the introduced parameter ν_{app} varies from 1.518×10^{-5} m^2.s^{-1} to 2.386×10^{-4} m^2.s^{-1}. Note that this combination is of course completely dependent on the system and on the operating conditions.

6.3.2 Simplified inverse problem

Training and results

Based on the results of Sec. 6.3.1, the inverse problem is modified by replacing parameters ν_{in} and G_s by a single variable ν_{app} (see Eq. 6.6). Hence, the modelling of this modified problem is done with the neural network architecture of Fig. 6.21A. It is composed of two convolutional layers (cv 1 and cv 2), that are equivalent to those shown in Fig. 6.13 and Fig. 6.16. Following the convolution layers, a fully-connected layer of 40 neurons is set. Finally, the output layer is composed of 3 neurons, each neuron being related to one of the RBCs parameters (see output layer in Fig. 6.21A). All the activation functions of the model are sigmoid functions except the output layer, which takes identity activation functions. The use of a sigmoid function for the output layer would not be relevant for this regression problem because it could only render values included in [0 ; 1]. The numerical database of Tab. D.1 is split into two parts: a test dataset defined by cases {319, 321, 326, 329, 344, 349, 351, 355, 359, 366, 369, 370, 375, 381, 382}; a training dataset made up of the other cases (viz. cases 86-382 without the test data). The learning step is performed in 80000 epochs with a batch size that equals the size of the training dataset. As previously done, the cost function that rates the model error is the RMS. In Fig. 6.21B, the evolutions of RMS errors for the training and test dataset are shown. The model converges rapidly and the CNN state of epoch 20000 is retained. In Fig. 6.21C, the predictions of the CNN for the training and test datasets are displayed against the target values. Predictions for both training and test data are located on the identity function, which validates the model training. It appears that the CNN is more accurate in the prediction of parameter r_a (see Fig. 6.21C), but results obtained for ν_{app} and $\mathcal{Q}$ are also satisfying.

Test on experimental data

Applying this model to an experimental acquisition, distributions of ν_{app}, $\mathcal{Q}$ (reduced volume) and r_a shown in Fig. 6.22 are obtained. Note that in the numerical database from which the model has been designed, r_a varies in between 16 μm and 20 μm, which corresponds to cases 6 to 10 of Chap. 4 (see Fig. 4.18), in terms of trajectory in the aperture. Hence, from the experimental acquisition, only pulses that satisfy $\mathcal{R} < 52$ % and $\mathcal{P}^r > 20$ % are retained for testing. This allows the extraction of experimental pulses that are superimposed with cases 6-10 in a $\mathcal{W}^r/\mathcal{P}^r$ plot (see Fig. 4.18). The considered experimental acquisition stems from an analysis performed with ABX Minidil and belongs to the normality definition of Sec. 6.1. Vertical lines that illustrate the boundaries of the numerical database are shown over the distributions of Fig. 6.22. As expected, the predicted r_a distribution is broadly included within the database range (see Fig. 6.22A). However, $\mathcal{Q}$ and ν_{app} distributions spread out of the simulated ranges (see Fig. 6.22B and C). The predicted reduced volumes ($\mathcal{Q}$) depict an intuitive symmetrical distribution that is centered around a reasonable value of 0.7. Regarding the ν_{app} distribution, one can doubt on the reliability of the model. Indeed, a substantial part of the acquisition is lo-

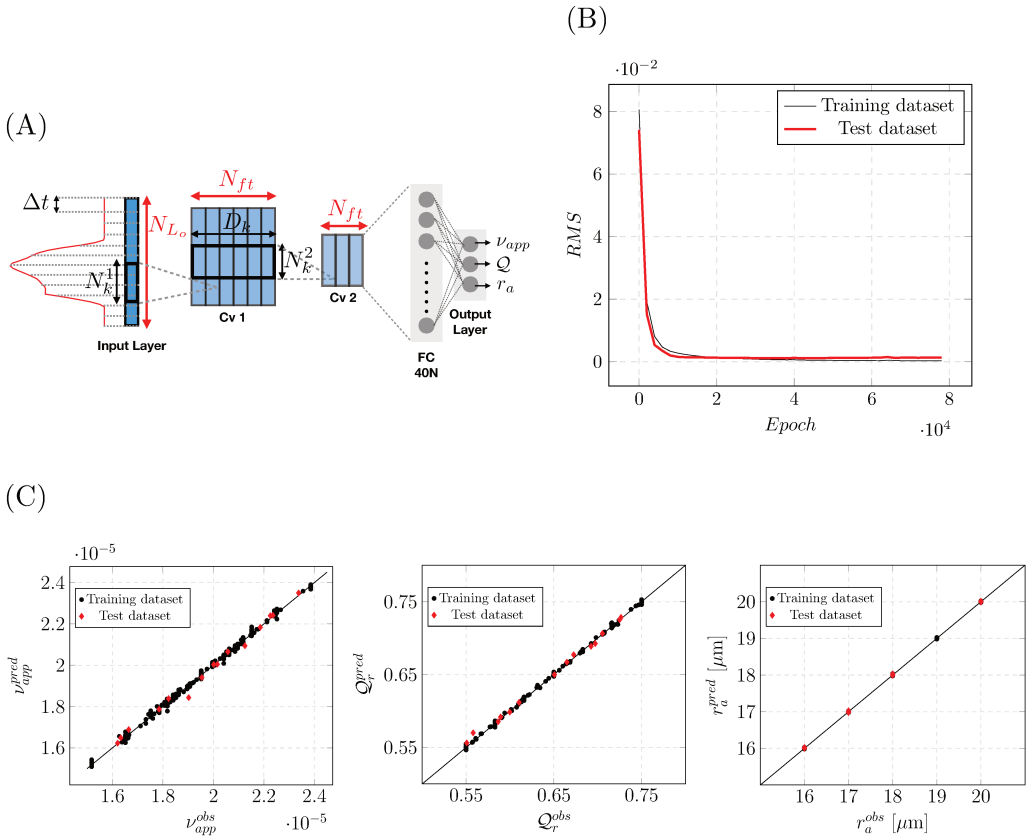

Figure 6.21 – Modelling the modified inverse problem with a CNN. The model architecture is illustrated in A. The electrical signature is given as input of the model and the CNN assesses the RBCs parameters. Picture B depicts the evolution of the RMS errors for the training and test datasets during the learning step. Figure C shows the correlations of the predicted RBC parameters with the expected values. The CNN of epoch 20000 was retained.

cated outside of the numerical range and the distribution profile is not symmetrical. Actually, several aspects may explain the strange behaviour of the model. First, the membrane viscosity was not accounted for in the simulations, despite the short loading times observed in this industrial configuration. As the internal viscosity, the membrane viscosity is expected to stiffen the cell and would probably be accounted for in ν_{app}. It is then probable that the simulated range of ν_{app} is not sufficiently extended. Besides, ABX Minidil has probably not a neutral impact on RBCs. Cells changes inherent to this suspending solution may shift the distributions outside of the simulated ranges.

In Fig. 6.23A and Fig. 6.23B, the predicted r_a is plotted against the metrics $\mathcal{W}^r$ and $\mathcal{P}^r$, respectively. The trajectory r_a correlates with $\mathcal{W}^r$ and $\mathcal{P}^r$, which suggests that the model accurately predicts the RBC trajectory (in the range simulated). Consequently, the approach of modelling an inverse problem from numerical simulations appears appropriate to characterize RBCs. However, the issues previously mentioned must be clarified to propose an accurate assessment of $\mathcal{Q}$ and especially ν_{app}.

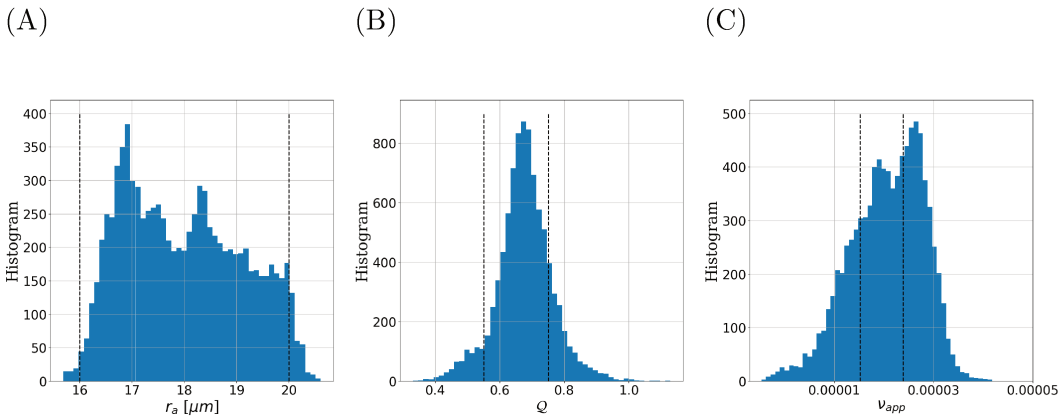

Figure 6.22 – Distributions of r_a (A), $\mathcal{Q}$ (B) and ν_{app} (C) predicted by the model of Fig. 6.21 for experimental data. Vertical dashed lines represented on these graphs refer to the bounds of the numerical database.

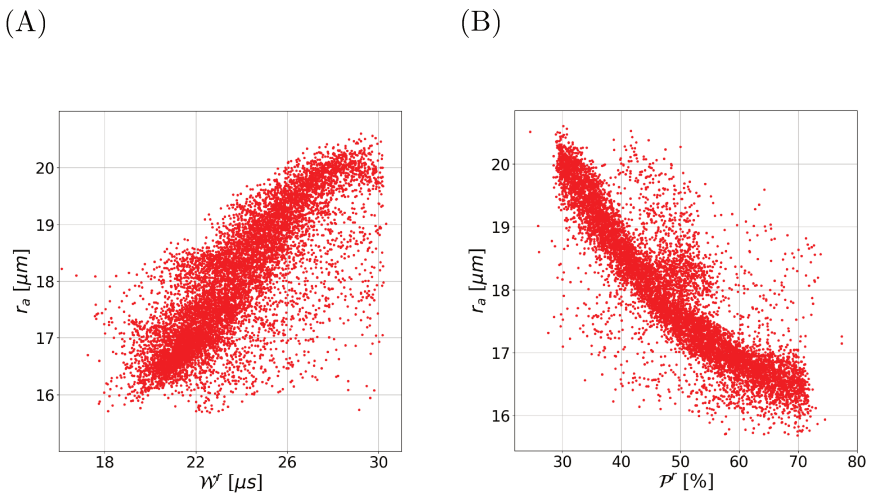

Figure 6.23 – Scatter graphs of r_a according to $\mathcal{W}^r$ (A) and $\mathcal{P}^r$ (B), for an experimental acquisition. Parameter r_a is predicted by the CNN of Fig. 6.21. Metrics $\mathcal{W}^r$ and $\mathcal{P}^r$ are computed by using a threshold of 0.5.

Despite uncertainties concerning the inverse model, its behavior when RBCs are modified with glutaraldehyde or SB3-12 was assessed. In Fig. 6.24A and B, $\mathcal{Q}$ and ν_{app} distributions are shown for three different SB3-12 concentrations (including 0 for reference). In the same way, Fig. 6.24C and D display respectively $\mathcal{Q}$ and ν_{app} histograms for three concentrations of glutaraldehyde. When increasing the SB3-12 concentration, the $\mathcal{Q}$ distribution is shifted to the right-hand side (see Fig. 6.24A), which is consistent with the fact that SB3-12 spherizes RBCs. However, ν_{app} decreases when adding SB3-12, which was not expected (see Fig. 6.24B). When treating cells with glutaraldehyde, the model predicts increases in $\mathcal{Q}$ and ν_{app}. The growth of ν_{app} is in agreement with previous observations reporting more rigid cells when treated with glutaraldehyde. At substantial concentration, glutaraldehyde was shown to alter RBCs shapes, but no quantitative measurements are available, to our knowledge. Hence, it is difficult to conclude on the reliability of the model that predicts a more spherical aspect of RBCs when glutaraldehyde is added in the suspending solution.

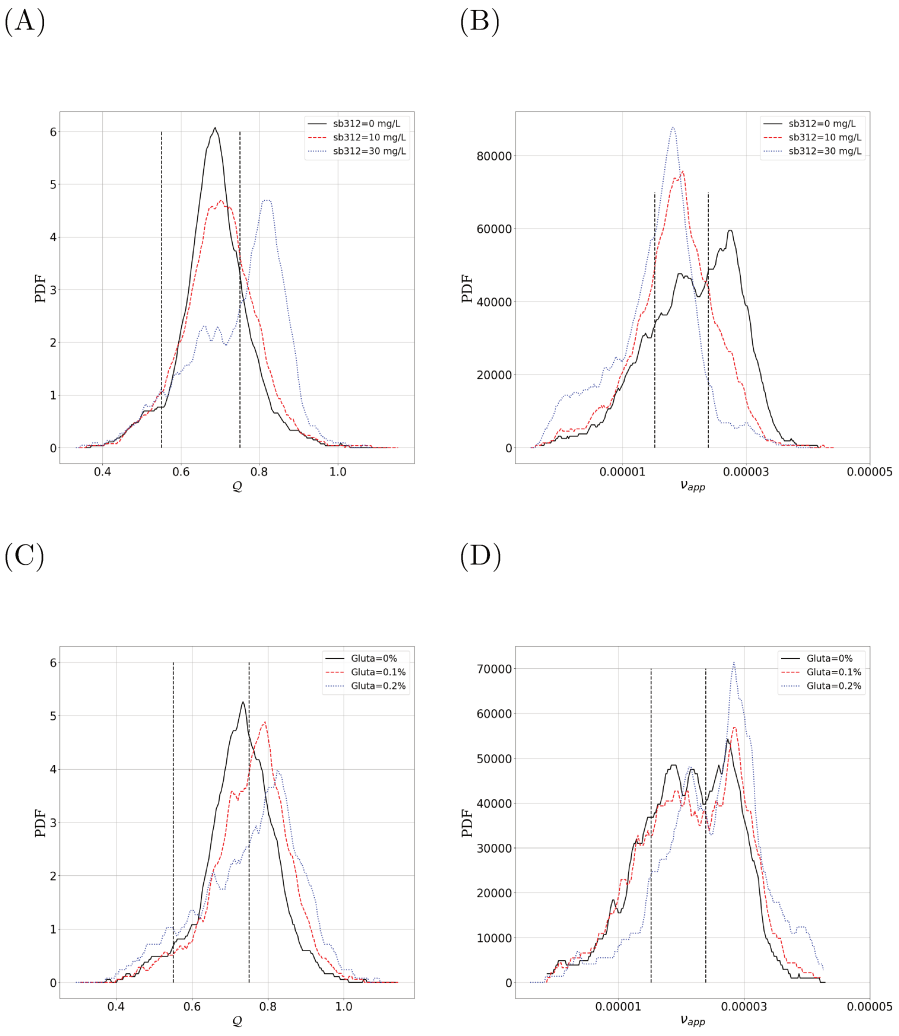

Figure 6.24 – Behavior of the CNN of Fig. 6.21 when RBCs are submitted to SB3-12 (A and B) and glutaraldehyde (C and D). Graphs A and C display $\mathcal{Q}$ Probability Density Functions (PDF) while B and D depict ν_{app} PDF.

Chapter 7

Conclusion

Chapter contents

7.1 Main results

This thesis presents a numerical study of electrical prints generated by particles flowing through the sensing region of a Coulter counter.

Due to substantial differences in velocities and length in industrial Coulter counters, there is a need of focusing the computation domain to the measurement region. In practice, calculations are performed by depositing the particle just before the aperture in a fluid domain restricted to the detection area. In Chap. 3 , this procedure was presented for the case of ABX Micros 60 (HORIBA Medical) and applied to the prediction of electrical pulses generated by rigid spheres. Spheres lead to 'bell-shaped' pulses when following a centred trajectory, while the signature tends to depict a 'M-shaped' by the walls. The typical 'M-shaped' is explained by regions with a dense electrical field that are around the aperture corners. Numerical results were shown to be in good agreement with an experimental pulses acquisition when a latex bead sample is analysed. Note that a strict comparison between these two approaches is not possible because of the accessibility of industrial systems: it is not possible to know where the particles pass in an experiment, which precludes the direct comparison. However, the pulse duration (rated by metric $\mathcal{W}^r$, see Eq. 3.3) is related to the particle trajectory, thus comparisons were performed by sampling the durations of the pulses and superimposing the shapes of the numerical and the experimental pulses having the same duration $\mathcal{W}^r$.

As a direct extension of Chap. 3 to deformable particles, Chap. 4 dealt with the case of RBCs. Contrary to rigid spheres, RBCs deform and may rotate before entering in the sensing region. Hence, the approach of starting the simulation by depositing a resting RBC near the aperture entrance (as it was done for spheres in Chap. 3) is not relevant: there is a need for accounting the cell dynamics before the aperture. However, due to low velocities in the upstream part of the orifice, simulating the whole RBC behaviour before it enters the aperture would lead to tremendous computational costs. In that respect, an original pipeline was proposed to tackle the numerical simulation of deformable particles in Coulter counters [162]. In this method, the upstream dynamics of RBCs is simulated in a relevant extensional configuration which is much smaller than the entire device. Once elongated by this extensional flow, the RBC is dropped just before the orifice entrance, in a reduced configuration of the complete geometry. This approach was validated by comparisons with a computation tackling the entire Coulter counter. In addition, it is shown to reduce the CPU cost by a factor of 8. By applying this original pipeline, a variety of RBCs dynamics was simulated. In the core region of the orifice, the RBC depicts an elongated shape that is aligned with the perforation. Closer to the edges, velocity shears make the RBC rotate, and a cell compression is observed while the particle turns in the shearing region. Centered paths render 'bell-shaped' pulses while rotating cells produce a peak on the electrical perturbation. Besides, it is stated that the closer the particle from the aperture wall, the sooner the cell rotation occurs, and so does the peak in the pulse. Then, a metric measuring the moment at which the peak occurs was introduced ($\mathcal{P}^r$, see Eq. 4.6). Combining $\mathcal{P}^r$ with $\mathcal{W}^r$ allows an arrangement of the pulses according to the RBCs trajectory. These tendencies, originally discovered in the numerical simulations results, are also observable in the experiments by analysing healthy blood samples. Furthermore, the use of $\mathcal{P}^r$ and $\mathcal{W}^r$ enables the extraction of experimental signatures that were predicted numerically. The good agreement found with the experimental data not only validates the introduced pipeline but also explains the huge variety of pulses signatures observed when analyzing a blood sample.

Considering both rigid spheres and deforming RBCs, two types of edge-effects were retrieved: electrical artefacts that are caused by the regions of high local electrical field; dynamical artefacts occurring when deforming and aspherical particles evolve near the wall in the shearing region. Shear velocity gradients deform and make the RBCs rotate, thus inducing a change of the cell shape factor that directly impact the electrical perturbation (see Eq. 1.2) Using the inertia equivalent ellipsoid and shape factor analytical models provided in the literature, the evolution of the RBC shape factor inside the aperture is provided. As stipulated by the empirical Eq. 1.2, a linear relationship between the electrical perturbation and the product of the shape factor with the squared electrical field is retrieved. Notice that, considering rigid spheres, for which the shape factor remains constant, it was shown that the squared electrical field is directly proportional to the electrical print. The use of the numerical simulation with the shape factor modelling allows a better understanding of the electrical and dynamical respective contributions to the edge-effects. The presented method represents also useful tool to assess the deformability contribution to

the pulse shape.

Numerical results highlighted volume overestimations when pulses impacted by edges-effects are considered. In the studied configuration, all RBCs impacted by electrical edge-effects are also impacted by dynamic artefacts. It is then proposed to filter pulses altered by dynamical edge-effects to achieve a more accurate assessment of cells volumes. Generally, the pulse maximum is taken as a measurement of the cell volume. The RBC rotation increases the shape factor f_s and thus the apparent volume for the Coulter counter. Hence, methods aiming at detecting whether the RBC rotates were introduced in Chap. 5. A first approach detects the peak of rotation by computing a width ratio, denoted by $\mathcal{R}$ (see Eq. 5.1). Calculating $\mathcal{R}$ for all pulses from an experimental acquisition and applying a convenient threshold on $\mathcal{R}$ for filtering irrelevant signals, symmetrical and Gaussian-like volume distributions were obtained. Note that without any filter, the observed volume distribution is right-skewed, as it was reported in the literature. Also, the $\mathcal{R}$ based filter shows a better correlation with hydrodynamical focusing (which is the reference in Coulter counters), in terms of average and standard deviation of measured volumes: in hydrofocused Coulter counters, cells are enforced to flow through the detection area by the core of the orifice, in such a way they are not impacted by edge-effects. A second method detects the rotation by a Neural Network (NN) modelling. Probably due to a stricter criterion for rotation detection, this second method appears to be limited to more centred path than the $\mathcal{R}$-based filter; a symmetrical distribution is also retrieved. The approach of detecting particle rotations from electrical pulses was subjected to patent protection, whose examination is still ongoing.

The last chapter (Chap. 6) lays the foundation of a possible characterization of the shape and the rheology of particles by the analysis of impedance pulses. By spherizing and stiffening RBCs with SB3-12 and glutaraldehyde (respectively), changes may quantitatively be observed on relevant two-dimensional graphs ($\mathcal{W}^r/\mathcal{P}^r$ and $\mathcal{R}/\mathcal{P}^r$, for instance). By defining boxes on the aforementioned graphs, proportions and averaged pulse signatures diverge from a predefined normality. Note that the normality is defined from several healthy blood samples that were not treated with glutaraldehyde nor SB3-12. Methods based on bi-dimensional graphs consist in calculating percentages or averaged metrics (viz. $\mathcal{R}$ and $\mathcal{P}^r$). Hence, only cases where a substantial part of the sample is abnormal may be sensed with such methods. This drawback was balanced by the use of Convolutional Neural Network (CNN). In a first CNN modelling, it was shown that abnormal signatures may be distinguished with an accuracy of about 96 %. Then, the abnormality type (SB3-12 or glutaraldehyde) appears to be achievable by a CNN trained to recognize three subgroups: normal RBCs, RBCs spherized by SB3-12 and RBCs rigidified with glutaraldehyde. A correctness of about 92 % was obtained for the diagnosis of the disorder type.

In the last part of Chap. 6, NNs are used for modelling the inverse problem of numerical simulations. This study aims at assessing the RBC parameters from the corresponding electrical pulse. Four parameters were retained in this study: (1) the cell trajectory, (2) the membrane shear modulus, (3) the internal viscosity, and (4) the RBC sphericity (or reduced volume). For this purpose, a database of about 300 pulses was generated in a numerical approach. It was observed that

the neural network fails in learning the inverse problem (given a pulse, provides the 4 parameters), while the direct problem is easily achieved. The direct problem indicating that several couples of shear modulus and internal viscosity may lead to the same pulse signature, the choice of combining them into a unique parameter similar to an apparent inner viscosity was made. Both internal viscosity and shear modulus drive the capability of the RBC to being compressed in the shearing region (near the orifice edges), thus they both induce variations of same nature on the pulse. Combining these two parameters in the apparent viscosity, the inverse problem is successfully learned by the CNN. Finally, when applying the CNN to experimental data, encouraging results are obtained. The predicted trajectories correlate with $\mathcal{P}^r$ and $\mathcal{W}^r$, which agrees with statements of Chap. 4. Moreover, RBCs reduced volume and apparent viscosity, outcoming from the CNN, are assessed in reasonable ranges but would require further modelling efforts (discussed in the following).

7.2 Raised issues and perspectives

7.2.1 The close vicinity of the orifice edges

A part of the experimental acquisitions was not retrieved in the simulations. This portion represents approximatelly 6 % of the whole acquisition and is observed at $\mathcal{P}^r$ values arround 10 % on graphs $\mathcal{W}^r/\mathcal{P}^r$ and $\mathcal{R}/\mathcal{P}^r$. Considering a trajectory even closer to the aperture walls seems to explain this cluster (see App. B), but numerical instabilities encountered in such wall proximity make difficult any definitive conclusions.

Despite the lack of understanding of this specific part of the acquisition, it was shown that the related pulses signatures are reproducible from a healthy blood sample to another. Besides, they are also sensitive to alterations of RBCs. In a nutshell, this specific part of experimental acquisitions was not fully understood in the context of this thesis but was proven to be sensible to morphological and rheological disorders of RBCs. Hence, further numerical efforts are intended in the future to reproduce accurately this type of signatures and understand the involved mechanisms.

7.2.2 Completeness of the numerical model

The range of shear rates experienced by the cell in Coulter counters is much higher than the configurations generally studied in the literature. Nevertheless, RBC deformations remain moderate. The RBC exposure times to these high shear rates being very short, the internal viscosity plays an important role in maintaining the cell shape. The same should be true for the membrane viscosity, although it was not modelled in the present study.

As the membrane viscosity, dielectrophoretic (DEP) forces acting on the membrane were not taken into account, although RBC electro-deformations were reported[116, 132] in the range of the electrical field observed in the studied configuration (of the order of 1.0×10^6 V.m^{-1}). Further investigations about the impact of DEP forces and membrane viscosity should be performed in the future. Still, good comparison

with experimental data was obtained, that demonstrated that the proposed pipeline (Chap. 4) and current assumptions (Chap. 2) are appropriate to represent the main mechanisms at play.

Nevertheless, when applying the inverse modelling of Chap. 6 on experimental data, it appears that key components are likely missing in the numerical model. Indeed it was suggested that the membrane viscosity would play an important role in the original apparent viscosity. Hence, answers on the real impact of missing physics on the results are needed before claiming a quantitative assessment of the RBC features with an inverse modeling.

7.2.3 Improvements of abnormalities sensors

In Chap. 6, boxes on relevant two-dimensional representations of pulses were defined manually to measure the state of normality of the sample. Note that this choice is probably not optimal, and a better definition of boxes would potentially emphasize abnormalities. Machine learning approaches based on k-mean methods may provide automatically the set of boxes, for instance.

As preliminary modellings, CNNs detecting abnormal pulses were shown to provide encouraging results. Because 'bell-shaped' pulses are not relevant for processing other information than its volume, a WR based filter is applied to the acquisition before the use of such CNNs. This could alter the evaluation of sub-population percentages. For example, adding SB3-12 or glutaraldehyde may change the proportion of pulses along the WR axis. Hence, the proportion of signatures rejected by the WR filter would depend on the RBCs morphology and rheology. In this context assessing sub-populations after a WR separation cannot render the actual proportion of abnormal cells. Further studies are required to fix this issue. Note that interchanging the 'sheathing' fluid and the 'blood sample' in a hydro-focused Coulter counter could represent an appropriate answer to this issue.

Detecting small populations of abnormal cells would require an improvement of the current CNN models. For example, with an accuracy of the order of 96 %, detecting a pathological population of 1% appears to be an intricate task. As previously suggested, a cleaning of the training and test datasets from coincidences (pulses generated by several particles in the sensing region) must be performed. Removing coincidences from the acquisitions may be done by increasing the dilution rate of the blood sample in the electrolytic solution during the analysis. Another approach is to conceive a method dedicated to the filtering of electrical prints arising from such artefact.

Appendix A

Modeling of the cytosol density

The internal density of RBCs is higher than plasma, water, and also the electrolytic solution in which they are suspended in Coulter counters. Remind that such solutions are mostly composed of water. In particular, when flowing near the orifice walls, RBCs undergo curved trajectories at a significant velocity. This point gives rise to a fundamental question: are inertial effects important in such configurations?

This section presents the developments made in the context of this thesis to account for the internal density of RBCs. The improved model is validated with a study of Uhlmann, which provides data for a bead falling in a viscous fluid. Finally, the impact of cytosol density on the electrical measurement of RBCs is assessed.

A.1 Two-phase flow model

A.1.1 Modelling equations

Accounting for a different density inside the RBC membrane implies a two-phase flow modelling that can be described with the following Navier Stokes equations:

$$\frac{\partial \rho \vec{u}}{\partial t} + \nabla.(\rho \vec{u} \otimes \vec{u}) = -\nabla P + \nabla.[\mu \nabla \vec{u}] + \nabla.[\mu (\nabla \vec{u})^T] + \vec{f_v} \tag{A.1}$$

$$\frac{\partial \rho}{\partial t} + \nabla.(\rho \vec{u}) = 0 \tag{A.2}$$

Here, μ denotes the dynamic viscosity that equal $\rho \times \nu$. Note that Eq. 2.47 and . 2.48 presented in Chap. 2 are simplified versions of Eq. A.1 and . A.2, in the case where ρ is constant in the fluid domain.

Since the two phases are unmiscible and incompressible, the density ρ of a fluid particle should be preserved. Consequently, ρ must satisfies:

$$\begin{aligned} &\frac{D\rho}{Dt} = 0 \\ \iff &\frac{\partial \rho}{\partial t} + \vec{u} \nabla.\rho = 0 \end{aligned} \tag{A.3}$$

Combining Eq. A.2 with Eq. A.3 provides the following divergence free condition for the velocity:

$$\nabla.\vec{u} = 0 \tag{A.4}$$

In this respect, the problem consists in solving Eq. A.1 and Eq. A.4.

A.1.2 Numerical treatement

In order to obtain an explicit advancement equation for the velocity $\vec{u}$, the momentum equation (Eq. A.1) is subject to the following developments. First, the temporal derivative of $\rho\vec{u}$ in Eq. A.1 is derived as follow :

$$\rho\frac{\partial\vec{u}}{\partial t}+\vec{u}\frac{\partial\rho}{\partial t}+\nabla.(\rho\vec{u}\otimes\vec{u})=-\nabla P+\nabla.[\mu\nabla\vec{u}]+\nabla.[\mu(\nabla\vec{u})^T]+\vec{f_v} \tag{A.5}$$

Then, by injecting Eq. A.2 in Eq. A.5 leads to:

$$\rho\frac{\partial\vec{u}}{\partial t}-\vec{u}\nabla.(\rho\vec{u})+\nabla.(\rho\vec{u}\otimes\vec{u})=-\nabla P+\nabla.[\mu\nabla\vec{u}]+\nabla.[\mu(\nabla\vec{u})^T]+\vec{f_v} \tag{A.6}$$

Finally, $\frac{\partial\vec{u}}{\partial t}$ takes the following expression:

$$\frac{\partial\vec{u}}{\partial t}=\frac{1}{\rho}\vec{u}\nabla.(\rho\vec{u})-\frac{1}{\rho}\nabla.(\rho\vec{u}\otimes\vec{u})-\frac{1}{\rho}\nabla P+\frac{1}{\rho}\nabla.[\mu\nabla\vec{u}]+\frac{1}{\rho}\nabla.[\mu(\nabla\vec{u})^T]+\frac{1}{\rho}\vec{f_v} \tag{A.7}$$

The time advancement of Eq. A.4 and A.7 is done with a prediction correction method. From the quantities at the beginning of the time step (indicated with a superscript n), a predicted velocity $\vec{u}^*$ is obtained by advancing Eq. A.7 without the pressure term. For the sake of simplicity, an explicit Euler scheme is used in the developments:

$$\begin{aligned}\frac{\vec{u}^*-\vec{u}^n}{\Delta t}=&\frac{1}{\rho^n}\vec{u}^n\nabla.(\rho^n\vec{u}^n)-\frac{1}{\rho^n}\nabla.(\rho^n\vec{u}^n\otimes\vec{u}^n)\\&+\frac{1}{\rho^n}\nabla.[\mu^n\nabla\vec{u}^n]+\frac{1}{\rho^n}\nabla.[\mu^n(\nabla\vec{u}^n)^T]+\frac{1}{\rho^n}\vec{f}_v^n\end{aligned} \tag{A.8}$$

Note that contrary to the predicted velocity $\vec{u}^*$, the actual velocity at the end of the time step ($\vec{u}^{n+1}$) should depend on the pressure gradient as follows:

$$\begin{aligned}\frac{\vec{u}^{n+1}-\vec{u}^n}{\Delta t}=&\frac{1}{\rho^n}\vec{u}^n\nabla.(\rho^n\vec{u}^n)-\frac{1}{\rho^n}\nabla.(\rho^n\vec{u}^n\otimes\vec{u}^n)-\frac{1}{\rho^n}\nabla P^{n+1}\\&+\frac{1}{\rho^n}\nabla.[\mu^n\nabla\vec{u}^n]+\frac{1}{\rho^n}\nabla.[\mu^n(\nabla\vec{u}^n)^T]+\frac{1}{\rho^n}\vec{f}_v^n\end{aligned} \tag{A.9}$$

Then, subtracting Eq. A.9 with Eq. A.8 gives:

$$\frac{\vec{u}^{n+1}-\vec{u}^*}{\Delta t}=-\frac{1}{\rho^n}\nabla.P^{n+1} \tag{A.10}$$

Finally, by applying the divergence operator to both sides of Eq. A.10 and imposing that $\vec{u}^{n+1}$ is divergence free, the following Poisson equation for the pressure is obtained:

$$\nabla.[\frac{1}{\rho^n}\nabla.P^{n+1}]=\frac{1}{\Delta t}\nabla.\vec{u}^* \tag{A.11}$$

In summary, the predicted velocity $\vec{u}^*$ is advanced with Eq. A.8 in a first time. Provided $\vec{u}^*$ is known, Eq. A.11 represents a linear system for P^{n+1}. Hence, Eq. A.11 is solved with a DPCG method[105] to assess the pressure, and P^{n+1} is then used to compute the velocity at the end of the time step ($\vec{u}^{n+1}$), as stated by Eq. A.10.

Equations. A.8, A.10 and A.11 are discretized in space by employing a finite-volume method (See Sec. 2.1.2). The three steps composing the time advancement

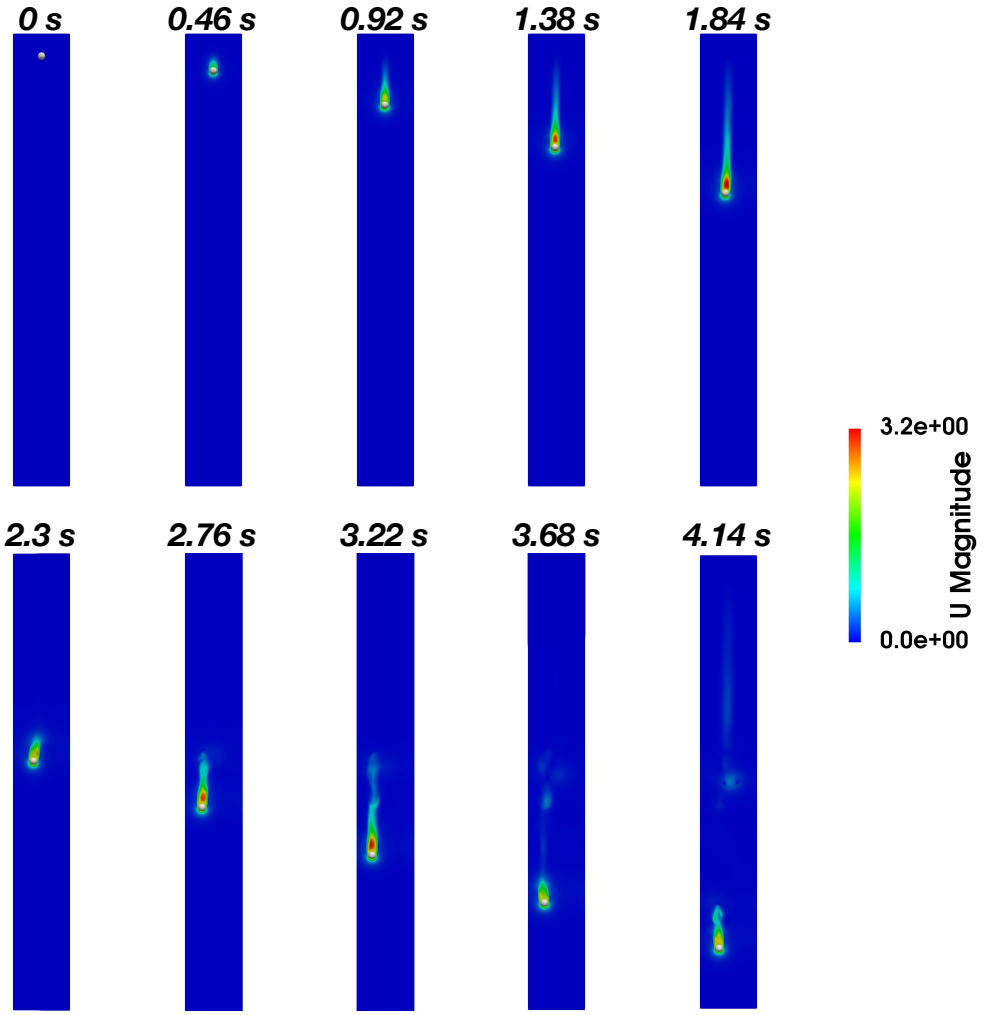

Figure A.1 – Simulation of a rigid bead falling in a viscous fluid. The bead is represented over a cut view of the fluid domain on which the velocity magnitude is shown.

of fluid equations are coupled with the solid membrane with a similar procedure than in Sec. 2.2 (see Fig. 2.10). Note that μ^n and ρ^n are calculated from the membrane location $\vec{X}^n$ at the beginning of the time step. More precisely, the indicator function I is assessed from $\vec{X}^n$ as done Sec. 2.2.2 with Eq. 2.90. Then, μ and ρ are set as:

$$\mu = \mu_{ext} + (\mu_{ext} - \mu_{in})I, \tag{A.12}$$

and

$$\rho = \rho_{ext} + (\rho_{ext} - \rho_{in})I, \tag{A.13}$$

Subscripts *in* and *ext* stem from internal and external parts of the membrane.

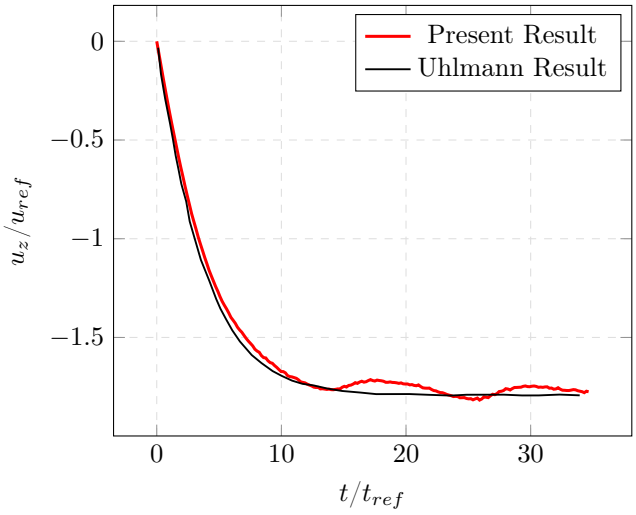

Figure A.2 – Vertical velocity of the bead when falling in a viscous fluid. The presented results are compared with those of Uhlmann[167].

A.2 Test case: bead falling in a viscous and incompressible fluid

This section aims at validating the implementation presented in the previous section. The tested configuration concerns a bead falling in an incompressible and Newtonian fluid. In this context, the configuration presented by Uhlmann[167] is retained. The fluid domain Ω_f is defined as [0, 1.25 m] × [0, 1.25 m] × [0, 10 m]. The external fluid has a density (ρ_{ext}) and a dynamic viscosity (μ_{ext}) of 1000 kg.m^{-3} and 1.04238 Pa.s, respectively. A source term modelling the gravity is added in the right-hand side of the momentum equation: $\vec{g}$=(0, 0, -9.81 m.s^{-2}). A density ratio (ρ_{in}/ρ_{ext}) of 2.56 is applied in such a way the particle falls in the $\vec{g}$ direction. The spherical membrane has a radius R_b of 1/12 m and the different moduli required for the modelling (see Eq. 2.52 and Eq. 2.69) are set as: $G_s = 2.5$ N.m^{-1}, $E_a = 2.5 \times 10^{5}$ N.m^{-1}, $E_b = 6.0$ J and $c_o = 12$ m^{-1}. Besides the viscosity ratio is set to μ_{in}/μ_{ext} is imposed to 50. In this way, the particle conserves its spherical aspect during the entire simulation. The fluid and solid grid are respectively defined with triangular and tetrahedral elements whose typical size equals 0.013 m. Figure. A.1 shows a sequence of sphere positions over a cut view of the fluid domain. The velocity magnitude is represented in the cut view. Note that the cutting plane passes through the sphere center of mass. Hence the slice of the fluid domain may differ from a picture to another in Fig. A.1.

From the series of sphere positions, the time evolution of the particle vertical velocity (u_z) is calculated and compared with results of Uhlmann[167] in Fig. A.2. Bead velocities are scaled with u_{ref} that equals $\sqrt{|\vec{g}|2r_a}$. Moreover, in Fig. A.2, the time scale is dimensionless since it is divided by $t_{ref} = \sqrt{2r_a/|\vec{g}|}$. The bead velocity increases in a transition period (viz. $t/t_{ref} < 10$) and then stabilizes at a velocity u_z/u_{ref} around 1.75. The present simulation displays an oscillating behavior of the velocity, that occurs after the transition phase. This was not reported by Uhlmann, as Fig. A.2 shows. Nevertheless, these oscillations appear to occur around velocities

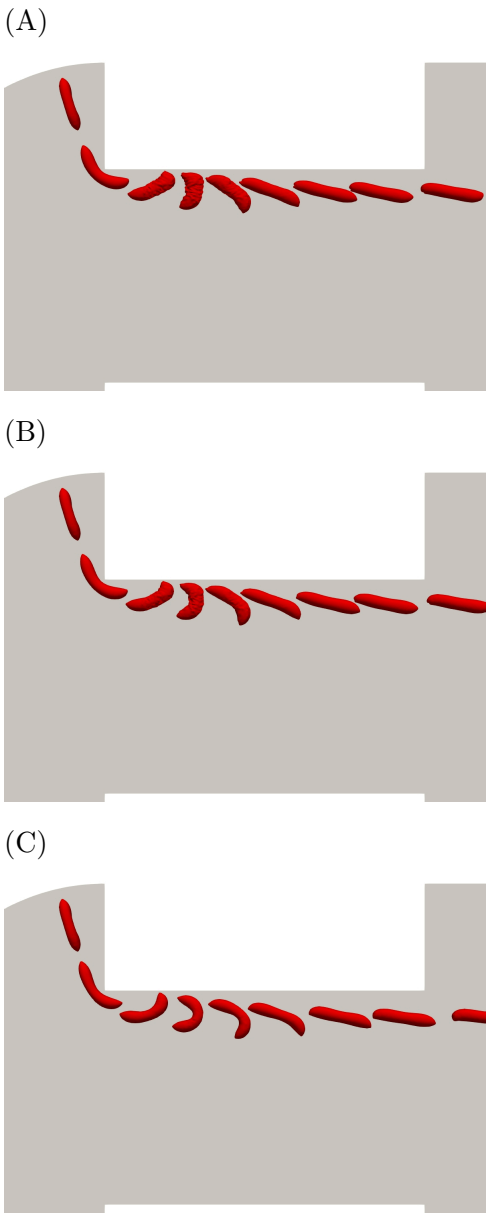

Figure A.3 – Consecutive RBC positions in the aperture for three different internal densities: (A), (B) and (C) are simulated with densities of 1000 kg.m^3, 1200 kg.m^3 and 2000 kg.m^3, respectively.

supported by Uhlmann and the proposed method is overall in good agreement with the reference.

A.3 Heavier RBC in a Coulter counter

In this section, the impact of the cytosol density on the impedance pulse is assessed. The case 10 performed in Chap. 4 (see Sec. 4.3) is performed two times more, but by imposing internal densities (ρ_{in}) of 1200 kg.m^3 and 2000 kg.m^3. As a reminder, the membrane is defined as follows: G_s=2.5$\times$ 10^{-6} N.m^{-1}, E_a=2.5$\times$ 10^{-1} N.m^{-1},

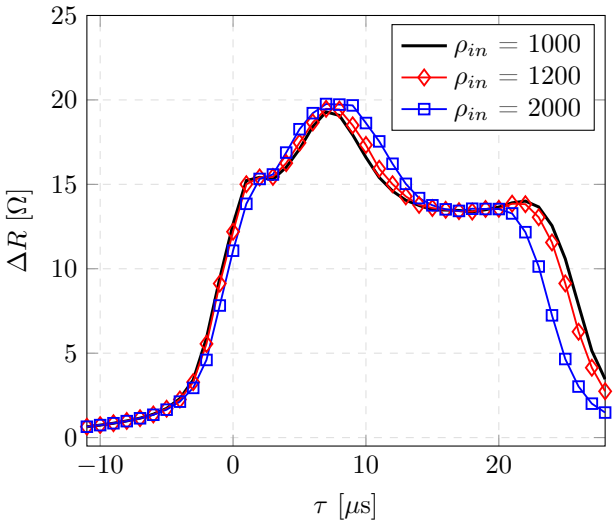

Figure A.4 – Impedence pulses obtained at different cytosol densities (ρ_{in}).

E_b=6.0 × 10^{-19} J, c_0=0. The internal kinematic viscosity is set as 18×10^{-6} $m^2.s^{-1}$. Note also that the external fluid has a kinematic viscosity (ν_{ext}) and a density (ρ_{ext}) of 1×10^{-6} $m^2.s^{-1}$ and 1000 $kg.m^3$, respectively. The cases with internal densities of 1200 $kg.m^3$ and 2000 $kg.m^3$ will be compared with case 10 that is actually equivalent to a simulation performed at ρ_{in} = 1000 $kg.m^3$ (that equals to the external density).

An internal density of 1200 $kg.m^3$ is consistent with physiological values [106]. Hence, the case performed with ρ_{in} = 2000 $kg.m^3$ is definetly to large. The plasma has a density similar to water (1000 $kg.m^3$), thus explaining the sedimentation of RBCs under gravity. The dynamics obtained for the different internal densities are shown in Fig. A.3. Overally, the trajectory is not significantly impacted when increasing ρ_{in} from 1000 to 2000 $kg.m^3$ (see Fig. A.3A, B and C). Nevertheless, by comparing Fig. A.3A and C, it is observed that imposing an internal density equalling twice the external density deflects the RBC trajectory to the orifice core region, that is physically meaningful. Indeed, the RBC inertia is higher at ρ_{in} = 2000 $kg.m^3$, thus it is more difficult for the cell to pursue the streamline on the bend at the aperture inlet. Besides, when increasing the internal density, the cell tends to take a crescent shape after the inlet bend. When turning in the shearing region, the RBC is harder to set in motion with an higher ρ_{in}. Consequently, the RBC resists more to the rotation, which yield a crescent shape (see Fig. A.3C).

In Fig. A.4, pulses related to the dynamics of Fig. A.3 are shown. Globally, increasing ρ_{in} reduces the pulse length. Increasing ρ_{in} to 2000 $kg.m^3$ yields a substantial impact on the pulse (see Fig. A.4), but remind that such value is not relevant. However, considering an internal density equaling 1200 $kg.m^3$, no significant difference with 1000 $kg.m^3$ is observed. One conclude that the impact of the cytosol density on the electrical pulse is negligible, in a reasonable physiological range.

Appendix B

Issues and preliminary results for very near wall trajectories

In Fig. 4.18 of Chap. 4, a cluster located at $\mathcal{P}^r$ around 10 % is not retrieved numerically by considering trajectories of Fig. 4.10. This part of the experimental acquisition is related to larger pulses (viz. larger $\mathcal{W}^r$) than the remaining data. Hence, a computation performed by using a streamline closer to the wall than all cases of Fig. 4.10 is presented in the following. As presented in Chap. 4, the streamline extracted from the carrying flow is a key component of the pipeline for the numerical simulation of deformable particles in Coulter counters. Although RBCs are not enforced to pursue the streamline, it gives an a priori idea on where the particle is going to flow in the orifice. The computation presented hereafter is not included in the main part of this thesis because numerical instabilities make the results questionable. Still, the presented findings appear to confirm that the aforementionned pulses population is associated to trajectories in a really close vincinity of walls.

From computation NSS0 of Sec. 3.1.1 a streamline passing by point (0, 23 μm, 0) is chosen. For comparison purposes, case 10 of Fig. 4.10 was performed from a streamline going through (0, 20 μm, 0). Then, applying the pipeline of Fig. 4.2 renders results of Fig. B.1. In the **top** row, the RBC dynamics inside the aperture is shown. Besides, a zoom in the membrane highlights the issues encountered during such computations. Indeed, triangular elements describing the membrane intersect at some points, which is definitely not physical. Although this computation is shown to be unstable, the related pulse is located in the cluster that has not been retrieved previously (see **bottom** row in Fig. B.1). As shown by the pulses signatures in Fig. B.1, this cluster is made of pulses for which the electrical peak is higher than the peak of rotation. The electrical peak arises from the dense electrical field near the aperture corners. Remind that this phenomenon explained the typical 'M-shapped' pulses observed for spheres. In that sense, the metric $\mathcal{P}^r$ (see Eq. 4.6) does not locate the peak of rotation but the substantial electrical peak at the very beginning of the pulse. This explains why this pulse population is isolated in the $\mathcal{P}^r/\mathcal{W}^r$ representation of the acquisition.

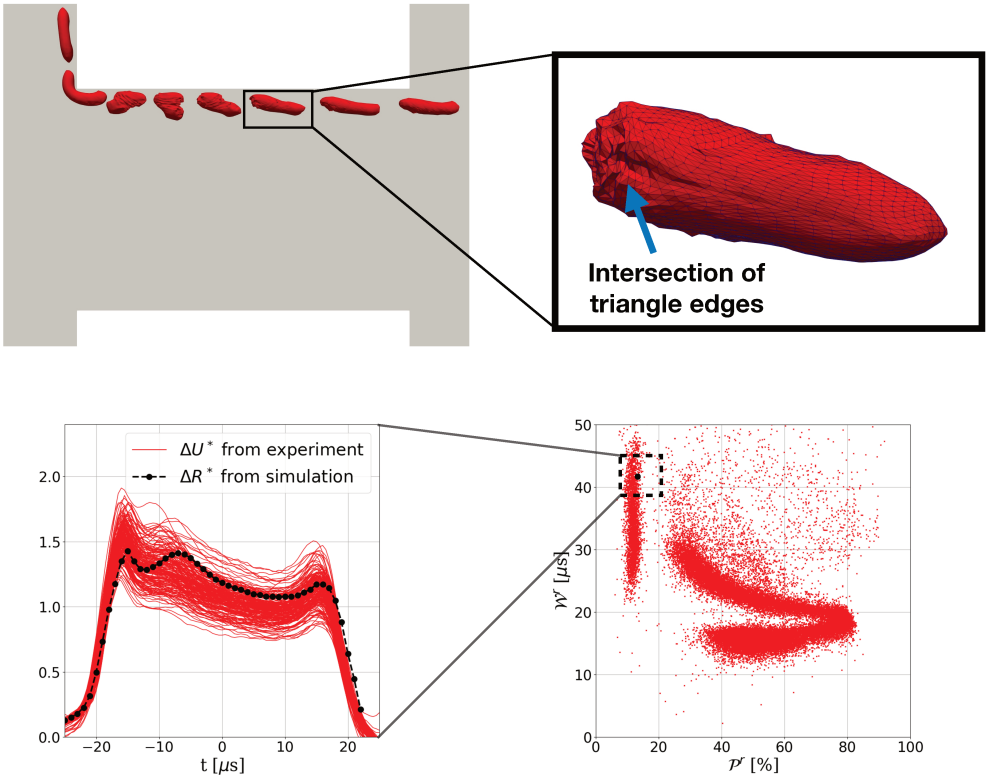

Figure B.1 – Numerical simulation of a RBC when a streamline passing by point (0, 23 μm, 0) is considered in the pipeline of Chap. 4. The RBC parameters are taken as in Sec. 4.3. The **top** row shows a series of RBC following shapes inside the orifice. The **bottom** row display the associated electrical print superimposed with experimental pulses. In addition, the location of this numerical pulse on a $\mathcal{W}^r/\mathcal{P}^r$ graph is provided.

Appendix C

Neural Networks

In the present work, NNs are used to build models allowing an assessment of cells features when they flow in a Coulter counter. For example, cells features may include the mechanical behaviour, the shape, or the trajectory of RBCs. These indications should be deduced from the electrical pulses, which implies NNs that take a temporal signal (viz. a pulse) as an income for rendering the cell characteristics.

Neural Networks (NNs) are one of the numerous machine learning methods. The reader is referred to [59] for an overview of existing methods. Briefly, machine learning consists in building a predictive model from a database. The two main branches in machine learning are supervised and unsupervised learning. The latter is not treated in this work. In supervised learning problems, the database is composed by a number N_{data} of observations that are couples a^{in}/a^{obs}. Machine learning models are constructed in a way that they predict a value a^{pred} as close as a^{obs} from the corresponding a^{in}, including for values that were not used to build the model. Hence, the dataset from which the model is derived (also referred as training database) must be representative of all the possible observations so that a substantial number of data (N_{data}) is generally required.

NNs are models built by combining simple mathematical objects called neurons (see Fig. C.1). Given a number N of inputs x_i, it computes z, the sum of x_i weighted by parameters w_i:

$$z = \sum_{i=1}^{N} x_i w_i \tag{C.1}$$

Then, an activation function f_a is applied to the weighted sum z, that leads to the neural output y:

$$\begin{aligned} y &= f_a(z) \\ &= f_a\left(\sum_{i=1}^{N} x_i w_i\right) \end{aligned} \tag{C.2}$$

The combination of these elementary neurons enables the construction of complex and non-linear models. If the number of neurons is sufficient, NNs were proven to approach any continuous functions in a compact subset of space [22, 66]. Moreover, NNs may tackle problems of arbitrary dimensions.

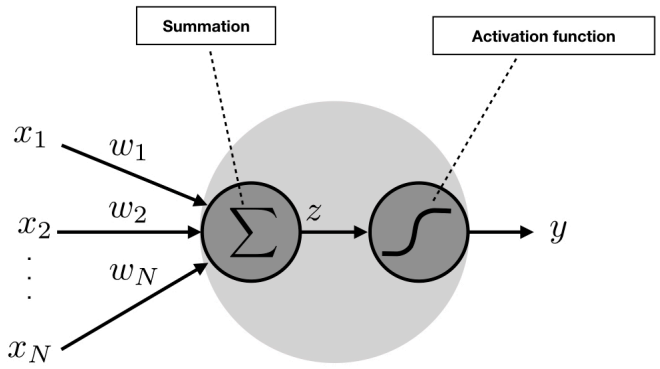

Figure C.1 – Principle of an elementary neuron that computes y from a given number of inputs x_i.

C.1 Introduction to Multi Layer Perceptrons

Let consider a problem in which N_o variables must be deduced from N_i inputs. Elementary neurons (see Fig. C.1) may be combined to design a more complex relation between inputs and outputs. The most known, used and described neurons arrangement is called Multi-Layer Perceptron (MLP) [45, 73, 120, 139]: neurons are organized in layers, and each neuron is linked with those of the neighbouring layers only (see Fig. C.2).

C.1.1 Construction and prediction of a MLP

Figure. C.2 is a diagram of an arbitrary MLP. The NN is composed by L_o layers. The outcome of the n-th neuron of the l-th layer is denoted by a_n^l and given as an input to each neuron of layer $l+1$. The weight linking the n-th neuron of layer l with the m-th neuron of layer $l+1$ is referred as $w_{n,m}^{l+1}$. Hence, versions of Eq. C.1 and Eq. C.2 suited to any neuron of a MLP write:

$$z_n^{l+1} = \sum_{m=1}^{N_l} a_m^l w_{m,n}^{l+1}, \tag{C.3}$$

and

$$\begin{aligned} a_n^{l+1} &= f_a(z_n^{l+1}) \\ &= f_a\left(\sum_{m=1}^{N_l} a_m^l w_{m,n}^{l+1}\right), \end{aligned} \tag{C.4}$$

respectively. With N_l, the number of neuron in layer l. In particular, the layer numbered by 1 takes the problem input size ($N_1 = N_i$) while the output layer (L_o) contains N_{L_o} neuron that equals the problem outcome dimension (N_o). This way, given a_m^1 (for m in [1 , N_i]) and $w_{m,n}^l$ (for m in [1 , N_{l-1}], n in [1 , N_l] and l in [2 ,

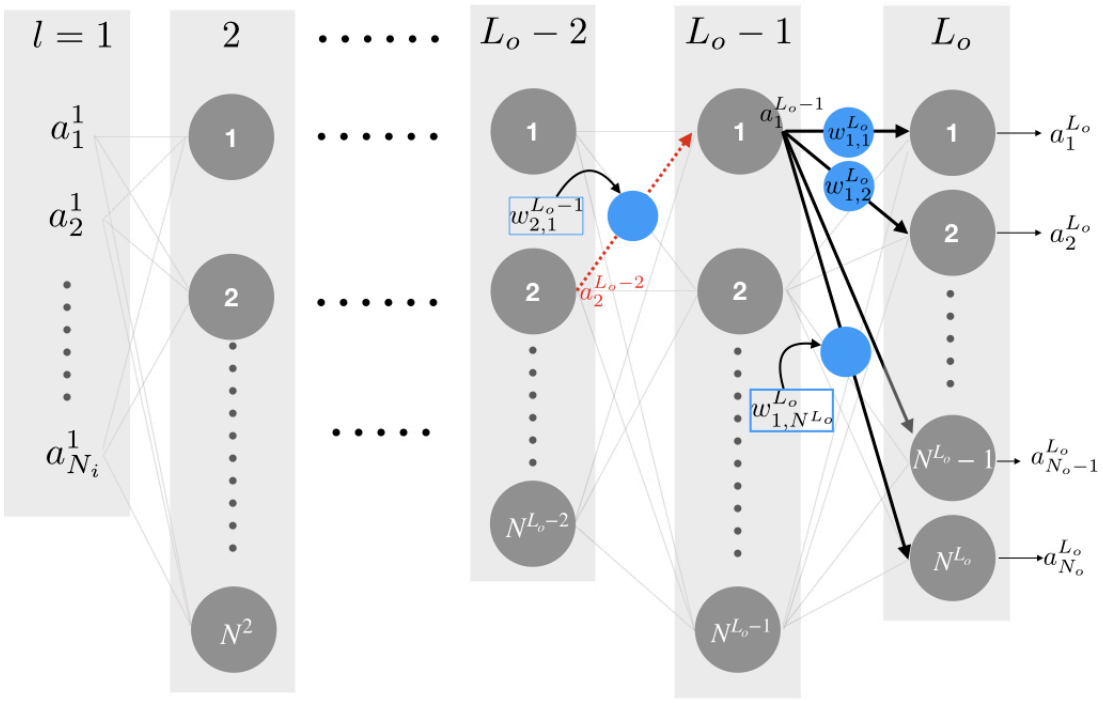

Figure C.2 – Principle of an arbitrary multilayer perceptron, an organisation of neurons by L_o successive layers. Inputs of the model a_n^1 are given in the first layer while the predictions $a_n^{L_o}$ (ie. the output of the model) are extracted from the last layer of the model (L_o).

L_o]), the MLP prediction (viz. $a_n^{L_o}$ for n in [1 , N_o]) is assessed by the feed-forward algorithm (see Alg. 1) that propagates the income in the MLP, layer by layer.

Algorithm 1 Feed forward algorithm

Require: input parameters a_m^1 and all weights $w_{m,n}^l$
  $l \leftarrow 2$
  while $l \leq L_o$ **do**
    $n \leftarrow 1$
    while $n \leq N_l$ **do**
      $z_n^l \leftarrow 0$
      $m \leftarrow 1$
      while $m \leq N_{l-1}$ **do**
        $z_n^l \leftarrow z_n^l + a_m^{l-1} w_{m,n}^l$
        $m \leftarrow m + 1$
      end while
      $a_n^l = f_a(z_n^l)$
      $n \leftarrow n + 1$
    end while
    $l \leftarrow l + 1$
  end while

C.1.2 Model training

Note that the model prediction depends on the MLP weights ($w^l_{m,n}$). Given a dataset composed by N_{data} observations, or couples a^{in}/a^{obs} (or a^1/a^{obs}), the learning step consists in the enhancing of the NN weights in such a way the errors between the model predictions a^{pred} (or a^{L_o}) and the actual values a^{obs} are minimized. This optimization problem is solved with a gradient descent method. More precisely, the MLP weights are updated as follow:

$$w^l_{m,n} \leftarrow w^l_{m,n} - \alpha \times \frac{\partial F_L}{\partial w^l_{m,n}} \tag{C.5}$$

With F_L, the loss function that quantifies the error between the predicted outcome a^{L_o} and the target value a^{obs} (note that a^{obs} and a^{L_o} have the same dimension). An example of loss function could be:

$$F_L(a^{L_o}, a^{obs}) = \sum_{n=1}^{N_{L_o}} (a^{obs}_n - a^{L_o}_n)^2 \tag{C.6}$$

In other words, given an initial guess for the weights and a couple a^1/a^{obs}, Alg. 1 is performed to calculate a^{L_o}, that is then compared with a^{obs} by F_L . Then, the derivatives of F_L according to the different weights ($\frac{\partial F_L}{\partial w^l_{m,n}}$) are used to update the model as stated in Eq. C.5.

In the following, $\frac{\partial F_L}{\partial w^l_{m,n}}$ is derived for a weight linked to the output layer (L_o) and for one that is located in a deeper layer. Based on these two examples, a generalization of an explicit and exact descent gradient algorithm for the updating of the NN weights is introduced. Known as 'back propagation', this approach was introduced by Rumelhart [142] and improved by many authors [8, 65, 96, 119, 126, 180]. Moreover, this method can easily be adapted with improved versions of the gradient descent algorithm, that are available in the literature [27, 81, 128].

Computation of the gradient for a weight located before the output layer: As an example, $\frac{\partial F_L}{\partial w^{L_o}_{1,1}}$ (see Fig. C.2) is treated. The chain rule allows the following developement of $\frac{\partial F_L}{\partial w^{L_o}_{1,1}}$:

$$\frac{\partial F_L}{\partial w^{L_o}_{1,1}} = \frac{\partial F_L}{\partial a^{L_o}_1} \times \frac{\partial a^{L_o}_1}{\partial z^{L_o}_1} \times \frac{\partial z^{L_o}_1}{\partial w^{L_o}_{1,1}} \tag{C.7}$$

The expressions of $\frac{\partial F_L}{\partial a^{L_o}_1}$ and $\frac{\partial a^{L_o}_1}{\partial z^{L_o}_1}$ are known by definition and are denoted by $F'_L(a^{L_o}_1)$ and $f'_a(z^{L_o}_1)$, respectively. Besides, regarding Eq. C.3, term $\frac{\partial z^{L_o}_1}{\partial w^{L_o}_{1,1}}$ equals $a^{L_o-1}_1$. Consequently Eq. C.7 may be rewritten as follow:

$$\frac{\partial F_L}{\partial w^{L_o}_{1,1}} = F'_L(a^{L_o}_1) \times f'_a(z^{L_o}_1) \times a^{L_o-1}_1 \tag{C.8}$$

Now, defining $\delta^{L_o}_i$ as:

$$\delta^{L_o}_i = F'_L(a^{L_o}_i) \times f'_a(z^{L_o}_i), \tag{C.9}$$

Eq. C.8 finally writes:

$$\frac{\partial F_L}{\partial w_{1,1}^{L_o}} = a_1^{L_o-1} \times \delta_1^{L_o} \tag{C.10}$$

Computation of the gradient for a weight located in a deeper layer: Term $\frac{\partial F_L}{\partial w_{2,1}^{L_o-1}}$ (see Fig. C.2) is dealt with in the following. Once again, the chain rule is used:

$$\frac{\partial F_L}{\partial w_{2,1}^{L_o-1}} = \frac{\partial F_L}{\partial a_1^{L_o-1}} \times \frac{\partial a_1^{L_o-1}}{\partial z_1^{L_o-1}} \times \frac{\partial z_1^{L_o-1}}{\partial w_{2,1}^{L_o-1}} \tag{C.11}$$

In Eq. C.11, $f_a'(z_1^{L_o-1})$ and $a_2^{L_o-2}$ appear directly (see Eq. C.3 and Eq. C.4, respectively). Hence, Eq. C.11 leads to:

$$\frac{\partial F_L}{\partial w_{2,1}^{L_o-1}} = \frac{\partial F_L}{\partial a_1^{L_o-1}} \times f_a'(z_1^{L_o-1}) \times a_2^{L_o-2} \tag{C.12}$$

Moreover, it should be noted that term $\frac{\partial F_L}{\partial a_1^{L_o-1}}$ of Eq. C.12 may be derived as follows:

$$\begin{aligned} \frac{\partial F_L}{\partial a_1^{L_o-1}} &= \sum_{i=1}^{N_{L_o}} \frac{\partial F_L}{\partial a_i^{L_o}} \times \frac{\partial a_i^{L_o}}{\partial z_i^{L_o}} \times \frac{\partial z_i^{L_o}}{\partial a_1^{L_o-1}} \\ &= \sum_{i=1}^{N_{L_o}} \delta_i^{L_o} \times w_{1,i}^{L_o} \end{aligned} \tag{C.13}$$

The first line of Eq. C.13 illustrates that F_L depends on $a_1^{L_o-1}$ through the N_{L_o} ouputs $a_i^{L_o}$. This is highlighted in Fig. C.2 by the continuous black arrows emerging from the first neuron of layer numbered by $L_o - 1$. The second line of Eq. C.13 is simply deduced from Eq. C.9 and Eq. C.3. Consequently, substituting Eq. C.13 in Eq. C.12 provides the following expression:

$$\frac{\partial F_L}{\partial w_{2,1}^{L_o-1}} = a_2^{L_o-2} \times f_a'(z_1^{L_o-1}) \times \sum_{i=1}^{N_{L_o}} \delta_i^{L_o} \times w_{1,i}^{L_o} \tag{C.14}$$

Finally, by introducing $\delta_1^{L_o-1}$ as:

$$\delta_1^{L_o-1} = f_a'(z_1^{L_o-1}) \times \sum_{i=1}^{N_{L_o}} \delta_i^{L_o} \times w_{1,i}^{L_o}, \tag{C.15}$$

Eq. C.14 yields:

$$\frac{\partial F_L}{\partial w_{2,1}^{L_o-1}} = a_2^{L_o-2} \times \delta_1^{L_o-1} \tag{C.16}$$

Generalization: In an analogous way, Eq. C.14 and Eq. C.16 may be developed for any weight in a hidden layer. Hence, Eq. C.10 and C.16 may be generalized to all neurons of the MLP:

$$\frac{\partial F_L}{\partial w_{m,n}^{l}} = a_m^{l-1} \times \delta_n^{l}, \tag{C.17}$$

with δ_n^l depending on whether the output layer L_o is considered or not, as illustrated by Eq. C.9 and Eq. C.15:

$$\delta_n^l = \begin{cases} f_a'(z_n^l) \times F_L'(a_n^l) & , l = L_o \\ f_a'(z_n^l) \times \sum_{i=1}^{N_{l+1}} \delta_i^{l+1} \times w_{n,i}^{l+1} & , l < L_o \end{cases} \tag{C.18}$$

Equation C.18 is the basis of the 'back propagation' algorithm that is presented in Alg. 2. Provided that z_n^l, a_n^l and $w_{m,n}^l$ are known, the $\delta_n^{L_o}$ are evaluated for a first time. Then, δ_n^l is propagated backward and layer by layer, up to the input L_1.

Algorithm 2 Back propagation

Require: z_n^l, a_n^l and $w_{m,n}^l$
Ensure: δ_n^l
  $l \leftarrow L_o$
  while $l \geq 1$ **do**
    $n \leftarrow 1$
    while $n \leq N^l$ **do**
      if $l = L_o$ **then**
        $\delta_n^l \leftarrow F_L'(a_n^l)$
      else
        $\delta_n^l \leftarrow 0$
        $m \leftarrow 0$
        while $m \leq N^{l+1}$ **do**
          $\delta_n^l \leftarrow \delta_n^l + \delta_m^{l+1} \times w_{n,m}^{l+1}$
          $m \leftarrow m + 1$
        end while
      end if
      $\delta_n^l \leftarrow \delta_n^l \times f_a'(z_n^l)$
      $n \leftarrow n + 1$
    end while
    $l \leftarrow l - 1$
  end while

Summary of the training procedure: Given a database containing N_{data} pairs a^1/a^{obs}, the training procedure of the model is performed as follow: (1) From an observation a^1/a^{obs} coming from the database, Alg. 1 is performed in order to assess z_n^l and a_n^l for each neuron of the NN. In particular, running Alg. 1 provides the model prediction $a_n^{L_o}$. (2) With a_n^l known for all neurons of the model, the back propagation algorithm (Alg. 2) is used to compute δ_n^l. (3) The gradients are then computed according to Eq. C.17 and the model weights $w_{m,n}^l$ are finally updated according to Eq. C.5. (4) A new couple a^1/a^{obs} is then chosen randomly from the data base and the procedure is restarted from step 1. Repeating this process for a sufficient number of observations, the model is expected to converge to an optimal solution.

Mini-batch descent gradient: Rather than a classical 'batch gradient descent' (BGD) that computes the error on the entire dataset to update the parameters, the

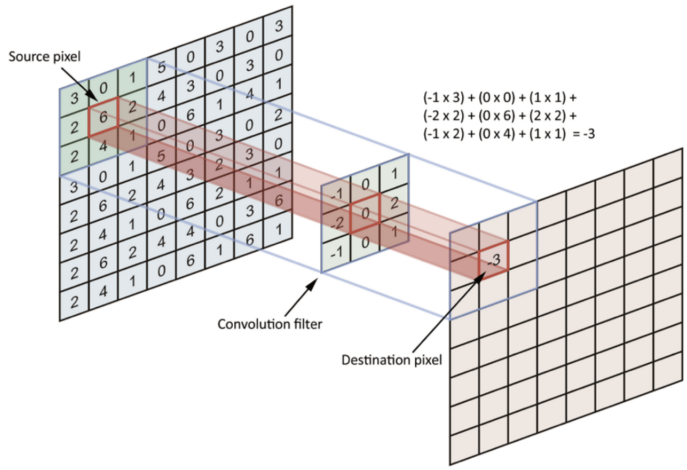

Figure C.3 – Principle of a convolution kernel applied on a portion of a source image as presented in https://towardsdatascience.com/. The image is defined as a two dimensional arrangement of pixels. The kernel is a matrix of size 3×3 that is applied to a part of the initial image that have the same size.

presented method upgrade the weights once for each observation. This approach is referred to as 'stochastic gradient descent' (SGD). An intermediate method is the 'mini-batch gradient descent' (MBGD) in which a small number of samples defined as 'batch' are treated at the same time. In such a strategy, the loss function is generally averaged over the batch:

$$F_L^G = \frac{1}{bs} \sum_{i=1}^{bs} F_L(a_i^{L_o}, a_i^{obs}) \tag{C.19}$$

With bs denoting the batch size and F_L^G referring to a general loss function. Note that if $bs = 1$, MBGD is equivalent to SGD while if $bs = N_{data}$ (the dataset size), MGBD is analogous to BGD. Using F_L^G instead of F_L in a MBSD strategy, implies the updating of the model weights by the F_L gradients averaged over the mini-batch:

$$w_{m,n}^l \leftarrow w_{m,n}^l - \alpha \times \sum_{i=1}^{bs} \left. \frac{\partial F_L}{\partial w_{m,n}^l} \right|_i \tag{C.20}$$

Training the model with MBSD is performed in several iterations called 'epochs'. In an epoch, the entire dataset is randomly divided in N_{data}/bs batches. For each batch, the model is updated according to Eq. C.20. The process is then stopped according to a criterion on the global error F_L^G, or when the maximal number of epochs is reached.

C.2 A few words on Convolutional Neural Networks

MLPs presented in the last section (see Fig. C.2) are fully-connected, which means each neuron is connected to all neurons of the previous and the following layers. Dealing with structured data like images or temporal series, Convolutional Neural

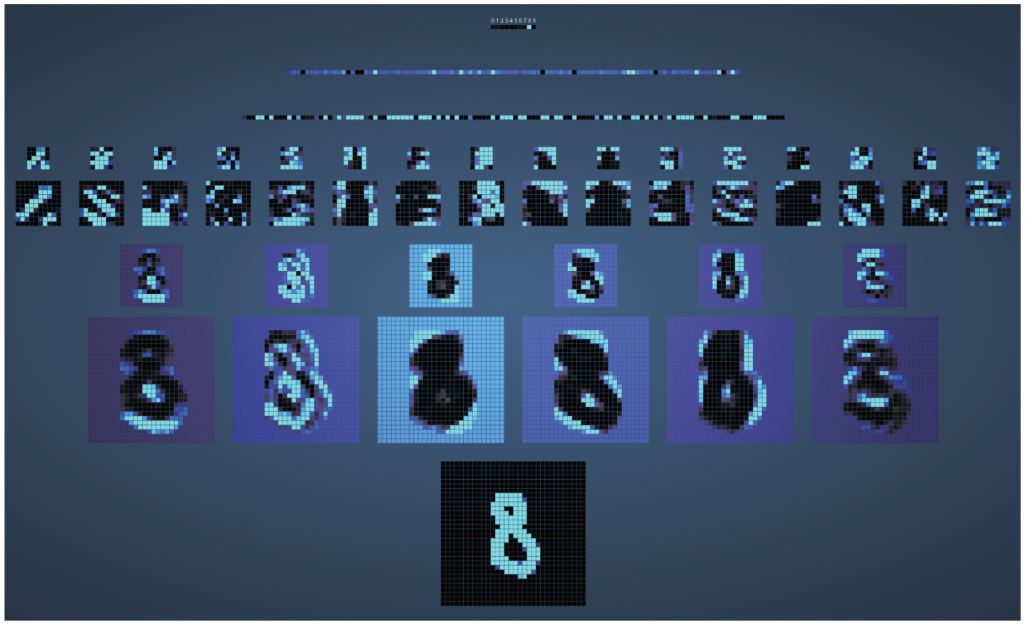

Figure C.4 – Convolutional neural network designed for the recognition of handwritten numbers provided by [58]. This model may be tested online at http://scs.ryerson.ca/~aharley/vis/. Successive convolutions performed on the initial image are provided by the software.

Networks (CNN) were shown to yield excellent results while involving fewer connections between neighbouring layers. In particular, CNNs imply convolution layers that are not fully-connected. By structured data, it is meant data in which the arrangement of the variables contains information. This appears intuitively when considering pixels composing an image. Instead of computing a neuron outlet by calculating the weighted sum over all neurons of the previous layer (according to Eq. C.4), in convolution layers, only a small part of former neurons is considered. This is done by scanning the preceding layer with a convolution kernel. Specific kernels are often employed in the image processing area for edges detection, features detection or smoothing, for example. This explains why CNNs have been widely used for image recognition [85]. Hence, in this brief introduction to CNNs, the example of image processing is retained. In a last section, an illustration of how applying CNNs to electrical pulses is presented.

C.2.1 Convolution kernel

Given a picture of dimension $N_h^p \times N_w^p \times D$, a convolution kernel (or filter) defined as a squared matrix $N_k \times N_k \times D$ is applied to groups of neighbouring pixels having the same size as the filter. The third dimension D equals 1 if the image is in level of gray, or 3 for a colored image (According to the RGB model), for instance. Figure. C.3 illustrates how a filter handles a pixel group to generate a new pixel (denoted by 'destination pixel'). In this example, $D = 1$ while $N_k = 3$. Considering a MLP, the destination pixel would be linked to all pixels of the source image, while using a 3×3 kernel, only 9 pixels are accounted for. This allows a

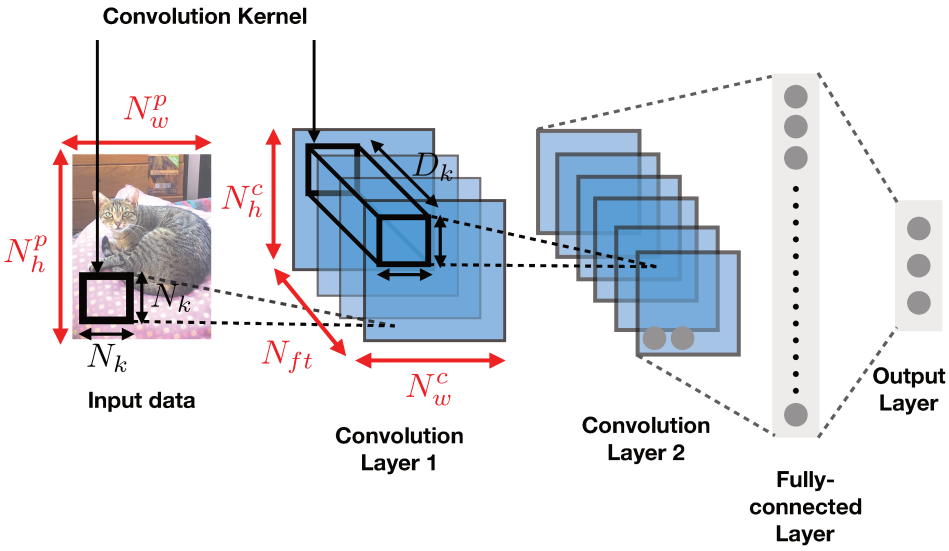

Figure C.5 – Diagram of a CNN dedicated to image treatments. The first layer ('Input data') takes an image of size $N_h^p \times N_w^p$ and two convolution layers are applied prior to two fully connected layers. N_h^p and N_w^p denote the number of pixels describing each picture directions.

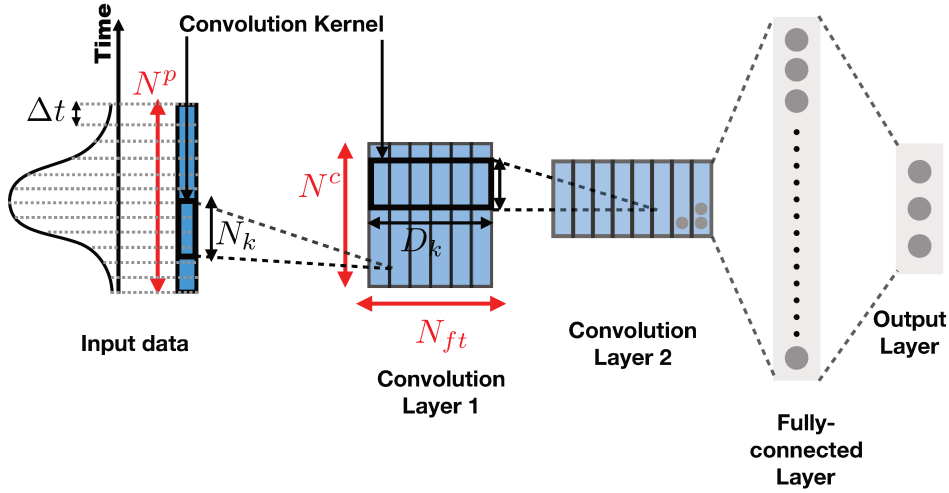

Figure C.6 – Diagram of a CNN dedicated to times series. The first layer ('Input data') reads a signal of size N^p and two convolution layers are applied prior to two fully-connected layers. Note that N^p represents the number of time steps describing the signal.

substantial reduction in the number of model weights. Scanning the source image with the kernel provides a filtered image, also called features map. During the scan, the kernel is moved on the initial picture with a pixel increment S.

C.2.2 Convolution Layer

Several kernels and as many features maps are included in a convolution layer. In Fig. C.4 an initial handwritten image leads to 6 filtered images by the use of six

kernels, for instance. This CNN was designed and trained to recognize handwritten numbers [58] and is available (http://scs.ryerson.ca/~aharley/vis/). A number may be drawn directly on the web page and the CNN renders on live the model prediction. Moreover, an insight of the successive filterings applied on the image is provided. When N_{ft} kernels are involved, a convolution layer, leads to an image of dimension $N_h^c \times N_w^c \times N_{ft}$. In which $N_h^c = \frac{N_h^p - N_k}{S}$, $N_w^c = \frac{N_w^p - N_k}{S}$, and $N_h^p \times N_w^p$ is the size of the source image. This is illustrated in Fig. C.5 in which the 'input data' is filtered in N_{ft} features maps in 'Convolution Layer 1'. All features map are placed in parallel (see Fig. C.5), thus implying a three dimensional picture. Generally, all features maps of a convolution layer arise from kernels of the same size. Hence, if a convolution layer follows another one, the dimension D_k of its kernels equals the number of features maps N_{ft} of the preceding layer, as illustrated in Fig. C.5. Values composing kernels matrices are weights updated during the training step by proceeding as in Sec. C.1. Hence, the CNN identifies automatically the relevant filters to render the optimal results, regarding the training database. In summary, a convolution layer is defined by the number of kernels N_{ft}, the kernels size N_k, and the filter increment S. Note that kernels dimensions D_k are not user-defined parameters, since they depend on the previous layer. Regarding CNNs of Fig. C.4 and Fig. C.5, it should be noted that the last layers of the model are fully-connected layer (as in a MLP). Actually, a NN is said CNN if its first hidden layer is a convolutional layer.

C.2.3 CNN for electrical pulses

Images processing was taken as an example in this brief introduction to CNNs. However, electrical pulses may also be viewed as structured data, but with a sole dimension N^p. Hence the use of CNNs to detect relevant one-dimensional patterns in an electrical pulse seems appropriate. Dealing with temporal series should imply one dimensional kernels (see Fig. C.6). Besides, note that the notion of pixel (for images) is equivalent to the concept of time step when treating temporal signals. The CNN shown in Fig. C.6 is inspired from Fig. C.5 but is devoted to one-dimensional time series sequences.

Appendix D

Numerical Database

As part of this thesis, Neural Networks (NN) were trained on the basis of numerical data. In this appendix, all simulations performed in the aims of building the numerical databases are reported. Numerical simulation are achieved with the method presented in Sec. 4.1 and only five parameters are varied in the computations: the internal viscosity ν_{in}, the shear modulus G_s, the reduced volume $\mathcal{Q}$, the streamline on which the cell is deposited, and the membrane surface S_m. The streamline is parametrized by r_a, defining the point (0, r_a, 0) to which it gets through. Having shown negligible effects on the impedance pulse the remaining parameters are kept constant in all cases presented in the following. More precisely, the curavature modulus, the spontaneous curvature and the area modulus are set as: $E_b = 6 \times 10^{-19}$ J, $c_o = 0\ m^{-1}$ and E_a= 2.5 $\times$ 10^{-1} N.m^{-1}. All simulated cases are shown in Tab. D.1.

Given the membrane surface S_m, the reduced volume $\mathcal{Q}$ tells us the volume enclosed by the cell. Equivalently, $\mathcal{Q}$ specifies S_m if the cell volume is provided. Hence, a change of $\mathcal{Q}$ may be done by a modification of the membrane surface or the cell volume. In practice, the cell shape is obtained from a discocyte membrane of given S_m (filled out in Tab. D.1) with an initial reduced volume of 0.65. Provided S_m and $\mathcal{Q}$, the cell reference volume $V_p = \mathcal{Q}\frac{4}{3}\pi\sqrt{\frac{S_m}{4\pi}}^3$ is taken as an input by solver FSIS (see Sec. 2.2) in a preliminary simulation. In this calculation, the 'volume conservation' routine ensures a cell volume of V_p, and the area modulus E_a ensures a membrane surface of S_m. The final cell shape then results in the competition between bending and shear resistances. Hence, at the end of the equilibrium shape calculation, the cell has the expected reduced volume of $\mathcal{Q}$. The computation of membrane equilibrium shapes with solver FSIS was detailed in [46] and used in [91], for instance.

As mentioned in Sec. 3.2, a specific fluid grid is required for each considered streamline (ie. r_a). For the sake of convenience, r_a is included in [16 μm, 17 μm, 18 μm, 19 μm, 20 μm].

D.1 Database employed in the detection of RBCs rotation

In Sec. 5.3, a NN is trained to isolate pulses generated by RBCs rotating in the aperture from those induced by cells showing a constant orientation. In this modelling, the training procedure makes use of cases 1-85. Reminding that the rotation experienced by RBCs is closely linked to the followed trajectory, the dataset spreads over a range of r_a covering a substantial part of the aperture. Besides, parameters ν_{in}, G_s, $\mathcal{Q}$ and S_m are varied in order to make the model robust with respect to the RBCs morphology and rheology.

D.2 Database used for the assessement of RBCs parameters

The purpose of Sec. 6.3 is to build a NN capable of rendering the RBC parameters from the associated impedance pulse. In that sense, cases 86-382 of Tab. D.1 are considered. Note that the membrane surface S_m is the same for all this dataset. That means cell volumes may differ in these different cases, depending on the reduced volume $\mathcal{Q}$. The pulse amplitude is proportional to the cell volume, but in the approach of Sec. 6.3 pulses are scaled with their respective maximum before being processed by NNs. Hence, variations in S_m (and thus in volume) would not have impacted the modelling. In Fig. D.1 cases 86-382 are represented on a three dimensionnal plot according to ν_{in}, G_s and $\mathcal{Q}$. The parameter a_r is not shown in the graph, and remind that S_m is constant for all these cases. The first part of this database (86-318) is regularly sampled as shown by red bold circles, while the second part (319-382) is subject to random sampling by the use of a Latin HyperCube (LHC) method. Briefly, the range covered by the regular sampling (see Fig. D.1) was split into 63 subsets of equal dimensions. Then, a set of parameters (ν_{in}, G_s and $\mathcal{Q}$) is chosen randomly in each subset, thus leading to 63 cases (319-382 in Tab. D.1). Parameter r_a is drawn randomly in [16 μm, 17 μm, 18 μm, 19 μm, 20 μm].

Table D.1 – Numerical database

N_o	$\nu_{in}[m^2.s^{-1}]$	$G_s[N.m^{-1}]$	$\mathcal{Q}$	$r_a[m]$	$S_m[\mu m^2]$
1	1.500e-05	2.500e-06	0.650	0.0	134
2	1.500e-05	2.500e-06	0.650	1.5e-05	134
3	1.500e-05	2.500e-06	0.650	1.6e-05	134
4	1.500e-05	2.500e-06	0.650	1.7e-05	134
5	1.500e-05	2.500e-06	0.650	1.8e-05	134
6	1.500e-05	2.500e-06	0.650	1.9e-05	134
7	1.500e-05	2.500e-06	0.650	2.0e-05	134
8	1.800e-05	2.500e-06	0.650	0.0	134
9	1.800e-05	2.500e-06	0.650	5.0e-06	134
10	1.800e-05	2.500e-06	0.650	1.0e-05	134
11	1.800e-05	2.500e-06	0.650	1.25e-05	134

Table D.1 – Numerical database

NO	$\nu_{in}[m^2.s^{-1}]$	$G_s[N.m^{-1}]$	$\mathcal{Q}$	$r_a[m]$	$S_m[\mu m^2]$
12	1.800e-05	2.500e-06	0.650	1.5e-05	134
13	1.800e-05	2.500e-06	0.650	1.6e-05	134
14	1.800e-05	2.500e-06	0.650	1.7e-05	134
15	1.800e-05	2.500e-06	0.650	1.8e-05	134
16	1.800e-05	2.500e-06	0.650	1.9e-05	134
17	1.800e-05	2.500e-06	0.650	2.0e-05	134
18	2.100e-05	2.500e-06	0.650	0.0	134
19	2.100e-05	2.500e-06	0.650	1.5e-05	134
20	2.100e-05	2.500e-06	0.650	1.6e-05	134
21	2.100e-05	2.500e-06	0.650	1.7e-05	134
22	2.100e-05	2.500e-06	0.650	1.8e-05	134
23	2.100e-05	2.500e-06	0.650	1.9e-05	134
24	2.100e-05	2.500e-06	0.650	2.0e-05	134
25	1.800e-05	4.000e-05	0.650	0.0	134
26	1.800e-05	4.000e-05	0.650	1.5e-05	134
27	1.800e-05	4.000e-05	0.650	1.6e-05	134
28	1.800e-05	4.000e-05	0.650	1.7e-05	134
29	1.800e-05	4.000e-05	0.650	1.8e-05	134
30	1.800e-05	4.000e-05	0.650	1.9e-05	134
31	1.800e-05	4.000e-05	0.650	2.0e-05	134
32	1.800e-05	1.600e-04	0.650	0.0	134
33	1.800e-05	1.600e-04	0.650	1.5e-05	134
34	1.800e-05	1.600e-04	0.650	1.6e-05	134
35	1.800e-05	1.600e-04	0.650	1.7e-05	134
36	1.800e-05	1.600e-04	0.650	1.8e-05	134
37	1.800e-05	1.600e-04	0.650	1.9e-05	134
38	1.800e-05	1.600e-04	0.650	2.0e-05	134
39	1.800e-05	2.500e-06	0.650	0.0	125
40	1.800e-05	2.500e-06	0.650	1.5e-05	125
41	1.800e-05	2.500e-06	0.650	1.6e-05	125
42	1.800e-05	2.500e-06	0.650	1.7e-05	125
43	1.800e-05	2.500e-06	0.650	1.8e-05	125
44	1.800e-05	2.500e-06	0.650	1.9e-05	125
45	1.800e-05	2.500e-06	0.650	2.0e-05	125
46	1.800e-05	2.500e-06	0.650	0.0	142
47	1.800e-05	2.500e-06	0.650	1.5e-05	142
48	1.800e-05	2.500e-06	0.650	1.6e-05	142
49	1.800e-05	2.500e-06	0.650	1.7e-05	142
50	1.800e-05	2.500e-06	0.650	1.8e-05	142
51	1.800e-05	2.500e-06	0.650	1.9e-05	142
52	1.800e-05	2.500e-06	0.650	2.0e-05	142

Table D.1 – Numerical database

NO	$\nu_{in}[m^2.s^{-1}]$	$G_s[N.m^{-1}]$	$\mathcal{Q}$	$r_a[m]$	$S_m[\mu m^2]$
53	1.800e-05	2.500e-06	0.650	23.0e-6	134
54	1.800e-05	2.500e-06	0.650	22.0e-6	134
55	1.800e-05	2.500e-06	0.650	21.0e-6	134
56	1.800e-05	2.500e-06	0.650	14.0e-6	134
57	1.800e-05	2.500e-06	0.650	13.0e-6	134
58	1.800e-05	2.500e-06	0.650	12.0e-6	134
59	1.800e-05	2.500e-06	0.650	11.0e-6	134
60	1.800e-05	2.500e-06	0.750	0.0	134
61	1.800e-05	2.500e-06	0.750	1.5e-05	134
62	1.800e-05	2.500e-06	0.750	1.6e-05	134
63	1.800e-05	2.500e-06	0.750	1.7e-05	134
64	1.800e-05	2.500e-06	0.750	1.8e-05	134
65	1.800e-05	2.500e-06	0.750	1.9e-05	134
66	1.800e-05	2.500e-06	0.750	2.0e-05	134
67	1.800e-05	2.500e-06	0.750	2.1e-05	134
68	1.800e-05	2.500e-06	0.750	2.2e-05	134
69	1.800e-05	2.500e-06	0.750	2.3e-05	134
70	1.800e-05	2.500e-06	0.850	0.0	134
71	1.800e-05	2.500e-06	0.850	1.5e-05	134
72	1.800e-05	2.500e-06	0.850	1.6e-05	134
73	1.800e-05	2.500e-06	0.850	1.7e-05	134
74	1.800e-05	2.500e-06	0.850	1.8e-05	134
75	1.800e-05	2.500e-06	0.850	1.9e-05	134
76	1.800e-05	2.500e-06	0.850	2.0e-05	134
77	1.800e-05	2.500e-06	0.850	2.1e-05	134
78	1.800e-05	2.500e-06	0.850	2.2e-05	134
79	1.800e-05	2.500e-06	0.850	2.3e-05	134
80	1.800e-05	4.000e-05	0.650	23.0e-6	134
81	1.800e-05	4.000e-04	0.650	22.0e-06	134
82	1.800e-05	4.000e-03	0.650	21.0e-05	134
83	1.800e-05	1.600e-04	0.650	23.0e-6	134
84	1.800e-05	1.600e-03	0.650	22.0e-06	134
85	1.800e-05	1.600e-02	0.650	21.0e-05	134
86	1.500e-05	2.500e-06	0.550	1.6e-05	134
87	1.500e-05	2.500e-06	0.550	1.8e-05	134
88	1.500e-05	2.500e-06	0.550	2.0e-05	134
89	1.500e-05	2.500e-06	0.650	1.6e-05	134
90	1.500e-05	2.500e-06	0.650	1.8e-05	134
91	1.500e-05	2.500e-06	0.650	2.0e-05	134
92	1.500e-05	2.500e-06	0.750	1.6e-05	134
93	1.500e-05	2.500e-06	0.750	1.8e-05	134

Table D.1 – Numerical database

NO	$\nu_{in}[m^2.s^{-1}]$	$G_s[N.m^{-1}]$	$\mathcal{Q}$	$r_a[m]$	$S_m[\mu m^2]$
94	1.500e-05	2.500e-06	0.750	2.0e-05	134
95	1.500e-05	2.125e-05	0.550	1.6e-05	134
96	1.500e-05	2.125e-05	0.550	1.8e-05	134
97	1.500e-05	2.125e-05	0.550	2.0e-05	134
98	1.500e-05	2.125e-05	0.650	1.6e-05	134
99	1.500e-05	2.125e-05	0.650	1.8e-05	134
100	1.500e-05	2.125e-05	0.650	2.0e-05	134
101	1.500e-05	2.125e-05	0.750	1.6e-05	134
102	1.500e-05	2.125e-05	0.750	1.8e-05	134
103	1.500e-05	2.125e-05	0.750	2.0e-05	134
104	1.500e-05	4.000e-05	0.550	1.6e-05	134
105	1.500e-05	4.000e-05	0.550	1.8e-05	134
106	1.500e-05	4.000e-05	0.550	2.0e-05	134
107	1.500e-05	4.000e-05	0.650	1.6e-05	134
108	1.500e-05	4.000e-05	0.650	1.8e-05	134
109	1.500e-05	4.000e-05	0.650	2.0e-05	134
110	1.500e-05	4.000e-05	0.750	1.6e-05	134
111	1.500e-05	4.000e-05	0.750	1.8e-05	134
112	1.500e-05	4.000e-05	0.750	2.0e-05	134
113	1.800e-05	2.500e-06	0.550	1.6e-05	134
114	1.800e-05	2.500e-06	0.550	1.8e-05	134
115	1.800e-05	2.500e-06	0.550	2.0e-05	134
116	1.800e-05	2.500e-06	0.650	1.6e-05	134
117	1.800e-05	2.500e-06	0.650	1.8e-05	134
118	1.800e-05	2.500e-06	0.650	2.0e-05	134
119	1.800e-05	2.500e-06	0.750	1.6e-05	134
120	1.800e-05	2.500e-06	0.750	1.8e-05	134
121	1.800e-05	2.500e-06	0.750	2.0e-05	134
122	1.800e-05	2.125e-05	0.550	1.6e-05	134
123	1.800e-05	2.125e-05	0.550	1.8e-05	134
124	1.800e-05	2.125e-05	0.550	2.0e-05	134
125	1.800e-05	2.125e-05	0.650	1.6e-05	134
126	1.800e-05	2.125e-05	0.650	1.8e-05	134
127	1.800e-05	2.125e-05	0.650	2.0e-05	134
128	1.800e-05	2.125e-05	0.750	1.6e-05	134
129	1.800e-05	2.125e-05	0.750	1.8e-05	134
130	1.800e-05	2.125e-05	0.750	2.0e-05	134
131	1.800e-05	4.000e-05	0.550	1.6e-05	134
132	1.800e-05	4.000e-05	0.550	1.8e-05	134
133	1.800e-05	4.000e-05	0.550	2.0e-05	134
134	1.800e-05	4.000e-05	0.650	1.6e-05	134

Table D.1 – Numerical database

NO	$\nu_{in}[m^2.s^{-1}]$	$G_s[N.m^{-1}]$	$\mathcal{Q}$	$r_a[m]$	$S_m[\mu m^2]$
135	1.800e-05	4.000e-05	0.650	1.8e-05	134
136	1.800e-05	4.000e-05	0.650	2.0e-05	134
137	1.800e-05	4.000e-05	0.750	1.6e-05	134
138	1.800e-05	4.000e-05	0.750	1.8e-05	134
139	1.800e-05	4.000e-05	0.750	2.0e-05	134
140	2.100e-05	2.500e-06	0.550	1.6e-05	134
141	2.100e-05	2.500e-06	0.550	1.8e-05	134
142	2.100e-05	2.500e-06	0.550	2.0e-05	134
143	2.100e-05	2.500e-06	0.650	1.6e-05	134
144	2.100e-05	2.500e-06	0.650	1.8e-05	134
145	2.100e-05	2.500e-06	0.650	2.0e-05	134
146	2.100e-05	2.500e-06	0.750	1.6e-05	134
147	2.100e-05	2.500e-06	0.750	1.8e-05	134
148	2.100e-05	2.500e-06	0.750	2.0e-05	134
149	2.100e-05	2.125e-05	0.550	1.6e-05	134
150	2.100e-05	2.125e-05	0.550	1.8e-05	134
151	2.100e-05	2.125e-05	0.550	2.0e-05	134
152	2.100e-05	2.125e-05	0.650	1.6e-05	134
153	2.100e-05	2.125e-05	0.650	1.8e-05	134
154	2.100e-05	2.125e-05	0.650	2.0e-05	134
155	2.100e-05	2.125e-05	0.750	1.6e-05	134
156	2.100e-05	2.125e-05	0.750	1.8e-05	134
157	2.100e-05	2.125e-05	0.750	2.0e-05	134
158	2.100e-05	4.000e-05	0.550	1.6e-05	134
159	2.100e-05	4.000e-05	0.550	1.8e-05	134
160	2.100e-05	4.000e-05	0.550	2.0e-05	134
161	2.100e-05	4.000e-05	0.650	1.6e-05	134
162	2.100e-05	4.000e-05	0.650	1.8e-05	134
163	2.100e-05	4.000e-05	0.650	2.0e-05	134
164	2.100e-05	4.000e-05	0.750	1.6e-05	134
165	2.100e-05	4.000e-05	0.750	1.8e-05	134
166	2.100e-05	4.000e-05	0.750	2.0e-05	134
167	1.600e-05	8.750e-06	0.583	1.6e-05	134
168	1.600e-05	8.750e-06	0.583	1.7e-05	134
169	1.600e-05	8.750e-06	0.583	1.8e-05	134
170	1.600e-05	8.750e-06	0.583	1.9e-05	134
171	1.600e-05	8.750e-06	0.583	2.0e-05	134
172	1.600e-05	8.750e-06	0.716	1.6e-05	134
173	1.600e-05	8.750e-06	0.716	1.7e-05	134
174	1.600e-05	8.750e-06	0.716	1.8e-05	134
175	1.600e-05	8.750e-06	0.716	1.9e-05	134

Table D.1 – Numerical database

NO	$\nu_{in}[m^2.s^{-1}]$	$G_s[N.m^{-1}]$	$\mathcal{Q}$	$r_a[m]$	$S_m[\mu m^2]$
176	1.600e-05	8.750e-06	0.716	2.0e-05	134
177	1.600e-05	3.375e-05	0.583	1.6e-05	134
178	1.600e-05	3.375e-05	0.583	1.7e-05	134
179	1.600e-05	3.375e-05	0.583	1.8e-05	134
180	1.600e-05	3.375e-05	0.583	1.9e-05	134
181	1.600e-05	3.375e-05	0.583	2.0e-05	134
182	1.600e-05	3.375e-05	0.716	1.6e-05	134
183	1.600e-05	3.375e-05	0.716	1.7e-05	134
184	1.600e-05	3.375e-05	0.716	1.8e-05	134
185	1.600e-05	3.375e-05	0.716	1.9e-05	134
186	1.600e-05	3.375e-05	0.716	2.0e-05	134
187	2.000e-05	8.750e-06	0.583	1.6e-05	134
188	2.000e-05	8.750e-06	0.583	1.7e-05	134
189	2.000e-05	8.750e-06	0.583	1.8e-05	134
190	2.000e-05	8.750e-06	0.583	1.9e-05	134
191	2.000e-05	8.750e-06	0.583	2.0e-05	134
192	2.000e-05	8.750e-06	0.716	1.6e-05	134
193	2.000e-05	8.750e-06	0.716	1.7e-05	134
194	2.000e-05	8.750e-06	0.716	1.8e-05	134
195	2.000e-05	8.750e-06	0.716	1.9e-05	134
196	2.000e-05	8.750e-06	0.716	2.0e-05	134
197	2.000e-05	3.375e-05	0.583	1.6e-05	134
198	2.000e-05	3.375e-05	0.583	1.7e-05	134
199	2.000e-05	3.375e-05	0.583	1.8e-05	134
200	2.000e-05	3.375e-05	0.583	1.9e-05	134
201	2.000e-05	3.375e-05	0.583	2.0e-05	134
202	2.000e-05	3.375e-05	0.716	1.6e-05	134
203	2.000e-05	3.375e-05	0.716	1.7e-05	134
204	2.000e-05	3.375e-05	0.716	1.8e-05	134
205	2.000e-05	3.375e-05	0.716	1.9e-05	134
206	2.000e-05	3.375e-05	0.716	2.0e-05	134
207	1.700e-05	1.500e-05	0.616	2.0e-05	134
208	1.700e-05	1.500e-05	0.616	2.0e-05	134
209	1.700e-05	1.500e-05	0.683	2.0e-05	134
210	1.700e-05	1.500e-05	0.683	2.0e-05	134
211	1.700e-05	2.750e-05	0.616	2.0e-05	134
212	1.700e-05	2.750e-05	0.616	2.0e-05	134
213	1.700e-05	2.750e-05	0.683	2.0e-05	134
214	1.700e-05	2.750e-05	0.683	2.0e-05	134
215	1.900e-05	1.500e-05	0.616	2.0e-05	134
216	1.900e-05	1.500e-05	0.616	2.0e-05	134

Table D.1 – Numerical database

NO	$\nu_{in}[m^2.s^{-1}]$	$G_s[N.m^{-1}]$	$\mathcal{Q}$	$r_a[m]$	$S_m[\mu m^2]$
217	1.900e-05	1.500e-05	0.683	2.0e-05	134
218	1.900e-05	1.500e-05	0.683	2.0e-05	134
219	1.900e-05	2.750e-05	0.616	2.0e-05	134
220	1.900e-05	2.750e-05	0.616	2.0e-05	134
221	1.900e-05	2.750e-05	0.683	2.0e-05	134
222	1.900e-05	2.750e-05	0.683	2.0e-05	134
223	1.600e-05	8.750e-06	0.650	1.6e-05	134
224	1.600e-05	8.750e-06	0.650	1.8e-05	134
225	1.600e-05	8.750e-06	0.650	2.0e-05	134
226	1.600e-05	2.125e-05	0.583	1.6e-05	134
227	1.600e-05	2.125e-05	0.583	1.8e-05	134
228	1.600e-05	2.125e-05	0.583	2.0e-05	134
229	1.600e-05	2.125e-05	0.650	1.6e-05	134
230	1.600e-05	2.125e-05	0.650	1.8e-05	134
231	1.600e-05	2.125e-05	0.650	2.0e-05	134
232	1.600e-05	2.125e-05	0.716	1.6e-05	134
233	1.600e-05	2.125e-05	0.716	1.8e-05	134
234	1.600e-05	2.125e-05	0.716	2.0e-05	134
235	1.600e-05	3.375e-05	0.650	1.6e-05	134
236	1.600e-05	3.375e-05	0.650	1.8e-05	134
237	1.600e-05	3.375e-05	0.650	2.0e-05	134
238	1.800e-05	8.750e-06	0.583	1.6e-05	134
239	1.800e-05	8.750e-06	0.583	1.8e-05	134
240	1.800e-05	8.750e-06	0.583	2.0e-05	134
241	1.800e-05	8.750e-06	0.650	1.6e-05	134
242	1.800e-05	8.750e-06	0.650	1.8e-05	134
243	1.800e-05	8.750e-06	0.650	2.0e-05	134
244	1.800e-05	8.750e-06	0.716	1.6e-05	134
245	1.800e-05	8.750e-06	0.716	1.8e-05	134
246	1.800e-05	8.750e-06	0.716	2.0e-05	134
247	1.800e-05	2.125e-05	0.583	1.6e-05	134
248	1.800e-05	2.125e-05	0.583	1.8e-05	134
249	1.800e-05	2.125e-05	0.583	2.0e-05	134
250	1.800e-05	2.125e-05	0.650	1.6e-05	134
251	1.800e-05	2.125e-05	0.650	1.8e-05	134
252	1.800e-05	2.125e-05	0.650	2.0e-05	134
253	1.800e-05	2.125e-05	0.716	1.6e-05	134
254	1.800e-05	2.125e-05	0.716	1.8e-05	134
255	1.800e-05	2.125e-05	0.716	2.0e-05	134
256	1.800e-05	3.375e-05	0.583	1.6e-05	134
257	1.800e-05	3.375e-05	0.583	1.8e-05	134

Table D.1 – Numerical database

NO	$\nu_{in}[m^2.s^{-1}]$	$G_s[N.m^{-1}]$	$\mathcal{Q}$	$r_a[m]$	$S_m[\mu m^2]$
258	1.800e-05	3.375e-05	0.583	2.0e-05	134
259	1.800e-05	3.375e-05	0.650	1.6e-05	134
260	1.800e-05	3.375e-05	0.650	1.8e-05	134
261	1.800e-05	3.375e-05	0.650	2.0e-05	134
262	1.800e-05	3.375e-05	0.716	1.6e-05	134
263	1.800e-05	3.375e-05	0.716	1.8e-05	134
264	1.800e-05	3.375e-05	0.716	2.0e-05	134
265	2.000e-05	8.750e-06	0.650	1.6e-05	134
266	2.000e-05	8.750e-06	0.650	1.8e-05	134
267	2.000e-05	8.750e-06	0.650	2.0e-05	134
268	2.000e-05	2.125e-05	0.583	1.6e-05	134
269	2.000e-05	2.125e-05	0.583	1.8e-05	134
270	2.000e-05	2.125e-05	0.583	2.0e-05	134
271	2.000e-05	2.125e-05	0.650	1.6e-05	134
272	2.000e-05	2.125e-05	0.650	1.8e-05	134
273	2.000e-05	2.125e-05	0.650	2.0e-05	134
274	2.000e-05	2.125e-05	0.716	1.6e-05	134
275	2.000e-05	2.125e-05	0.716	1.8e-05	134
276	2.000e-05	2.125e-05	0.716	2.0e-05	134
277	2.000e-05	3.375e-05	0.650	1.6e-05	134
278	2.000e-05	3.375e-05	0.650	1.8e-05	134
279	2.000e-05	3.375e-05	0.650	2.0e-05	134
280	1.700e-05	1.500e-05	0.616	17.0e-6	134
281	1.700e-05	1.500e-05	0.650	17.0e-6	134
282	1.700e-05	1.500e-05	0.650	19.0e-6	134
283	1.700e-05	2.125e-05	0.616	17.0e-6	134
284	1.700e-05	2.125e-05	0.616	19.0e-6	134
285	1.700e-05	2.125e-05	0.650	17.0e-6	134
286	1.700e-05	2.125e-05	0.650	19.0e-6	134
287	1.700e-05	2.125e-05	0.683	17.0e-6	134
288	1.700e-05	2.125e-05	0.683	19.0e-6	134
289	1.700e-05	2.750e-05	0.650	17.0e-6	134
290	1.700e-05	2.750e-05	0.650	19.0e-6	134
291	1.800e-05	1.500e-05	0.616	17.0e-6	134
292	1.800e-05	1.500e-05	0.616	19.0e-6	134
293	1.800e-05	1.500e-05	0.650	17.0e-6	134
294	1.800e-05	1.500e-05	0.650	19.0e-6	134
295	1.800e-05	1.500e-05	0.683	17.0e-6	134
296	1.800e-05	1.500e-05	0.683	19.0e-6	134
297	1.800e-05	2.125e-05	0.616	17.0e-6	134
298	1.800e-05	2.125e-05	0.616	19.0e-6	134

Table D.1 – Numerical database

NO	$\nu_{in}[m^2.s^{-1}]$	$G_s[N.m^{-1}]$	$\mathcal{Q}$	$r_a[m]$	$S_m[\mu m^2]$
299	1.800e-05	2.125e-05	0.650	17.0e-6	134
300	1.800e-05	2.125e-05	0.650	19.0e-6	134
301	1.800e-05	2.125e-05	0.683	17.0e-6	134
302	1.800e-05	2.125e-05	0.683	19.0e-6	134
303	1.800e-05	2.750e-05	0.616	17.0e-6	134
304	1.800e-05	2.750e-05	0.616	19.0e-6	134
305	1.800e-05	2.750e-05	0.650	17.0e-6	134
306	1.800e-05	2.750e-05	0.650	19.0e-6	134
307	1.800e-05	2.750e-05	0.683	17.0e-6	134
308	1.800e-05	2.750e-05	0.683	19.0e-6	134
309	1.900e-05	1.500e-05	0.650	17.0e-6	134
310	1.900e-05	1.500e-05	0.650	19.0e-6	134
311	1.900e-05	2.125e-05	0.616	17.0e-6	134
312	1.900e-05	2.125e-05	0.616	19.0e-6	134
313	1.900e-05	2.125e-05	0.650	17.0e-6	134
314	1.900e-05	2.125e-05	0.650	19.0e-6	134
315	1.900e-05	2.125e-05	0.683	17.0e-6	134
316	1.900e-05	2.125e-05	0.683	19.0e-6	134
317	1.900e-05	2.750e-05	0.650	17.0e-6	134
318	1.900e-05	2.750e-05	0.650	19.0e-6	134
319	1.590e-05	6.004e-06	0.551	2.0e-05	134
320	1.650e-05	8.650e-06	0.601	2.0e-05	134
321	1.548e-05	1.021e-05	0.697	1.7e-05	134
322	1.544e-05	1.174e-05	0.724	1.6e-05	134
323	1.515e-05	1.910e-05	0.557	2.0e-05	134
324	1.561e-05	1.464e-05	0.634	1.9e-05	134
325	1.502e-05	1.905e-05	0.698	1.8e-05	134
326	1.519e-05	2.046e-05	0.725	1.6e-05	134
327	1.562e-05	2.400e-05	0.591	2.0e-05	134
328	1.623e-05	2.422e-05	0.613	2.0e-05	134
329	1.599e-05	2.599e-05	0.673	1.8e-05	134
330	1.567e-05	2.949e-05	0.717	2.0e-05	134
331	1.592e-05	3.402e-05	0.577	1.7e-05	134
332	1.532e-05	3.991e-05	0.631	1.6e-05	134
333	1.649e-05	3.518e-05	0.660	2.0e-05	134
334	1.537e-05	3.121e-05	0.715	1.6e-05	134
335	1.744e-05	8.919e-06	0.568	1.8e-05	134
336	1.746e-05	8.901e-06	0.622	2.0e-05	134
337	1.658e-05	1.046e-05	0.668	1.8e-05	134
338	1.747e-05	1.153e-05	0.723	1.7e-05	134
339	1.655e-05	1.236e-05	0.561	1.8e-05	134

Table D.1 – Numerical database

NO	$\nu_{in}[m^2.s^{-1}]$	$G_s[N.m^{-1}]$	$\mathcal{Q}$	$r_a[m]$	$S_m[\mu m^2]$
340	1.796e-05	1.925e-05	0.610	1.8e-05	134
341	1.653e-05	1.573e-05	0.669	1.7e-05	134
342	1.680e-05	1.422e-05	0.720	1.8e-05	134
343	1.681e-05	2.307e-05	0.578	1.8e-05	134
344	1.656e-05	2.330e-05	0.610	2.0e-05	134
345	1.688e-05	2.534e-05	0.656	2.0e-05	134
346	1.653e-05	2.371e-05	0.706	1.9e-05	134
347	1.749e-05	3.886e-05	0.594	1.7e-05	134
348	1.790e-05	3.072e-05	0.621	1.7e-05	134
349	1.692e-05	3.675e-05	0.665	2.0e-05	134
350	1.718e-05	3.265e-05	0.708	2.0e-05	134
351	1.835e-05	9.450e-06	0.600	1.6e-05	134
352	1.839e-05	1.161e-05	0.613	1.6e-05	134
353	1.877e-05	5.642e-06	0.665	2.0e-05	134
354	1.849e-05	4.686e-06	0.707	1.8e-05	134
355	1.913e-05	1.431e-05	0.558	1.8e-05	134
356	1.911e-05	1.293e-05	0.602	1.8e-05	134
357	1.865e-05	1.534e-05	0.693	1.9e-05	134
358	1.930e-05	2.055e-05	0.738	1.8e-05	134
359	1.869e-05	2.638e-05	0.587	2.0e-05	134
360	1.946e-05	3.018e-05	0.650	1.7e-05	134
361	1.923e-05	2.624e-05	0.680	2.0e-05	134
362	1.927e-05	2.634e-05	0.743	1.7e-05	134
363	1.826e-05	3.321e-05	0.590	2.0e-05	134
364	1.922e-05	3.145e-05	0.608	1.7e-05	134
365	1.927e-05	3.511e-05	0.664	1.9e-05	134
366	1.906e-05	3.913e-05	0.705	1.7e-05	134
367	2.067e-05	3.003e-06	0.558	1.9e-05	134
368	2.065e-05	6.120e-06	0.631	1.8e-05	134
369	2.099e-05	3.652e-06	0.692	1.8e-05	134
370	1.958e-05	6.020e-06	0.725	1.8e-05	134
371	2.058e-05	1.591e-05	0.567	1.7e-05	134
372	1.988e-05	1.672e-05	0.615	1.7e-05	134
373	1.966e-05	1.202e-05	0.666	2.0e-05	134
374	2.082e-05	1.819e-05	0.747	1.7e-05	134
375	2.021e-05	2.865e-05	0.589	1.8e-05	134
376	2.041e-05	2.875e-05	0.641	1.6e-05	134
377	2.020e-05	2.701e-05	0.681	1.7e-05	134
378	2.029e-05	2.896e-05	0.718	1.8e-05	134
379	2.009e-05	3.605e-05	0.562	1.8e-05	134
380	2.096e-05	3.632e-05	0.644	2.0e-05	134

Table D.1 – Numerical database

NO	$\nu_{in}[m^2.s^{-1}]$	$G_s[N.m^{-1}]$	$\mathcal{Q}$	$r_a[m]$	$S_m[\mu m^2]$
381	2.064e-05	3.834e-05	0.651	1.8e-05	134
382	1.966e-05	3.781e-05	0.726	1.7e-05	134

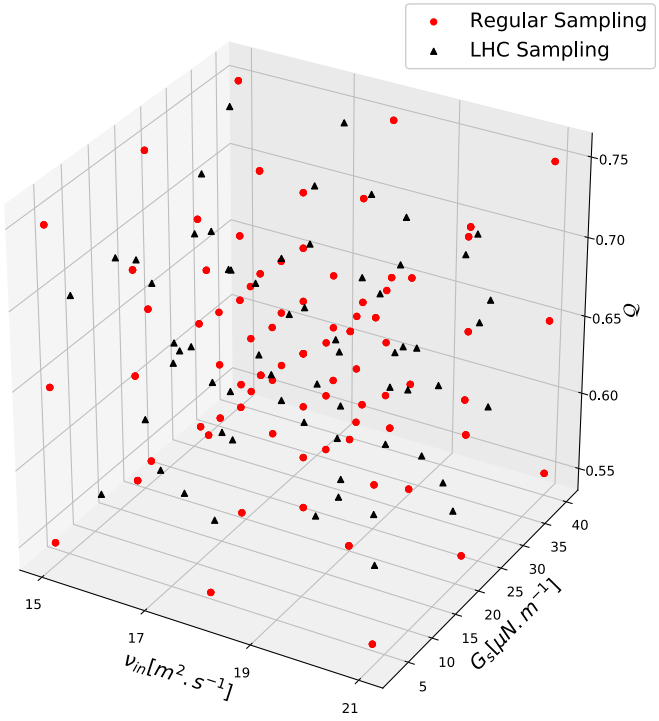

Figure D.1 – Three-dimensional plot of the Numerical database considered in models of Sec. 6.3. This database is related to cases 86-382 of Tab. D.1. A part of the database was performed in a random manner using a Latin Hyper Cube (LHC) procedure (shown in black triangles). The remaining part is made up of computations regularly spaced (shown in red bold points). The regular and the LHC samplings refer to cases 86-318 and 319-382, respectively.

Appendix E

Notations related to pulses

In the framework of this thesis, experimental tension pulses (ΔU) and numerical resistive pulses (ΔR) are dealt with. It is proposed to scale pulses from both sources with the aim of making them relative to the cells volumes, thus ΔU^* and ΔR^* were introduced. Several metrics computed from electrical prints are used ($\mathcal{W}$, $\mathcal{P}$, $\mathcal{R}$) and equivalents for scaled pulses are required ($\mathcal{W}^r$, $\mathcal{P}^r$). This scaling procedure is essential for providing comparisons between predictions arising from simulations with data from experiments (see Chap. 3 and Chap. 4). Besides, this convention underlies the normality defined in Chap. 6, which is independent from the differences of cells volumes from a blood sample to another. This appendix summarizes notations and metrics related to both experimental and numerical pulses.

E.1 Numerical pulses

Let consider a RBC of given parameters whose dynamics and electrical print ΔR for a specific trajectory are simulated. The maximum (in ohms) of the electrical print is denoted by ΔR_m. Considering the same RBC (same parameters) but undergoing a centred trajectory yields a 'bell-shaped' signature, for which the maximum is referred as $\Delta R_m|_{bs}$ (see **top** row of Fig. E.1). Then, the dimensionless numerical pulse ΔR^* is defined by scaling ΔR with $\Delta R_m|_{bs}$. 'Bell-shaped' signatures are assumed to be a robust measurement of the cells volumes. It should be noted that assessing ΔR^* requires two simulations unless the considered particle path is centred, and $\Delta R_m = \Delta R_m|_{bs}$.

For the case of a resistive pulse, $\mathcal{W}$ demands a resistive threshold ($thresh$), so as $\mathcal{P}$ (see expressions in Fig. E.1). In contrast, $\mathcal{W}^r$ and $\mathcal{P}^r$ require dimensionless thresholds ($thresh'$) that are relative to $\Delta R_m|_{bs}$. In this respect, $\mathcal{W}^r$, $\mathcal{P}^r$ and ΔR^* are dimensionless quantities that are relative to the cell volume (assessed by $\Delta R_m|_{bs}$).

E.2 Experimental pulses

Experimental pulses are measured as tension variations ΔU. With a notation similar to numerical data, the maximum of an experimental tension pulse is denoted by ΔU_m. Considering an entire experimental acquisition in which cells of different

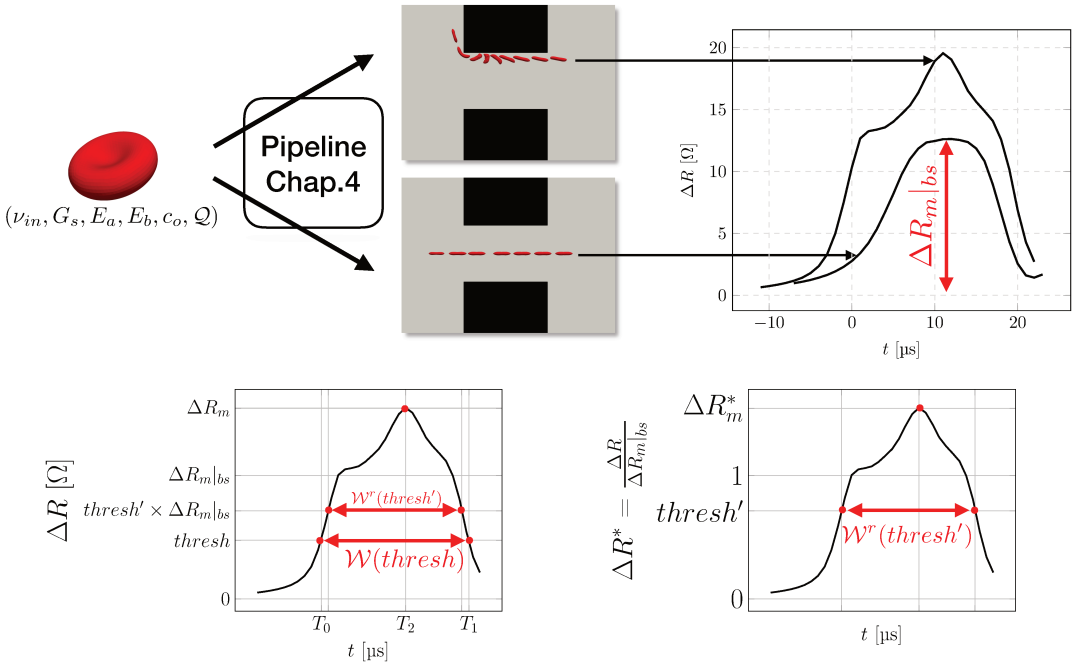

$$\mathcal{W}(thresh) = T_1 - T_0 \qquad \mathcal{W}^r(thresh') = \mathcal{W}(thresh' \times \Delta R_m|_{bs})$$
$$\mathcal{P}(thresh) = \frac{T_2 - T_0}{T_1 - T_0} \times 100 \qquad \mathcal{P}^r(thresh') = \mathcal{P}(thresh' \times \Delta R_m|_{bs})$$

Figure E.1 – Notations related to numerical resistive pulses (ΔR). ΔR^* is obtained by scaling the pulse with the maximum of the electrical signature obtained with the same cell, but following a centred trajectory ($\Delta R_m|_{bs}$). Metrics $\mathcal{W}$ and $\mathcal{P}$ involve a threshold (see $thresh$) that expresses in ohms. In contrast, $\mathcal{W}^r$ and $\mathcal{P}^r$ depends on a dimensionless threshold (see $thresh'$). Hence they are relative to $\Delta R_m|_{bs}$.

sizes are monitored, the mean cell volume (MCV) is measured by $\overline{\Delta U}_m|_{bs}$, the averaged maximum of bell-shaped signatures within the whole acquisition (see Fig. E.2). Methods for isolating such type of pulses are proposed in Chap. 5. Hence, defining $\Delta U^* = \Delta U / \overline{\Delta U}_m|_{bs}$ provides experimental pulses relative to the MCV.

Calculating $\mathcal{W}$ and $\mathcal{P}$ for an experimental pulse requires a threshold ($thresh$) expressed in volts (see expressions in Fig. E.2). In contrast, $\mathcal{W}^r$ and $\mathcal{P}^r$ require dimensionless thresholds ($thresh'$) that are relative to $\overline{\Delta U}_m|_{bs}$. In this respect, $\mathcal{W}^r$, $\mathcal{P}^r$ and ΔU^* are dimensionless quantities that are relative to the MCV (assessed by $\overline{\Delta U}_m|_{bs}$).

E.3 Width ratio metric

The metric $\mathcal{R}$ introduced in Chap. 5 expresses as:

$$\mathcal{R} = \frac{\mathcal{W}(p_u \times \Delta R_m)}{\mathcal{W}(p_d \times \Delta R_m)} \times 100, \tag{E.1}$$

or

$$\mathcal{R} = \frac{\mathcal{W}(p_u \times \Delta U_m)}{\mathcal{W}(p_d \times \Delta U_m)} \times 100, \tag{E.2}$$

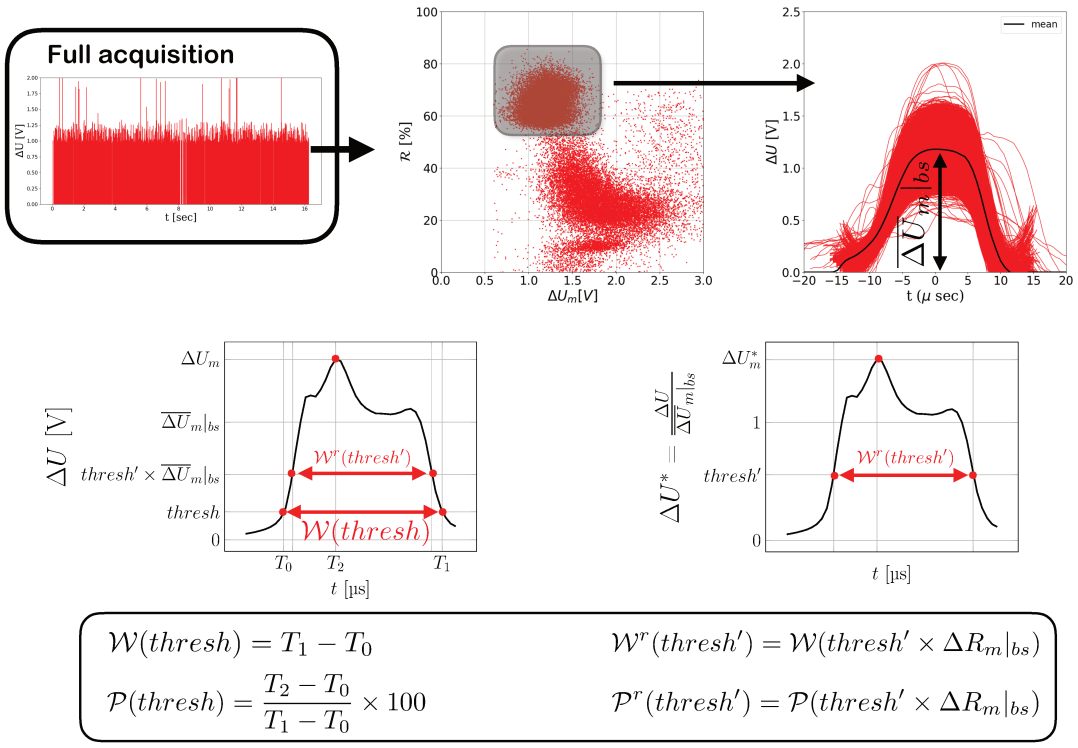

$$\mathcal{W}(thresh) = T_1 - T_0 \qquad \mathcal{W}^r(thresh') = \mathcal{W}(thresh' \times \Delta R_m|_{bs})$$

$$\mathcal{P}(thresh) = \frac{T_2 - T_0}{T_1 - T_0} \times 100 \qquad \mathcal{P}^r(thresh') = \mathcal{P}(thresh' \times \Delta R_m|_{bs})$$

Figure E.2 – Notations related to experimental tension pulses (ΔU). ΔU^* is obtained by scaling the pulse with the maximum of the 'bell-shaped' signatures arising from the acquisition ($\overline{\Delta U}_m|_{bs}$). 'Bell-shaped' pulses are extracted by employing the filtering methods introduced in Chap. 5 (the $\mathcal{R}$-based filter is shown as an illustration). Metrics $\mathcal{W}$ and $\mathcal{P}$ involve a threshold (see *thresh*) that expresses in volts. In contrast, $\mathcal{W}^r$ and $\mathcal{P}^r$ depends on a dimensionless threshold (see *thresh*′). Hence they are relative to $\overline{\Delta U}_m|_{bs}$.

depending on whether a resistive or experimental pulse is considered, respectively. Parameters p_u and p_d are dimensionless user-defined parameters. It should be noted that $\mathcal{R}$ involves computing two pulse widths ($\mathcal{W}$) that are relative to the maximum (ΔR_m or ΔU_m). Hence, the calculation of $\mathcal{R}$ is independent from the cell volume and the source from which the pulse arises (viz. experiments or simulations).

Bibliography

[1] M. Abkarian, M. Faivre, and H. A. Stone. High-speed microfluidic differential manometer for cellular-scale hydrodynamics. *Proceedings of the National Academy of Sciences*, 103(3):538–542, jan 2006.

[2] M. Abkarian, M. Faivre, and A. Viallat. Swinging of red blood cells under shear flow. *Physical Review Letters*, 98(188302), 2007.

[3] M. Abkarian and A. Viallat. Vesicles and red blood cells in shear flow. *Soft Matter*, 4:653–657, 2008.

[4] M. Abkarian and A. Viallat. Fluid-structure interactions in low-Reynolds-number flows. *On the importance of red blood cells deformability in blood flow. Royal Society of Chemistry, London*, pages 347–462, 2016.

[5] P. Agre, J. F. Casella, W. H. Zinkham, C. McMillan, and V. Bennett. Partial deficiency of erythrocyte spectrin in hereditary spherocytosis. *Nature*, 314(6009):380–383, Mar. 1985.

[6] P. Bagchi, P. C. Johnson, and A. S. Popel. Computational fluid dynamic simulation of aggregation of deformable cells in a shear flow. *Journal of Biomechanical Engineering*, 127(4):1070–1080, 2005.

[7] P. Balogh and P. Bagchi. A computational approach to modeling cellular-scale blood flow in complex geometry. *Journal of Computational Physics*, 334:280 – 307, 2017.

[8] S. Becker and Y. Lecun. Improving the convergence of back-propagation learning with second-order methods. 01 1989.

[9] H. Bow, I. V. Pivkin, M. Diez-Silva, S. J. Goldfless, M. Dao, J. C. Niles, S. Suresh, and J. Han. A microfabricated deformability-based flow cytometer with application to malaria. *Lab on a Chip*, 11(6):1065, 2011.

[10] M. O. Breitmeyer, E. N. Lightfoot, and W. H. Dennis. Model of red blood cell rotation in the flow toward a cell sizing orifice. *European Biophysics Journal*, 11:146–157, 1971.

[11] K. E. Bremmell, A. Evans, and C. A. Prestidge. Deformation and nanorheology of red blood cells: An AFM investigation. *Colloids and Surfaces B: Biointerfaces*, 50(1):43–48, jun 2006.

[12] S. B. Brian. On the distribution of red cell volumes. *Blood*, 31:503–515, 1968.

[13] D. D. Carlo, D. Irimia, R. G. Tompkins, and M. Toner. Continuous inertial focusing, ordering, and separation of particles in microchannels. *Proceedings of the National Academy of Sciences*, 104(48):18892–18897, nov 2007.

[14] S. Cha, T. Shin, S. S. Lee, W. Shim, G. Lee, S. J. Lee, Y. Kim, and J. M. Kim. Cell stretching measurement utilizing viscoelastic particle focusing. *Analytical Chemistry*, 84(23):10471–10477, nov 2012.

[15] J.-M. Charrier, S. Shrivastava, and R. Wu. Free and constrained inflation of elastic membranes in relation to thermoforming non-axisymmetric problems. *The Journal of Strain Analysis for Engineering Design*, 24(2):55–74, 1989.

[16] S. Chien, S. Usami, and J. F. Bertles. Abnormal rheology of oxygenated blood in sickle cell anemia. *Journal of Clinical Investigation*, 49:623–634, 1970.

[17] A. Chorin. Numerical solution of the Navier–Stokes equations. *Mathematics of Computation*, 22:745–762, 1968.

[18] J. Conboy, N. Mohandas, G. Tchernia, and Y. W. Kan. Molecular basis of hereditary elliptocytosis due to protein 4.1 deficiency. *New England Journal of Medicine*, 315(11):680–685, sep 1986.

[19] D. Cordasco and P. Bagchi. Intermittency and synchronized motion of red blood cell dynamics in shear flow. *Journal of Fluid Mechanics*, 759:472–488, 2014.

[20] D. Cordasco, Yazdani, and P. Bagchi. Comparison of erythrocyte dynamics in shear flow under different stress-free configurations. *Physics of Fluids*, 26(041902), 2014.

[21] W. H. Coulter. Means for counting particles suspended in a fluid, Oct. US Patent 2,656,508. 1953.

[22] G. Cybenko. Approximation by superpositions of a sigmoidal function. *Mathematics of Control, Signals and Systems*, 2(4):303–314, Dec 1989.

[23] M. Dao, C. Lim, and S. Suresh. Mechanics of the human red blood cell deformed by optical tweezers. *Journal of the Mechanics and Physics of Solids*, 51(11-12):2259–2280, nov 2003.

[24] E. M. Darling and D. D. Carlo. High-throughput assessment of cellular mechanical properties. *Annual Review of Biomedical Engineering*, 17(1):35–62, dec 2015.

[25] W. R. Dodson III and P. Dimitrakopoulos. Tank-treading of erythrocytes in strong shear flows via a nonstiff cytoskeleton-based continuum computational modeling. *Biophysical Journal*, 99:2906–2916, 2010.

[26] V. Doyeux, Y. Guyot, V. Chabannes, C. Prud'homme, and M. Ismail. Simulation of two-fluid flows using a finite element/level set method. Application to bubbles and vesicle dynamics. *Journal of Computational and Applied Mathematics*, 246:251–259, 2013.

[27] J. Duchi, E. Hazan, and Y. Singer. Adaptive subgradient methods for online learning and stochastic optimization. *J. Mach. Learn. Res.*, 12:2121–2159, July 2011.

[28] J. S. Dudani, D. R. Gossett, H. T. K. Tse, and D. D. Carlo. Pinched-flow hydrodynamic stretching of single-cells. *Lab on a Chip*, 13(18):3728, 2013.

[29] C. Dupont, A.-V. Salsac, B. Barthès-Biesel, M. Vidrascu, and P. Le Tallec. Coupling boundary integral and shell finite element methods to study the fluid structure interactions of a microcapsule in a simple shear flow. In *International Conference on Boundary Element and Meshless Techniques (Beteq), July 2013, Palaiseau, France*, 2013.

[30] C. Dupont, A.-V. Salsac, B. Barthès-Biesel, M. Vidrascu, and P. Le Tallec. Influence of bending resistance on the dynamics of a spherical capsule in shear flow. *Physics of Fluids*, 27(051902), 2015.

[31] F. Durst, S. Ray, B. Ünsal, and O. A. Bayoumi. The development lengths of laminar pipe and channel flows. *Journal of Fluids Engineering*, 127(6):1154–1160, June 2005.

[32] C. D. Eggleton and A. S. Popel. Large deformation of red blood cell ghosts in a simple shear flow. *Physics of Fluids*, 10(8):1834–1845, 1998.

[33] E. A. Evans and Y. C. Fung. Improved measurements of the erythrocyte geometry. *Microvascular Research*, 4:335–347, 1972.

[34] T. C. Evans and D. Jehle. The red blood cell distribution width. *The Journal of Emergency Medicine*, 9:71–74, jan 1991.

[35] A. Farutin, T. Biben, and C. Misbah. 3D numerical simulations of vesicle and inextensible capsule dynamics. *Journal of Computational Physics*, 275:539–568, 2014.

[36] D. A. Fedosov, B. Caswell, and G. Karniadakis. Systematic coarse-graining of spectrin-level red blood cell models. *Computer Methods in Applied Mechanics and Engineering*, 199:1937–1948, 2010.

[37] D. A. Fedosov, B. Caswell, and G. E. Karniadakis. A multiscale red blood cell model with accurate mechanics, rheology, and dynamics. *Biophysical Journal*, 98:2215–2225, 2010.

[38] D. A. Fedosov, B. Caswell, and G. E. Karniadakis. A multiscale red blood cell model with accurate mechanics, rheology, and dynamics. *Biophysical Journal*, 98:2215–2225, 2010.

[39] D. A. Fedosov, W. Pan, B. Caswell, G. Gompper, and G. E. Karniadakis. Predicting human blood viscosity in silico. *Proceedings of the National Academy of Sciences USA*, 108(29):11772–11777, 2011.

[40] D. A. Fedosov, M. Peltomäki, and G. Gompper. Deformation and dynamics of red blood cells in flow through cylindrical microchannels. *Soft Matter*, 10:4258–4267, 2014.

[41] E. Foessel, J. Walter, A.-V. Salsac, and D. Barthès-Biesel. Influence of internal viscosity on the large deformation and buckling of a spherical capsule in a simple shear flow. *Journal of Fluid Mechanics*, 672:477–486, 2011.

[42] A. M. Forsyth, J. Wan, W. D. Ristenpart, and H. A. Stone. The dynamic behavior of chemically "stiffened" red blood cells in microchannel flows. *Microvascular Research*, 80(1):37–43, jul 2010.

[43] J. B. Freund. Numerical simulation of flowing blood cells. *Annual Review of Fluid Mechanics*, 46:67–95, 2014.

[44] F. H. Gardner, J. D. Bessman, and J. Gilmer, P. Ridgway. Improved Classification of Anemias by MCV and RDW. *American Journal of Clinical Pathology*, 80(3):322–326, 09 1983.

[45] M. Gardner and S. Dorling. Artificial neural networks (the multilayer perceptron)—a review of applications in the atmospheric sciences. *Atmospheric Environment*, 32(14-15):2627–2636, aug 1998.

[46] E. Gibaud. *Numerical simulation of red blood cells flowing in a blood analyzer.* PhD thesis, Université de Montpellier, 2015.

[47] E. Gibaud, S. Mendez, D. Isèbe, and F. Nicoud. Numerical modelling of the dynamics of isolated red blood cells flowing in a cytometer. In *6th European Conference on Computational Fluid Dynamics (WCCM XI - ECCM V - ECFD VI), Barcelona, SPAIN, 20-25 July 2014.*, 2014.

[48] F. K. Glenister. Contribution of parasite proteins to altered mechanical properties of malaria-infected red blood cells. *Blood*, 99(3):1060–1063, feb 2002.

[49] D. Golibersuch. Method and apparatus for measuring small aspherical particles, Oct. US Patent 2,656,508. 1953.

[50] D. Golibersuch. Observation of aspherical particle rotation in poiseuille flow via the resistance pulse technique: I. application to human erythrocytes. *Biophysical Journal*, 13(3):265 – 280, 1973.

[51] D. R. Gossett, H. T. K. Tse, S. A. Lee, Y. Ying, A. G. Lindgren, O. O. Yang, J. Rao, A. T. Clark, and D. D. Carlo. Hydrodynamic stretching of single cells for large population mechanical phenotyping. *Proceedings of the National Academy of Sciences*, 109(20):7630–7635, apr 2012.

[52] M. Gross, T. Krüger, and F. Varnik. Rheology of dense suspensions of elastic capsules: normal stresses, yield stress, jamming and confinement effects. *Soft Matter*, 10:4360–4372, 2014.

[53] N. B. Grover, J. Naaman, S. Ben-Sasson, and F. Doljanski. Electrical sizing of particles in suspensions: I. theory. *Biophysical Journal*, 9:1398–1414, 1969.

[54] N. B. Grover, J. Naaman, S. Ben-Sasson, and F. Doljanski. Electrical sizing of particles in suspensions: III. rigid spheroids and red blood cells. *Biophysical Journal*, 12:1099–1116, 1972.

[55] J. Guck, R. Ananthakrishnan, H. Mahmood, T. J. Moon, C. C. Cunningham, and J. Käs. The optical stretcher: A novel laser tool to micromanipulate cells. *Biophysical Journal*, 81(2):767–784, aug 2001.

[56] J. Guck, S. Schinkinger, B. Lincoln, F. Wottawah, S. Ebert, M. Romeyke, D. Lenz, H. M. Erickson, R. Ananthakrishnan, D. Mitchell, J. Käs, S. Ulvick, and C. Bilby. Optical deformability as an inherent cell marker for testing malignant transformation and metastatic competence. *Biophysical Journal*, 88(5):3689–3698, may 2005.

[57] J. Guo, T. S. Pui, A. R. A. Rahman, and Y. Kang. 3d numerical simulation of a coulter counter array with analysis of electrokinetic forces. *Electrophoresis*, 34(3):417–424, 2013.

[58] A. W. Harley. An interactive node-link visualization of convolutional neural networks. In G. Bebis, R. Boyle, B. Parvin, D. Koracin, I. Pavlidis, R. Feris, T. McGraw, M. Elendt, R. Kopper, E. Ragan, Z. Ye, and G. Weber, editors, *Advances in Visual Computing*, pages 867–877, Cham, 2015. Springer International Publishing.

[59] T. Hastie, R. Tibshirani, and J. Friedman. *The Elements of Statistical Learning*. Springer New York, 2009.

[60] A. Hategan, R. Law, S. Kahn, and D. E. Discher. Adhesively-tensed cell membranes: Lysis kinetics and atomic force microscopy probing. *Biophysical Journal*, 85(4):2746–2759, oct 2003.

[61] X. He and D. N. Ku. Unsteady entrance flow development in a straight tube. *Journal of Biomechanical Engineering*, 116(3):355–360, aug 1994.

[62] B. P. Heath, N. Mohandas, J. L. Wyatt, and S. B. Shohet. Deformability of isolated red blood cell membranes. *Biochimica et Biophysica Acta (BBA) - Biomembranes*, 691(2):211–219, oct 1982.

[63] W. Helfrich. Elastic properties of lipid bilayers: Theory and possible experiments. *Z. Naturforsch*, 28 c:693–703, 1973.

[64] S. Hénon, G. Lenormand, A. Richert, and F. Gallet. A new determination of the shear modulus of the human erythrocyte membrane using optical tweezers. *Biophysical Journal*, 76(2):1145–1151, feb 1999.

[65] Y. Hirose, K. Yamashita, and S. Hijiya. Back-propagation algorithm which varies the number of hidden units. *Neural Networks*, 4(1):61–66, jan 1991.

[66] K. Hornik. Approximation capabilities of multilayer feedforward networks. *Neural Networks*, 4(2):251 – 257, 1991.

[67] X.-Q. Hu, A.-V. Salsac, and D. Barthès-Biesel. Flow of a spherical capsule in a pore with circular or square cross-section. *Journal of Fluid Mechanics*, 705:176–194, 2012.

[68] J. Hurley. Sizing particles with a Coulter counter. *Biophysical Journal*, 10:74–79, 1970.

[69] D. Isèbe and P. Nérin. Numerical simulation of particle dynamics in an orifice-electrode system. Application to counting and sizing by impedance measurement. *International Journal for Numerical Methods in Biomedical Engineering*, 29(4):462–475, 2013.

[70] K. Ishizuka, H. Matsubayashi, and M. Nishimori. Particle counting method and particle counting appartus, July. WO Patent 099116A1. 2015.

[71] M. Ismail and A. Lefebvre-Lepot. A'necklace' model for vesicles simulations in 2D. *International Journal for Numerical Methods in Fluids*, 76:835–854, 2014.

[72] C. Iss, D. Midou, A. Moreau, D. Held, A. Charrier, S. Mendez, A. Viallat, and E. Helfer. Self-organization of red blood cell suspensions under confined 2d flows. *Soft Matter*, 15:2971–2980, 2019.

[73] A. Jain, J. Mao, and K. Mohiuddin. Artificial neural networks: a tutorial. *Computer*, 29(3):31–44, mar 1996.

[74] V. Kachel. Sizing of cells by the electrical resistance pulse technique: Methodology and application in cytometric systems. *Cell Analysis*, 1:195–331, 1982.

[75] V. Kachel. Electrical resistance pulse sizing: Coulter sizing. In *Flow Cytometry and Sorting, Second Edition*, number 4, pages 45–80. Wiley-Liss, Inc., 1990.

[76] V. Kachel. Basic principles of electrical sizing of cells and particles and their realization in the new instrument "metricell". *J Histochem Cytochem.*, 24(1):211–230, Aug. 2019.

[77] A. Kamruzzahan, F. Kienberger, C. M. Stroh, J. Berg, R. Huss, A. Ebner, R. Zhu, C. Rankl, H. J. Gruber, and P. Hinterdorfer. Imaging morphological details and pathological differences of red blood cells using tapping-mode AFM. *Biological Chemistry*, 385(10), jan 2004.

[78] V. Kantsler, E. Segre, and V. Steinberg. Vesicle dynamics in time-dependent elongation flow: Wrinkling instability. *Physical Review Letters*, 99(178102), 2007.

[79] C. Kelemen, S. Chien, and G. M. Artmann. Temperature transition of human hemoglobin at body temperature: Effects of calcium. *Biophysical Journal*, 80:2622–2630, 2001.

[80] J. Kim and P. Moin. Application of a fractional-step method to incompressible Navier-Stokes equations. *Journal of Computational Physics*, 59:308–323, 1985.

[81] D. P. Kingma and J. Ba. Adam: A Method for Stochastic Optimization. 2014.

[82] Y. Koma, A. Onishi, H. Matsuoka, N. Oda, N. Yokota, Y. Matsumoto, M. Koyama, N. Okada, N. Nakashima, D. Masuya, H. Yoshimatsu, and Y. Suzuki. Increased red blood cell distribution width associates with cancer stage and prognosis in patients with lung cancer. *PLoS ONE*, 8(11):e80240, nov 2013.

[83] B. Kone, M. Maiga, B. Baya, Y. Sarro, N. Coulibaly, A. Kone, B. Diarra, M. Sanogo, A. Togo, D. Goita, M. Dembele, M. A. Polis, J. Warfield, M. Belson, S. Dao, S. Orsega, R. L. Murphy, S. Diallo, and S. Siddiqui. Establishing reference ranges of hematological parameters from malian healthy adults. *Journal of blood & lymph*, 7(29423342):154, 2017.

[84] M. Kraushaar. *Application of the compressible and low-mach number approaches to large-eddy simulation of turbulent flows in aero-engines.* PhD thesis, Université de Toulouse, 2011.

[85] A. Krizhevsky, I. Sutskever, and G. E. Hinton. Imagenet classification with deep convolutional neural networks. In F. Pereira, C. J. C. Burges, L. Bottou, and K. Q. Weinberger, editors, *Advances in Neural Information Processing Systems 25*, pages 1097–1105. Curran Associates, Inc., 2012.

[86] T. Krüger. Effect of tube diameter and capillary number on platelet margination and near-wall dynamics. *Rheologica Acta*, 55(6):511–526, 2016.

[87] T. Krüger, F. Varnik, and D. Raabe. Efficient and accurate simulations of deformable particles immersed in a fluid using a combined immersed boundary lattice Boltzmann finite element method. *Computers and Mathematics with Applications*, 61:3485–3505, 2011.

[88] E. Lac and D. Barthès-Biesel. Deformation of a capsule in simple shear flow: Effect of membrane prestress. *Physics of Fluids*, 17(072105), 2005.

[89] E. Lac, D. Barthès-Biesel, N. A. Pelekasis, and J. Tsamopoulos. Spherical capsules in three-dimensional unbounded Stokes flows: effect of the membrane constitutive law and onset of buckling. *Journal of Fluid Mechanics*, 516:303–334, 2004.

[90] E. Lac, A. Morel, and D. Barthès-Biesel. Hydrodynamic interaction between two identical capsules in simple shear flow. *Journal of Fluid Mechanics*, 573:149–169, 2007.

[91] L. Lanotte, J. Mauer, S. Mendez, D. A. Fedosov, J.-M. Fromental, V. Clavería, F. Nicoud, G. Gompper, and M. Abkarian. Red cells' dynamic morphologies govern blood shear thinning under microcirculatory flow conditions. *Proceedings of the National Academy of Sciences USA*, 113(47):13289–13294, 2016.

[92] J. M. Lappé, B. D. Horne, S. H. Shah, H. T. May, J. B. Muhlestein, D. L. Lappé, A. G. Kfoury, J. F. Carlquist, D. Budge, R. Alharethi, T. L. Bair, W. E. Kraus, and J. L. Anderson. Red cell distribution width, c-reactive protein, the complete blood count, and mortality in patients with coronary disease and a normal comparison population. *Clinica Chimica Acta*, 412(23-24):2094–2099, nov 2011.

[93] H. Lee, S.-Y. Kong, J. Y. Sohn, H. Shim, H. S. Youn, S. Lee, H. J. Kim, and H.-S. Eom. Elevated red blood cell distribution width as a simple prognostic factor in patients with symptomatic multiple myeloma. *BioMed Research International*, 2014:1–8, 2014.

[94] G. Lenormand, S. Hénon, A. Richert, J. Siméon, and F. Gallet. Direct measurement of the area expansion and shear moduli of the human red blood cell membrane skeleton. *Biophysical Journal*, 81(1):43–56, jul 2001.

[95] J. Li, M. Dao, C. T. Lim, and S. Suresh. Spectrin-level modeling of the cytoskeleton and optical tweezers stretching of the erythrocyte. *Biophysical Journal*, 88:3707–3719, 2005.

[96] J. Li, J. hang Cheng, J. yuan Shi, and F. Huang. Brief introduction of back propagation (BP) neural network algorithm and its improvement. In *Advances in Intelligent and Soft Computing*, pages 553–558. Springer Berlin Heidelberg, 2012.

[97] Y. Li, E. Jung, W. Lee, H. G. Lee, and J. Kim. Volume preserving immersed boundary methods for two-phase fluid flows. *International Journal for Numerical Methods in Fluids*, 69:842–858, 2012.

[98] C. Lim, M. Dao, S. Suresh, C. Sow, and K. Chew. Corrigendum to "large deformation of living cells using laser traps" [acta materialia 52 (2004) 1837–1845]. *Acta Materialia*, 52(13):4065–4066, aug 2004.

[99] G. Lippi and G. Cervellin. Risk assessment of post-infarction heart failure. systematic review on the role of emerging biomarkers. *Critical Reviews in Clinical Laboratory Sciences*, 51(1):13–29, jan 2014.

[100] W. K. Liu, Y. Chen, R. A. Uras, and C. T. Chang. Generalized multiple scale reproducing kernel particle methods. *Computer Methods in Applied Mechanics and Engineering*, 139:91–157, 1996.

[101] W. K. Liu, S. Jun, and Y. F. Zhang. Reproducing kernel particle methods. *International Journal for Numerical Methods in Fluids*, 20:1081–1106, 1995.

[102] Y. Liu and W. K. Liu. Rheology of red blood cell aggregation by computer simulation. *Journal of Computational Physics*, 220:139–154, 2006.

[103] E. Loiseau, G. Massiera, S. Mendez, P. Aguilar Martinez, and M. Abkarian. Microfluidic study of enhanced deposition of sickle cells at acute corners. *Biophysical Journal*, 108:2623–2632, 2015.

[104] M. MacMeccan, J. R. Clausen, G. P. Neitzel, and C. K. Aidun. Simulating deformable particle suspensions using a coupled lattice-Boltzmann and finite-element method. *Journal of Fluid Mechanics*, 618:13–39, 2009.

[105] M. Malandain, N. Maheu, and V. Moureau. Optimization of the deflated conjugate gradient algorithm for the solving of elliptic equations on massively parallel machines. *Journal of Computational Physics*, 238:32–47, 2013.

[106] A. Matsunaga, Y. Imai, C. Wagner, and T. Ishikawa. Reorientation of a single red blood cell during sedimentation. *Journal of Fluid Mechanics*, 806:102–128, 2016.

[107] J. Mauer, S. Mendez, L. Lanotte, F. Nicoud, M. Abkarian, G. Gompper, and D. A. Fedosov. Flow-induced transitions of red blood cell shapes under shear. *Physical Review Letters*, 121(11), sep 2018.

[108] J. L. McWhirter, H. Noguchi, and G. Gompper. Flow-induced clustering and alignment of vesicles and red blood cells in microcapillaries. *Proceedings of the National Academy of Sciences USA*, 106(15):6039–6043, 2009.

[109] J. L. McWhirter, H. Noguchi, and G. Gompper. Deformation and clustering of red blood cells in microcapillary flows. *Soft Matter*, 7:10967–10977, 2011.

[110] S. Mendez and M. Abkarian. In-plane elasticity controls the full dynamics of red blood cells in shear flow. *Physical Review Fluids*, 3(101101(R)), 2018.

[111] S. Mendez, E. Gibaud, and F. Nicoud. An unstructured solver for simulations of deformable particles in flows at arbitrary Reynolds numbers. *Journal of Computational Physics*, 256(1):465–483, 2014.

[112] J. P. Mills, M. Diez-Silva, D. J. Quinn, M. Dao, M. J. Lang, K. S. W. Tan, C. T. Lim, G. Milon, P. H. David, O. Mercereau-Puijalon, S. Bonnefoy, and S. Suresh. Effect of plasmodial RESA protein on deformability of human red blood cells harboring plasmodium falciparum. *Proceedings of the National Academy of Sciences*, 104(22):9213–9217, may 2007.

[113] N. Mohandas and E. A. Evans. Mechanical properties of the red cell membrane in relation to molecular structure and genetic defects. *Annual Review of Biophysics and Biomolecular Structure*, 23:787–818, 1994.

[114] F. M. M. Morel. QUANTITATION OF HUMAN RED BLOOD CELL FIXATION BY GLUTARALDEHYDE. *The Journal of Cell Biology*, 48(1):91–100, jan 1971.

[115] G. Nash, E. O'Brien, E. Gordon-Smith, and J. Dormandy. Abnormalities in the mechanical properties of red blood cells caused by plasmodium falciparum. *Blood*, 74(2):855–861, 1989.

[116] N. A. Nodargi, P. Bisegna, and F. Caselli. Effective computational modeling of erythrocyte electro-deformation. *Meccanica*, 52(3):613–631, Feb 2017.

[117] H. Noguchi and G. Gompper. Shape transitions of fluid vesicles and red blood cells in capillary flows. *Proceedings of the National Academy of Sciences USA*, 102(40):14159–14164, 2005.

[118] K. Ohene-Frempong, S. J. Weiner, L. A. Sleeper, S. T. Miller, S. Embury, J. W. Moohr, D. L. Wethers, C. H. Pegelow, F. M. Gill, and t. C. S. o. Sickle Cell Disease. Cerebrovascular accidents in sickle cell disease: Rates and risk factors. *Blood*, 91(1):288–294, 1998.

[119] A. V. Ooyen and B. Nienhuis. Improving the convergence of the back-propagation algorithm. *Neural Networks*, 5(3):465–471, jan 1992.

[120] U. Orhan, M. Hekim, and M. Ozer. EEG signals classification using the k-means clustering and a multilayer perceptron neural network model. *Expert Systems with Applications*, 38(10):13475–13481, sep 2011.

[121] W. Pan, B. Caswell, and G. E. Karniadakis. A low-dimensional model for the red blood cell. *Soft Matter*, 6:4366–4376, 2010.

[122] Y. Park, M. Diez-Silva, G. Popescu, G. Lykotrafitis, W. Choi, M. S. Feld, and S. Suresh. Refractive index maps and membrane dynamics of human red blood cells parasitized by plasmodium falciparum. *Proceedings of the National Academy of Sciences*, 105(37):13730–13735, sep 2008.

[123] S. Perrotta, P. G. Gallagher, and N. Mohandas. Hereditary spherocytosis. *The Lancet*, 372(9647):1411–1426, oct 2008.

[124] C. S. Peskin. Numerical analysis of blood flow in the heart. *Journal of Computational Physics*, 25:220–252, 1977.

[125] C. S. Peskin. The immersed boundary method. *Acta Numerica*, 11:479–517, 2002.

[126] V. Phansalkar and P. Sastry. Analysis of the back-propagation algorithm with momentum. *IEEE Transactions on Neural Networks*, 5(3):505–506, may 1994.

[127] A. Pinelli, I. Z. Naqavi, U. Piomelli, and J. Favier. Immersed-boundary methods for general finite-difference and finite-volume Navier–Stokes solvers. *Journal of Computational Physics*, 229:9073–9091, 2010.

[128] B. T. Polyak and A. B. Juditsky. Acceleration of stochastic approximation by averaging. *SIAM Journal on Control and Optimization*, 30(4):838–855, jul 1992.

[129] C. Price-Jones. The diameters of red cells in pernicious anæmia and in anæmia following hæmorrhage. *The Journal of Pathology and Bacteriology*, 25(4):487–504, 1922.

[130] T. Puiseux. *Numerical simulations for phase-contrast Magnetic Resonance Imaging*. PhD thesis, Université de Montpellier, 2019.

[131] T. Puiseux, A. Sewonu, O. Meyrignac, H. Rousseau, F. Nicoud, S. Mendez, and R. Moreno. Reconciling PC-MRI and CFD: an in-vitro study. *accepted in NMR in Biomedicine*, 2019.

[132] Y. Qiang, J. Liu, and E. Du. Dielectrophoresis testing of nonlinear viscoelastic behaviors of human red blood cells. *Micromachines*, 9(1), 2018.

[133] Z. Qin, J. Zhe, and G.-X. Wang. Effects of particle's off-axis position, shape, orientation and entry position on resistance changes of micro coulter counting devices. *Measurement Science and Technology*, 22:045804, 03 2011.

[134] M. Radmacher, R. Tillamnn, M. Fritz, and H. Gaub. From molecules to cells: imaging soft samples with the atomic force microscope. *Science*, 257(5078):1900–1905, sep 1992.

[135] S. Ramanujan and C. Pozrikidis. Deformation of liquid capsules enclosed by elastic membranes in simple shear flow: large deformations and the effect of fluid viscosities. *Journal of Fluid Mechanics*, 361:117–143, 1998.

[136] R. Rand and A. Burton. Mechanical properties of the red cell membrane. *Biophysical Journal*, 4(2):115–135, mar 1964.

[137] D. A. Reasor, J. R. Clausen, and C. K. Aidun. Coupling the lattice-Boltzmann and spectrin-link methods for the direct numerical simulation of cellular blood flow. *International Journal for Numerical Methods in Fluids*, 68:767–781, 2012.

[138] D. C. Rees, T. N. Williams, and M. T. Gladwin. Sickle-cell disease. *The Lancet*, 376(9757):2018–2031, dec 2010.

[139] M. Riedmiller. Advanced supervised learning in multi-layer perceptrons — from backpropagation to adaptive learning algorithms. *Computer Standards & Interfaces*, 16(3):265–278, jul 1994.

[140] A. M. Roma, C. S. Peskin, and M. J. Berger. An adaptive version of the immersed boundary method. *Journal of Computational Physics*, 153:509–534, 1999.

[141] M. J. Rosenbluth, W. A. Lam, and D. A. Fletcher. Analyzing cell mechanics in hematologic diseases with microfluidic biophysical flow cytometry. *Lab on a Chip*, 8(7):1062, 2008.

[142] D. E. Rumelhart, G. E. Hinton, and R. J. Williams. Parallel distributed processing: Explorations in the microstructure of cognition, vol. 1. chapter Learning Internal Representations by Error Propagation, pages 318–362. MIT Press, Cambridge, MA, USA, 1986.

[143] I. Safeukui, P. A. Buffet, S. Perrot, A. Sauvanet, B. Aussilhou, S. Dokmak, A. Couvelard, D. C. Hatem, N. Mohandas, P. H. David, O. Mercereau-Puijalon, and G. Milon. Surface area loss and increased sphericity account for the splenic entrapment of subpopulations of plasmodium falciparum ring-infected erythrocytes. *PLoS ONE*, 8(3):e60150, mar 2013.

[144] G. L. Salvagno, F. Sanchis-Gomar, A. Picanza, and G. Lippi. Red blood cell distribution width: A simple parameter with multiple clinical applications. *Critical Reviews in Clinical Laboratory Sciences*, 52(2):86–105, dec 2014.

[145] Seretis. Is red cell distribution width a novel biomarker of breast cancer activity? data from a pilot study. *Journal of Clinical Medicine Research*, 2013.

[146] D. Shin and K. Athanasiou. Cytoindentation for obtaining cell biomechanical properties. *Journal of Orthopaedic Research*, 17(6):880–890, nov 1999.

[147] J. H. Siggers and S. L. Waters. Steady flows in pipes with finite curvature. *Physics of Fluids*, 17(7):077102, jul 2005.

[148] J. Sigüenza. *Fluid-structure interaction problems involving deformable membranes: application to blood flows at macroscopic and microscopic scales*. PhD thesis, University of Montpellier, 2016.

[149] J. Sigüenza, S. Mendez, and F. Nicoud. Characterisation of a dedicated mechanical model for red blood cells: numerical simulations of optical tweezers experiment. *Computer Methods in Biomechanics and Biomedical Engineering*, 17(supp. 1):28–29, 2014.

[150] J. Sigüenza, S. Mendez, and F. Nicoud. How should the optical tweezers experiment be used to characterize the red blood cell membrane mechanics? *Biomechanics and Modeling in Mechanobiology*, 16:1645–1657, 2017.

[151] R. Skalak, A. Tozeren, R. P. Zarda, and S. Chien. Strain energy function of red blood cell membranes. *Biophysical Journal*, 13:245–264, 1973.

[152] J. M. Skotheim and T. W. Secomb. Red blood cells and other nonspherical capsules in shear flow: Oscillatory dynamics and the tank-treading-to-tumbling transition. *Physical Review Letters*, 98(078301), 2007.

[153] R. Specogna and F. Trevisan. A discrete geometric approach to solving time independent schrödinger equation. *Journal of Computational Physics*, 230:1370–1381, 2011.

[154] L. G. S. L. Spielman. Improving resolution in coulter counting by hydrodynamic focusing. *Journal of Colloid and Interface Science*, 26:175–182, 1968.

[155] I. Sraj, C. D. Eggleton, R. Jimenez, E. Hoover, J. Squier, J. Chichester, and D. W. M. Marr. Cell deformation cytometry using diode-bar optical stretchers. *Journal of Biomedical Optics*, 15(4):047010, 2010.

[156] G. D. Stefano, F. M. Denaro, and G. Riccardi. High-order filtering for control volume flow simulation. *International Journal for Numerical Methods in Fluids*, 37(7):797–835, 2001.

[157] A. R. Subhashree, P. J. Parameaswari, B. Shanthi, C. Revathy, and B. O. Parijatham. The reference intervals for the haematological parameters in healthy

adult population of chennai, southern india. *Journal of clinical and diagnostic research : JCDR*, 6(23373026):1675–1680, Dec. 2012.

[158] Y. Sui, X. B. Chen, Y. T. Chew, P. Roy, and H. T. Low. Numerical simulation of capsule deformation in simple shear flow. *Computers and Fluids*, 39:242–250, 2010.

[159] Y. Sui, Y. T. Chew, P. Roy, Y. P. Cheng, and H. T. Low. Dynamic motion of red blood cells in simple shear flow. *Physics of Fluids*, 20(112106), 2008.

[160] Y. Sui, H. T. Low, Y. T. Chew, and P. Roy. Tank-treading, swinging, and tumbling of liquid-filled elastic capsules in shear flow. *Physical Review E*, 77(016310), 2008.

[161] N. Takeishi, M. E. Rosti, Y. Imai, S. Wada, and L. Brandt. Haemorheology in dilute, semi-dilute and dense suspensions of red blood cells. *Journal of Fluid Mechanics*, 872:818–848, jun 2019.

[162] P. Taraconat, J.-P. Gineys, D. Isebe, F. Nicoud, and S. Mendez. Numerical simulation of deformable particles in a coulter counter. *International Journal for Numerical Methods in Biomedical Engineering*, aug 2019.

[163] G. Tchernia, N. Mohandas, and S. B. Shohet. Deficiency of skeletal membrane protein band 4.1 in homozygous hereditary elliptocytosis. implications for erythrocyte membrane stability. *Journal of Clinical Investigation*, 68(2):454–460, aug 1981.

[164] B. Timité, C. Castelain, and H. Peerhossaini. Pulsatile viscous flow in a curved pipe: Effects of pulsation on the development of secondary flow. *International Journal of Heat and Fluid Flow*, 31(5):879–896, oct 2010.

[165] G. Tomaiuolo, L. Lanotte, G. Ghigliotti, C. Misbah, and S. Guido. Red blood cell clustering in poiseuille microcapillary flow. *Physics of Fluids*, 24(051903), 2012.

[166] G. Tomaiuolo, M. Simeone, V. Martinelli, B. Rotoli, and S. Guido. Red blood cell deformation in microconfined flow. *Soft Matter*, 5:3736–3740, 2009.

[167] M. Uhlmann. An immersed boundary method with direct forcing for the simulation of particulate flows. *Journal of Computational Physics*, 209(2):448–476, nov 2005.

[168] S. O. Unverdi and G. Tryggvason. A front-tracking method for viscous, incompressible, multi-fluid flows. *Journal of Computational Physics*, 100:25–37, 1992.

[169] S. Vantieghem. *Numerical simulations of quasi-static magnetohydrodynamics using an unstructured finite volume solver: development and applications*. PhD thesis, Université Libre de Bruxelles, 2011.

[170] S. Velick and M. Gorin. The electrical conductance of suspensions of ellipsoids and its relation to the study of avian erythrocytes. *Journal of General Physiology*, 23(6):753–71, 1940.

[171] J. Walter, A.-V. Salsac, and D. Barthès-Biesel. Ellipsoidal capsules in simple shear flow: prolate versus oblate initial shapes. *Journal of Fluid Mechanics*, 676:318–347, 2011.

[172] J. Walter, A.-V. Salsac, D. Barthès-Biesel, and P. Le Tallec. Coupling of finite element and boundary integral methods for a capsule in a Stokes flow. *International Journal for Numerical Methods in Engineering*, 83:829–850, 2010.

[173] C. S. Waterman, E. E. J. Atkinson, B. J. Wilkins, C. L. Fischer, and S. L. Kimzey. Improved measurement of erythrocyte volume distribution by aperture-counter signal analysis. *Clinical Chemistry*, 21(9):1201–1211, 1975.

[174] J. H. Williamson. Low-storage Runge-Kutta schemes. *Journal of Computational Physics*, 35:48–56, 1980.

[175] A. Z. K. Yazdani and P. Bagchi. Three-dimensional numerical simulation of vesicle dynamics using a front-tracking method. *Physical Review E*, 85(056308), 2012.

[176] A. Z. K. Yazdani and P. Bagchi. Influence of membrane viscosity on capsule dynamics in shear flow. *Journal of Fluid Mechanics*, 718:569–595, 2013.

[177] A. Z. K. Yazdani, R. M. Kalluri, and P. Bagchi. Tank-treading and tumbling frequencies of capsules and red blood cells. *Physical Review E*, 83(046305), 2011.

[178] A. Yeşil, E. Senateş, I. V. Bayoğlu, E. D. Erdem, R. Demirtunç, and A. O. Kurdaş Övünç. Red cell distribution width: a novel marker of activity in inflammatory bowel disease. *Gut and Liver*, 5(22195244):460–467, Dec. 2011.

[179] J. Zhang, P. C. Johnson, and A. S. Popel. Effects of erythrocyte deformability and aggregation on the cell free layer and apparent viscosity of microscopic blood flows. *Microvascular Research*, 77:265–272, 2009.

[180] J.-R. Zhang, J. Zhang, T.-M. Lok, and M. R. Lyu. A hybrid particle swarm optimization–back-propagation algorithm for feedforward neural network training. *Applied Mathematics and Computation*, 185(2):1026–1037, feb 2007.

[181] H. Zhao, A. H. G. Isfahani, L. N. Olson, and J. B. Freund. A spectral boundary integral method for flowing blood cells. *Journal of Computational Physics*, 229:3726–3744, 2010.

[182] Y. Zheng, J. Chen, T. Cui, N. Shehata, C. Wang, and Y. Sun. Characterization of red blood cell deformability change during blood storage. *Lab Chip*, 14(3):577–583, 2014.

[183] Y. Zheng, E. Shojaei-Baghini, A. Azad, C. Wang, and Y. Sun. High-throughput biophysical measurement of human red blood cells. *Lab on a Chip*, 12(14):2560–2567, 2012.

[184] O. Y. Zhong-can and W. Helfrich. Bending energy of vesicle membranes: General expressions for the first, second, and third variation of the shape energy and applications to spheres and cylinders. *Physical Review A*, 39(10):5280–5288, 1989.

[185] V. Zmijanovic, S. Mendez, V. Moureau, and F. Nicoud. About the numerical robustness of biomedical benchmark cases: Interlaboratory FDA's idealized medical device. *International Journal for Numerical Methods in Biomedical Engineering*, 33(1):e02789:1–17, 2017.

Abstract

In Coulter counters, cells counting and volumetry is achieved by monitoring their electrical print when they flow through a polarized micro-orifice. However, the volume measurement may be impaired when the trajectory of the cell is in the vicinity of the aperture edges due to complex dynamics and deformations of the cell.

In this thesis, numerical simulations of the dynamics and electrical signature of red blood cells (RBCs) in a Coulter counter are presented, accounting for the deformability of the cells. In particular, a specific numerical pipeline is developed to overcome the challenge of the multi-scale nature of the problem. It consists in segmenting the whole computation of the cell dynamics and electrical response in a series of dedicated computations, with a saving of one order of magnitude in computational time. This numerical pipeline is used with rigid spheres and deformable red blood cells in an industrial Coulter counter geometry and compared with experimental measurements. The simulations not only reproduce electrical signatures typical of those measured experimentally, but also provide an understanding of the key mechanisms at play in the complex signatures induced by RBCs following a near-wall trajectory.

Based on this new understanding provided by numerical simulations, a filtering strategy is introduced, which allows the filtering of pulses induced by near-wall paths which are irrelevant for the cells sizing. The method is shown to retrieve the expected symmetrical distribution of RBCs and provides results comparable to hydrodynamical focusing, a more intricate implementation of the Coulter principle. Such a result paves the way for a robust assessment of haematological parameters with a cheaper and simpler implementation, compared to hydrofocused devices.

The impact of the cell morphology and rheology on the electrical print is evidenced for near-wall trajectories. Indeed, by altering the cell deformability and sphericity, the electrical pulses are proven to differ from predefined normality of measurements. Furthermore, neural network modellings are performed in the aims of assessing such RBC properties. Among the proposed processing, classification of normal, stiffened and spherical RBCs is provided. Finally, the inverse problem of numerical simulations is achieved, thus allowing the evaluation of the mechanical parameters of RBCs.

Keywords : *Computational Fluid dynamics ; Fluid-Structure Interaction, Red Blood Cells ; Coulter counter ; Impedance Measurements ; Neural Networks*

Résumé

Le comptage et la volumétrie des cellules sanguines est réalisé par l'analyse des signatures électriques provenant de leur passage dans un micro-orifice polarisé. Cependant, les mesures peuvent être altérées par des dynamiques et déformations complexes de la cellule lorsque la trajectoire empruntée est proche des parois de l'orifice.

Dans cette thèse, des dynamiques de Globules Rouges (GRs) dans un compteur Coulter et les signatures électriques correspondantes sont simulées. La prise en compte de la déformabilité des GRs implique de se confronter au caractère multi-échelle de ce type de configuration. Une méthode est proposée pour contourner cette difficulté de modélisation. En particulier, le calcul de la dynamique et de la perturbation électrique est fractionné en une séquence de simulations spécifiques, et le coût de calcul est réduit d'un ordre de grandeur. La méthode proposée est utilisée pour simuler des signaux de sphères rigides et de GRs, et les résultats sont validés par comparaisons avec des données expérimentales. L'association des signaux expérimentaux à des dynamiques de GRs dans l'orifice fournit une compréhension inédite des mécanismes en jeu dans les signatures complexes observées lorsque la cellule emprunte une trajectoire proche-paroi.

Cette connaissance nouvelle des signatures a permis l'élaboration d'une nouvelle approche de tri permettant d'isoler les pulses associées aux passages en bord, non adaptés pour la volumétrie des cellules. La méthode introduite retrouve la distribution symétrique attendue pour le volume des GRs et donne des résultats comparables à la focalisation hydrodynamique, une implémentation plus complexe du principe Coulter. Les résultats ainsi obtenus ouvrent la voie à une mesure des paramètres hématologiques plus précise tout en conservant la simplicité et le coût modéré d'un système classique.

L'impact des paramètres morphologiques et rhéologiques des cellules sur les signatures correspondants à des passages proche paroi est illustré. En modifiant la déformabilité et la sphéricité des GRs dans une approche expérimentale, les mesures diffèrent d'une normalité préétablie. De plus, des modélisations par réseaux de neurones sont réalisées dans le but d'accéder aux propriétés du GR à partir du pulse électrique. Parmi les traitements proposés, une classification des GRs normaux, rigides et sphériques est réalisée. Enfin, la modélisation du problème inverse des simulations numériques est effectuée afin d'évaluer de manière quantitative les paramètres mécaniques des GRs.

Mots-clefs : *Mécanique des fluides numérique ; Interaction Fluide-Structure ; Globules Rouges ; Compteur Coulter ; Mesures d'impédance ; Réseaux de neurones*